Article:
Lyutikov, M, Komissarov, S, Sironi, L et al. (2018) Particle acceleration in explosive relativistic reconnection events and Crab Nebula gamma-ray flares. Journal of Plasma Physics, 84 (2). 635840201. ISSN: 0022-3778

https://doi.org/10.1017/S0022377818000168

Particle acceleration in explosive relativistic reconnection events and Crab Nebula gamma-ray flares

Maxim Lyutikov,[1] Lorenzo Sironi[2], Sergey Komissarov[1,3], Oliver Porth[3,4]

[1] *Department of Physics, Purdue University, 525 Northwestern Avenue, West Lafayette, IN 47907-2036, USA; lyutikov@purdue.edu*

[2] *Harvard-Smithsonian Center for Astrophysics, 60 Garden Street, Cambridge, MA 02138, USA; lsironi@cfa.harvard.edu*

[3] *School of Mathematics, University of Leeds, LS29JT Leeds, UK; s.s.komissarov@leeds.ac.uk*

[4] *Institut für Theoretische Physik, J. W. Goethe-Universität, D-60438, Frankfurt am Main, Germany porth@th.physik.uni-frankfurt.de*

ABSTRACT

We develop a model of particle acceleration in explosive reconnection events in relativistic magnetically-dominated plasmas and apply it to explain gamma-ray flares from the Crab Nebula. The model relies on development of current-driven instabilities on macroscopic scales (not related to plasma skin depths), driven by large-scales magnetic stresses (of the type "parallel currents attract"). Using analytical and numerical methods (fluid and particle-in-cell simulations), we study a number of model problems involving merger of both current-carrying and zero total current magnetic flux tubes in relativistic magnetically-dominated plasma: (i) we extend Syrovatsky's classical model of explosive X-point collapse to magnetically-dominated plasmas; (ii) we consider instability of two-dimensional force-free system of magnetic islands/flux tubes (2D "ABC" structures); (iii) we consider merger of two zero total poloidal current magnetic flux tubes. In all cases regimes of spontaneous and driven evolution are investigated.

We identify two stages of particle acceleration: (i) fast explosive prompt X-point collapse and (ii) ensuing island merger. The fastest acceleration occurs during the initial catastrophic X-point collapse, with the reconnection electric field of the order of the magnetic field. During the X-point collapse particles are accelerated by charge-starved electric fields, which can reach (and even exceed) values of the local magnetic field. The explosive stage of reconnection produces non-thermal power-law tails with slopes that depend on the average magnetization σ. For plasma magnetization $\sigma \leq 10^2$ the spectrum power law index is $p < 2$; in this case the maximal energy depends linearly on the size of the reconnecting islands. For higher magnetization, $\sigma \geq 10^2$, the spectra are soft, $p < 2$, yet the maximal energy γ_{max} can still exceed the average magnetic energy per particle, $\sim \sigma$, by orders of magnitude (if p is not too close to unity). The X-point collapse stage is followed by magnetic island merger that dissipates a large fraction of the initial magnetic energy in a regime of forced magnetic reconnection, further accelerating the particles, but proceeds at a slower reconnection rate.

Crab flares result from the initial explosive stages of magnetic island mergers of magnetic flux tubes produced in the bulk of nebula at intermediate polar regions. The Crab pulsar produces polar-angle dependent magnetized wind which is magnetically-dominated at medium polar angles. Post-termination shock plasma flow in the wind sectors with magnetization $\sigma \geq 1$ naturally generates large-scale highly magnetized structures, even in the case of mildly magnetized wind. Internal kink-like instabilities lead to the formation of macroscopic current-carrying magnetic flux tubes that merge explosively. Importantly, the reconnection/acceleration is driven by large-scales magnetic stresses (not related to the development of the slow tearing mode). Sectors of the wind contributing to flares have high magnetization, $10 \leq \sigma \leq 100$.

The model has all the ingredients needed for Crab flares: natural formation of highly magnetized regions, explosive dynamics on light travel time, development of high electric fields on macroscopic scales and

acceleration of particles to energies well exceeding the average magnetic energy per particle.

Contents

1. Crab Nebula gamma-ray flares: observational constraints and theoretical challenges

The detection of flares from Crab Nebula by AGILE and Fermi satellites (Tavani et al. 2011; Abdo et al. 2011; Buehler et al. 2012) is one of the most astounding discoveries in high energy astrophysics. The unusually short durations, high luminosities, and high photon energies of the Crab Nebula gamma-ray flares require reconsideration of our basic assumptions about the physical processes responsible for acceleration of the highest-energy emitting particles in the Crab Nebula, and, possibly in other high-energy astrophysical sources. During flares, the Crab Nebula gamma-ray flux above 100 MeV exceeded its average value by a factor of several or higher, while in other energy bands nothing unusual was observed (Weisskopf et al. 2013).

The discovery of flares from Crab Nebula, exhibiting unusually short durations, high luminosities, and high photon energies, challenges our understanding of particle acceleration in PWNe, and, possibly in other high-energy astrophysical sources. On the one hand, the low magnetization numerical models of Crab Nebula (Komissarov & Lyubarsky 2004; Del Zanna et al. 2004; Lyutikov et al. 2016) are able to reproduce the morphological details of the Crab Nebula down to intricate details. Lyutikov et al. (2016) demonstrated that the inner knot of the Crab nebula is produced by a low magnetization section of the pulsar wind passing through the termination shock. The implied acceleration mechanism is then the acceleration at the termination shock (Rees & Gunn 1974; Kennel & Coroniti 1984), presumably via the stochastic Fermi-type process. This is currently the dominant paradigm.

On the other hand, contrary to the exceptionally detailed explanation of the morphological features, low magnetization models cannot reproduce the spectrum both of the stationary emission (Lyutikov 2010) and especially of the flares (Clausen-Brown & Lyutikov 2012). Even before the discovery of Crab flares Lyutikov (2010) argued that the observed cutoff in synchrotron spectrum of the Crab Nebula at ~ 100 MeV in the persistent Crab Nebula emission is too high to be consistent with the stochastic shock acceleration. Indeed, balancing electrostatic acceleration in a regular electric field with synchrotron energy losses yields the synchrotron photon energy $\epsilon_{\rm max} \sim \eta\hbar\frac{mc^3}{e^2} \approx 100$ MeV. where η is the ratio of the average *accelerating* electric field to magnetic field strengths. Since high conductivity of astrophysical plasma ensures that in most circumstances $\eta \leq 1$, the observed value of the cutoff is right at the very limit. This estimate is confirmed by self-consistent PIC simulations of particle acceleration rates at unmagnetized shocks (Sironi et al. 2013).

During the gamma-ray flares the cutoff energy approached even higher value of ~ 400 MeV, suggesting Doppler boosting or a different acceleration mechanism. In addition, recent optical observations show no significant variability of the brightest features associated with the termination shock (Weisskopf et al. 2013; Rudy et al. 2015a), apparently ruling out the shock acceleration as a mechanism behind the flares. Thus, *low magnetization models reproduce the Crab PWN morphology, but the implied acceleration mechanism, the stochastic shock acceleration, fails to reproduce the spectrum.*

There is a number of possible resolutions of the problem. First, bulk relativistic motion reduces the requirement on the acceleration rate in the rest frame by the Doppler factor. Though no relativistic motion is observed in the bulk of the nebula, it is possible to have mildly relativistic motion, with the Doppler factor of a few, in specific locations, *e.g.,* near the axial part of the flow produced by a highly anisotropic pulsar wind (Komissarov & Lyubarsky 2004; Komissarov & Lyutikov 2011). A highly anisotropic pulsar wind produces non-spherical termination shock, in which case the post-shock Lorentz factor can be at least of the order of the inverse of the angle of attack and even higher for high-sigma wind. [1] Sonic perturbation propagating from the downstream flow can then induce short variations in the synchrotron emission (Lyutikov et al. 2012).

An alternative possibility is that magnetic reconnection in *highly magnetized plasma* is responsible for the acceleration of the wind leptons (Lyutikov 2010; Cerutti et al. 2014a, 2013). How can these contradicting arguments (*i.e.,* low magnetization that explains the morphology and high magnetization needed for efficient acceleration) be reconciled? Sironi & Spitkovsky (2011a); Komissarov (2013); Lyubarsky (2012) pointed out that while particle acceleration may be efficient at the termination shock of the equatorial striped section of pulsar wind, it is unlikely to operate in the polar section which is free from stripes (see also Sironi & Spitkovsky (2012)). Through this section of the shock, a highly magnetized plasma must be injected into the nebula and the magnetic reconnection in this plasma could be responsible for the observed flares. Moreover, the magnetic dissipation is needed to reconcile the observed sub-equipartition magnetic field of the Crab Nebula with its theoretical models. This conclusion is supported by the recent 3D numerical simulations of PWNe by Porth et al. (2013), who demonstrated that indeed magnetic flux can be efficiently dissipated via reconnection events. In the model of Porth et al. (2013) the pulsar wind has both the low-sigma sectors (this reproduces the overall morphology of the PWN), as well as high-sigma sectors (this allows the existence of highly magnetized plasma in the post-shock region). It is within these highly magnetized regions, at intermediate latitudes, that we envision the reconnection processes taking place.

The microphysics of the acceleration in relativistic reconnection layers has been addressed by a number of collaborations (*e.g.,* Bessho & Bhattacharjee 2012; Guo et al. 2015; Deng et al. 2015, and others). In particular, the Colorado group (Uzdensky et al. 2011; Cerutti et al. 2012a,c, 2013) simulated the development of the tearing mode in the relativistic highly magnetized plasma aiming to explain Crab flares. In tearing mode instability of a relativistic current layer (see also Lyutikov 2003a; Komissarov et al. 2007): after a short time a *quasi-stationary* relativistic reconnection reconnection layer is set-up. One of the demands on the acceleration mechanism imposed by the observations of Crab flares is that acceleration must proceed exceptionally fast and occur on macroscopic scales. This requirement is, generally, not satisfied in tearing-mode based models.

There is a number of features of the approach of the Colorado group that we find unsatisfactory. First, in the collisionless plasma the typical thickness of the tearing-mode driven reconnection layer is microscopic - related to the plasma skin depth. The length of the magnetic flux tube might be somewhat larger than it's transverse size, but not much larger: long thin current-carrying flux tubes created during the development of a tearing mode are unstable due to kink instability on scales, typically, few times their transverse size Zenitani & Hoshino (2007); Daughton et al. (2011); Karimabadi et al. (2013). As we argue below in §9.5, a typical potential available over a few skin depths is too small

[1] Parameter σ is defined as twice the ratio of the rest-frame magnetic energy density to plasma enthalpy w (rest mass energy density for cold plasma, $\sigma = B^2/(4\pi w) \to B^2/(4\pi n m_e c^2)$

to account for the observed particles' energies. (In the presence of the guide field, on the one hand, the flux tubes are stabilized, and can extend to scales much longer than the transverse size of few skin depth, but on the other hand the reconnection rate, and thus the efficiency of acceleration are reduced (Zenitani & Hoshino 2008).) Second, in a quasi-stationary regime and at scales much larger than the skin depth the velocity of the inflow into the reconnection layer is small, much smaller than the speed of light. Recent studies of relativistic reconnection by means of 2D and 3D PIC simulations have demonstrated that, for a reference magnetization $\sigma = 10$ (i.e., ten times more energy in magnetic fields than in the plasma rest mass), the reconnection rate in anti-parallel reconnection (i.e., in the absence of a guide field perpendicular to the reconnection plane) is much smaller in 3D, where $r_{\rm rec} \sim 0.02$, than in 2D, where $r_{\rm rec} \sim 0.1$ (Sironi & Spitkovsky 2014). As a result of slow inflowing velocity, much smaller than the speed of light, it is hard to (i) produce electric fields within the reconnection region that are of the same order as magnetic fields; (ii) it is hard to reconcile the overall energetics of flares: small inflow velocities do not allow the emission to tap a sufficiently large volume of magnetic energy during the short duration of the flares. Also, the development of the tearing mode generally does not lead to global reconfigurations - it typically results in a local dissipation event (like saw-tooth oscillations in TOKAMAKs Fisch 1987). Finally, and most importantly, Crab flares require acceleration to Lorentz factors $\gamma \sim 10^9$. In the simulations of (Uzdensky et al. 2011; Cerutti et al. 2012a,c, 2013) *all* the particles present within the acceleration region are accelerated. If all the particles within a volume are accelerated, their terminal Lorentz factor is $\gamma_{p,max} \sim \sigma$. This requires regions with magnetization $\sigma \sim 10^9$ - such highly magnetized regions are unlikely to exist with the Nebula. Finally, the initial set-up in the simulations by (Uzdensky et al. 2011; Cerutti et al. 2012a,c, 2013) is not force-free - it already has particles with energy σ, while the final $\gamma_{p,max} \sim 4\sigma$.

In this paper we develop an alternative model of reconnection in highly magnetized plasma, that overcomes all of the above-mentioned problems related to the tearing-mode instabilities in the plane-parallel geometry. Most importantly, reconnection in our model is explosive, occurs on macroscopic scales (not related to plasma skin depth), the electric fields approach magnetic fields in the bulk and, thus, are an order of magnitude higher than in the case considered by Cerutti et al. (2012a,c) (large inflow velocities allow to tap into larger energy containing volume and larger number of particles). Importantly, only a small relative number of particles is accelerated - thus, the terminal Lorentz factor is not limited by σ.

2. Large scale dynamics of PWNe - formation of current-carrying flux tubes

2.1. Post-shock flow of magnetized plasma: natural formation of highly magnetized regions

The powerful Crab flares require that energy from a macroscopic scale is made available to the acceleration process. As we will discuss in the following, current-driven MHD instabilities like the coalescence of parallel currents and the "X-point collapse" can be a viable way to achieve this. One of the key questions is then how a violently unstable and highly magnetized configuration is setup in the first place. To locate potential sites for the flaring region, we need to identify regions of high sigma and analyze the flow structure in these candidate flaring regions. Here we use the result of simulations by Porth et al. (2014a). Although the scales required for the "daily" flare duration are not resolved by the simulation (its resolution is > 3 light-days), it is instructive to correlate the high-sigma region (that forms as a consequence of flow-expansion) with the current distribution in the simulations.

As Lyutikov et al. (2016) discuss, the modeling of the inner knot of the Crab Nebula requires that the equatorial flow is weakly magnetized. Intermediate latitudes can still be highly magnetized. In fact, highly magnetized regions in the bulk of the nebula can be achieved via flow expansion at intermediate latitude regions *starting with only mildly magnetized wind*. In Fig. 1 we show the magnetization in the xy-plane from simulations of (Porth et al. 2014a). One can clearly see that the magnetization rises well above the maximal injected value of $\sigma = 1$. The highest value of $\sigma \approx 8$ in the snapshot is achieved at the point where radial expansion reverses and forms the plume-like polar flow.

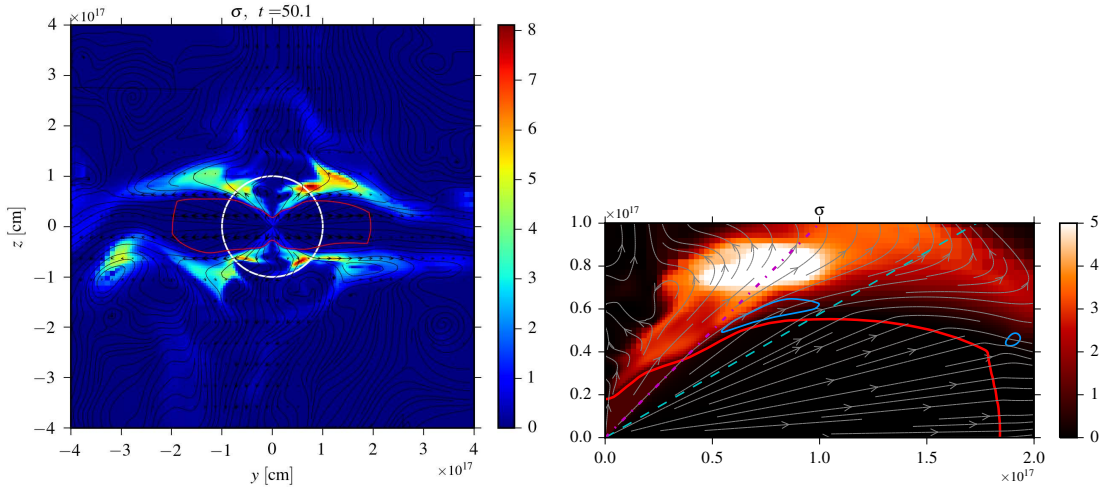

Fig. 1.— *Left panel.* Magnetization in the yz plane, also indicating the location of the spherical cuts as white circles. The radii are $r \in [1, 1.5, 2, 2.5, 3] \times 10^{17}$cm. *Right panel.* Zoom-in on the central part. The dashed line is the line of view and the blue curves show the regions of enhanced observed emissivity (the inner knot Lyutikov et al. 2016). The dot-dashed line separates the high and low magnetization regions of the wind. The arrowed lines are the instantaneous stream lines. There is a clearly visible region of high magnetization at intermediate latitudes.

The theory behind the formation of highly magnetized regions starting with only mildly magnetized conditions at the reverse shock is discussed in §9.2

2.2. Current filamentation

As the mildly relativistic post-shock flow decelerates, it comes into a global causal contact. Once causally connected, the almost purely toroidal magnetic configuration of the nebula flow is liable to current-driven instabilities (e.g. Begelman 1998; Mizuno et al. 2011). As pointed out by Lyubarsky (2012), in a highly magnetized expanding post-shock flow, the flow lines are in fact focussed to the axis via the magnetic hoop-stress which can act as an additional trigger for instability. Thereby the innermost flow reaches the recollimation point first and is expected to experience violent instability and magnetic dissipation. Lyubarsky (2012) hence argues that the γ-ray flares originate in the polar region at the base of the observed jet/plume. On the one hand, the simulations of Porth et al. (2014a) are in agreement with this dynamical picture and show development of $m \sim few$ modes that lead to the formation of current filaments at the jet base. On the other hand, for numerical stability, Porth et al. (2014a) could only study moderate polar magnetizations of $\sigma \leq 3$ which disfavours rapid particle acceleration. Even without this technical limitation, for non-vanishing wind power, the axis itself cannot carry a DC Poynting flux. Because of this, we are interested in flow lines from intermediate latitudes that acquire high sigma due to flow expansion.

To visualize the current in the simulations, we now cut the domain by spherical surfaces and investigate current-magnitude and magnetization in the $\phi\theta$-plane. The white circles in Fig. 1 indicates the location of the innermost spherical test-surface shown in the top panel of Fig. 2. In general, the current exhibits a quadrupolar morphology, it is distributed smoothly over the polar regions and returns near the equator. When the test-surface crosses over the termination shock, we observe an increased return-current due to the shock jump of B_ϕ. Although the field is predominantly toroidal in the high sigma downstream region, perturbations from the unstable jet occasionally lead to current filaments and even reversals just downstream of the termination shock.

With increasing distance from the termination-shock, the flow becomes more and more turbulent which leads to increased filamentation and copious sign changes of the radial current. In the underlying simulations, the magnetization in the turbulent regions has dropped already below unity which disfavours rapid particle acceleration at distances larger than a few termination shock radii. It is interesting to point out that although the magnetic field injected in the model decreases gradually over a large striped region of 45°, an equatorial current sheet develops none the less in the nebula. This can be seen in the lower panel of Fig.2 which corresponds to a surface outside of the termination shock at $r = 3 \times 10^{17}$cm.

To better understand the geometry of the current and magnetic field, we display a representative volume rendering of the polar region in Fig. 3. In the rendering, one can see the violently unstable polar beam embedded into the more regular high-σ region comprised of toroidal field lines. The plume forms downstream of this structure and is also strongly perturbed. A part of the disrupted plume approaches the termination shock as a flux-tube. The presence of such a configuration where two flux tubes can come together very close to the high sigma region lets us speculate that Crab flares might originate when the right geometry (e.g. parallel flux tubes) coincides with high magnetization as present in the nebula even for moderate wind magnetization. For higher magnetizations of the polar beam, the mechanism described by Lyubarsky (2012) could directly act also without first having to rely on enhancement of σ via flow expansion. Extrapolating from the moderate sigma simulations where the polar beam is highly unstable and forms a filamented current, this seems feasible at the very least.

A targeted investigation of the Crab nebula polar flow also with higher magnetization of σ up to 10 was performed by Mignone et al. (2013) through injecting a jet into the shocked nebula ambient. The model is appropriate for the lightyear scale plume but lacks the formation of the jet via the hoop-stress in the nebula. To match the kinked morphology of the observations of the plume, models with moderate bulk Lorentz factors $\Gamma = 2$ are favoured. Fragmentation of the current and highly intermittent structures also develop in the large scale flow, but with time-scales of not much less than a year. The highest variability and potential reconnection sites are localized at the termination zone of the jet at

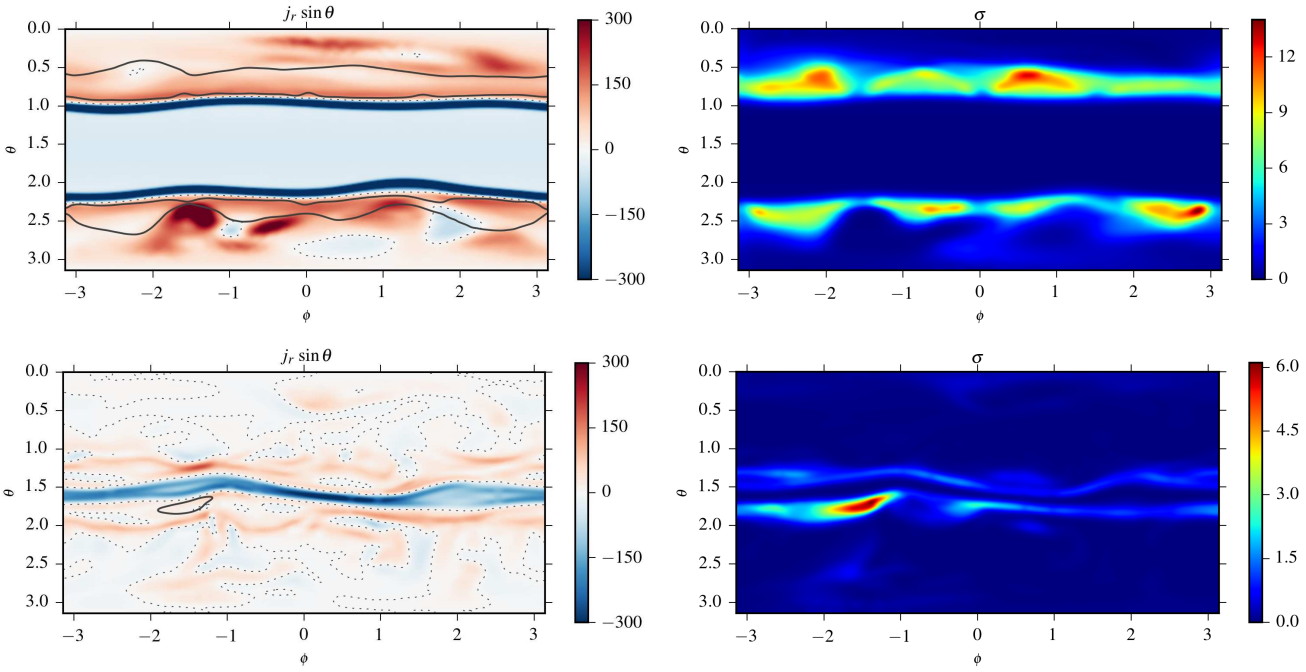

Fig. 2.— Distribution of the radial current, $j_r \sin\theta$ *(left)* and magnetization σ *(right)*. Dashed contours indicate the sign changes of the current and solid contours indicate levels of $\sigma = 4$. *Top:* Sphere with $r = 10^{17}$cm, one can see formation of current filaments (*e.g.,* regions $\theta \approx 2.5$ and $\phi \approx -1.5, -0.5$). The current direction can even reverse, (the region $\theta \approx 2.7$, $\phi \approx -1$). *Bottom:* Sphere with $r = 3 \times 10^{17}$cm. Here the current is highly filamentary and an equatorial current-sheet has developed. The average magnetization in the current sheet and in the turbulent flow is < 1 but magnetically dominated regions can still be obtained ($\sigma \approx 6$ at $\theta \approx 1.75$, $\phi \approx -1.5$).

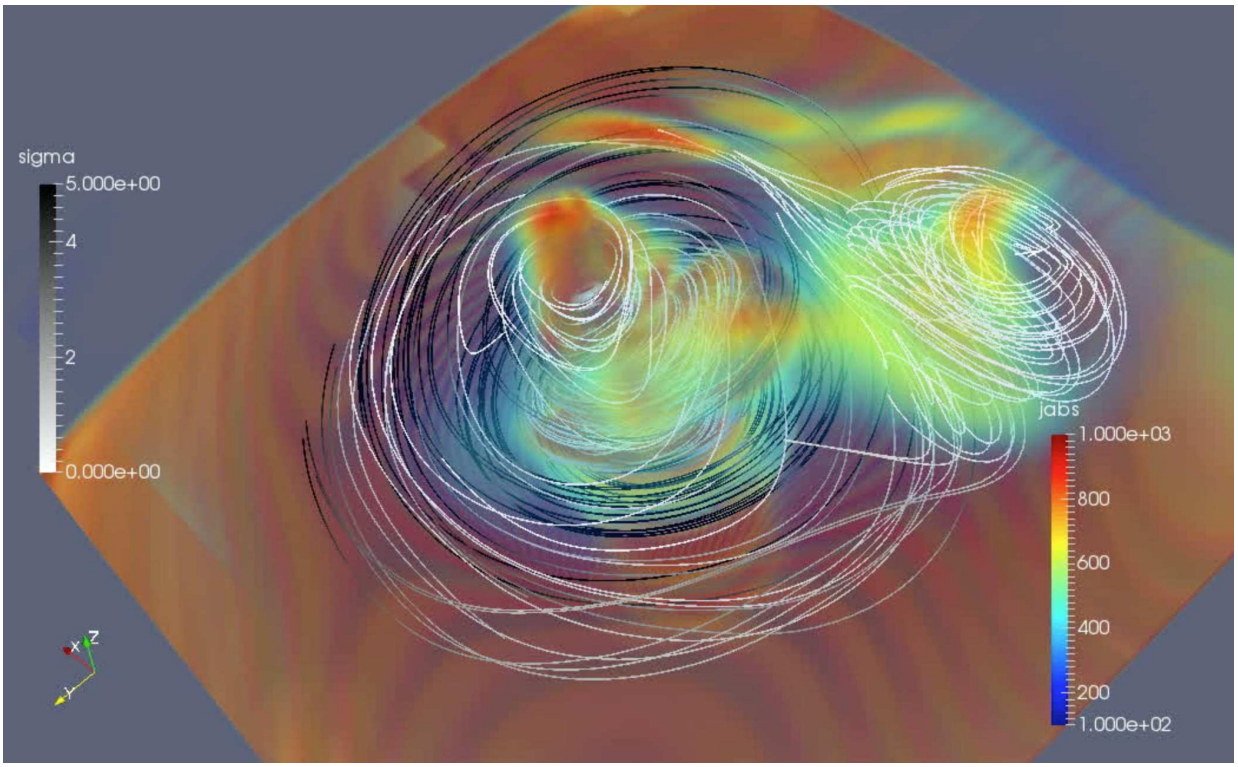

Fig. 3.— 3D volume rendering showing current filamentation of the polar beam just downstream of the termination shock. The shock surface is indicated as the orange plane and we draw field-lines shaded from white ($\sigma = 0$) to black ($\sigma = 5$). One clearly sees two current filaments producing structures similar to magnetic flux tubes. As discussed in Porth et al. (2014a), streamlines from intermediate latitudes reach the axis behind this inner violently unstable region and form a plume-like outflow of moderate velocity $v \approx 0.7c$.

the edge of the nebula. At this point the magnetization has dropped considerably due to internal dissipation. These features speak against the large scale jet as a site for the γ-ray flares.

In conclusion, large scale simulations indicate that even for mildly magnetized winds (for wind magnetization $\sigma_w \geq$ few) the post-shock flow naturally forms highly magnetized regions. These regions are unstable to large scale current-driven instabilities that lead to the formation of current/magnetic filaments. In the following sections we discuss a number of plasma-physical models that can lead to impulsive particle acceleration in such configurations.

3. X-point collapse in force-free plasma

Explosive release of magnetic energy is a well known phenomenon in laboratory and space plasmas (*e.g.,* Priest & Forbes 2000). One of the promising line of research follows the work of Syrovatskii (Imshennik & Syrovatskiĭ 1967; Syrovatskii 1975, 1981) on the explosive collapse of a magnetic X-point (see also Cowley & Artun 1997). In this Section we consider explosive X-point collapse and particle acceleration in highly magnetized relativistic plasma.

3.1. Dynamic force-free plasma

The properties of plasma in many high energy astrophysics sources are very different from those of more conventional Solar and laboratory plasmas. The principal difference is that it is relativistically strongly magnetized, $\sigma = u_B/u_p \gg 1$, where $u_B = B^2/8\pi$ is the magnetic energy density and u_p is the plasma energy density (including the rest mass). The parameter regime of highly magnetized plasma, $\sigma \gg 1$, implies that (i) the inertia of this plasma is dominated by the magnetic fieldand not by the particle rest mass, $B^2/8\pi \gg \rho c^2$, (ii) the propagation speed of Alfvén waves approaches the speed of light, (iii) the conduction current flows mostly along the magnetic fieldlines, (iv) the displacement current $(c/4\pi)\partial_t \mathbf{E}$ may be of the same order as the conduction current, $\mathbf{j}$, (v) the electric charge density, ρ_e, may be of the order of j/c. These are very different from the properties of laboratory plasmas, plasmas of planetary magnetospheres, and the interplanetary plasma, the cases where plenty of experimental data and theoretical results exist (Lyutikov & Lazarian 2014).

The large expected value of σ (or small $1/\sigma$) may be used as an expansion parameter in the equations of relativistic magnetohydrodynamics. The zero order equations describe the so-called relativistic force-free approximation. One may see this limit as the model where massless charged particles support currents and charge densities such that the total Lorentz force vanishes all the time (this also insures the ideal condition $\mathbf{E}\cdot\mathbf{B} = 0$.) This allows one to related the current to electro-magnetic fields (Uchida 1997; Gruzinov 1999)

$$\mathbf{J} = \frac{c}{4\pi}\frac{(\mathbf{E}\times\mathbf{B})\nabla\cdot\mathbf{E} + (\mathbf{B}\cdot\nabla\times\mathbf{B} - \mathbf{E}\cdot\nabla\times\mathbf{E})\mathbf{B}}{B^2} \tag{1}$$

This may be considered as the Ohm's law for ideal relativistic force-free electro-dynamics (the electromagnetic invariant $\mathbf{E}\cdot\mathbf{B} = 0$; that electromagnetic energy is conserved, $\mathbf{E}\cdot\mathbf{J} = 0$.)

In a modification of the ideal approach, one can also study dissipative processes in force-free electro-dynamics (*e.g.,* Lyutikov 2003a; Li et al. 2012, ; importantly, only parallel component of the electric current is subject to resistive dissipation). In §4.1 we use a variant of the resistive force-free, Eq. (15).

3.2. Stressed X-point collapse in force-free plasma: analytical solution

Let us consider the X-point collapse in a force-free plasma, with the Ohm's law given by (1). Consider a vicinity of a magnetic X-point. The non-current-carrying configuration has null lines intersecting at 90 degrees. Following the classic work on the collapse of a non-relativistic X-point (Dungey 1953; Imshennik & Syrovatskiĭ 1967; Priest & Forbes 2000), let us assume that the initial configuration is squeezed by a factor λ, so that the initial configuration has a vector potential $A_z \propto x^2 - y^2/\lambda^2$. In addition, we assume that there is an axial constant magnetic field B_0. [2]

[2] In Appendix A we demonstrate, using force-free and PIC simulations, that an unstressed X-point is stable to small-scale perturbations.

We are looking for time evolution of a vector potential of the type

$$A_z = -\left(\frac{x^2}{a(t)^2} - \frac{y^2}{b(t)^2}\right)\frac{B_\perp}{2L}, \tag{2}$$

where parameters $B_\perp$ and L characterize the overall scaling of the magnetic field and the spacial scale of the problem. The evolving electric and magnetic fields are then

$$\begin{aligned}\mathbf{B} &= \mathrm{curl}\, A_z\mathbf{e}_z + B_0\mathbf{e}_z\\ \mathbf{E} &= -\partial_t\mathbf{A} + \nabla\Phi(t,x,y)\end{aligned} \tag{3}$$

The ideal condition $\mathbf{E}\cdot\mathbf{B} = 0$ then gives

$$\mathbf{E}\cdot\mathbf{B} = \left(-x^2\frac{\partial_t a}{a^3} + y^2\frac{\partial_t b}{b^3}\right)\frac{B_\perp B_0}{cL} + \left(\frac{x\partial_y\Phi}{a^2} + \frac{y\partial_x\Phi}{b^2}\right)\frac{B_\perp}{L} \tag{4}$$

The initial condition for the squeezed X-point and the ideal condition requires

$$\begin{aligned}b(t) &= \lambda/a(t)\\ \Phi &= xy\frac{B_0}{c}\partial_t \ln a\end{aligned} \tag{5}$$

(Since $\Delta\Phi = 0$ there is no induced charge density.) Parameter a characterizes the "squeezeness" of the configuration.

Near the X-point, $x, y \to 0$, we have $B^2 = B_0^2$, $\mathbf{B}\cdot\mathrm{curl}\,\mathbf{B} \approx \frac{B_0 B_\perp}{L}(1/a^2 - (a/\lambda)^2)$, $\mathbf{E}\cdot\mathrm{curl}\,\mathbf{E} \approx 2\frac{B_0 B_\perp}{c^2 L}\dot{a}^2(x^2/a^4 + (y/\lambda)^2$, $\mathrm{div}\mathbf{E} = 0$. In this limit the induction equation gives

$$\partial_t^2 \ln a = \mathcal{A}\left(\frac{a^4 - \lambda^2}{\lambda^4}\right),\ \mathcal{A} = \frac{c^2}{L^2}\frac{B_\perp^2}{B_0^2} \tag{6}$$

Eq. (6) describes the time evolution of the "squeezeness" parameter a. For a given $a(t)$ the electromagnetic fields are

$$\begin{aligned}\mathbf{B} &= \left\{\frac{a^2}{\lambda^2}\frac{y}{L}B_\perp, \frac{x}{La^2}B_\perp, B_0\right\}\\ \mathbf{E} &= \left\{\frac{yB_0}{c}, \frac{xB_0}{c}, -\frac{x^2\lambda^2 + y^2a^4}{cL\lambda^2a^2}\right\}\partial_t \ln a\end{aligned} \tag{7}$$

These solutions are valid for $x, y \le (B_0/B_\perp)L$, or, in other words, as long as the in-plane magnetic field is smaller that B_0. (Note that for the unsqueezed configuration, $\lambda = \alpha = 1$, the magnetic field near the null is an expansion of a force-free multiple island configuration (29) with $B_\perp = B_0/(2\pi)$.)

Solutions of the equations (6) show that "the sqeezinees" parameter $a(t)$ has a finite time singularity for $\lambda < 1$: in finite time a becomes infinite, see Fig. 5. (For $\lambda > 1$ in finite time a becomes zero, so that b becomes infinite.) Thus, we have generalized the classic solution of Imshennik & Syrovatskiĭ (1967) to the case of force-free plasma. At the moment when one of the parameters a or b becomes zero, the current sheet forms, see Fig. 4.

The structure of the electric field in the $x-y$ plane does not change during the collapse and qualitatively resembles the initial configuration of the magnetic field. The z-component of the electric field evolves from a slightly squeezed parabola at small times, $E_z \propto (x^2\lambda^2 + y^2a^4)$ to a trough-shape at later times, $E_z \propto y^2$. (At time $t = 0$ the electric field is zero.)

For small times $t \to 0$ (when $|a-1| << 1$), with initial conditions $a(0) = 1$, $a'(0) = 0$, and assuming that the initial "squeezing" is small, $\lambda = 1 - \epsilon$, $\epsilon \ll 1$, the solution is

$$a = 1 + \epsilon\sinh^2\left(\frac{ct}{L}\frac{B_\perp}{B_0}\right) \tag{8}$$

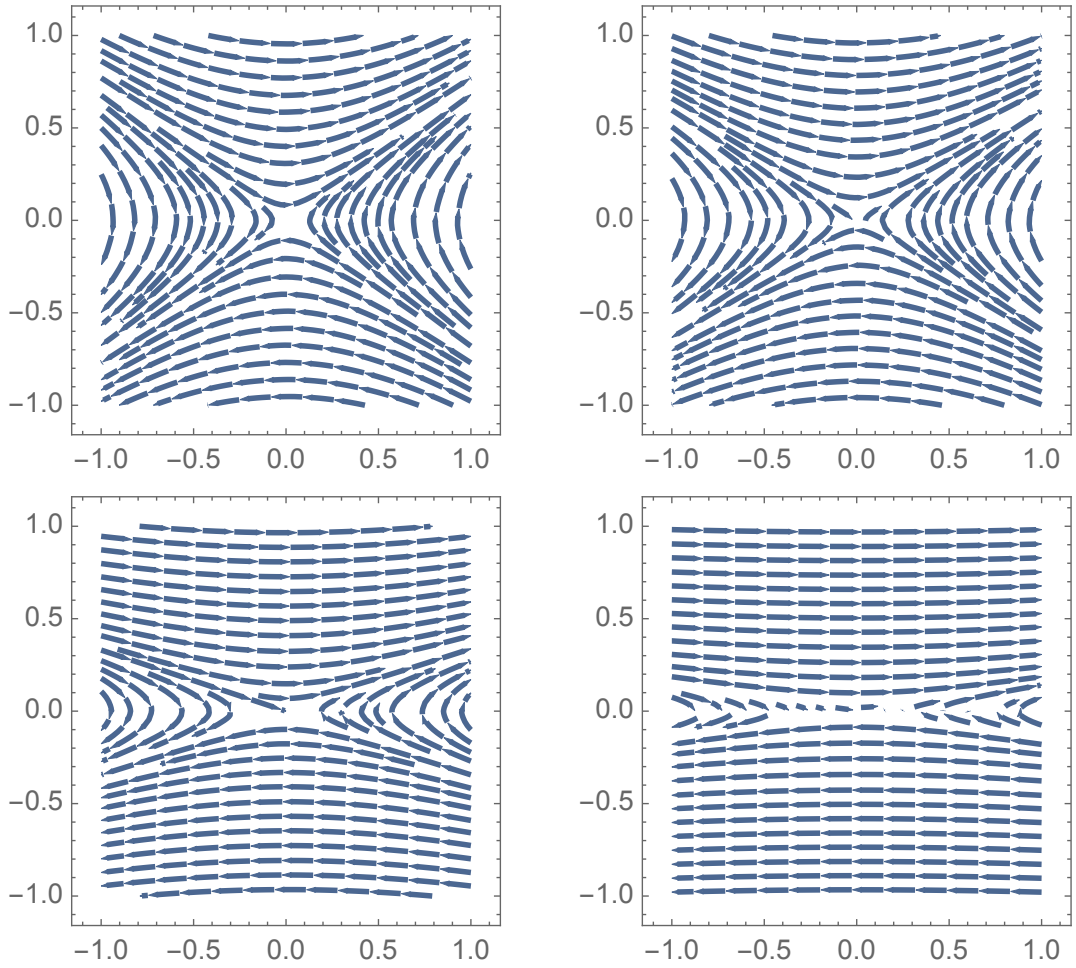

Fig. 4.— Structure of the magnetic field in the $x-y$ plane during X-point collapse in force-free plasma. The initial configuration on the left is slightly "squeezed". On dynamical time scale the X-point collapses to form a current sheet, right Fig.. The structure of the electric field in the $x-y$ plane does not change during the collapse and qualitatively resembles the $t=0$ configuration of the magnetic field.

Thus, the typical collapse time is

$$\tau \sim \frac{L}{c}\frac{B_0}{B_\perp} \tag{9}$$

is of the order of the Alfvén (light) crossing time of the initial configuration.

At these early times the electric field grows exponentially in time

$$\mathbf{E} = \{y, x, -\frac{x^2+y^2}{L}\frac{B_\perp}{B_0}\}\sinh\left(2\frac{ct}{L}\frac{B_\perp}{B_0}\right)\frac{B_\perp \epsilon}{L} \tag{10}$$

Note, that the ratio of the electric field, dominated mostly by E_z, to the magnetic field, dominated at late times by B_x,

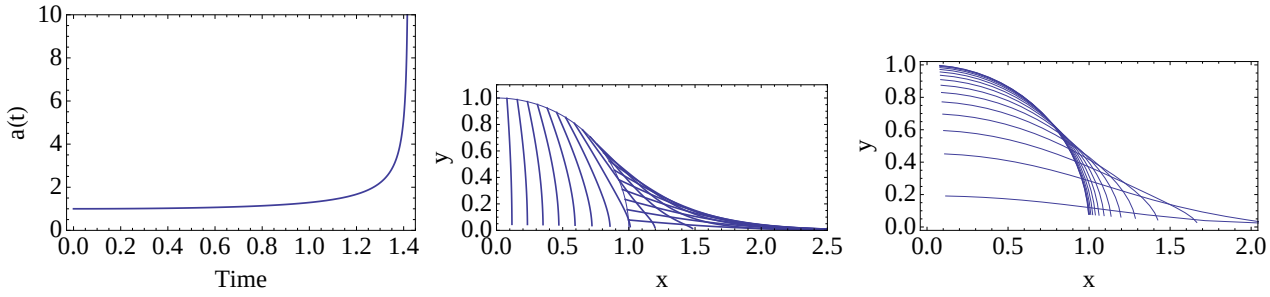

Fig. 5.— *Left Panel*: An example of the evolution of the parameter $a(t)$, Eq. (6). Initially an X-point is squeezed by ten percent, $\lambda = 0.9$, parameter $\mathcal{A} = 1$. Evolution occurs on the dynamical time scale, until a singularity at $t = 1.42$, so that the fast growing stage of the collapse proceeds much quicker. *Center Panel.* Particles' drift trajectories during the collapse of the X-point. Initially particles are located on a unit circle. (Different fluid elements do not intersect: trajectories show time evolution of each fluid element.) *Right Panel* Temporal evolution of the initially isotropic distribution of particles. During the X-point collapse, the particles are "squeezed" towards the neural layer.

increases with y (distances away from the newly forming current sheet),

$$\frac{E_z}{B_x} \sim \frac{y}{x_0}\frac{B_\perp}{B_0} \tag{11}$$

Thus, the analytical model predicts that the electric field becomes of the order of the magnetic field in the whole domain. This is confirmed by numerical simulations, §4.

At early times the electromagnetic drift velocity is

$$\begin{aligned} v_x &= \frac{x}{L}\epsilon \sinh\left(2\frac{ct}{L}\frac{B_\perp}{B_0}\right)\frac{B_\perp}{B_0} \\ v_y &= -v_x(y/x) \end{aligned} \tag{12}$$

At these times the particle drift motion follows a trajectory in the $x-y$ plane $y \propto 1/x$. During the final collapse, in the limit $a \to \infty$, the particle distribution is further squeezed towards the neutral layer, $y \propto 1/(a^2\sqrt{\ln x})$ (though in this limit the drift approximation becomes inapplicable.) This shows that the X-point is stretched in one direction and is compressed in the other direction (note that $\nabla \mathbf{v} = 0$ - collapse is incompressible at the initial stage).

We have also verified that the evolution of the system in case of slowly developing or periodic stress proceeds in a similar fashion, Fig. 6. The collapse develops slowly until stress reaches, approximately, 50% value, after which collapse proceeds very fast. If subject to periodic perturbation, *e.g.,* $\lambda = 1 - \delta\sin(\omega t)$, the collapse always occurs - reversing the stress does not stop the collapse, only prolongs it, Fig. 6.b.

3.3. Expected charge starvation during collapse

During the X-point collapse the electromagnetic fields and currents experience a sharp growth, especially near the null line. The current density at the null line is

$$J_z \approx \frac{c}{4\pi}\frac{B_\perp}{L}a(t)^2 \tag{13}$$

(assuming $a \gg 1$). Since $a \to \infty$ during collapse, the current density similarly increases during the collapse. As the parameter a grows, this imposes larger and larger demand on the velocity of the current-carrying particles. But the

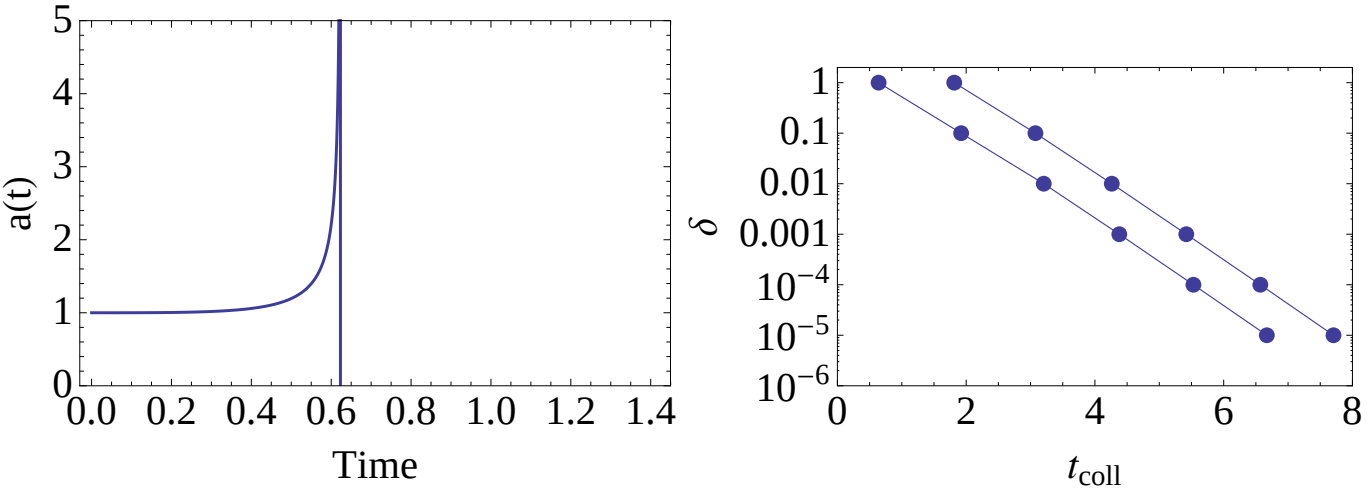

Fig. 6.— Left Panel. Collapse of an X-point with gradually building stress, $\lambda = (1 - t/\tau)$, compare with Fig. 8. Right Panel. Time to collapse (when the solution of Eq. (6) becomes zero or infinity) of an X-point subject to a periodic perturbation $\lambda = 1 - \delta \sin(\omega t)$ for $\omega = 1$ (lower curve) and $\omega = .1$ (upper curve). Time to collapse depends logarithmically on the amplitude of perturbations and is typically of the order of a few.

maximum current density cannot exceed $J_z < 2en_e c$. Thus, if

$$a(t) > \sqrt{\frac{L}{\delta}} \frac{1}{\sigma^{1/4}} \tag{14}$$

the current becomes charge-starved (here, $\delta = c/\omega_p$, $\omega_p^2 = 4\pi n_e e^2/m_e$ are plasma skin depth and plasma frequencies)

In our PIC simulations, §4.2, $L/\delta = 800$, while $\sigma_L = 4 \times 10^3 - 4 \times 10^4$, where we have defined σ_L to be the value of the magnetization at L. At different distances, the magnetization changes with the square of the distance. Thus we expect that the charge starvation occurs approximately at $a \sim$ few, when the opening of the X-point becomes tens of degrees. These estimates are in agreement with the PIC runs.

Thus, in an ideal relativistic force-free plasma a stressed X-point undergoes a finite time collapse. The assumption of the force-free plasma will be broken down when the inflow velocity would become of the order of the Alfvén velocity and/or when the charge starvation regime is reached. Then, the maximum electric field is $E \sim \beta_A B_\perp$ which is of the order of B_0, magnetic field in the bulk, for $\sigma \geq 1$.

4. X-point collapse: numerical simulations

4.1. Force-free simulations: X-point collapse

Next we compare the analytical results described above with numerical simulations. First we do force-free simulations. In force-free simulations, we solve the system of Maxwell equations supplemented with the Ohm law

$$\mathbf{j} = \varrho \frac{\mathbf{E}\times\mathbf{B}}{B^2} c + \kappa_{\parallel}\mathbf{E}_{\parallel} + \kappa_{\perp}\mathbf{E}_{\perp}. \tag{15}$$

In the Ohm law, the first term represents the drift current, where the electric charge density ρ is found from the Gauss law. The second and third terms are the conductivity current along and perpendicular to the magnetic field respectively. $\kappa_{\perp}$ is set to zero unless $E > B$, in which case it is set to a high value in order to quickly obtain $E \leq B$. $\kappa_{\parallel}$ is always set to a high value in order to quickly drive the solution towards the force-free state with $E_{\parallel} = 0$. The numerical approach is described in details in Komissarov et al. (2007). It is second order in space and time with the source terms treated using the Strand-splitting algorithm. The method of Generalized Lagrange Multiplier (GLM) is employed to keep the magnetic field almost divergence-free.

The X-point collapse simulations are initialized with vanishing electric field and the magnetic field described by Eq. (7), with parameters $a = 1$, $\lambda = \sqrt{0.5}$, $L = 1$, $B_{\perp} = 1$ $B_0 = 1$. The computational grid is a two-dimensional Cartesian grid with 400×400 cells covering the x-y domain $[-2, 2] \times [-2, 2]$. We imposed the zero-gradient boundary conditions, which leads to deformations of the X-point configuration near boundaries which propagate towards the center with the speed of light. However, these waves do not reach the central area of interest on the simulation time scale. Fig. 7 shows the magnetic field lines and the strength of the guide field B_0 in the central area of the size L at four instances during the time interval $[0, 1]$. One can see the expected rapid collapse of the squeezed X-point.

Fig. 8 shows the evolution of the parameter a, which is measured using Eq.7 as

$$a(t) = \lambda^{1/2}(xB_x/yB_y)^{1/4}\,,$$

and the strength of the electric field, both computed at the point $(x, y) = (-0.1, 0.1)$. which is inside the domain of applicability of the solution (8), namely $x, y \ll (B_0/B_{\perp})\lambda^2 L$. One can see that although the characteristic time scale is close to $\tau = 1$ based on the analytical solution, the numerical solution does not quite follow the analytical one. This is because the constraint on the length scale also sets the limitation on the time-scale $t \ll (B_0/B_{\perp})\lambda^2(L/c) = \lambda^2\tau$. Moreover, as one can see in Fig. 7, the guide field already shows significant evolution on this time-scale, contrary to what is assumed in the analytic solution.

For $t \gg \tau$ the solution exhibits self-similar evolution – this is expected as the only characteristic length scale of this problem is $l_g = (B_0/B_{\perp})L$. Its main properties are illustrated in Fig. 9. The contours of $B^2 - E^2$ are elongated along the x axis. The X-point is replaced by a thin current sheet with two Y-points at its ends. Ahead of each of Y-point there are bow-shaped regions where the drift speed is very close to c and $E \simeq B$.

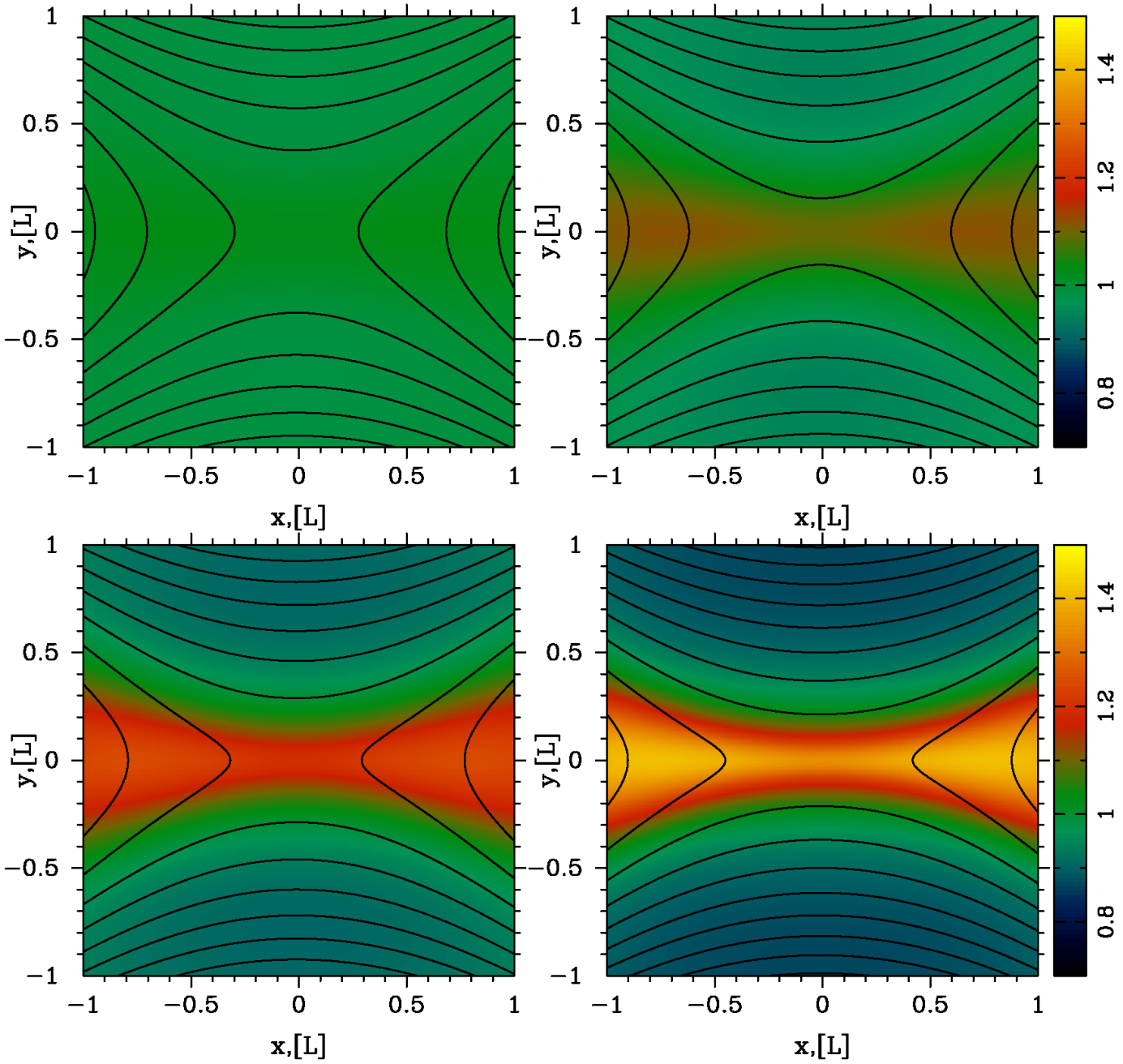

Fig. 7.— Initial phase of a solitary X-point collapse in FF simulations. The plots show B_z at t =0.25, 0.5, 0.75 and 1. These plots are to be compared with Fig. 10, which shows the results of PIC simulations with the same initial setup.

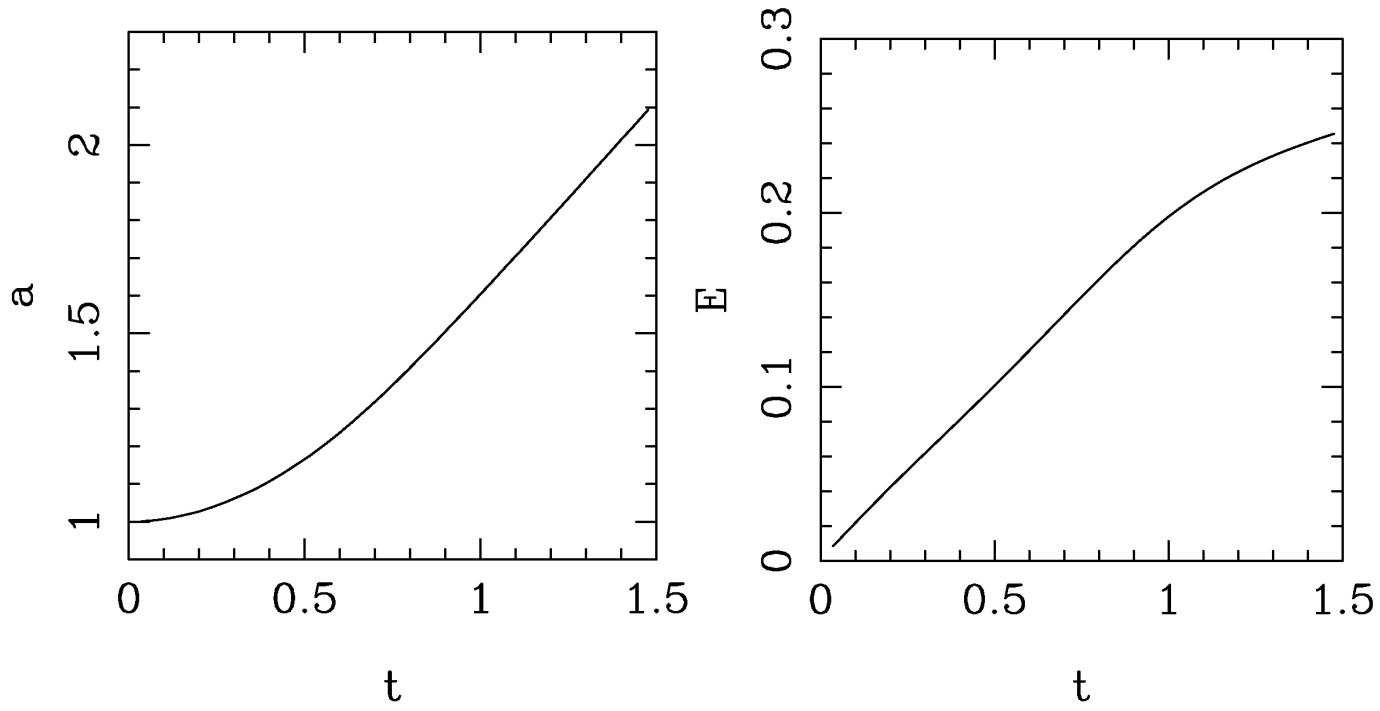

Fig. 8.— Evolution of the parameter $a(t)$ (left panel) and the total electric field strength $E(t)$ (right panel) during the initial phase. The measurements are taken at the point $(x, y) = (-0.1, 0.1)$. The analytical solution gives the collapse time $\tau = 1.0$. These results are sufficiently close, considering the fact that Eq. (6) was derived as an asymptotic limit near the X-point.

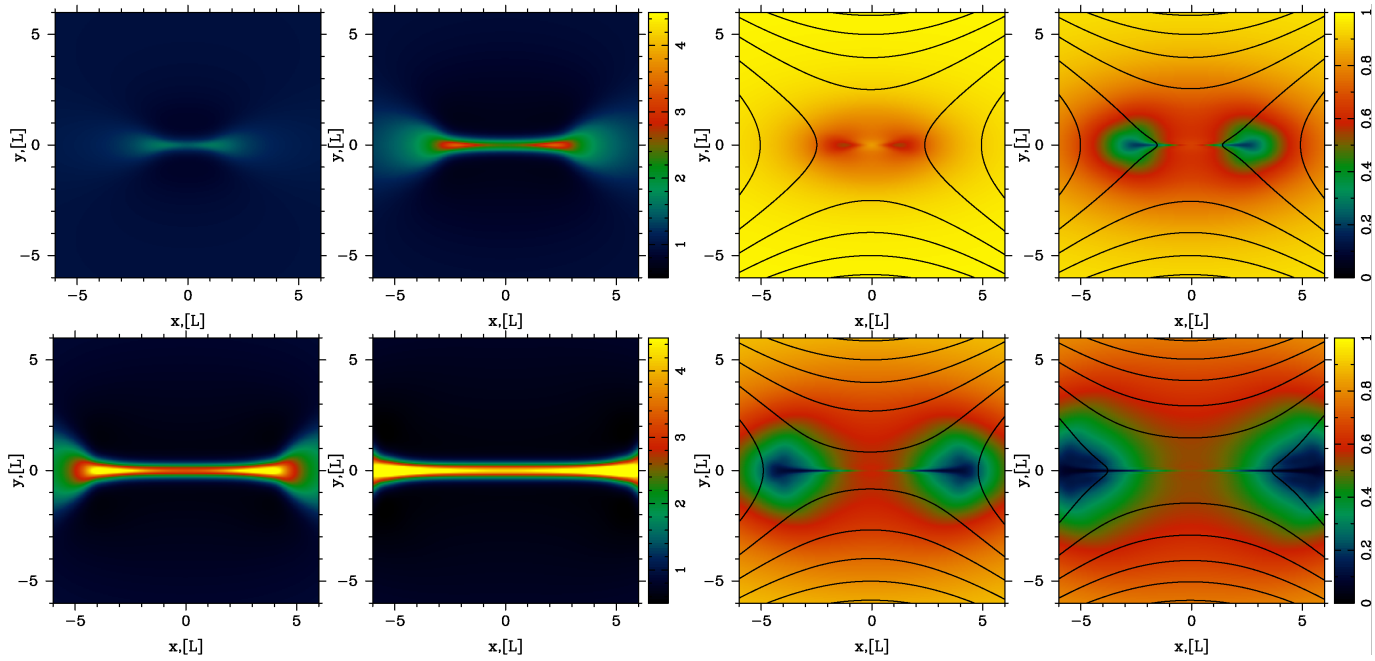

Fig. 9.— Long-term evolution of stressed solitary X-point in FF simulations. The left panel shows the B_z component of the magnetic field. The right panel shows $1 - E^2/B^2$ (colour) and magnetic field lines The plots show the numerical solution at $t = 1.5$, 3, 4.5 and 6. PIC simulations for the same initial configuration are shown in Figures 13 and 14.

4.2. PIC simulations of stressed X-point collapse

4.2.1. Overall principles and parameters of PIC simulations

The most fundamental method for simulating the kinetic dynamics of a reconnecting plasma involves the use of particle-in-cell (PIC) codes, that evolve the discretized equations of electrodynamics — Maxwell's equations and the Lorentz force law (Hockney & Eastwood 1981; Birdsall & Langdon 1991). PIC codes can model astrophysical plasmas from first principles, as a collection of charged macro-particles — each representing many physical particles — that are moved by integration of the Lorentz force.[3] The electric currents associated with the macro-particles are deposited on a grid, where Maxwell's equations are discretized. Electromagnetic fields are then advanced via Maxwell's equations, with particle currents as the source term. Finally, the updated fields are extrapolated to the particle locations and used for the computation of the Lorentz force, so the loop is closed self-consistently.

We study the collapse of a solitary X-point with 2D PIC simulations, employing the massively parallel electromagnetic PIC code TRISTAN-MP (Buneman 1993; Spitkovsky 2005). Our computational domain is a square in the $x-y$ plane, which is initialized with a uniform density of cold electron-positron plasma (the composition of pulsar wind nebulae is inferred to have negligible ion/proton component). The simulation is initialized with a vanishing electric field and with the magnetic field appropriate for a stressed X-point collapse (see Eq. (7)) with $\lambda = 1/\sqrt{2}$, for direct comparison with the force-free results described above.[4] The stressed X-point configuration would require a particle current in the direction perpendicular to the simulation plane, to sustain the curl of the field (which, on the other hand, is absent in the case of an unstressed X-point). In our setup, the computational particles are initialized at rest, but such electric current gets self-consistently built up within a few timesteps. At the boundaries of the box, the field is reset at every timestep to the initial configuration. This leads to a deformation of the self-consistent X-point evolution which propagates from the boundaries toward the center at the speed of light. However, our domain is chosen to be large enough such that this perturbation does not reach the central area of interest within the timespan covered by our simulations.

We perform two sets of simulations. First, we explore the physics at relatively early times with a 2D Cartesian grid of 32768×32768 cells. The spatial resolution is such that the plasma skin depth $c/\omega_{\rm p}$ is resolved with 10 cells.[5] The unit length is $L = 800\, c/\omega_{\rm p}$, so that the domain size is a square with $\simeq 4L$ on each side. The physical region of interest is the central $2L \times 2L$ square. The simulation is evolved up to $\sim L/c$, so that the artificial perturbation driven by the boundaries does not affect the region of interest. In a second set of simulations, we explore the physics at late times, with a 2D Cartesian box of 40960×40960 cells, with spatial resolution $c/\omega_{\rm p} = 1.25$ cells. With the unit length still being $L = 800\, c/\omega_{\rm p}$, the overall system is a square of $\simeq 41L$ on each side. At early times, the evolution is entirely consistent with the results of the first set of simulations described above, which suggests that a spatial resolution of $c/\omega_{\rm p} = 1.25$ cells is still sufficient to capture the relevant physics (more generally, we have checked for numerical convergence from $c/\omega_{\rm p} = 1.25$ cells up to $c/\omega_{\rm p} = 20$ cells). We follow the large-scale system up to $\sim 6L/c$, so that the evolution of the physical region at the center stays unaffected by the boundary conditions.

For both sets of simulations, each cell is initialized with two positrons and two electrons (with a small thermal dispersion of $kT/mc^2 = 10^{-4}$), but we have checked that our results are the same when using up to 24 particles per

[3] For this work, we employ the Vay pusher, since we find that it is more accurate than the standard Boris algorithm in dealing with the relativistic drift velocities associated with the reconnection flows (Vay 2008).

[4] We have also explicitly verified that an unstressed X-point (i.e., with $\lambda = 1$) is stable.

[5] In the case of a cold plasma, the skin depth is defined as $c/\omega_{\rm p} = \sqrt{mc^2/4\pi ne^2}$. For a hot plasma, it is defined as $c/\omega_{\rm p} = \sqrt{mc^2[1+(\hat{\gamma}-1)^{-1}kT/mc^2]/4\pi ne^2}$, where $\hat{\gamma}$ is the adiabatic index.

cell. In order to reduce noise in the simulation, we filter the electric current deposited onto the grid by the particles, effectively mimicking the effect of a larger number of particles per cell (Spitkovsky 2005; Belyaev 2015).

We explore the dependence of our results on two physical parameters, namely the strength of the guide field and the flow magnetization. In one set of simulations, the strength of the guide field B_0 (which is uniform across the box) is chosen to be equal to the in-plane field $B_\perp$ at the scale L, as measured along the unstressed direction (i.e., the x direction, in our setup). Due to the linear increase of the in-plane fields with distance from the center, along the stressed direction (i.e., the x direction, in our setup) the in-plane and guide fields will be equal at a distance of $\lambda^2 L = L/2$ from the center. The case of guide-field collapse allows for a direct comparison with analytical theory and force-free results. In the second set of simulations, we initialize the system with a vanishing guide field. This case will be relevant for our investigation of the collapse of ABC structures. There, we will demonstrate that particle acceleration is most efficient at null points, i.e., where both the in-plane fields and the out-of-plane guide field vanish.

In addition to the guide field strength, we investigate the dependence of our results on the flow magnetization, which for a cold electron-positron plasma is defined as $\sigma = B^2/4\pi mnc^2$.[6] The physics of X-point collapse has been widely studied in the literature with PIC simulations (Tsiklauri & Haruki 2007, 2008; Graf von der Pahlen & Tsiklauri 2014; von der Pahlen & Tsiklauri 2014), but only in the non-relativistic regime $\sigma \ll 1$. To the best of our knowledge, our investigation is the first to focus on the relativistic regime $\sigma \gg 1$, which is appropriate for relativistic astrophysical outflows. In the following, we identify our runs via the initial value of the magnetization σ_L at the distance L (along the unstressed x direction), measured only with the in-plane fields (so, excluding the guide field).[7] We explore three values of σ_L: 4×10^2, 4×10^3 and 4×10^4.

4.2.2. Stressed X-point collapse with guide field

Figure 10 shows the initial phase ($ct/L \leq 1$) of the collapse of a solitary X-point in PIC simulations with $\lambda = 1/\sqrt{2}$ and with guide field $B_0 = B_\perp$, for two different magnetizations: $\sigma_L = 4 \times 10^3$ (left) and $\sigma_L = 4 \times 10^4$ (right). The expected rapid collapse of the squeezed X-point is clearly visible, and in excellent agreement with the 2D results of force-free simulations, as shown in Fig. 7. The out-of-plane magnetic field B_z is compressed toward the $y = 0$ plane, in agreement with force-free results, but in apparent contradiction with the analytical solution, that assumed no evolution of the guide field. The 2D pattern of B_z in PIC simulations is remarkably independent of the magnetization (compare left and right), for the early phases presented in Fig. 10.

The fact that PIC results at early times are independent of σ_L is further illustrated in Fig. 11, where we present the temporal evolution of various quantities from PIC simulations of solitary X-point collapse with guide field $B_0 = B_\perp$, for three values of the magnetization: $\sigma_L = 4 \times 10^2$ (blue), $\sigma_L = 4 \times 10^3$ (green) and $\sigma_L = 4 \times 10^4$ (red). Both the value of $a(t) = \lambda^{1/2}(B_x/B_y)^{1/4}$ and of the electric field $E(t)$ (in units of B_0) at the location $(-0.1L, 0.1L)$ are independent of σ_L, as long as $ct/L \lesssim 1$, and they are in excellent agreement with the results of force-free simulations presented in Fig. 8. In other words, the physics at early times is entirely regulated by large-scale electromagnetic stresses, with no appreciable particle kinetic effects. Carried along by the converging magnetic fields of the collapsing X-point, particles are flowing into the central region, with a reconnection speed of $\sim 0.2c$ (averaged over a square of side equal to L around the center). This should be compared with the typical reconnection rate measured in relativistic guide-field reconnection in the case

[6] In the case of a hot plasma, the general definition of the magnetization is $\sigma = B^2/4\pi w$, where $w = nmc^2 + \hat{\gamma}p/(\hat{\gamma} - 1)$; here, w is the enthalpy, p is the pressure and $\hat{\gamma}$ is the adiabatic index.

[7] Given the form assumed for the magnetic fields, and since the particle density is uniform in our simulation domain, the magnetization increases quadratically with distance from the X-point.

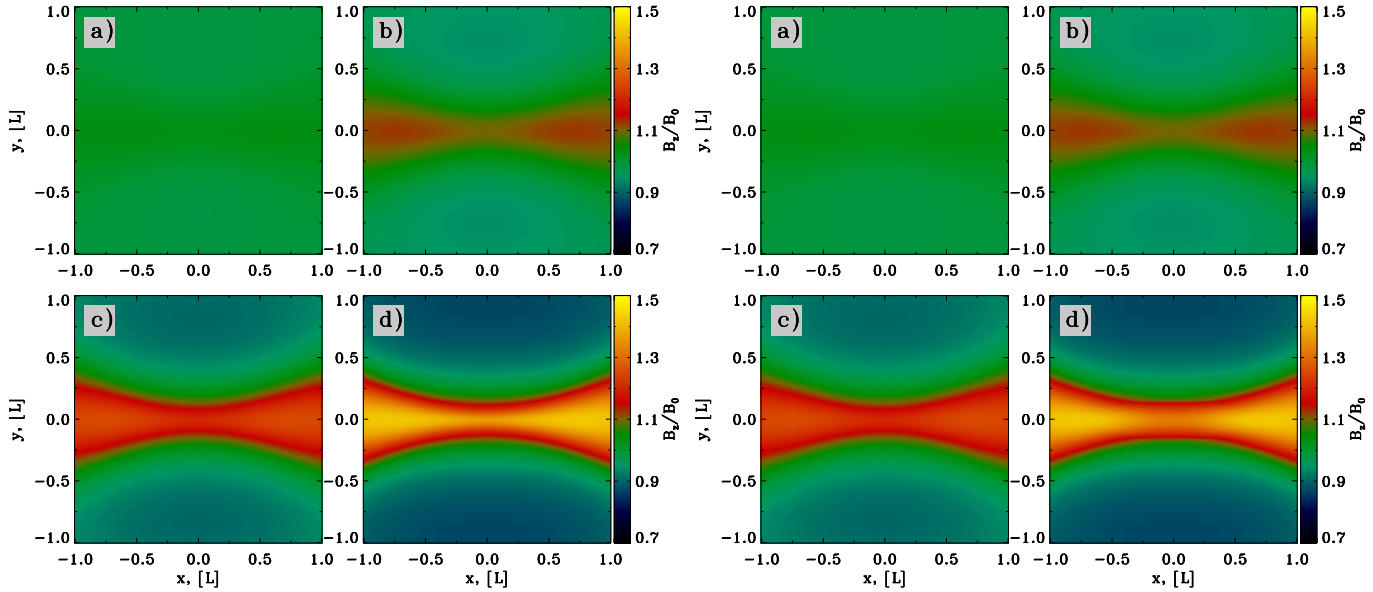

Fig. 10.— Initial phase of a solitary X-point collapse in PIC simulations with guide field $B_0 = B_\perp$, for two different magnetizations: $\sigma_L = 4 \times 10^3$ (left) and $\sigma_L = 4 \times 10^4$ (right). The plots show the out-of-plane field B_z at ct/L =0.25, 0.5, 0.75 and 1, from panel (a) to (d). This figure corresponds to Fig. 7, which shows the results of force-free simulations.

of a plane-parallel field configuration, i.e., when the in-plane fields are initialized along the x direction throughout the domain. Such a configuration leads to $v_{\rm rec}/c \sim 0.02$ for a guide field equal to the alternating field (Sironi & Spitkovsky 2016, in prep.), which is much smaller than the value attained in the present case of X-point collapse.[8]

As the system evolves and the $a(t)$ parameter increases, the electric current is bound to become charge-starved, as we have argued in Sect. 3.3. In Fig. 11, this is clearly indicated by the time when the force-free condition $\mathbf{E} \cdot \mathbf{B} = 0$ is violated, as shown in panel (d). In agreement with the argument in Sect. 3.3, higher values of σ_L lead to an earlier onset of charge starvation: the simulation with $\sigma_L = 4 \times 10^4$ becomes charge starved at $ct/L \simeq 0.75$, the simulation with $\sigma_L = 4 \times 10^3$ at $ct/L \simeq 1.1$ and the simulation with $\sigma_L = 4 \times 10^2$ at $ct/L \simeq 1.5$. The onset of charge starvation is accompanied by a deviation of the curves in panels (a) and (b) from the results of force-free simulations, where the condition $\mathbf{E} \cdot \mathbf{B} = 0$ is imposed by hand at all times.

The physics of charge starvation is illustrated in Fig. 12, for the case $\sigma_L = 4 \times 10^4$ that corresponds to the red curves in Fig. 11. In response to the growing electromagnetic stress (and so, to the increasing curl of the magnetic field), the z velocity of the charge carriers has to increase (Fig. 12(a), for positrons), while their density stays nearly unchanged. When the drifting speed reaches the speed of light, at $ct/L \simeq 0.8$ in Fig. 12(a), the particle electric current cannot sustain the curl of the magnetic field any longer, and the system must deviate from the force-free condition $\mathbf{E} \cdot \mathbf{B} = 0$. In fact, panel (b) shows that the value of $\mathbf{E} \cdot \mathbf{B}$ departs from zero at $ct/L \simeq 0.8$, i.e., right when the particle drift velocity approaches the speed of light. The nonzero $\mathbf{E} \cdot \mathbf{B}$ triggers the onset of efficient particle acceleration, as shown by the profile of the mean particle Lorentz factor in panel (c). Indeed, the locations of efficient particle acceleration (i.e., where

[8] We point out that the value we obtain is consistent with the findings of Liu et al. (2015). The critical difference, though, is that their measurement was performed on microscopic skin-depth scales, whereas our results show that significant reconnection speeds can be achieved over macroscopic scales $L \gg c/\omega_{\rm p}$.

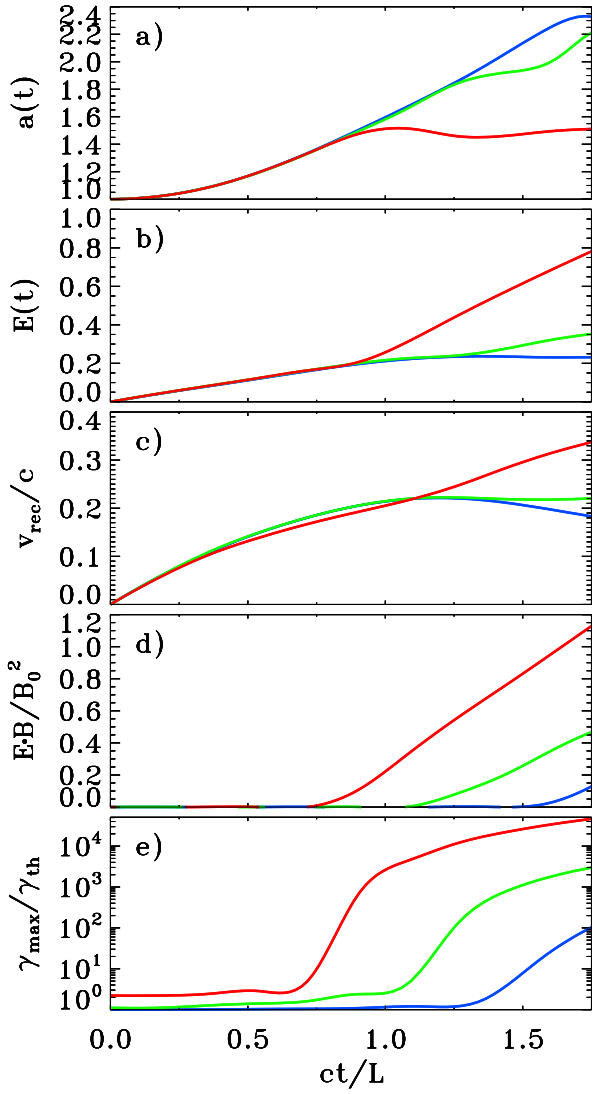

Fig. 11.— Temporal evolution of various quantities from PIC simulations of solitary X-point collapse with guide field $B_0 = B_\perp$, for three values of the magnetization: $\sigma_L = 4 \times 10^2$ (blue), $\sigma_L = 4 \times 10^3$ (green) and $\sigma_L = 4 \times 10^4$ (red). As a function of time, we plot: (a) the value of $a(t) = \lambda^{1/2}(B_x/B_y)^{1/4}$ at the location $(-0.1L, 0.1L)$, to be compared with the result of force-free simulations in the left panel of Fig. 8; (b) the value of the electric field strength $E(t)$ at the location $(-0.1L, 0.1L)$ in units of B_0, to be compared with the result of force-free simulations in the right panel of Fig. 8; (c), the reconnection rate, defined as the inflow speed along the y direction averaged over a square of side equal to L around the central region; (d) the parameter $\mathbf{E}\cdot\mathbf{B}/B_0^2$, which explicitly shows when the force-free condition $\mathbf{E}\cdot\mathbf{B} = 0$ is broken; (d) the maximum particle Lorentz factor $\gamma_{\rm max}$ (as defined in Eq. (16)), in units of the thermal value $\gamma_{\rm th} \simeq 1 + (\hat{\gamma} - 1)^{-1} kT/mc^2$, which in this case of a cold plasma reduces to $\gamma_{\rm th} \simeq 1$.

$\langle\gamma\rangle \gg 1$) are spatially coincident with the regions where $\mathbf{E}\cdot\mathbf{B} \neq 0$. There, the pressure of accelerated particles provides a significant back-reaction onto the field collapse, and the agreement with the force-free results necessarily fails.

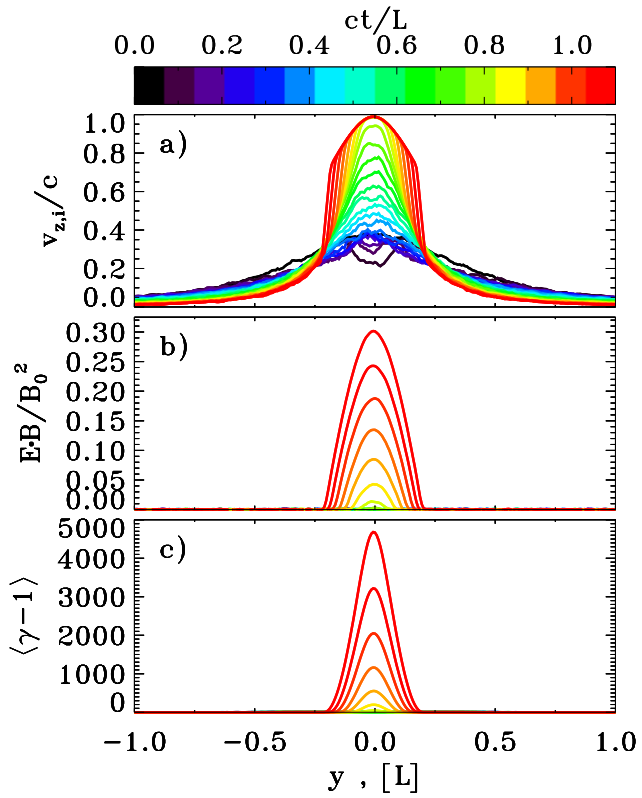

Fig. 12.— Spatial profiles of various quantities from a PIC simulation of solitary X-point collapse with guide field $B_0 = B_\perp$ and magnetization $\sigma_L = 4 \times 10^4$, which corresponds to the red curves in Fig. 11. As a function of the coordinate y along the inflow direction, we plot: (a) the bulk speed of positrons, in units of the speed of light (the bulk speed of electrons is equal and opposite); (b) the parameter $\mathbf{E} \cdot \mathbf{B}/B_0^2$, which explicitly shows when the force-free condition $\mathbf{E} \cdot \mathbf{B} = 0$ is falsified; (c) the mean particle Lorentz factor.

As shown in Fig. 11(e), the maximum particle energy dramatically increases, after the onset of charge starvation. It is this rapid period of acceleration that will be extensively studied in the following sections. Here, and hereafter, the maximum particle Lorentz factor plotted in Fig. 11(e) is defined as

$$\gamma_{\rm max} = \frac{\int \gamma^{n_{\rm cut}} dN/d\gamma \, d\gamma}{\int \gamma^{n_{\rm cut}-1} dN/d\gamma \, d\gamma} \tag{16}$$

where $n_{\rm cut}$ is empirically chosen to be $n_{\rm cut} = 6$ (see also Bai et al. 2015). If the particle energy spectrum takes the form $dN/d\gamma \propto \gamma^{-s} \exp(-\gamma/\gamma_{\rm cut})$ with power-law slope s and exponential cutoff at $\gamma_{\rm cut}$, then our definition yields $\gamma_{\rm max} \sim (n_{\rm cut} - s)\, \gamma_{\rm cut}$.

As the collapse proceeds beyond $ct/L \sim 1$, the system approaches a self-similar evolution, as we have already emphasized for our force-free simulations (see Fig. 9). As shown in Fig. 13, the X-point evolves into a thin current sheet with two Y-points at its ends. The current sheet is supported by the pressure of the compressed guide field (as it is apparent in Fig. 13) and by the kinetic pressure of the accelerated particles. As illustrated in Fig. 13, the current sheet is thinner for lower magnetizations, at fixed $L/\, c/\omega_{\rm p}$ (compare $\sigma_L = 4 \times 10^3$ on the left and $\sigma_L = 4 \times 10^4$ on the right). Roughly, the thickness of the current sheet at this stage is set by the Larmor radius $r_{\rm L,hot} = \sqrt{\sigma_L}\, c/\omega_{\rm p}$ of the

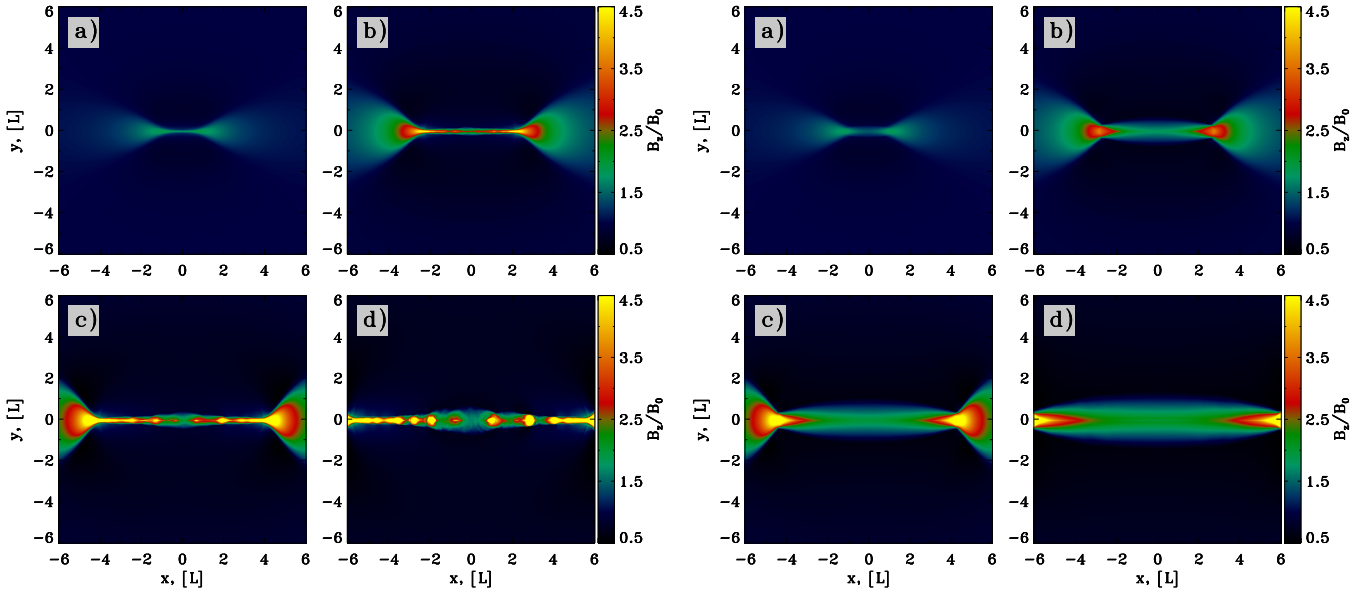

Fig. 13.— Late time evolution of the X-point collapse in PIC simulations with guide field $B_0 = B_\perp$, for two different magnetizations: $\sigma_L = 4 \times 10^3$ (left) and $\sigma_L = 4 \times 10^4$ (right). The plots show the out-of-plane field at ct/L =1.5, 3, 4.5, 6, from panel (a) to (d). This figure corresponds to the left side of Fig. 9, which shows the results of force-free simulations.

high-energy particles heated/accelerated by reconnection, which explains the variation of the current sheet thickness with σ_L in Fig. 13. A long thin current sheet is expected to fragment into a chain of plasmoids/magnetic islands (e.g., Uzdensky et al. 2010), when the length-to-thickness ratio is much larger than unity. At fixed time (in units of L/c), so at fixed sheet length, it is then more likely that the fragmentation into plasmoids appears at lower magnetizations, since a lower σ_L results in a thinner current sheet. This is in agreement with Fig. 13, and we have further checked that the current sheet in the simulation with $\sigma_L = 4 \times 10^2$ starts fragmenting at even earlier times.

In the small-scale X-points in between the self-generated plasmoids, the electric field can approach and exceed the magnetic field. This is apparent in Fig. 14 — referring to the same simulations as in Fig. 13 — where we show the value of $1 - E^2/B^2$, which quantifies the strength of the electric field relative to the magnetic field. In the case of $\sigma_L = 4 \times 10^3$ (left side), the *microscopic* regions in between the plasmoids are characterized by $E > B$ (see, e.g., at the center of panel (d)). In addition, ahead of each of the two Y-points, a bow-shaped area exists where $E \sim B$ (e.g., at $|x| \sim 5L$ and $y \sim 0$ in panel (c)). The two Y-points move at the Alfvén speed, which is comparable to the speed of light for our $\sigma_L \gg 1$ plasma. So, the fact that $E \sim B$ ahead of the Y-points is just a manifestation of the relativistic nature of the reconnection outflows. For $\sigma_L = 4 \times 10^3$ (left side in Fig. 14), the electric energy in the bulk of the inflow region is much smaller than the magnetic energy, corresponding to $1 - E^2/B^2 \sim 0.6$. Or equivalently, the reconnection speed is significantly smaller than the speed of light. The highly relativistic case of $\sigma_L = 4 \times 10^4$ (right panel in Fig. 14) shows a different picture. Here, a large volume with $E \sim B$ develops in the inflow region. In other words, the reconnection speed approaches the speed of light in a *macroscopic* region. In the next subsection, we will show that an inflow speed near the speed of light (or equivalently, $E \sim B$) is a generic by-product of high-σ_L reconnection.[9]

[9]In retrospect, the fact that this conclusion also holds for the case of guide-field X-point collapse is not surprising. At the initial time, only the region within a radius $\lesssim L$ from the current sheet has a guide field stronger than the in-plane fields. This implies that at late times,

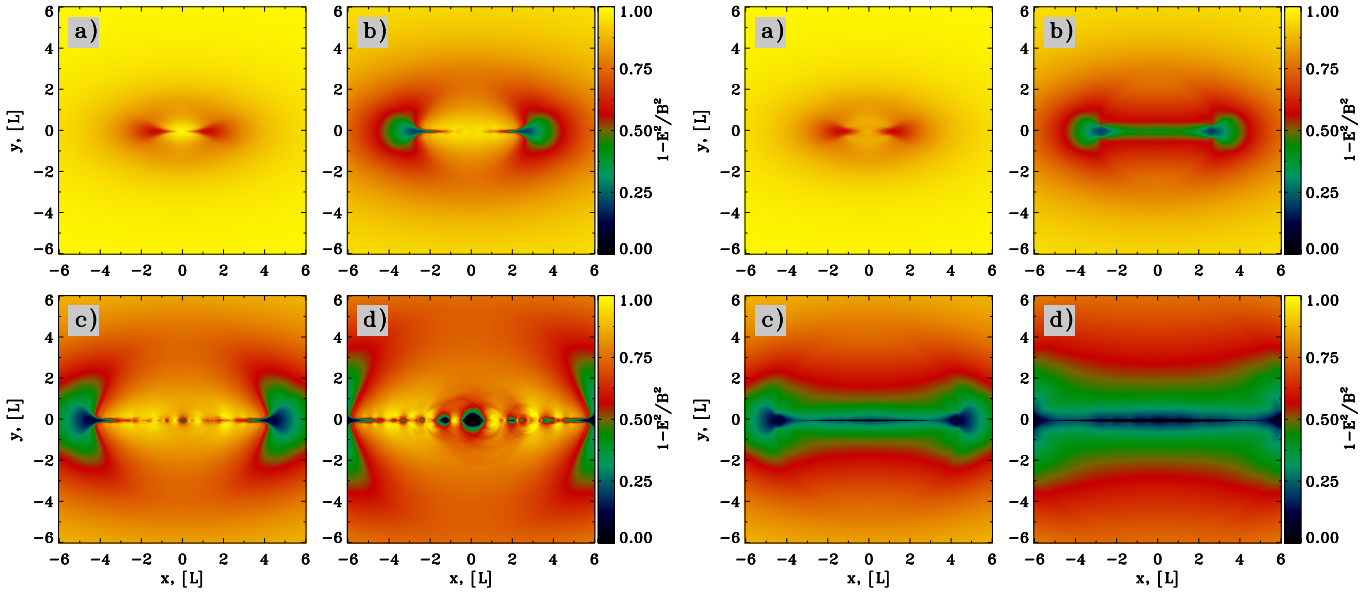

Fig. 14.— Late time evolution of the X-point collapse in PIC simulations with guide field $B_0 = B_\perp$, for two different magnetizations: $\sigma_L = 4 \times 10^3$ (left) and $\sigma_L = 4 \times 10^4$ (right). The plots show the quantity $1 - E^2/B^2$ at ct/L =1.5, 3, 4.5, 6, from panel (a) to (d) (strictly speaking, we plot $\max[0, 1 - E^2/B^2]$, for direct comparison with force-free simulations, that implicitly constrain $E \leq B$). This figure corresponds to the right side of Fig. 9, which shows the results of force-free simulations.

4.2.3. Stressed X-point collapse without guide field

Figure 15 shows the initial phase ($ct/L \leq 1$) of the collapse of a solitary X-point in PIC simulations with $\lambda = 1/\sqrt{2}$ and with zero guide field, for two different magnetizations: $\sigma_L = 4 \times 10^3$ (left) and $\sigma_L = 4 \times 10^4$ (right). We plot the quantity $1 - E^2/B^2$ (more precisely, we present $\max[0, 1 - E^2/B^2]$), in order to identify the regions where the electric field is comparable to the magnetic field (green or blue areas in the plot). For both $\sigma_L = 4 \times 10^3$ (left) and $\sigma_L = 4 \times 10^4$ (right), the current sheet is subject to copious fragmentation into plasmoids since early times, in contrast with the guide-field case (compare with Fig. 10). There, the current sheet was supported by the pressure of the compressed guide field, and therefore its thickness was larger, making it less prone to fragmentation (at a fixed time ct/L). In addition, a comparison of Fig. 15, which refers to early times (up to $ct/L = 1$), with Fig. 16, that follows the system up to $ct/L = 6$, shows the remarkable self-similarity of the evolution, for both magnetizations. As the current sheet stretches longer, the two bow-shaped heads propagating outward become larger (with a typical size along y that is always comparable to the half-length of the reconnection layer). At the same time, the size of the largest plasmoids generated in the current sheet is always a fixed fraction (~ 0.1) of the overall length of the layer.

In Figs. 15 and 16, the plasmoids generated by the secondary tearing instability (Uzdensky et al. 2010) appear as yellow structures, i.e., with magnetic energy much larger than the electric energy. In contrast, the region in between each pair of plasmoids harbors an X-point, where the electric field can exceed the magnetic field. The typical size of such X-points is much smaller than the overall length of the system (and consequently, of the size of the initial collapsing

when regions initially at a distance $\gtrsim L$ are eventually advected to the center, the guide field at the current sheet will be sub-dominant with respect to the in-plane fields, so that the results of guide-field reconnection will resemble the case of a vanishing guide field.

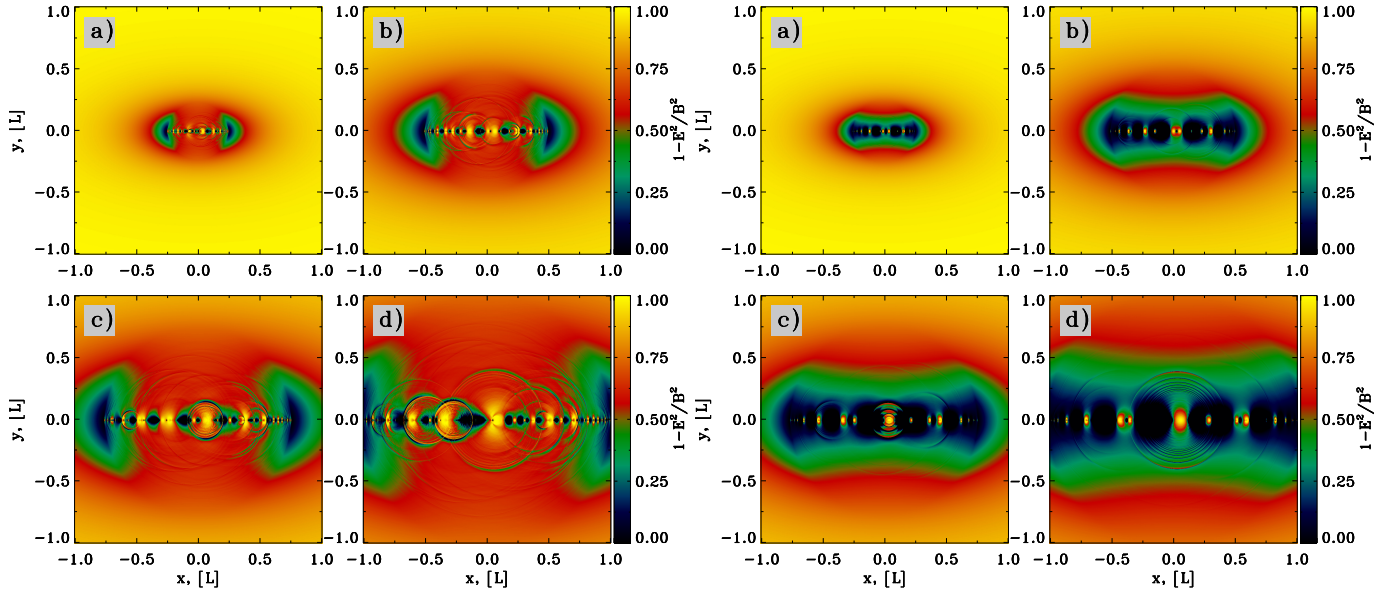

Fig. 15.— Initial phase of a solitary X-point collapse in PIC simulations with zero guide field, for two different magnetizations: $\sigma_L = 4 \times 10^3$ (left) and $\sigma_L = 4 \times 10^4$ (right). The plots show the quantity $1 - E^2/B^2$ (strictly speaking, we plot $\max[0, 1 - E^2/B^2]$) at ct/L =0.25, 0.5, 0.75 and 1, from panel (a) to (d).

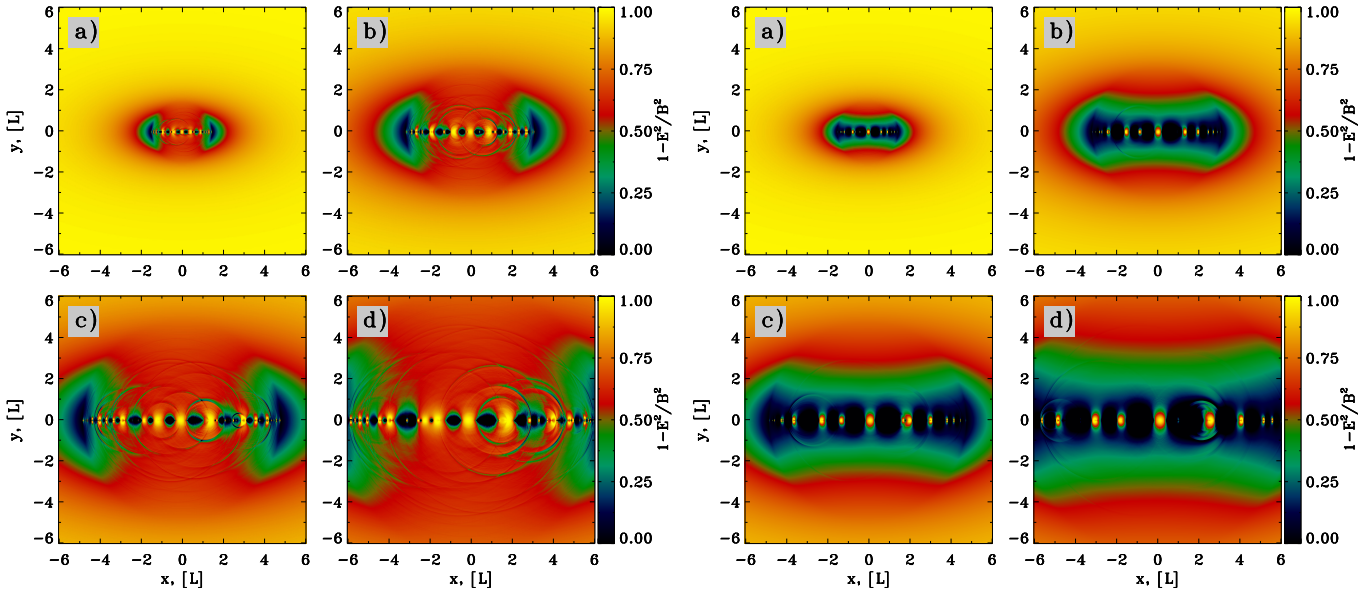

Fig. 16.— Late time evolution of the X-point collapse in PIC simulations with zero guide field, for two different magnetizations: $\sigma_L = 4 \times 10^3$ (left) and $\sigma_L = 4 \times 10^4$ (right). The plots show the quantity $1 - E^2/B^2$ (strictly speaking, we plot $\max[0, 1 - E^2/B^2]$) at ct/L =1.5, 3, 4.5, 6, from panel (a) to (d).

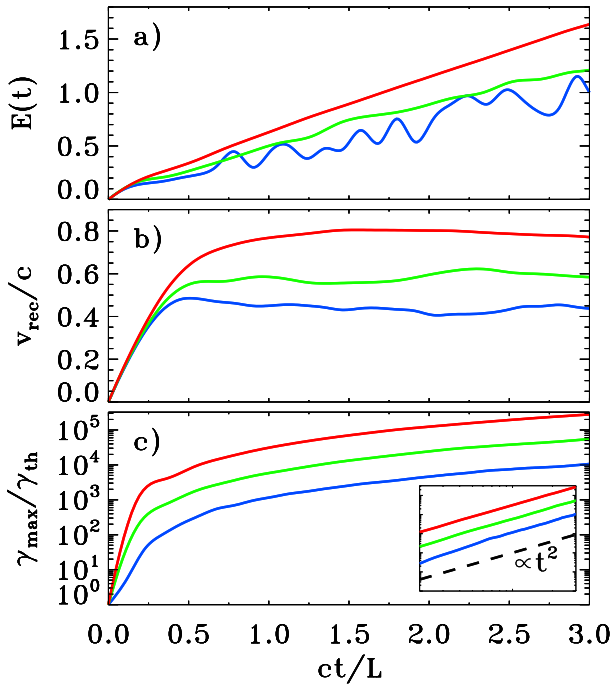

Fig. 17.— Temporal evolution of various quantities from PIC simulations of solitary X-point collapse with zero guide field, for three values of the magnetization: $\sigma_L = 4 \times 10^2$ (blue), $\sigma_L = 4 \times 10^3$ (green) and $\sigma_L = 4 \times 10^4$ (red). The corresponding plot for the case of nonzero guide field is in Fig. 11. As a function of time, we plot: (a) the value of the electric field strength $E(t)$ at the location $(-0.1L, 0.1L)$ in units of the initial magnetic field at $x = L$; (b), the reconnection rate, defined as the inflow speed along the y direction averaged over a square of side equal to L around the central region; (c) the maximum particle Lorentz factor $\gamma_{\rm max}$ (as defined in Eq. (16)), in units of the thermal value $\gamma_{\rm th} \simeq 1 + (\hat{\gamma} - 1)^{-1} kT/mc^2$, which in this case of a cold plasma reduces to $\gamma_{\rm th} \simeq 1$; the inset in panel (c) shows the same quantity on a double logarithmic scale, demonstrating that $\gamma_{\rm max} \propto t^2$ (black dashed line).

X-point). Yet, the X-points in the current layer play a major role for particle injection into the acceleration process, as we argue in the next subsection.

As observed in the case of guide-field collapse, the two bow-shaped regions ahead of the Y-points (to the left and to the right of the reconnection layer) are moving relativistically, yielding $E \sim B$ (green and blue colors in the figures). In addition, in the high-magnetization case $\sigma_L = 4 \times 10^4$ (right side of Figs. 15 and 16), a *macroscopic* region appears in the bulk inflow where the electric field is comparable to the magnetic field. Here, the inflow rate approaches the speed of light, as we have already described in the case of guide-field reconnection (right side of Fig. 14).

This is further illustrated in Fig. 17, where we present the temporal evolution of various quantities, from a suite of PIC simulations of X-point collapse with vanishing guide field, having three different magnetizations: $\sigma_L = 4 \times 10^2$ (blue), $\sigma_L = 4 \times 10^3$ (green) and $\sigma_L = 4 \times 10^4$ (red). The reconnection rate $v_{\rm rec}/c$ (panel (b)), which is measured as the inflow speed averaged over a *macroscopic* square of side equal to L centered at $x = y = 0$, shows in the asymptotic state (i.e., at $ct/L \gtrsim 0.5$) a clear dependence on σ_L, reaching $v_{\rm rec}/c \sim 0.8$ for our high-magnetization case $\sigma_L = 4 \times 10^4$ (red). This trend has already been described by Liu et al. (2015). The critical difference, though, is that their measurement

was performed on *microscopic* skin-depth scales, whereas our results show that reconnection velocities near the speed of light can be achieved over *macroscopic* scales $L \gg c/\omega_{\rm p}$. In addition, such inflow speed is significantly larger than what is measured on macroscopic scales in the case of plane-parallel steady-state reconnection, where the reconnection rate typically approaches $v_{\rm rec}/c \sim 0.2$ in the high-magnetization limit (Sironi & Spitkovsky 2014; Guo et al. 2015).

The dependence of the reconnection speed on σ_L is also revealed in Fig. 17(a), where we present the temporal evolution of the electric field $E(t)$ measured at $(x, y) = (-0.1L, 0.1L)$, in units of the initial magnetic field at $x = L$. The variation in slope in Fig. 17(a) is indeed driven by the different reconnection speeds, since $E \sim v_{\rm rec}B/c$ in the inflow region. Interestingly, the electric field increases linearly with time. This is ultimately a result of the linear increase of the initial magnetic field with distance from the center. Assuming a constant reconnection speed, as time progresses the plasma that is now advected into the current sheet was initially located farther and farther away. The plasma carries its frozen-in magnetic field, which is then linearly increasing over time. From $E \sim v_{\rm rec}B/c$ and taking a constant reconnection rate, this explains the linear increase of the electric field.

The temporal evolution of the electric field has a direct impact on the maximum particle energy, which is shown in Fig. 17(c). Quite generally, its time evolution will be

$$\gamma_{\rm max} mc^2 \sim eEct \sim ev_{\rm rec}Bt \tag{17}$$

Since both E and B in the reconnection region are scaling linearly with time (see Fig. 17(a)), one expects $\gamma_{\rm max} \propto t^2$, as indeed confirmed by the inset of panel (c) (compare with the dashed black line). This scaling is faster than in plane-parallel steady-state reconnection, where $E(t)$ is constant in time, leading to $\gamma_{\rm max} \propto t$. From the scaling in Eq. (17), one can understand the different normalizations of the curves in Fig. 17(c). At a given time t, the magnetic field $B(t)$ that is now present in the central region was initially at a distance $\sim v_{\rm rec}t$, if we assume a constant reconnection rate. Due to the linear increase of the initial magnetic field with distance from the center, we find that $B(t) \propto \sqrt{\sigma_L} v_{\rm rec}t$. This leads to $\gamma_{\rm max} \propto v_{\rm rec}^2 \sqrt{\sigma_L} t^2$. This implies that, at a fixed time, the case with $\sigma_L = 4 \times 10^4$ should be accelerating the particles to an energy that is ~ 30 times larger than for $\sigma_L = 4 \times 10^2$, as a result of both the variation in σ_L and in the reconnection speed. This is in excellent agreement with the curves in Fig. 17(c) (compare blue and red).

4.2.4. Particle acceleration and emission signatures

In this section, we explore the physics of particle acceleration in a stressed X-point collapse with vanishing guide field and $\sigma_L = 4 \times 10^2$, and we present the resulting particle distribution and synchrotron emission spectrum. In Fig. 18, we follow the trajectories of a number of particles, selected such that their Lorentz factor exceeds a given threshold $\gamma_0 = 30$ within the time interval $1.4 \leq ct_0/L \leq 1.7$, as indicated by the vertical dashed lines in the top panel. The temporal evolution of the Lorentz factor of such particles, presented in the top panel for the 30 positrons reaching the highest energies, follows the track $\gamma \propto t^2 - t_0^2$ that is expected from $d\gamma/dt \propto E(t) \propto t$. Here, t_0 is the injection time, when γ first exceeds the threshold γ_0. The individual histories of single positrons might differ substantially, but overall the top panel of Fig. 18 suggests that the acceleration process is dominated by direct acceleration by the reconnection electric field, as indeed it is expected for our configuration of a large-scale stressed X-point (see Sironi & Spitkovsky 2014; Guo et al. 2015; Nalewajko et al. 2015, for a discussion of acceleration mechanisms in plane-parallel reconnection). We find that the particles presented in the top panel of Fig. 18 are too energetic to be confined within the small-scale plasmoids in the current sheet, so any acceleration mechanism that relies on plasmoid mergers is found to be unimportant, in our setup.

Particle injection into the acceleration process happens in the charge-starved regions where $E > B$, i.e., in the small-scale X-points that separate each pair of secondary plasmoids in the current sheet. Indeed, for the same particles

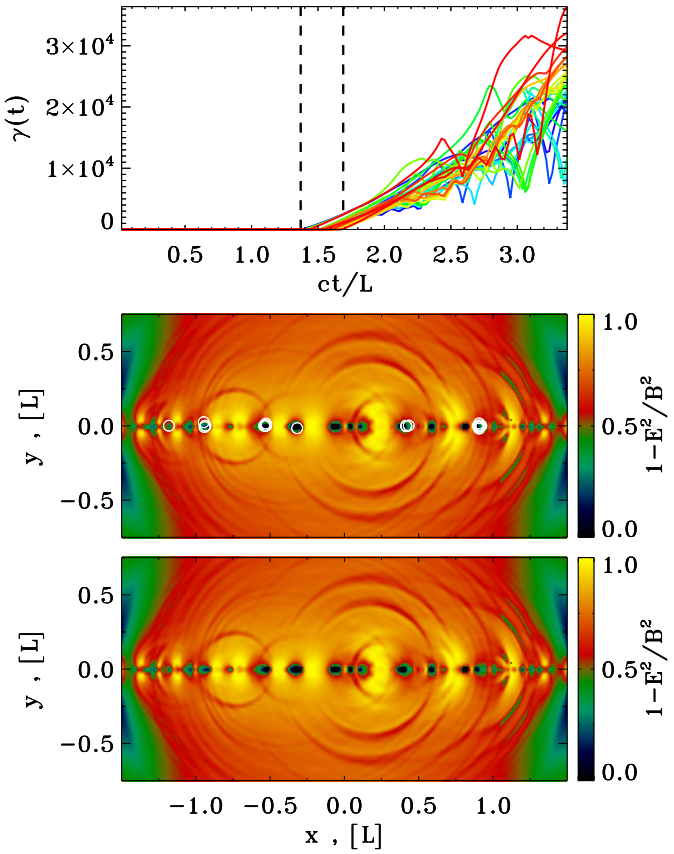

Fig. 18.— Physics of particle injection into the acceleration process, from a PIC simulation of stressed X-point collapse with vanishing guide field and $\sigma_L = 4 \times 10^2$. Top panel: we select all the particles that exceed the threshold $\gamma_0 = 30$ within a given time interval (chosen to be $1.4 \leq ct_0/L \leq 1.7$, as indicated by the vertical dashed lines), and we plot the temporal evolution of the Lorentz factor of the 30 particles that at the final time reach the highest energies. The particle Lorentz factor increases as $\gamma \propto t^2 - t_0^2$, where t_0 marks the onset of acceleration (i.e., the time when γ first exceeds γ_0). Middle panel: for the same particles as in the top panel, we plot their locations at the onset of acceleration with open white circles, superimposed over the 2D plot of $1 - E^2/B^2$ (more precisely, of $\max[0, 1 - E^2/B^2]$). Comparison of the middle panel with the bottom panel shows that particle injection is localized in the vicinity of the X-points in the current sheet (i.e., the blue regions where $E > B$).

as in the top panel, the middle panel in Fig. 18 presents their locations at the onset of acceleration with open white circles, superimposed over the 2D plot of $1 - E^2/B^2$ (more precisely, of $\max[0, 1 - E^2/B^2]$). Comparison of the middle panel with the bottom panel shows that particle injection is localized in the vicinity of the small-scale X-points in the current sheet (i.e., the blue regions where $E > B$). Despite occupying a small fraction of the overall volume, such regions are of paramount importance for particle acceleration.

The temporal evolution of the electron energy spectrum is presented in the top panel of Fig. 19. As the spectral cutoff

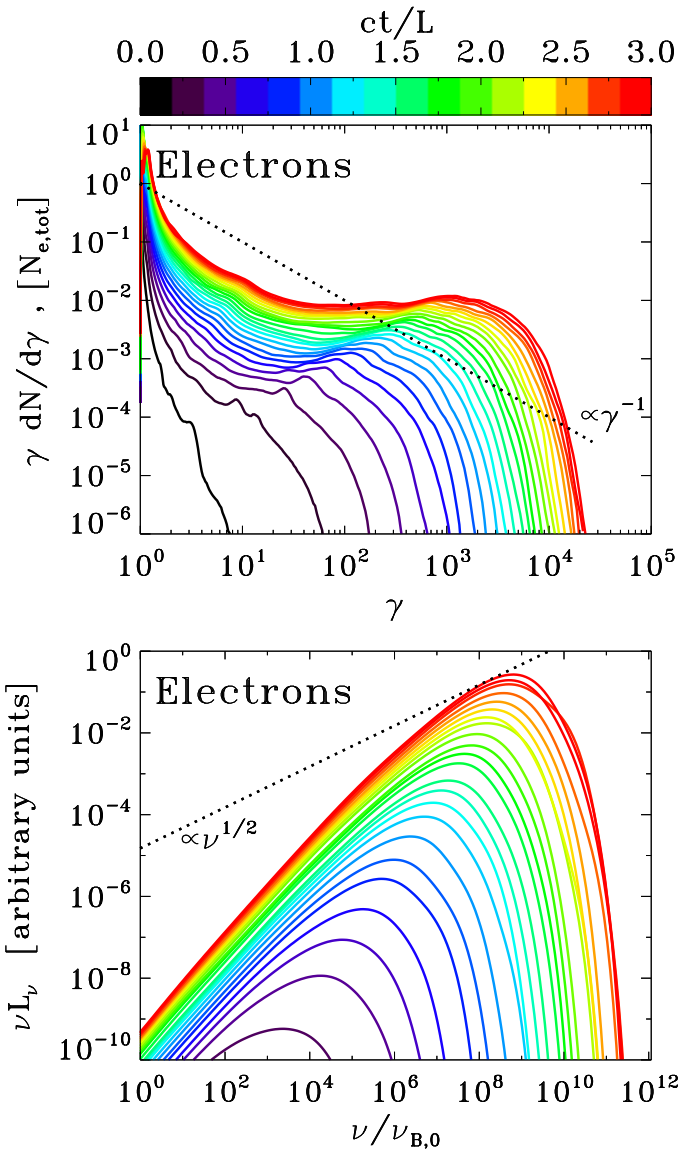

Fig. 19.— Particle energy spectrum and synchrotron spectrum from a PIC simulation of stressed X-point collapse with vanishing guide field and $\sigma_L = 4 \times 10^2$. Time is measured in units of L/c, see the colorbar at the top. Top panel: evolution of the electron energy spectrum normalized to the total number of electrons. At late times, the spectrum approaches a hard distribution $\gamma dN/d\gamma \propto$ const, much harder than the dotted line, which shows the case $\gamma dN/d\gamma \propto \gamma^{-1}$ corresponding to equal energy content in each decade of γ. Bottom panel: evolution of the angle-averaged synchrotron spectrum emitted by electrons. The frequency on the horizontal axis is in units of $\nu_{B,0} = \sqrt{\sigma_L}\omega_p/2\pi$. At late times, the synchrotron spectrum approaches a power law with $\nu L_\nu \propto \nu$, which just follows from the fact that the electron spectrum is $\gamma dN/d\gamma \propto$ const. This is much harder than the dotted line, which indicates the slope $\nu L_\nu \propto \nu^{1/2}$ resulting from an electron spectrum $\gamma dN/d\gamma \propto \gamma^{-1}$ (dotted line in the top panel).

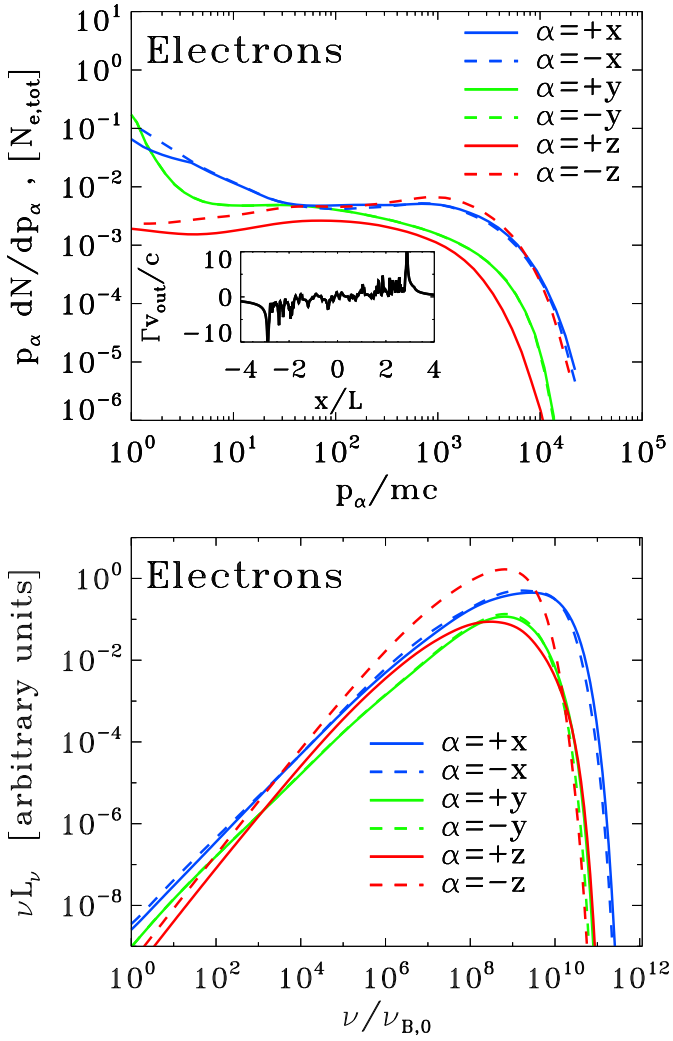

Fig. 20.— Particle momentum spectrum and anisotropy of the synchrotron spectrum from a PIC simulation of stressed X-point collapse with vanishing guide field and $\sigma_L = 4 \times 10^2$. Top panel: electron momentum spectrum at the final time along different directions, as indicated in the legend. The highest energy electrons are beamed along the direction x of the reconnection outflow (blue lines) and along the direction $-z$ of the accelerating electric field (red dashed line; positrons will be beamed along $+z$, due to the opposite charge). The inset shows the 1D profile along x of the bulk four-velocity in the outflow direction (i.e., along x), measured at $y = 0$. Bottom panel: synchrotron spectrum at the final time along different directions (within a solid angle of $\Delta\Omega/4\pi \sim 3\times10^{-3}$), as indicated in the legend. The resulting anisotropy of the synchrotron emission is consistent with the particle anisotropy illustrated in the top panel.

grows as $\gamma_{\rm max} \propto t^2$ (see also the inset in Fig. 17(c)), the spectrum approaches a hard power law $\gamma dN/d\gamma \propto$ const.[10] The measured spectral slope is consistent with the asymptotic power-law index obtained in the limit of high magnetizations

[10]The figure refers to the case $\sigma_L = 4\times10^2$. We find that the spectrum is even harder for higher magnetizations, approaching $\gamma dN/d\gamma \propto \gamma^{1/2}$ at the high-energy end.

from PIC simulations of relativistic plane-parallel reconnection (Sironi & Spitkovsky 2014; Guo et al. 2015; Werner et al. 2016). Due to energy conservation, such hard slopes would not allow the spectrum to extend much beyond the instantaneous value of the magnetization at the current sheet (as we have explained before, in our setup the magnetization at the current sheet increases quadratically with time, since $B(t) \propto t$), in line with the arguments of Sironi & Spitkovsky (2014) and Werner et al. (2016).

The particle distribution is significantly anisotropic. In the top panel of Fig. 20, we plot the electron momentum spectrum at the final time along different directions, as indicated in the legend. The highest energy electrons are beamed along the direction x of the reconnection outflow (blue lines) and along the direction $-z$ of the accelerating electric field (red dashed line; positrons will be beamed along $+z$, due to the opposite charge). This is consistent with earlier PIC simulations of plane-parallel reconnection in a small computational box, where the X-point acceleration phase was still appreciably imprinting the resulting particle anisotropy (Cerutti et al. 2012c, 2013, 2014b; Kagan et al. 2016). In contrast, plane-parallel reconnection in larger computational domains generally leads to quasi-isotropic particle distributions (Sironi & Spitkovsky 2014). In our setup of a large-scale X-point, we would expect the same level of strong anisotropy measured in small-scale X-points of plane-parallel reconnection, as indeed demonstrated in the top panel of Fig. 20. Most of the anisotropy is to be attributed to the "kinetic beaming" discussed by Cerutti et al. (2012c), rather than beaming associated with the bulk motion (which is only marginally relativistic, see the inset in the top panel of Fig. 20).

The angle-averaged synchrotron spectrum expected from a relativistic X-point collapse is shown in the bottom panel of Fig. 19. For each macro-particle in our PIC simulation, we compute the instantaneous radius of curvature and the corresponding synchrotron emission spectrum. We neglect synchrotron cooling in the particle equations of motion (unlike Cerutti et al. 2013, 2014b; Kagan et al. 2016), and we do not consider the effect of synchrotron self-absorption and the Razin suppression at low frequencies. At late times, the synchrotron spectrum approaches a power law with $\nu L_\nu \propto \nu$, which just follows from the fact that the electron spectrum is $\gamma dN/d\gamma \propto$ const. This is consistent with the spectrum of the Crab flares. The frequency on the horizontal axis is in units of $\nu_{B,0} = \sqrt{\sigma_L}\omega_{\rm p}/2\pi$. Given the maximum particle energy in the top panel, $\gamma_{\rm max} \sim 10^4$, one would expect the synchrotron spectrum to cut off at $\nu_{\rm max} \sim \gamma_{\rm max}^2 \nu_{B,0} \sim 10^8 \nu_{B,0}$, as indeed confirmed in the bottom panel. The bottom panel of Fig. 20 shows the synchrotron spectrum at the final time along different directions (within a solid angle of $\Delta\Omega/4\pi \sim 3 \times 10^{-3}$), as indicated in the legend. The resulting anisotropy of the synchrotron emission is consistent with the particle anisotropy illustrated in the top panel of Fig. 20. In addition, one can see that the resulting synchrotron spectrum along the direction $-z$ of the accelerating electric field (dashed red line) appears even harder than the spectrum along x or y.

5. Magnetic island merger in highly magnetized plasma - analytical considerations

Numerical simulations described above clearly show two stages of magnetic island merger - fast explosive stage and subsequent slower evolution. For intermediate times, the flux tubes show oscillations about some equilibrium position. Let us next construct an analytical model that captures the transition between the two stage. The fast explosive stage is driven by large scale stresses of the type "parallel currents attract". As an initial unstable configuration let us consider X-point configuration of two attracting line currents (Green 1965)

$$B_y + iB_x = \frac{4I_0 z}{c(a_0^2 - z^2)},\ z = x + iy \tag{18}$$

where a_0 is the initial distance between the centers of the islands This non-equilibrium configuration will evolve into configuration with Y-point along y-axis, $|y| < L$, see §3 and Fig. 21,

$$B_y + iB_x = \frac{4I_0 z}{c}\frac{a_0}{\sqrt{a_0^2 + L^2}}\frac{\sqrt{L^2 + z^2}}{a_0^2 - z^2} \tag{19}$$

For both configurations $\mathrm{curl}\,\mathbf{B} = 0$.

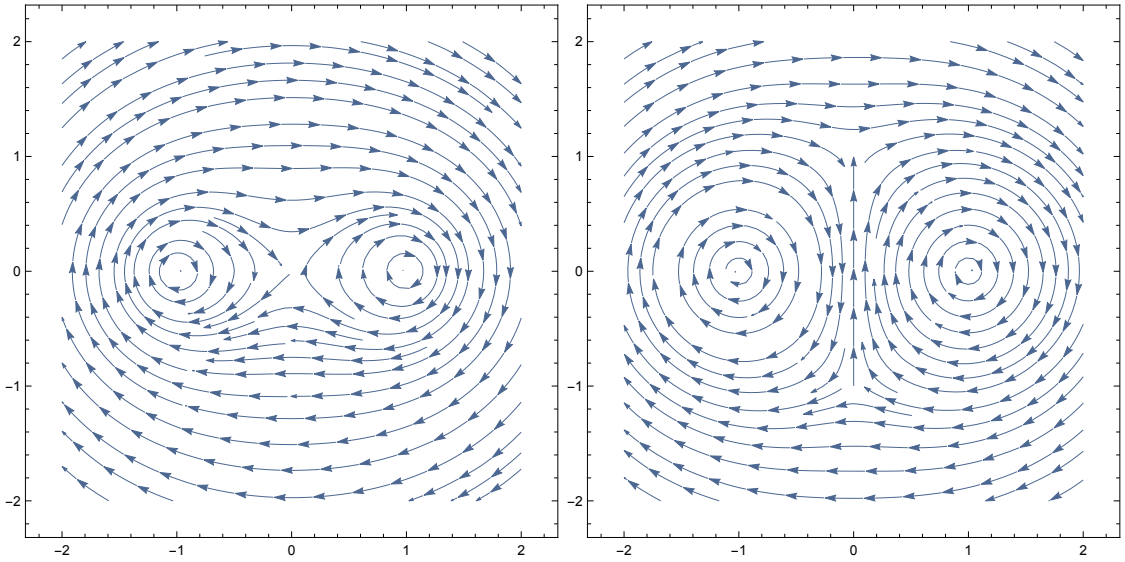

Fig. 21.— Unstable X-point configuration (Left Panel) oscillates around stable double Y-point configuration (Right Panel) .

There is a current sheet at $x = 0$ with surface current

$$g = 2B_y(x = 0)/(4\pi) = \frac{2}{\pi}\frac{\sqrt{L^2 - y^2}}{(a_0^2 + y^2)\sqrt{a_0^2 + L^2}} \tag{20}$$

The surface current is *in the opposite direction* to the initial line currents. The repulsive force is

$$\int_{-L}^{L} \frac{2gI_0}{\sqrt{a_0^2 + y^2}}\frac{1}{\sqrt{a_0^2 + y^2}}dy = \frac{2I_0^2 L^2}{c(a_0^2 + L^2)} \tag{21}$$

The total force per unit length (it can also be obtained by integrating the stress over the $x = 0$ surface is

$$F = -\frac{I_0^2}{2c^2 a_0}\frac{a_0^2 - L^2}{a_0^2 + L^2} \tag{22}$$

This balances the attractive force between the currents for $L = a_0$. Thus, attraction of parallel currents created a current sheet with the surface current flowing in the opposite direction; the repulsive force between each current and the current sheet balances exactly the attractive force between the currents. Evolution of the resulting equilibrium configuration will proceed on resistive time scales on the central current sheet.

We can also build a simple dynamic model of the current merger. Let us approximate the effective electromagnetic mass per unit length of a current-tube as

$$m_{eff}c^2 = \int_{a_{min}}^{a_0} \frac{4I_0^2}{2\pi} 2\pi r dr = (I_0/c)^2 \ln a_0/a_{min} \tag{23}$$

Thus, m_{eff} is nearly constant. Let us next relate the current sheet length L to the island separation l assuming that for distance $2l < 2a_0$ ($2a_0$ is the initial separation)

$$L^2 + l^2 = a_0^2 \tag{24}$$

Thus, the motion of the flux tubes obeys

$$\ddot{l} = \frac{I_0^2}{m_{eff}c}\left(\frac{1}{l} - 2\frac{l}{a_0^2}\right) \tag{25}$$

with initial conditions $l(0) = a_0$ and $l'(0) = 0$. Solution $l(t)$ shows oscillations with equilibrium value $l = a_0/\sqrt{2}$, minimal value $l_{min} = 0.45$, period of oscillations is $4.39a_0/c$. For small times $t \ll a_0\sqrt{c}/I$,

$$\begin{aligned} l &= a_0 - \frac{c^2t^2}{4a_0 \ln(a_0/a_{min})} \\ L &= \frac{ct}{\sqrt{2\ln a_0/a_{min}}} \end{aligned} \tag{26}$$

For a distributed current, $\ln a_0/a_{min} \sim$ few. Thus, the flux tubes oscillate around the equilibrium configuration, as the numerical simulations demonstrate.

Next, let us estimate the resulting electric field and the electric potential during the initial nearly ideal stage of oscillations. Given the evolution of the magnetic field described above, we can find a typical electric field (by integrating $\partial_t \mathbf{B} + \operatorname{curl} \mathbf{E} = 0$). We find at the point $x = y = 0$

$$\begin{aligned} \dot{B} &\approx \frac{2\sqrt{2}I_0}{a_0^2\sqrt{\ln a_0/a_{min}}} \\ E &= \frac{2I_0 t}{a_0^2\sqrt{\ln a_0/a_{min}}} \ln\left(\frac{2}{\ln a_0/a_{min}}(ct/a_0)^2\right) \end{aligned} \tag{27}$$

Thus, the electric field instantaneously becomes of the order of the magnetic field; at the point $x = 0, y = 0$,

$$E/B = \frac{\ln\left(\frac{2}{\ln a_0/a_{min}}(ct/a_0)^2\right)}{\sqrt{2}} \tag{28}$$

(value of magnetic field at the point $x = 0, y = 0$ also increases linearly with time).

The model presented above explains the two stages of the island merger observed in numerical simulations. Initially, the merger is driven by the attraction of parallel currents. This stage of the instability is very fast, proceeding on dynamical (Alfvén) time scale. After the perturbation reaches non-linear stage, it takes about one dynamical time scale to reach a new equilibrium consisting of two attracting current tubes and a repulsive current sheet in between. During the initial stage electric fields of the order of the magnetic fields develop. After the system reaches a new equilibrium the ensuing evolution proceeds on slower time-scales that depend on plasma resistivity.

6. Collapse of a system of magnetic islands

6.1. 2D magnetic ABC structures

In this section we consider large scale dynamics that can lead to the X-point collapse described above. As an initial pre-flare state of plasma we consider a 2D force-fee lattice of magnetic flux tubes

$$\begin{aligned} B_x &= -\sin(2\pi\alpha y)B_0\,, \\ B_y &= \sin(2\pi\alpha x)B_0\,, \\ B_z &= (\cos(2\pi\alpha x)+\cos(2\pi\alpha y))\,B_0\,, \end{aligned} \tag{29}$$

Fig. 22. This constitutes a lattice of force-free magnetic islands separated by 90^o X-points in equilibrium. Islands have alternating out-of-the-plane poloidal fields and alternating toroidal fields. Each magnetic flux tube carries a magnetic flux $\propto B_0/\alpha^2$, energy per unit length $\propto B_0^2/\alpha^2$, helicity per unit length $\propto B_0^2/(\alpha^3)$ and axial current $\propto B_0/(\alpha)$. Helicity of both types of flux tubes is of the same sign.

Previously, this configuration has been considered by Parker (1983) in the context of Solar magnetic fields; he suggested that this force-free configuration is unstable. Later Longcope & Strauss (1994) considered the evolution of the instability. In case of force-free plasma the instability has been recently considered by East et al. (2015). The configuration (29) belong to a family of ABC flows (Arnold-Beltrami-Childress, *e.g.,* Roberts 1972). ABC magnetic structures are known to be stable to ideal perturbations Arnold (1974); Molodensky (1974); Moffatt (1986) *provided* that all three corresponding coefficients are non-zero. Two-dimensional structures considered here do not satisfy this condition - in this case the islands can move with respect to each other, reducing their interaction energy, as we show below. The stable full 3D ABC structures do not allow for such motion. Full 3D ABC structures have all fields linked, while in case of 2D the neighboring cylinders are not linked together. The difference between stable 3D and unstable 2D ABC configurations illustrates a general principle that lower dimension magnetic structures are typically less stable.

We foresee that the configuration (29) is created by *large scale* turbulent processes described in §2.1, and *not* through slow evolution from smaller scales, via, *e.g.,* an inverse cascade-type process (Zrake 2014) - such cascade is expected to be highly dissipative, see Appendix C.

6.2. The nature of the instability

The instability of the 2D ABC configuration is of the kind "parallel currents attract". In the initial configuration the attraction of parallel currents is balanced by the repulsion of anti-parallel ones. Small amplitude fluctuations lead to fluctuating forces between the currents, that eventually lead to the disruption of the system. To identify the dominant instability mode let us consider a simplified model problem replacing each island by a solid tube carrying a given current. Such incompressible-type approximation is expected to be valid at early times, when the resulting motions are slow and the amount of the dissipated magnetic energy is small.

We identify two basic instability modes which we call the shear mode and the compression mode. Let us first consider a global shear mode, Fig. 23. Let us separate the 2D ABC equilibrium into a set of columns, labeled 1-2-3, Fig. 23. In the initial state the flux tubes in the columns 1 and 3 (dashed lines) are horizontally aligned with those in column 2. Let us shift columns 1 and 3 by a value $-dy$ (or, equivalently, shift the column 2 by $+dy$; corresponding horizontal displacement is $dx = \pm dy^2/2$. Let us consider forces on the central island (labeled by 0 in Fig. 23). The interaction of the central island with island 4 and 8 produces a force in the positive y direction $F_{y,4}+F_{y,8} \propto dy/2$. The sum of forces $F_{y,1}+F_{y,3}+F_{y,5}+F_{y,7} \propto dy/2$ also produces a force in the positive vertical direction. From the symmetry

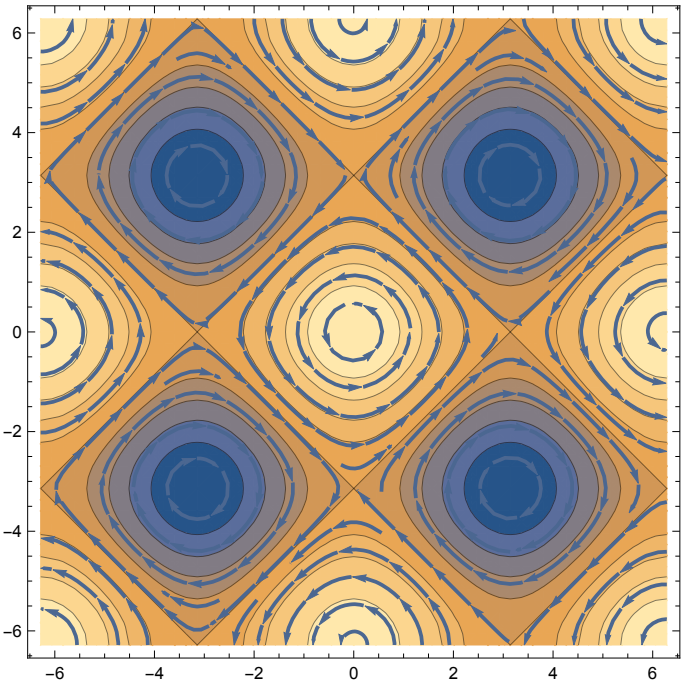

Fig. 22.— A 2D force-free system of magnetic islands (magnetic ABC structures). Color indicates out-of-the-plane magnetic field. Both types of islands have the same helicity. At the X-point the magnetic field and current are exactly zero.

of the problem it is clear that the sum of all the forces from all the islands produce a net force in the positive vertical direction - this amplifies the perturbations, leading to instability.

We can also compare directly the corresponding interaction energies of the two states pictured in Fig. 23. Let us approximate each flux tube as a line current I. Up to insignificant overall factor the interaction energy of two currents is $\propto I_1 I_2 \log r_{12}$ where r_{12} is the distance between the two currents. Consider an arbitrary flux tube. It's interaction with flux tubes located in the even row from a given one are the same in two cases. In the second case the interaction with flux tubes located in the odd rows is zero by symmetry, while in the initial state it is

$$E_{odd} = \sum_{n=0} (-1)^n \ln \sqrt{n^2 + (2m+1)^2}, \tag{30}$$

(here $2m+1$, $m = 0, 1, 2...$ is the number of a row from a given island, $n = 0, 1, 2...$ is the number of the islands in a row from a given islands). This sum (30) is positive: the interaction energy with the $n = 0$ island is always positive, $\propto \ln((2m+1)r_0)$; the sum over nth and $n+1$ islands is also positive, $\propto \ln((n+1)^2 + (2m+1)^2)/(n^2 + (2m+1)^2) > 0$. Thus, the energy of the second state in Fig. 23 is lower - this is the driver of the instability.

There is another instability mode that we identified, Fig. 24. Instead of coherent shift of the rows/columns it involve local re-arrangement of two pairs of flux tubes, Fig. 24. This configuration has a lower energy than the initial state: the forces of interaction of each touching pair of currents with all other touching pairs of currents is zero by symmetry. Thus, what is important is the change in the energy for each two pairs of currents, left panel. It is negative and is $\propto -\ln(2/\sqrt{3})$.

This simple model problem demonstrates semi-qualitatively the exponentially growing instability of a system of

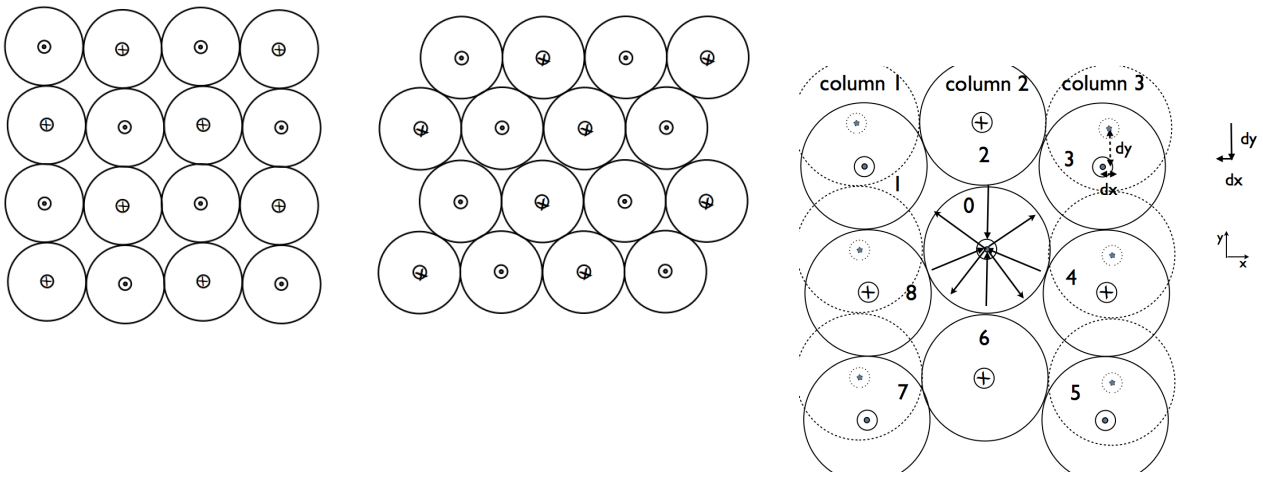

Fig. 23.— Qualitative picture of the development of shear-type instability. The initial magnetic 2D ABC structure (*Left Panel*) is unstable to long wavelength instability whereby each consecutive row is shifted by a half wave-length (*Right Panel*). A current sheet forms in-between the islands with co-aligned currents leading to catastrophic merger. Right Panel: The nature of the instability. Shifting alternating rows (or columns) of magnetic islands leads to a force dis-balance that amplified the perturbation. In the particular case, shifting first and third column leads to a force along the positive direction on the islands in the second column, amplifying the perturbations.

magnetic islands. The instability initially is ideal and proceeds on the dynamical time scale of an island, so that perturbations grow to non-linear stage in few dynamical time scales.

The above analytical considerations are clearly confirmed by numerical experiments as we discuss next.

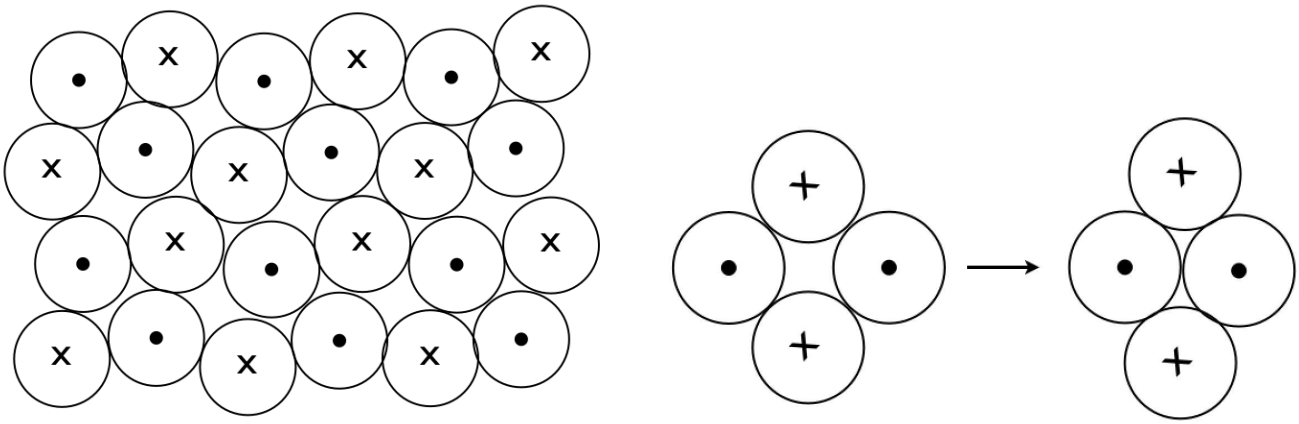

Fig. 24.— Second mode of instability.

6.3. 2D ABC instability: evolution in the force-free regime

6.3.1. Force-free simulations

Force-free simulations were carried out in a square domain of size $[-L, L] \times [-L, L]$ with 400 grid cells in each direction. Periodic boundary conditions were imposed on all boundaries. Four models with different magnetic Reynolds numbers $Re_m = 4\pi\kappa_\parallel L/c$ were investigated. Fig. 26 shows the evolution of the parameter $1 - E^2/B^2$, which is a Lorentz-invariant measure of the relative electric field strength, for the model with $Re_m = 10^3$. Until $t = 7$ this parameter remains very close to zero throughout the whole domain, indicating absence of current sheets and rapid motion in the bulk. Around $t = 7$, thin current sheets become visible in between magnetic islands (see the top-left panel of Fig. 26). After this time the evolution proceeds rapidly - small islands merge to form larger ones until only two islands remain as one can also see in Fig. 27, which shows the evolution of B_z. Models with higher Re_m show very similar evolution, with almost the same time for the onset of mergers and the same rate of magnetic dissipation after that. Fig. 28 shows the evolution of the total electromagnetic energy in the box. One can see that for $t < 7$, the energy significantly decreases in models with $Re_m = 10^3$ and $Re_m = 2 \times 10^3$ due to the Ohmic dissipation, whereas it remains more or less unchanged in the models with $Re_m > 5 \times 10^3$. The first "knee" on each curve corresponds to the onset of the first wave of merges. At $t > 7$ the magnetic dissipation rate no longer depends on Re_m. The characteristic time scale of the process is very short – only few light-crossings of the box.

Overall, the numerical results agree with our theoretical analysis (§s 6-5). The fact that the onset of mergers does not depend on Re_m supports the conclusion that the evolution starts as *an ideal instability, driven by the large-scale magnetic stresses.* This instability leads to the relative motion of flux tubes and development of stressed X-points, with highly unbalanced magnetic tension. They collapse and form current sheets (see Fig. 25).

Until $t \leq 7$ the instability develops in the linear regime and the initial periodic structure is still well preserved. At the non-linear stage, at $t \geq 7$, two new important effects come into play. Firstly, the magnetic reconnection leads to the emergence of closed magnetic field lines around two or more magnetic islands of similar polarity (see Fig. 28). Once formed, the common magnetic shroud pushes the islands towards the reconnection region in between via magnetic tension. Thus, this regime can be called a forced reconnection. As the reconnection proceeds, more common magnetic field lines develop, increasing the driving force. Secondly, the current of the current sheet separating the merging islands becomes sufficiently large to slow down the merger via providing a repulsive force (§5). Hence, the reconnection rate is determined both by the resisitivity of the current sheet and the overall magnetic tension of common field lines.

We have studied the same problem using PIC simulations of highly-magnetized plasma and their results are strikingly similar (compare Figs. 25-26-27 with Figs. 34-33). Not only they exhibit the same phases of evolution, but also very similar timescales. This shows that the details of microphysics are not important and the key role is played by the large-scale magnetic stresses.

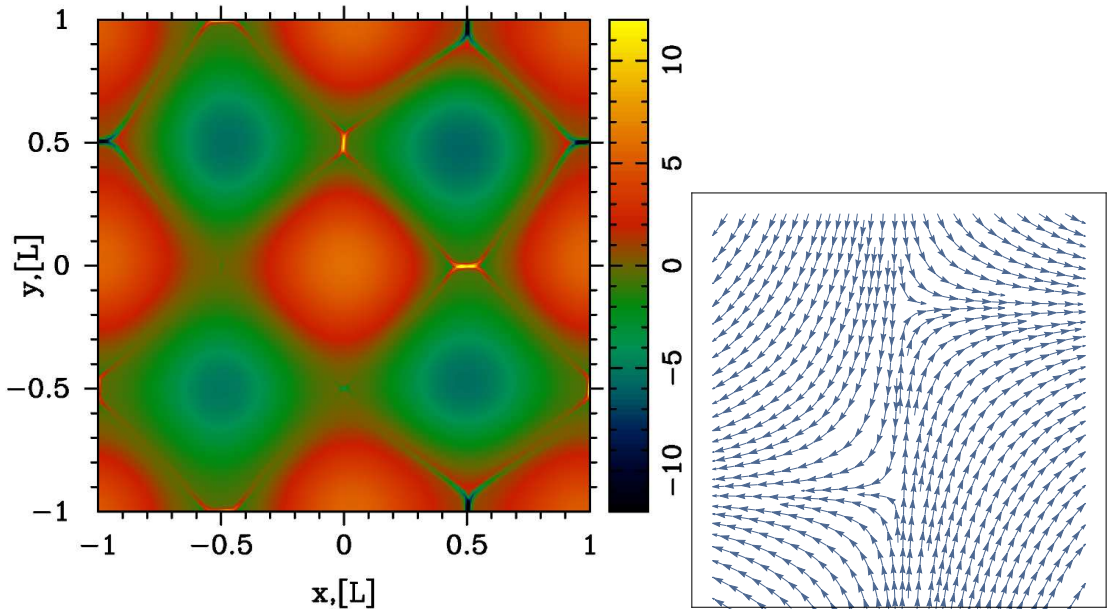

Fig. 25.— *Left Panel*: Initial stage of the development of instability in force-free simulations. The colour image shows the distribution of the current density j_z at $t = 7.4$ in the model with $Re_m = 10^3$. The newly formed current sheets are clearly visible. *Right Panel*: The developments of current sheet due to shift of magnetic islands in the theoretical model (in the initial configuration 2D ABC magnetic structure the two nearby rows of magnetic islands are shifted by some amount; this produces highly stressed configuration that would lead to X-point collapse).

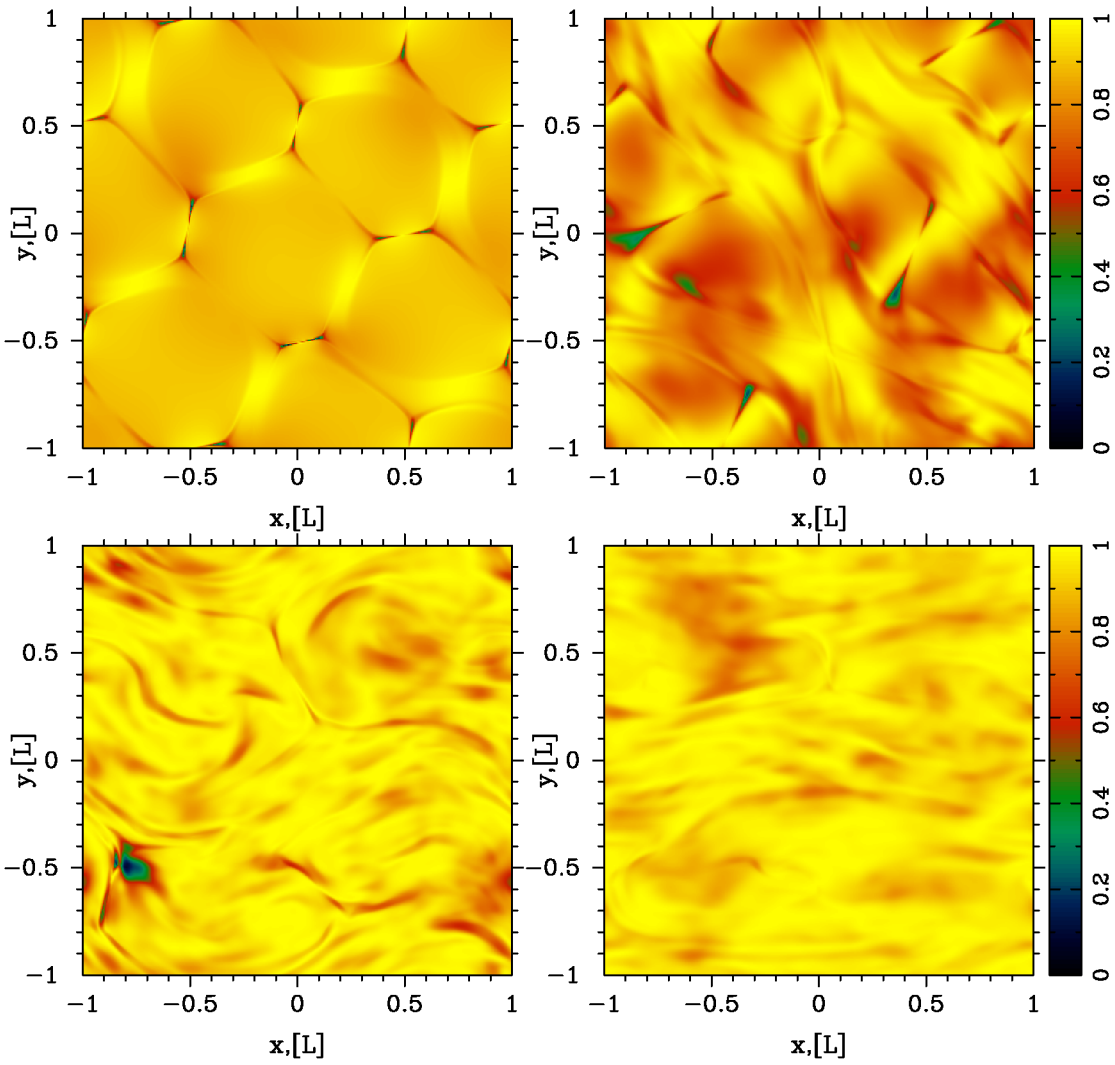

Fig. 26.— X-point collapse and island merging for a set of unstressed magnetic islands in force-free simulations. We plot $1 - E^2/B^2$ at times $t = 8.0, 10.0, 15.0$ and 20. Compare with results of PIC simulations, Fig. 33.

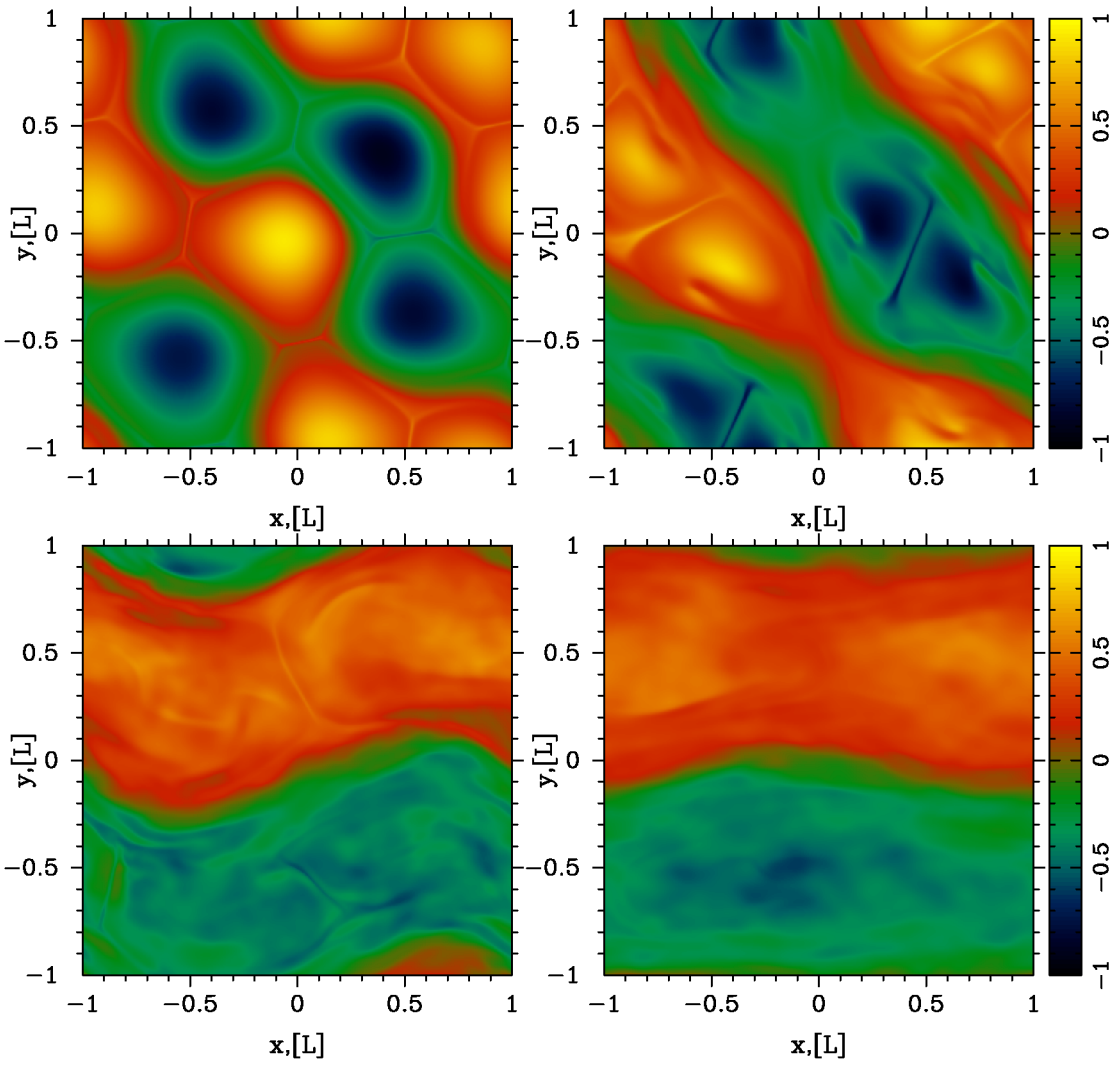

Fig. 27.— X-point collapse and island merging for a set of unstressed magnetic islands in force-free simulations. We plot $B_z/2B_0$ at times $t = 8.0, 10.0, 15.0$ and 20.

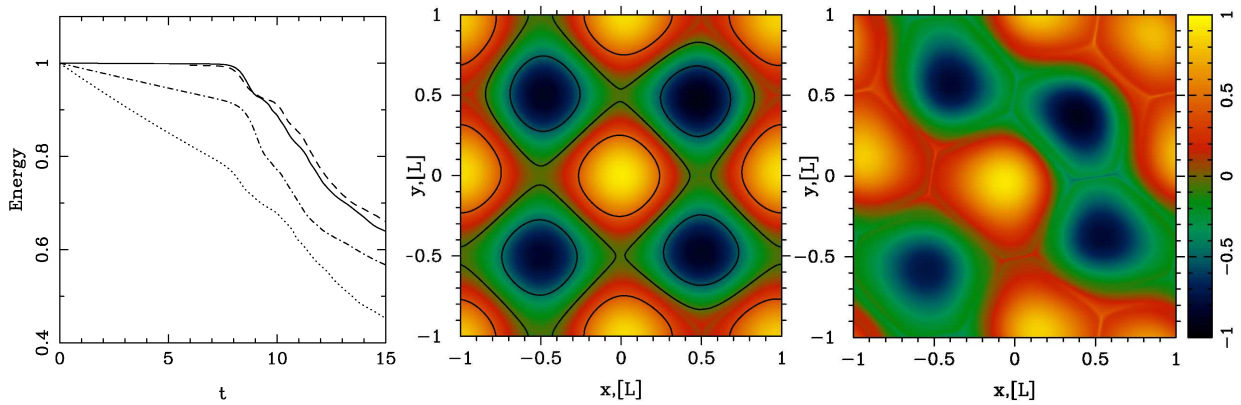

Fig. 28.— Left panel: Evolution of the total electromagnetic energy in the computational domain for the force-free models with $Re_m = 10^3$ (dotted), 2×10^3 (dash-dotted), 5×10^3 (dashed) and 2×10^4 (solid). In all models, the merger phase starts around $t = 8$, which corresponds to the first "knee" of these curves. Compare the temporal evolution of the electromagnetic in force-free simulations with those in PICs, Fig. 30. Middle and Right panels: Solutions at $t = 7.2$ (left) and $t = 8$ (right) for the model with $Re_m = 10^3$. The color-coded image shows $B_z/2B_0$. The contours are the magnetic field lines. One can see that some lines have become common for several islands.

6.4. 2D ABC instability: PIC simulations

We study the evolution of 2D ABC structures with PIC simulations, employing the electromagnetic PIC code TRISTAN-MP (Buneman 1993; Spitkovsky 2005). To the best of our knowledge, our investigation is the first to address with PIC simulations the dynamics and particle acceleration of high-magnetization ABC structures.

Our computational domain is a square in the $x-y$ plane with periodic boundary conditions in both directions. The simulation box is initialized with a uniform density of electron-positron plasma at rest, a vanishing electric field and with the magnetic field appropriate for the 2D ABC configuration, as described in Eq. 29. In addition to the unstressed geometry in Eq. 29, we also investigate the case of 2D magnetic structures with an initial stress, or with an initial velocity shear, as we specify below.

For our fiducial runs, the spatial resolution is such that the plasma skin depth $c/\omega_{\rm p}$ is resolved with 2.5 cells, but we have verified that our results are the same up to a resolution of $c/\omega_{\rm p} = 10$ cells. Since we investigate the case of both cold and hot background plasmas, our definition of the skin depth is $c/\omega_{\rm p} = \sqrt{mc^2[1+(\hat{\gamma}-1)^{-1}kT/mc^2]/4\pi ne^2}$, where $\hat{\gamma}$ is the adiabatic index. Each cell is initialized with two positrons and two electrons, but we have checked that our results are the same when using up to 16 particles per cell. In order to reduce noise in the simulation, we filter the electric current deposited onto the grid by the particles, mimicking the effect of a larger number of particles per cell (Spitkovsky 2005; Belyaev 2015).

Our unit of length is the diameter L of the ABC structures, and time is measured in units of L/c. Typically, our domain is a square of side $2L$, but we have investigated also rectangular domains with size $2L \times L$, and large square domains with dimensions $4L \times 4L$. In addition to the shape of the domain, we also vary the flow parameters, such as the temperature of the background plasma ($kT/mc^2 = 10^{-4}$, 10 and 10^2) and the flow magnetization. The general definition of the magnetization is $\sigma = B^2/4\pi w$, where $w = nmc^2 + \hat{\gamma}p/(\hat{\gamma}-1)$; here, w is the enthalpy, p is the pressure and $\hat{\gamma}$ is the adiabatic index. In the following, we identify our runs via the mean value $\sigma_{\rm in}$ of the magnetization measured with the in-plane fields (so, excluding the B_z field). As we argue below, it is the dissipation of the in-plane fields that primarily drives efficient heating and particle acceleration. The mean in-plane field corresponding to $\sigma_{\rm in}$ shall be called $B_{0,\rm in}$, and it will be our unit of measure of the electromagnetic fields. For the 2D ABC geometry, $B_{0,\rm in}$ is equal to the field B_0 in Eq. 29. We will explore a wide range of magnetizations, from $\sigma_{\rm in} = 3$ up to $\sigma_{\rm in} = 680$. The mean magnetization of the system, including all the magnetic field components, is $2\sigma_{\rm in}$.

It will be convenient to compare the diameter L of ABC structures to the characteristic Larmor radius $r_{\rm L,hot} = \sqrt{\sigma_{\rm in}}\, c/\omega_{\rm p}$ of the high-energy particles heated/accelerated by reconnection (rather than to the skin depth $c/\omega_{\rm p}$). We will explore a wide range of $L/r_{\rm L,hot}$, from $L/r_{\rm L,hot} = 31$ up to 502. We will demonstrate that the two most fundamental parameters that characterize a system of 2D ABC structures are the magnetization $\sigma_{\rm in}$ and the ratio $L/r_{\rm L,hot}$.

6.4.1. The instability of 2D ABC structures

Figure 29 illustrates the instability of a typical 2D ABC structure. The plot presents the 2D pattern of the out-of-plane field B_z (in units of $B_{0,\rm in}$) from a PIC simulation with $kT/mc^2 = 10^2$, $\sigma_{\rm in} = 42$ and $L = 126\, r_{\rm L,hot}$, performed within a large square domain of size $4L \times 4L$. Time is measured in units of L/c and indicated in the grey boxes within each panel. The system does not show any evidence of evolution until $ct/L \sim 4$. This is also confirmed by the temporal tracks shown in Fig. 30, where the top panel presents the energy partition among different components. Until $ct/L \sim 4$, all the energy is still in the magnetic field (solid blue line), and the state of the system is identical to the initial setup.

Quite abruptly, at $ct/L \sim 5$ (top right panel in Fig. 29), the system becomes unstable. The pattern of magnetic islands shifts along the oblique direction, in analogy to the mode illustrated in Fig. 23. In agreement with the fluid

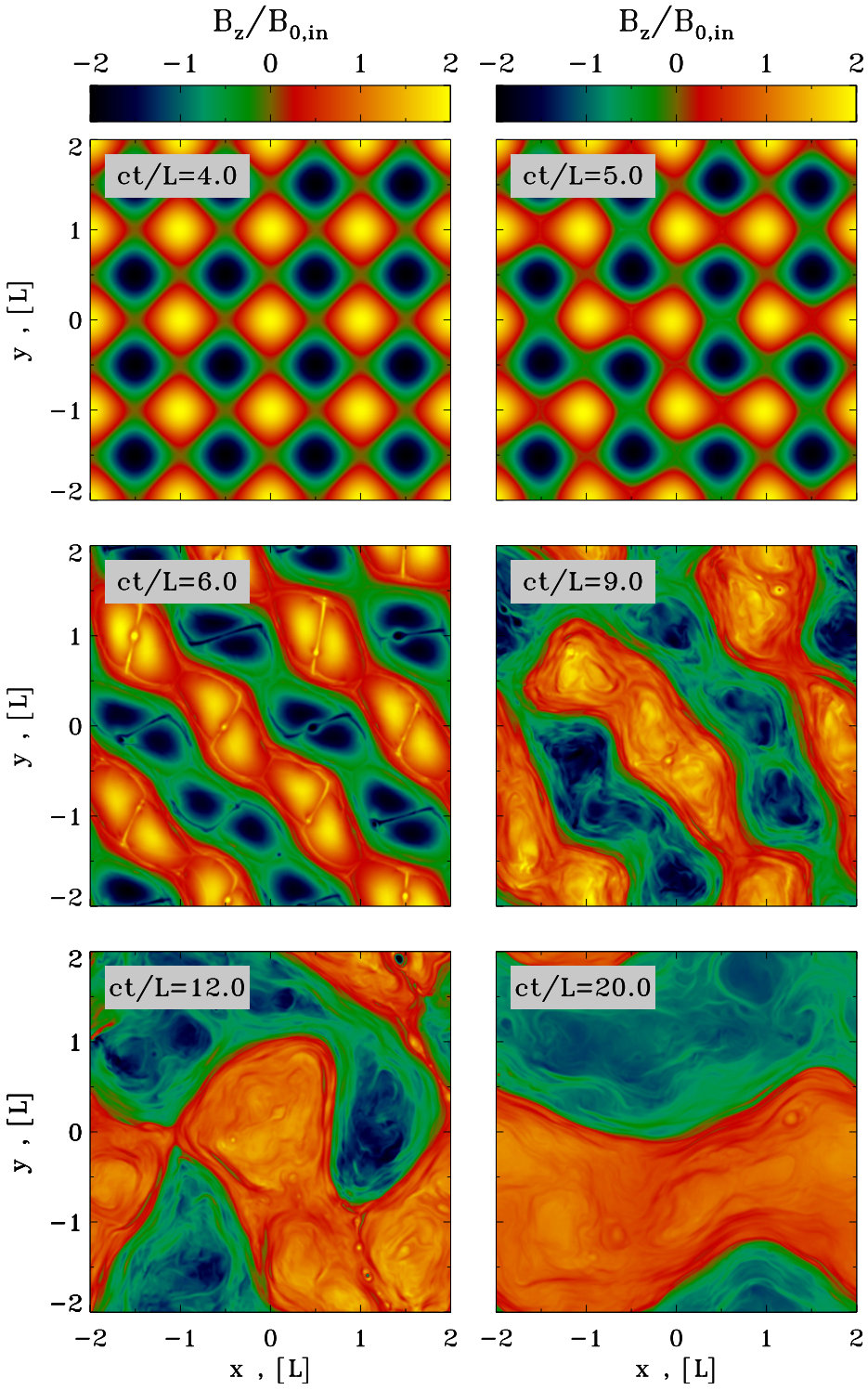

Fig. 29.— Temporal evolution of the instability of a typical 2D ABC structure (time is indicated in the grey box of each panel). The plot presents the 2D pattern of the out-of-plane field B_z (in units of $B_{0,\rm in}$) from a PIC simulation with $kT/mc^2 = 10^2$, $\sigma_{\rm in} = 42$ and $L = 126\, r_{\rm L,hot}$, performed within a large square domain of size $4L \times 4L$. The system stays unperturbed until $ct/L \simeq 4$, then it goes unstable via the oblique mode presented in Fig. 23. The instability leads to the formation of current sheets of length $\sim L$ (at $ct/L = 6$), and to the merger of islands with B_z fields of the same polarity. At the final time, the box is divided into two regions with B_z fields of opposite polarity. This should be compared with the force-free results in Fig. 27.

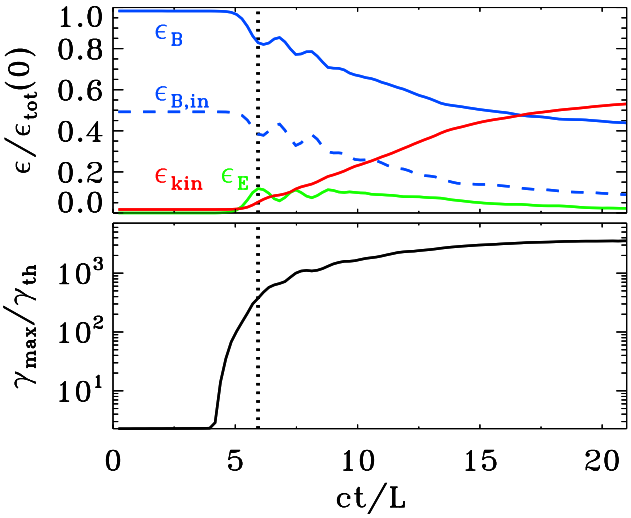

Fig. 30.— Temporal evolution of various quantities, from a 2D PIC simulation of ABC instability with $kT/mc^2 = 10^2$, $\sigma_{\rm in} = 42$ and $L = 126\, r_{\rm L,hot}$, performed within a large square domain of size $4L \times 4L$ (the same run as in Fig. 29). Top panel: fraction of energy in magnetic fields (solid blue), in-plane magnetic fields (dashed blue, with $\epsilon_{B,\rm in} = \epsilon_B/2$ in the initial configuration), electric fields (green) and particles (red; excluding the rest mass energy), in units of the total initial energy. Compare the temporal evolution of the electromagnetic in PIC simulations with those in force-free, Fig. 28. Bottom panel: evolution of the maximum Lorentz factor $\gamma_{\rm max}$, as defined in Eq. (16), relative to the thermal Lorentz factor $\gamma_{\rm th} \simeq 1 + (\hat{\gamma} - 1)^{-1} kT/mc^2$, which for our case is $\gamma_{\rm th} \simeq 300$. The development of the instability at $ct/L \simeq 5$ is accompanied by little field dissipation ($\epsilon_{\rm kin}/\epsilon_{\rm tot}(0) \sim 0.1$) but dramatic particle acceleration. In both panels, the vertical dotted black line indicates the time when the electric energy peaks, which happens shortly before the end of the most violent phase of instability.

simulations presented by East et al. (2015), our PIC results confirm that this is an ideal instability. The onset time is comparable to what is observed in force-free simulations (see Fig. 28) and it does not appreciably depend on numerical parameters (so, on the level of numerical noise). In particular, we find no evidence for an earlier onset time when degrading our numerical resolution (spatial resolution or number of particles per cell). As we show below, the onset time at $ct/L \sim 5$ is also remarkably independent of physical parameters, with only a moderate trend for later onset times at larger values of $L/r_{\rm L,hot}$. We have also investigated the dependence of the onset time on the number of ABC islands in the computational domain (or equivalently, on the box size in units of L). We find that square domains with $2L \times 2L$ or $4L \times 4L$ yield similar onset times, whereas the instability is systematically delayed (by a few L/c) in rectangular boxes with $2L \times L$, probably because this reduces the number of modes that can go unstable (in fact, we have verified that ABC structures in a periodic square box of size $L \times L$ are stable).

Following the instability onset, the evolution of the system proceeds on the dynamical time. Within a few L/c, as they drift along the oblique direction, neighboring islands with the same B_z polarity come into contact (middle left panel in Fig. 29 at $ct/L = 6$), the X-points in between each pair of islands collapse under the effect of large-scale stresses (see Sect. 4.2), and thin current sheets are formed. For the parameters of Fig. 29, the resulting current sheets are so long that they are unstable to the secondary tearing mode (Uzdensky et al. 2010), and secondary plasmoids are formed (e.g., see the plasmoid at $(x, y) = (-1.5L, L)$ at $ct/L = 6$). Below, we demonstrate that the formation of secondary plasmoids is primarily controlled by the ratio $L/r_{\rm L,hot}$. At the X-points, the magnetic energy is converted into particle energy by a reconnection electric field of order $\sim 0.3B_{\rm in}$, where $B_{\rm in}$ is the in-plane field (so, the reconnection rate is $v_{\rm rec}/c \sim 0.3$).[11] As shown in the top panel of Fig. 30, it is primarily the in-plane field that gets dissipated (compare the dashed and solid blue lines), driving an increase in the electric energy (green) and in the particle kinetic energy (red).[12] In this phase of evolution, the fraction of initial energy released to the particles is still small ($\epsilon_{\rm kin}/\epsilon_{\rm tot}(0) \sim 0.1$), but the particles advected into the X-points experience a dramatic episode of acceleration. As shown in the bottom panel of Fig. 30, the cutoff Lorentz factor $\gamma_{\rm max}$ of the particle spectrum presents a dramatic evolution, increasing from the thermal value $\gamma_{\rm th} \simeq 3kT/mc^2$ (here, $kT/mc^2 = 10^2$) by a factor of 10^3 within a couple of dynamical times. It is this phase of extremely fast particle acceleration that we associate with the generation of the Crab flares.

Over one dynamical time, the current sheets in between neighboring islands stretch to their maximum length of $\sim L$. This corresponds to the time when the electric energy peaks, which is indicated by the dotted black line in Fig. 30, and it shortly precedes the end of the most violent phase of instability. The peak time of the electric energy will be a useful reference point when comparing runs with different physical parameters. The first island merger event ends at $ct/L \sim 7$ with the coalescence of island cores. At later times, the system of magnetic islands will undergo additional merger episodes (i.e., at $ct/L \sim 9$ and 12), with the formation of current sheets and secondary plasmoids (see, e.g., at $(x, y) = (L, -1.5L)$ in the bottom left panel of Fig. 29), but the upper cutoff of the particle spectrum will not change by more than a factor of three (see the bottom panel in Fig. 30 at $ct/L \gtrsim 6$). As a consequence, the spectral cutoff at the final time is not expected to be significantly dependent on the number of lengths L in the computational domain, as we have indeed verified. Rather than dramatic acceleration of a small number of "lucky" particles, the late phases result in substantial heating of the bulk of the particles, as illustrated by the red line in the top panel of Fig. 30. As a consequence of particle heating, the effective magnetization of the plasma is only $\sigma_{\rm in} \sim 1$ after the initial merger episode (compare the dashed blue and solid red lines at $ct/L \sim 9$ and 12 in the top panel of Fig. 30), which explains why additional island mergers do not lead to dramatic particle acceleration. The rate of dissipation of magnetic energy into

[11] This value of the reconnection rate is roughly comparable to the results of solitary X-point collapse presented in Sect. 4.2. However, a direct comparison cannot be established, since in that case we either assumed a uniform nonzero guide field or a vanishing guide field. Here, the X-point collapse starts in regions with zero guide field. Yet, as reconnection proceeds, an out-of-plane field of increasing strength is advected into the current sheet.

[12] The out-of-plane field does not dissipate because island mergers always happen between pairs of islands having the same B_z polarity.

particle energy at late times is roughly consistent with the results of force-free simulations (see Fig. 28). At late times, the system saturates when only two regions are left in the box, having B_z fields of opposite polarity (bottom right panel in Fig. 29). In the final state, most of the in-plane magnetic energy has been trasferred to the particles (compare the red and dashed blue lines in the top panel of Fig. 30).

In Fig. 34 we compare the development of the two modes of instability, the shearing and the compressive one.

6.4.2. Particle acceleration and emission signatures

The evolution of the particle spectrum in the top panel of Fig. 31 illustrates the acceleration capabilities of the instability of ABC structures. Until $ct/L \sim 4$, the particle spectrum does not show any sign of evolution, and it does not deviate from the initial Maxwellian distribution peaking at $\gamma_{\rm th} \simeq 300$. From $ct/L \sim 4$ up to $ct/L \sim 8$ (from purple to light blue in the plot), the high-energy end of the particle spectrum undergoes a dramatic evolution, whereas the thermal peak is still unaffected (so, only a small fraction of the particles are accelerated). This is the most dramatic phase of particle acceleration, which we associate with the Crab flares. At the end of this explosive phase, the high-energy tail of the particle spectrum resembles a power law $dN/d\gamma \propto \gamma^{-s}$ with a hard slope $s \sim 1.5$. The angle-averaged synchrotron spectrum (bottom panel in Fig. 31) parallels the extreme evolution of the particle spectrum, with the peak frequency of νL_ν moving from the "thermal" value $\sim 10^8 \nu_{B,\rm in}$ (dominated by the emission of thermal particles with $\gamma \sim \gamma_{\rm th}$) up to $\sim 10^{13} \nu_{B,\rm in}$ within just a few dynamical times. Here, we have defined $\nu_{B,\rm in} = \sqrt{\sigma_{\rm in}}\omega_{\rm p}/2\pi$.

The evolution at later times, during subsequent merger episodes, is at most moderate. From $ct/L \sim 8$ up to the final time $ct/L \sim 20$ (from light blue to red in the plot), the upper energy cutoff of the particle spectrum only increases by a factor of three, and the peak synchrotron frequency only by a factor of ten. The most significant evolution of the electron spectrum at such late times involves the thermal peak of the distribution, which shifts up in energy by a factor of ~ 10. This confirms what we have anticipated above, i.e., that subsequent episodes of island mergers primarily result in particle heating, rather than non-thermal acceleration. At the final time, the particle high-energy spectrum resembles a power law $\gamma dN/d\gamma \propto \gamma^{-1}$ (compare with the dotted black line in the top panel) and, consequently, the angle-averaged synchrotron spectrum approaches $\nu L_\nu \propto \nu^{1/2}$ (compare with the dotted black line in the bottom panel).

The inset in the top panel of Fig. 31 shows the electron momentum distribution along different directions (as indicated in the legend), at the time when the electric energy peaks (as indicated by the dotted black line in Fig. 30). The electron distribution is roughly isotropic. This might appear surprising, since at this time the particles are being dramatically accelerated at the collapsing X-points in between neighboring islands, and in Sect. 4.2 we have demonstrated that the particle distribution during X-point collapse is highly anisotropic. The accelerated electrons were beamed along the reconnection outflow and in the direction opposite to the accelerating electric field (while positrons were parallel to the electric field). Indeed, the particle distribution at each X-point in the collapsing ABC structure shows the same anisotropy as for a solitary X-point.

The apparent isotropy in the inset of the top panel of Fig. 31 is a peculiar result of the ABC geometry. The middle left panel in Fig. 29 shows that in the $x-y$ plane the number of current sheets (and so, of reconnection outflows) oriented along x is roughly comparable to those along y. So, no preferred direction for the electron momentum spectrum is expected in the $x-y$ plane. In addition, in 2D ABC structures the accelerating electric field E_z has always the same polarity as the local out-of-plane magnetic field B_z (or equivalently, $\mathbf{E}\cdot\mathbf{B} > 0$ at X-points, as we explicitly show in the bottom panel in Fig. 33). In other words, current sheets that are colored in yellow in the middle left panel of Fig. 29 have $E_z > 0$, whereas $E_z < 0$ in current sheets colored in blue. Since the two options occur in equal numbers, no difference between the electron momentum spectrum in the $+z$ versus $-z$ direction is expected. Both the spatially-integrated electron momentum distribution (inset in the top panel) and the resulting synchrotron emission (inset in the bottom

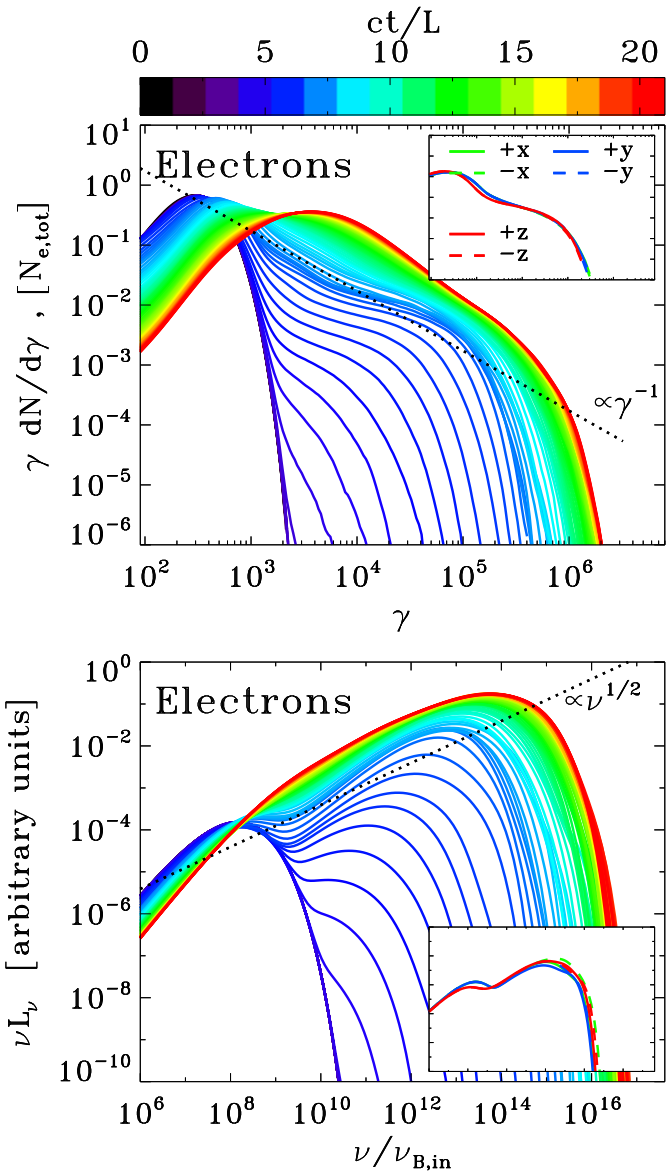

Fig. 31.— Particle spectrum and synchrotron spectrum from a 2D PIC simulation of ABC instability with $kT/mc^2 = 10^2$, $\sigma_{\rm in} = 42$ and $L = 126\,r_{\rm L,hot}$, performed within a large square domain of size $4L \times 4L$ (the same run as in Fig. 29 and Fig. 30). Time is measured in units of L/c, see the colorbar at the top. Top panel: evolution of the electron energy spectrum normalized to the total number of electrons. At late times, the spectrum approaches a distribution of the form $\gamma dN/d\gamma \propto \gamma^{-1}$, corresponding to equal energy content in each decade of γ (compare with the dotted black line). The inset in the top panel shows the electron momentum spectrum along different directions (as indicated in the legend), at the time when the electric energy peaks (as indicated by the dotted black line in Fig. 30). Bottom panel: evolution of the angle-averaged synchrotron spectrum emitted by electrons. The frequency on the horizontal axis is normalized to $\nu_{B,\rm in} = \sqrt{\sigma_{\rm in}}\omega_{\rm p}/2\pi$. At late times, the synchrotron spectrum approaches $\nu L_\nu \propto \nu^{1/2}$ (compare with the dotted black line), which just follows from the electron spectrum $\gamma dN/d\gamma \propto \gamma^{-1}$. The inset in the bottom panel shows the synchrotron spectrum at the time indicated in Fig. 30 (dotted black line) along different directions (within a solid angle of $\Delta\Omega/4\pi \sim 3\times10^{-3}$), as indicated in the legend in the inset of the top panel. The resulting isotropy of the synchrotron emission is consistent with the particle distribution illustrated in the inset of the top panel.

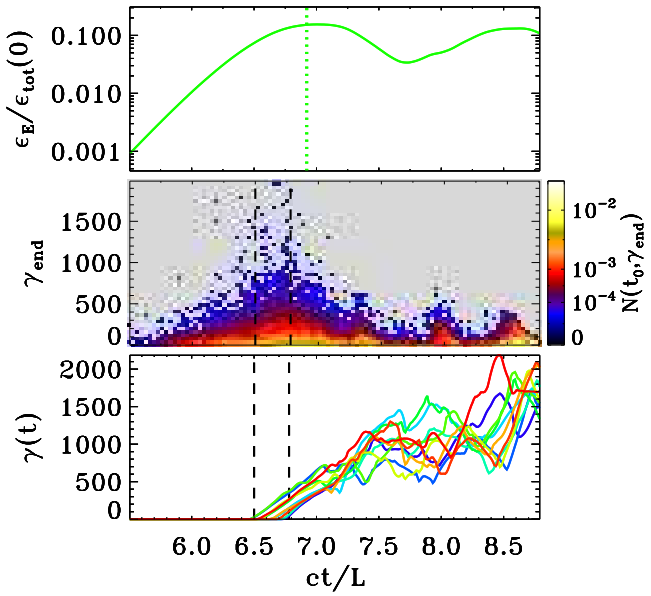

Fig. 32.— Physics of particle acceleration, from a 2D PIC simulation of ABC instability with $kT/mc^2 = 10^{-4}$, $\sigma_{\rm in} = 42$ and $L = 251\, r_{\rm L,hot}$, performed within a square domain of size $2L \times 2L$. Top panel: temporal evolution of the electric energy, in units of the total energy at the initial time. The dotted green vertical line marks the time when the electric energy peaks. Middle panel: 2D histogram of accelerated particles, normalized to the total number of particles. On the vertical axis we plot the final particle Lorentz factor $\gamma_{\rm end}$ (measured at the final time $ct/L = 8.8$), while the horizontal axis shows the particle injection time ct_0/L, when the particle Lorentz factor first exceeded the threshold $\gamma_0 = 30$. Bottom panel: we select all the particles that exceed the threshold $\gamma_0 = 30$ within a given time interval (chosen to be $6.5 \leq ct_0/L \leq 6.8$, as indicated by the vertical dashed black lines in the middle and bottom panels), and we plot the temporal evolution of the Lorentz factor of the ten particles that at the final time reach the highest energies.

panel) will then be nearly isotropic, for the case of ABC collapse.

Figs. 32 and 33 describe the physics of particle acceleration during the instability of ABC structures. We consider a representative simulation with $kT/mc^2 = 10^{-4}$, $\sigma_{\rm in} = 42$ and $L = 251\, r_{\rm L,hot}$, performed within a square domain of size $2L \times 2L$. In the middle panel of Fig. 32, we present a 2D histogram of accelerated particles. On the vertical axis we plot the final particle Lorentz factor $\gamma_{\rm end}$ (measured at $ct/L = 8.8$), while the horizontal axis shows the particle injection time ct_0/L, when the particle Lorentz factor first exceeded the threshold $\gamma_0 = 30$ of our choice. The histogram shows that the particles that eventually reach the highest energies are injected into the acceleration process around $6.5 \leq ct_0/L \leq 6.8$ (the two boundaries are indicated with vertical dashed black lines in the middle and bottom panels). For our simulation, this interval corresponds to the most violent stage of ABC instability, and it shortly precedes the time when the electric energy peaks (see the dotted green line in the top panel of Fig. 32) and the current sheets reach their maximum length $\sim L$.[13] In order to reach the highest energies, the accelerated particles should sample the full available potential of the current sheet, by exiting the reconnection layer when it reaches its maximal extent. Since they move at the speed of light along the sheet half-length $\sim 0.5L$, one can estimate that they should have been injected

[13]Even when we extend our time window up to $\sim 15L/c$, including additional merger episodes, we still find that the highest energy particles are injected during the initial ABC collapse.

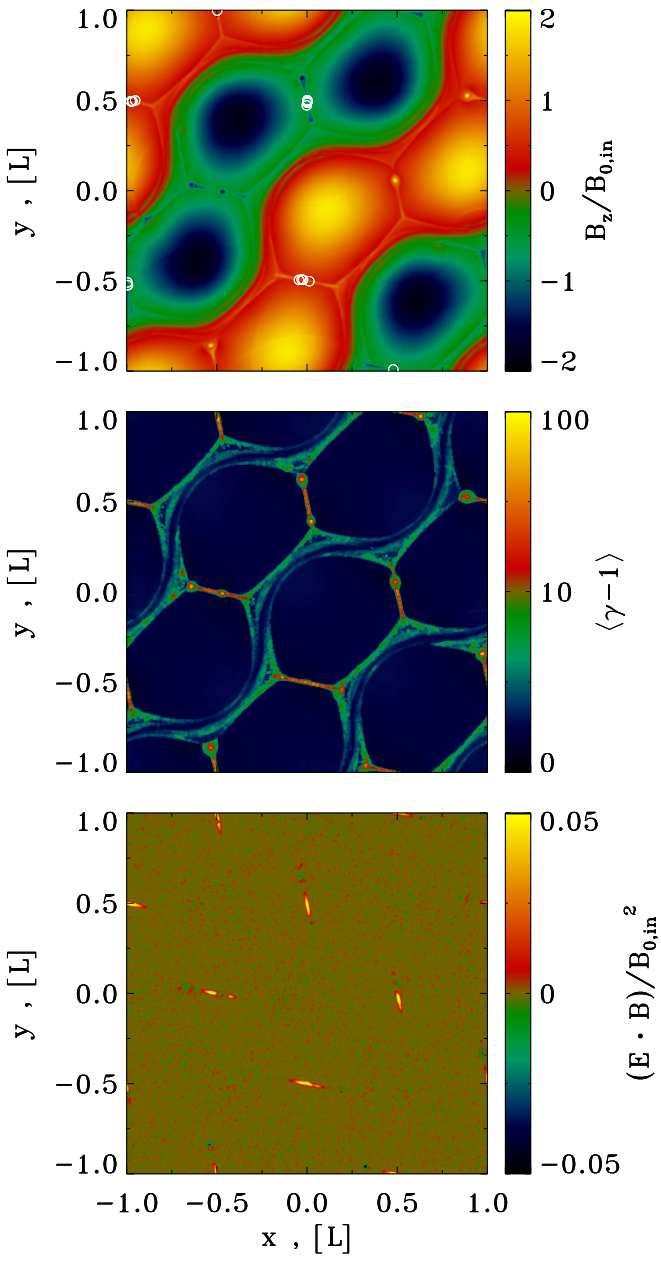

Fig. 33.— Physics of particle injection into the acceleration process, from a 2D PIC simulation of ABC instability with $kT/mc^2 = 10^{-4}$, $\sigma_{\rm in} = 42$ and $L = 251\, r_{\rm L,hot}$, performed within a square domain of size $2L \times 2L$ (same run as in Fig. 32). We plot the 2D ABC structure at $ct/L = 6.65$. Top panel: 2D plot of the out-of-plane field B_z, in units of $B_{0,\rm in}$. Among the particles that exceed the threshold $\gamma_0 = 30$ within the interval $6.5 \leq ct_0/L \leq 6.8$ (as indicated by the vertical dashed black lines in the middle and bottom panels of Fig. 32), we select the 20 particles that at the final time reach the highest energies, and with open white circles we plot their locations at the injection time t_0. Middle panel: 2D plot of the mean kinetic energy per particle $\langle\gamma - 1\rangle$. Bottom panel: 2D plot of $\mathbf{E}\cdot\mathbf{B}/B_{0,\rm in}^2$, showing in red and yellow the regions of charge starvation. Comparison of the top panel with the bottom panel shows that particle injection is localized in the charge-starved regions.

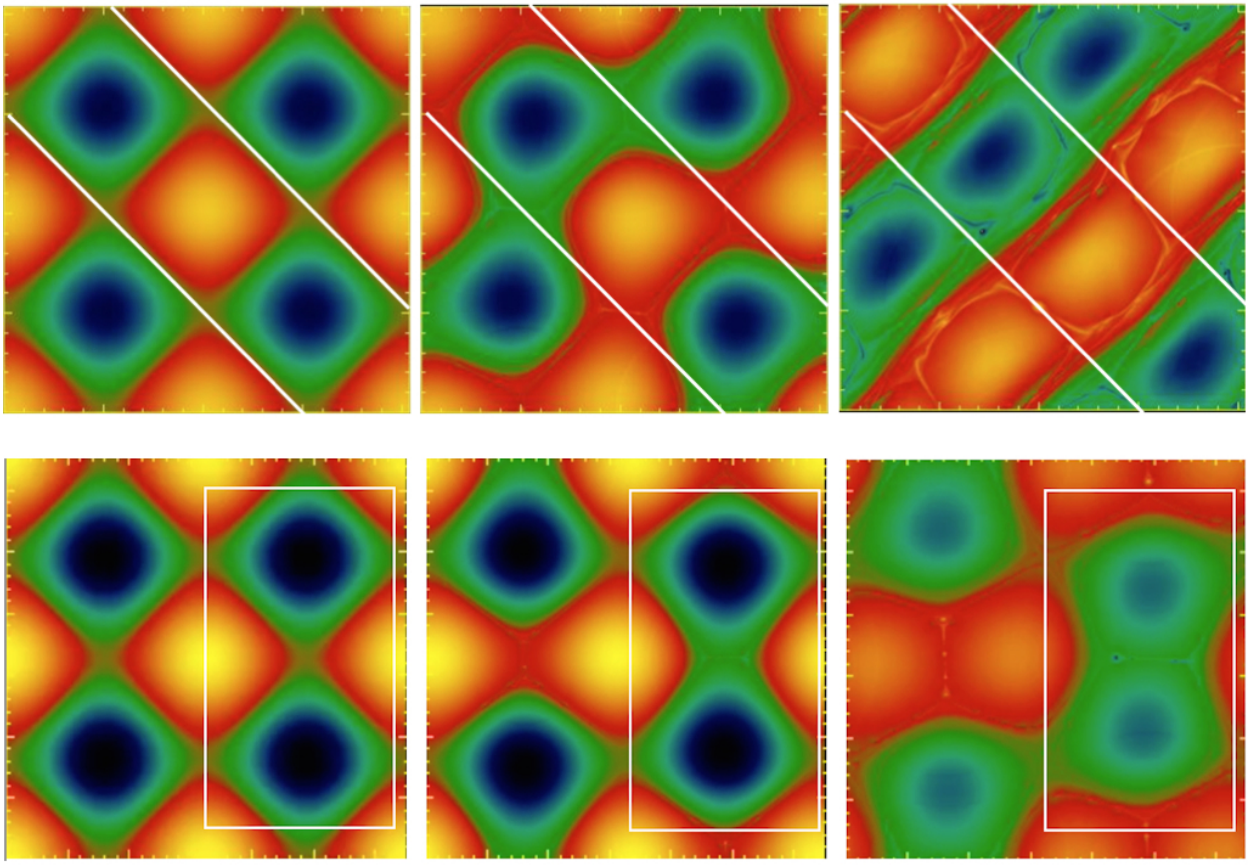

Fig. 34.— Snapshots of the numerical experiment demonstrating development of different modes of instability of 2D ABC structures. *Upper Panel*: The shearing mode. White line, separating different layers are added as a guide. These pictures clearly demonstrate that during the development of the instability two layers of magnetic islands are shifting with respect to each other. Right Panel: the compression mode. The white box demonstrates that a pair of aligned currents periodically approach each other.

$\sim 0.5L/c$ earlier than the peak time of the electric field. This is indeed in agreement with Fig. 32 (compare top and middle panels).

Among the particles injected within $6.5 \leq ct_0/L \leq 6.8$, the bottom panel in Fig. 32 shows the energy evolution of the ten positrons that reach the highest energies. We observe two distinct phases: an initial stage of direct acceleration by the reconnection electric field (at $6.5 \lesssim ct/L \lesssim 7.3$), followed by a phase of stochastic energy gains and losses (from $ct/L \sim 7.3$ up to the end). During the second stage, the pre-accelerated particles bounce off the wobbling/merging magnetic islands, and they further increase their energy via a second-order Fermi process. At the time of injection, the selected positrons were all localized in the vicinity of the collapsing X-points. This is shown in the top panel of Fig. 33, where we plot with open white circles the location of the selected positrons at the time of injection, superimposed over the 2D pattern of B_z at $t \sim 6.65L/c$. In the current sheets resulting from X-point collapse the force-free condition $\mathbf{E} \cdot \mathbf{B} = 0$ is violated (see the yellow regions in the bottom panel of Fig. 33), so that they are sites of efficient particle

acceleration (see also the middle panel in Fig. 33, showing the mean particle kinetic energy $\langle\gamma - 1\rangle$).

6.4.3. Dependence on the flow parameters

In this subsection, we explore the dependence of our results on the initial plasma temperature, the in-plane magnetization $\sigma_{\rm in}$ and the ratio $L/r_{\rm L,hot}$.

Figs. 35 and 36 describes the dependence of our results on the flow temperature, for a suite of three simulations of ABC collapse with fixed $\sigma_{\rm in} = 42$ and fixed $L/r_{\rm L,hot} = 251$, but different plasma temperatures: $kT/mc^2 = 10^{-4}$ (blue), $kT/mc^2 = 10$ (green) and $kT/mc^2 = 10^2$ (red). The definitions of both the in-plane magnetization $\sigma_{\rm in}$ and the plasma skin depth $c/\omega_{\rm p}$ (and so, also the Larmor radius $r_{\rm L,hot}$) account for the flow temperature, as described above. With this choice, Figs. 35 and 36 demonstrate that our results do not appreciably depend on the plasma temperature, apart from an overall shift in the energy scale. In particular, in the relativistic regime $kT/mc^2 \gg 1$, our results for different temperatures are virtually undistinguishable. The onset of the ABC instability is nearly the same for the three values of temperature we investigate (top panel in Fig. 35), the exponential growth is the same (with a rate equal to $\sim 4c/L$ for the electric energy, compare with the dashed black line) and the peak time is quite similar (with a minor delay for the non-relativistic case $kT/mc^2 = 10^{-4}$, in blue). At the onset of the ABC instability, the upper cutoff $\gamma_{\rm max}$ of the particle energy spectrum grows explosively. Once normalized to the thermal value $\gamma_{\rm th} \simeq 1 + (\hat{\gamma} - 1)^{-1} kT/mc^2$ (which equals $\gamma_{\rm th} \simeq 1$ for $kT/mc^2 \ll 1$ and $\gamma_{\rm th} \simeq 3kT/mc^2$ for $kT/mc^2 \gg 1$), the temporal evolution of $\gamma_{\rm max}$ does not appreciably depend on the initial temperature, especially in the relativistic regime $kT/mc^2 \gg 1$ (green and red lines).

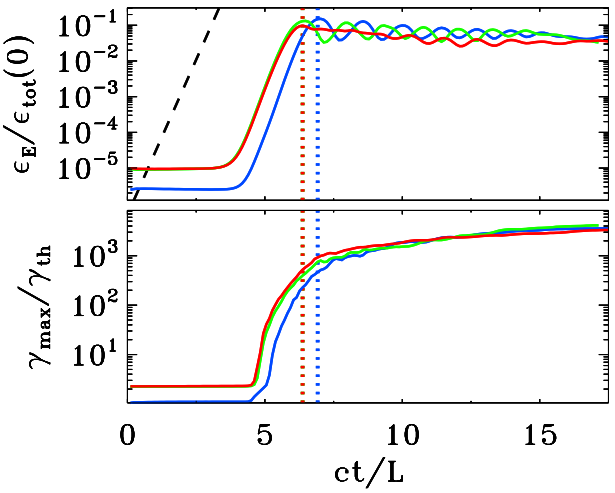

Fig. 35.— Temporal evolution of the electric energy (top panel, in units of the total initial energy) and of the maximum particle Lorentz factor (bottom panel; $\gamma_{\rm max}$ is defined in Eq. (16), and it is normalized to the thermal Lorentz factor $\gamma_{\rm th} \simeq 1 + (\hat{\gamma} - 1)^{-1} kT/mc^2$), for a suite of three PIC simulations of ABC collapse with fixed $\sigma_{\rm in} = 42$ and fixed $L/r_{\rm L,hot} = 251$, but different plasma temperatures: $kT/mc^2 = 10^{-4}$ (blue), $kT/mc^2 = 10$ (green) and $kT/mc^2 = 10^2$ (red). The dashed black line in the top panel shows that the electric energy grows exponentially as $\propto \exp(4ct/L)$. The vertical dotted lines mark the time when the electric energy peaks (colors correspond to the three values of kT/mc^2, as described above).

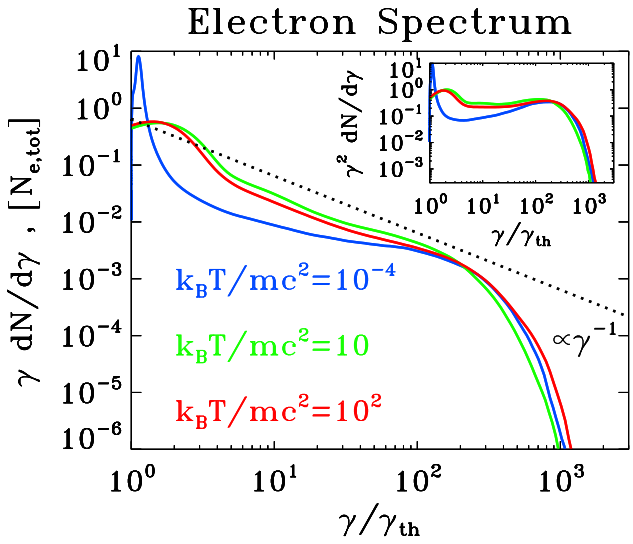

Fig. 36.— Particle spectrum at the time when the electric energy peaks, for a suite of three PIC simulations of ABC collapse with fixed $\sigma_{\rm in} = 42$ and fixed $L/r_{\rm L,hot} = 251$, but different plasma temperatures: $kT/mc^2 = 10^{-4}$ (blue), $kT/mc^2 = 10$ (green) and $kT/mc^2 = 10^2$ (red). The main plot shows $\gamma dN/d\gamma$ to emphasize the particle content, whereas the inset presents $\gamma^2 dN/d\gamma$ to highlight the energy census. The dotted black line is a power law $\gamma dN/d\gamma \propto \gamma^{-1}$, corresponding to equal energy content per decade (which would result in a flat distribution in the inset). The particle Lorentz factor on the horizontal axis is normalized to the thermal value $\gamma_{\rm th}$, to facilitate comparison among the three cases.

Similar conclusions hold for the particle spectrum $\gamma dN/d\gamma$ at the time when the electric energy peaks, presented in the main panel of Fig. 36. The spectra of $kT/mc^2 = 10$ (green) and $kT/mc^2 = 10^2$ (red) overlap, once the horizontal axis is normalized to the thermal Lorentz factor $\gamma_{\rm th}$. Their high-energy end approaches the slope $\gamma dN/d\gamma \propto \gamma^{-1}$ indicated with the dotted black line. This corresponds to a distribution with equal energy content per decade (which would result in a flat distribution in the inset, where we plot $\gamma^2 dN/d\gamma$ to emphasize the energy census). The spectrum for $kT/mc^2 = 10^{-4}$ (blue line) is marginally harder, but its high-energy part is remarkably similar.

We now investigate the dependence of our results on the magnetization $\sigma_{\rm in}$ and the ratio $L/r_{\rm L,hot}$, where $r_{\rm L,hot} = \sqrt{\sigma_{\rm in}}\, c/\omega_{\rm p}$. In Fig. 37, we present the 2D pattern of the out-of-plane field B_z (in units of $B_{0,\rm in}$) at the most violent time of ABC instability (i.e., when the electric energy peaks, as indicated by the vertical dotted lines in Fig. 38) from a suite of PIC simulations in a square domain $2L \times 2L$. In the left column, we fix $kT/mc^2 = 10^{-4}$ and $\sigma_{\rm in} = 42$ and we vary the ratio $L/r_{\rm L,hot}$, from 31 to 251 (from top to bottom). In the right column, we fix $kT/mc^2 = 10^2$ and $L/r_{\rm L,hot} = 63$ and we vary the magnetization $\sigma_{\rm in}$, from 3 to 170 (from top to bottom). The figure shows that the instability proceeds in a similar way in all the runs, even though some cases go unstable via the "parallel" mode depicted in Fig. 24 (e.g., see the top right panel) , others via the "oblique" mode described in Fig. 23 (e.g., see the bottom left panel). Here, "parallel" and "oblique" refer to the orientation of the wavevector with respect to the axes of the box.

The evolution is remarkably similar, whether the instability proceeds via the parallel or the oblique mode. Yet, some differences can be found: (*i*) In the oblique mode, all the null points are activated, i.e., they all evolve into a long thin current sheet suitable for particle acceleration; in contrast, in the parallel mode only half of the null points are activated (e.g., the null point at $x = 0$ and $y = 0.5L$ in the top right panel does not form a current sheet, and we have verified that it does not lead to significant particle acceleration). Everything else being equal, this results in a difference by a factor of two in the normalization of the high-energy tail of accelerated particles (i.e., the acceleration efficiency differs by a factor of two), as we have indeed verified. (*ii*) The current sheets of the parallel mode tend to stretch longer than for the oblique mode (by roughly a factor of $\sqrt{2}$), resulting in a difference of a factor of $\sqrt{2}$ in the maximum particle energy, everything else being the same. (*iii*) in the explosive phase of the instability, the oblique mode tends to dissipate some fraction of the out-of-plane field energy (still, a minor fraction as compared to the dissipated in-plane energy), whereas the parallel mode does not. Regardless of such differences, both modes result in efficient particle acceleration and heating, and in a similar temporal evolution of the rate of magnetic energy dissipation (with the kinetic energy fraction reaching $\epsilon_{\rm kin}/\epsilon_{\rm tot}(0) \sim 0.1$ during the explosive phase, and eventually saturating at $\epsilon_{\rm kin}/\epsilon_{\rm tot}(0) \sim 0.5$).

The 2D pattern of B_z shown in Fig. 37 shows a tendency for thinner current sheets at larger $L/r_{\rm L,hot}$, when fixing $\sigma_{\rm in}$ (left column in Fig. 37). Roughly, the thickness of the current sheet is set by the Larmor radius $r_{\rm L,hot}$ of the high-energy particles heated/accelerated by reconnection. In the right column, with $L/r_{\rm L,hot}$ fixed, the thickness of the current sheet is then a fixed fraction of the box size. In contrast, in the left column, the ratio of current sheet thickness to box size will scale as $r_{\rm L,hot}/L$, as indeed it is observed. A long thin current sheet is expected to fragment into a chain of plasmoids/magnetic islands (e.g., Uzdensky et al. 2010; Werner et al. 2016), when the length-to-thickness ratio is much larger than unity.[14] It follows that the cases in the right column will display a similar tendency for fragmentation (and in particular, they do not appreciably fragment), whereas the likelihood of fragmentation is expected to increase from top to bottom in the left column. In fact, for the case with $L/r_{\rm L,hot} = 251$ (left bottom panel), a number of small-scale plasmoids appear in the current sheets (e.g., see the plasmoid at $x = 0$ and $y = -0.5L$ in the left bottom panel). We find that as long as $\sigma_{\rm in} \gg 1$, the secondary tearing mode discussed by Uzdensky et al. (2010) — that leads to current sheet fragmentation — appears at $L/r_{\rm L,hot} \gtrsim 200$, in the case of ABC collapse.[15] In addition to the runs

[14]The fact that the ratio of lengths most important for regulating the reconnection physics is $L/r_{\rm L,hot}$ was already anticipated by Pétri & Lyubarsky (2007a) and Sironi & Spitkovsky (2011a), in the context of striped pulsar winds.

[15]This holds for both $kT/mc^2 \ll 1$ and $kT/mc^2 \gg 1$, with only a minor evidence for the transition happening at slightly smaller $L/r_{\rm L,hot}$

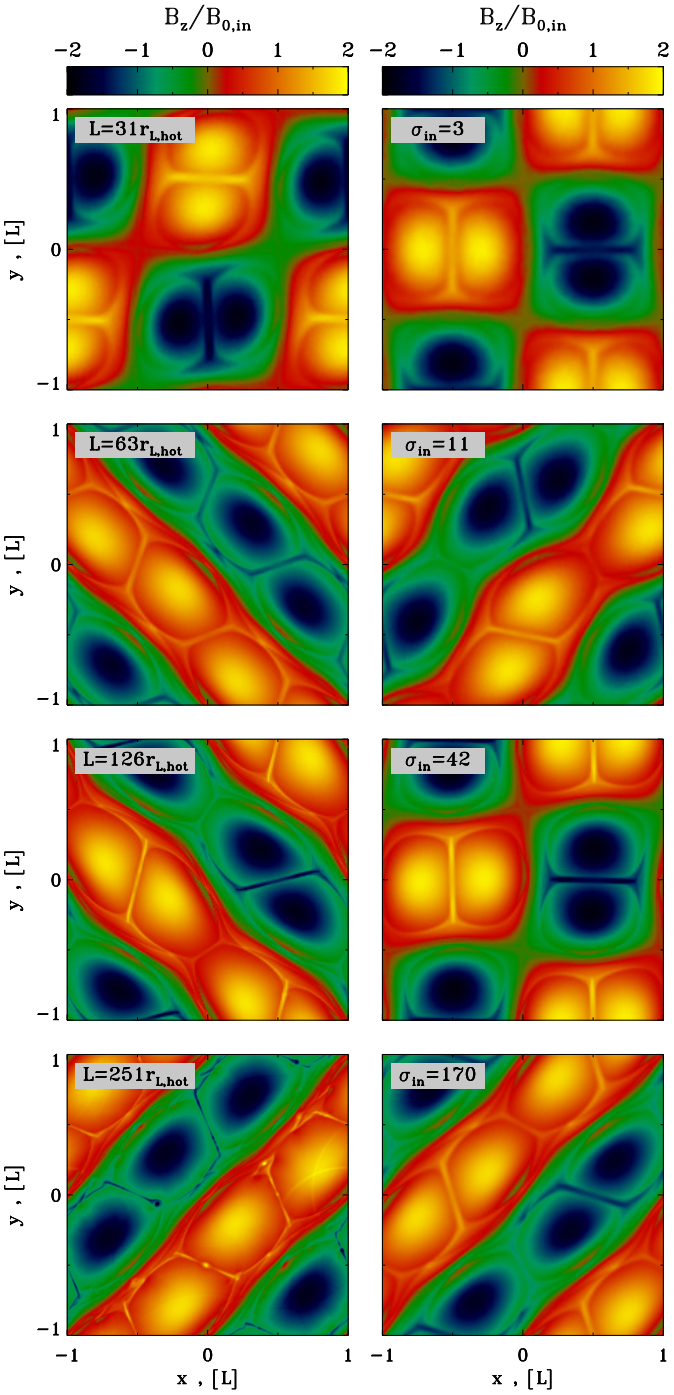

Fig. 37.— 2D pattern of the out-of-plane field B_z (in units of $B_{0,\rm in}$) at the most violent time of ABC instability (i.e., when the electric energy peaks, as indicated by the vertical dotted lines in Fig. 38) from a suite of PIC simulations. In the left column, we fix $kT/mc^2 = 10^{-4}$ and $\sigma_{\rm in} = 42$ and we vary the ratio $L/r_{\rm L,hot}$, from 31 to 251 (from top to bottom). In the right column, we fix $kT/mc^2 = 10^2$ and $L/r_{\rm L,hot} = 63$ and we vary the magnetization $\sigma_{\rm in}$, from 3 to 170 (from top to bottom). In all cases, the domain is a square of size $2L \times 2L$. The 2D structure of B_z in all cases is quite similar, apart from the fact that larger $L/r_{\rm L,hot}$ tend to lead to a more pronounced fragmentation of the current sheet. Some cases go unstable via the "parallel" mode depicted in Fig. 24, others via the "oblique" mode described in Fig. 23.

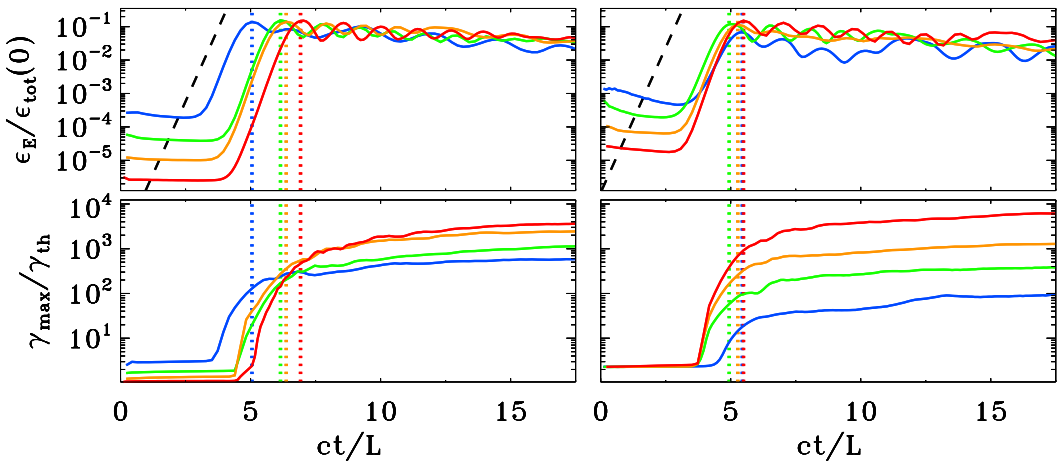

Fig. 38.— Temporal evolution of the electric energy (top panel, in units of the total initial energy) and of the maximum particle Lorentz factor (bottom panel; $\gamma_{\rm max}$ is defined in Eq. (16), and it is normalized to the thermal Lorentz factor $\gamma_{\rm th} \simeq 1 + (\hat{\gamma} - 1)^{-1} kT/mc^2$), for a suite of PIC simulations of ABC collapse (same runs as in Fig. 37). In the left column, we fix $kT/mc^2 = 10^{-4}$ and $\sigma_{\rm in} = 42$ and we vary the ratio $L/r_{\rm L,hot}$ from 31 to 251 (from blue to red). In the right column, we fix $kT/mc^2 = 10^2$ and $L/r_{\rm L,hot} = 63$ and we vary the magnetization $\sigma_{\rm in}$ from 3 to 170 (from blue to red). The maximum particle energy resulting from ABC collapse increases for increasing $L/r_{\rm L,hot}$ at fixed $\sigma_{\rm in}$ (left column) and for increasing $\sigma_{\rm in}$ at fixed $L/r_{\rm L,hot}$. The dashed black line in the top panel shows that the electric energy grows exponentially as $\propto \exp(4ct/L)$. The vertical dotted lines mark the time when the electric energy peaks (colors as described above).

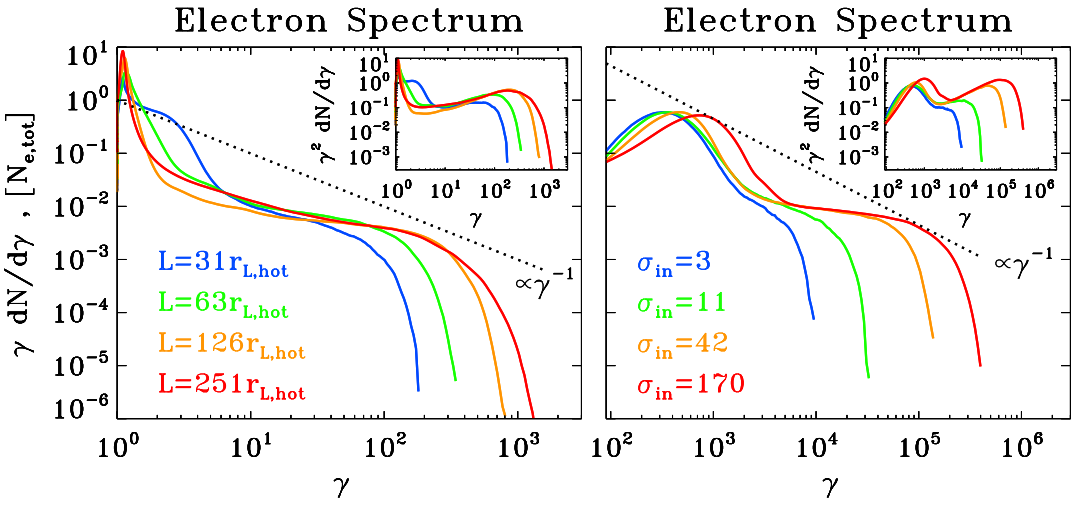

Fig. 39.— Particle spectrum at the time when the electric energy peaks, for a suite of PIC simulations of ABC collapse (same runs as in Fig. 37 and Fig. 38). In the left column, we fix $kT/mc^2 = 10^{-4}$ and $\sigma_{\rm in} = 42$ and we vary the ratio $L/r_{\rm L,hot}$ from 31 to 251 (from blue to red, as indicated by the legend). In the right column, we fix $kT/mc^2 = 10^2$ and $L/r_{\rm L,hot} = 63$ and we vary the magnetization $\sigma_{\rm in}$ from 3 to 170 (from blue to red, as indicated by the legend). The main plot shows $\gamma dN/d\gamma$ to emphasize the particle content, whereas the inset presents $\gamma^2 dN/d\gamma$ to highlight the energy census. The dotted black line is a power law $\gamma dN/d\gamma \propto \gamma^{-1}$, corresponding to equal energy content per decade (which would result in a flat distribution in the insets). The spectral hardness is not a sensitive function of the ratio $L/r_{\rm L,hot}$, but it is strongly dependent on $\sigma_{\rm in}$, with higher magnetizations giving harder spectra, up to the saturation slope of -1.

presented in Fig. 37, we have confirmed this result by covering the whole $\sigma_{\rm in} - L/r_{\rm L,hot}$ parameter space, with $\sigma_{\rm in}$ from 3 to 680 and with $L/r_{\rm L,hot}$ from 31 to 502.

We have performed an additional test to check that the current sheet thickness scales as $r_{\rm L,hot}$. When the reconnection layers reach their maximal extent (i.e., at the peak of the electric energy), the current sheet length should scale as L, whereas its thickness should be $\sim r_{\rm L,hot}$. Since the current sheets are characterized by a field-aligned electric field (see the bottom panel in Fig. 33), the fraction of box area occupied by regions with $\mathbf{E}\cdot\mathbf{B} \neq 0$ should scale as $r_{\rm L,hot}/L$. We have explicitly verified that this is indeed the case, both when comparing runs that have the same $L/r_{\rm L,hot}$ and for simulations that keep $\sigma_{\rm in}$ fixed.

The reconnection rate in all the cases we have explored is around $v_{\rm rec}/c \sim 0.3-0.5$. It shows a marginal tendency for decreasing with increasing $L/r_{\rm L,hot}$ (but we have verified that it saturates at $v_{\rm rec}/c \sim 0.3$ in the limit $L/r_{\rm L,hot} \gg 1$), and it moderately increases with $\sigma_{\rm in}$ (especially as we transition from the non-relativistic regime to the relativistic regime, but it saturates at $v_{\rm rec}/c \sim 0.5$ in the limit $\sigma_{\rm in} \gg 1$). Our measurements of the inflow speed (which we take as a proxy for the reconnection rate) are easier when the parallel mode dominates, since the inflow direction lies along one of the Cartesian axes, rather than for the oblique mode. In simulations with an aspect ratio of $2L \times L$, the parallel mode is the only one that gets triggered, and most of the measurements quoted above refer to this setup.

In Fig. 38 we present the temporal evolution of the runs whose 2D structure is shown in Fig. 37. In the left column, we fix $kT/mc^2 = 10^{-4}$ and $\sigma_{\rm in} = 42$ and we vary the ratio $L/r_{\rm L,hot}$ from 31 to 251 (from blue to red). In the right column, we fix $kT/mc^2 = 10^2$ and $L/r_{\rm L,hot} = 63$ and we vary the magnetization $\sigma_{\rm in}$ from 3 to 170 (from blue to red). The top panels show that the evolution of the electric energy (in units of the total initial energy) is remarkably similar for all the values of $L/r_{\rm L,hot}$ and $\sigma_{\rm in}$ we explore. In particular, the electric energy grows as $\propto \exp(4ct/L)$ in all the cases (see the dashed black lines), and it peaks at $\sim 10\%$ of the total initial energy. The only exception is the trans-relativistic case $\sigma_{\rm in} = 3$ and $L/r_{\rm L,hot} = 63$ (blue line in the top right panel), whose peak value is slightly smaller, due to the lower Alfvén speed. The onset time of the instability is also nearly independent of $\sigma_{\rm in}$ (top right panel), although the trans-relativistic case $\sigma_{\rm in} = 3$ (blue line) seems to be growing slightly later. As regard to the dependence of the onset time on $L/r_{\rm L,hot}$ at fixed $\sigma_{\rm in}$, the top left panel in Fig. 38 shows that larger values of $L/r_{\rm L,hot}$ tend to grow later, but the variation is only moderate: in all the cases the instability grows around $ct/L \sim 5$.

In the early stages of ABC instability, the cutoff Lorentz factor $\gamma_{\rm max}$ of the particle energy spectrum (as defined in Eq. (16)) grows explosively (see the two bottom panels in Fig. 38). If the origin of time is set at the onset time of the instability, the maximum energy is expected to grow as

$$\gamma_{\rm max} mc^2 \sim e v_{\rm rec} B_{\rm in} t \tag{31}$$

Due to the approximate linear increase of the in-plane magnetic field with distance from a null point, we find that $B_{\rm in} \propto \sqrt{\sigma_{\rm in}} v_{\rm rec} t/L$. This leads to $\gamma_{\rm max} \propto v_{\rm rec}^2 \sqrt{\sigma_{\rm in}} t^2/L$, with the same quadratic temporal scaling that was discussed for the solitary X-point collapse. Since the dynamical phase of ABC instability lasts a few L/c, the maximum particle Lorentz factor at the end of this stage should scale as $\gamma_{\rm max} \propto v_{\rm rec}^2 \sqrt{\sigma_{\rm in}} L \propto v_{\rm rec}^2 \sigma_{\rm in} (L/r_{\rm L,hot})$. If the reconnection rate does not significantly depend on $\sigma_{\rm in}$, this implies that $\gamma_{\rm max} \propto L$ at fixed $\sigma_{\rm in}$. The trend for an increasing $\gamma_{\rm max}$ with L at fixed $\sigma_{\rm in}$ is confirmed in the bottom left panel of Fig. 38, both at the final time and at the peak time of the electric energy (which is slightly different among the four different cases, see the vertical dotted colored lines).[16] Similarly, if the reconnection rate does not significantly depend on $L/r_{\rm L,hot}$, this implies that $\gamma_{\rm max} \propto \sigma_{\rm in}$ at fixed $L/r_{\rm L,hot}$. This linear dependence of $\gamma_{\rm max}$ on $\sigma_{\rm in}$ is confirmed in the bottom right panel of Fig. 38.

in ultra-relativistic plasmas.

[16] In contrast, a comparison at the same ct/L is not very illuminating, since larger values of $L/r_{\rm L,hot}$ tend to systematically have later instability onset times.

The dependence of the particle spectrum on $L/r_{\rm L,hot}$ and $\sigma_{\rm in}$ is illustrated in Fig. 39 (left and right panel, respectively), where we present the particle energy distribution at the time when the electric energy peaks (as indicated by the colored vertical dotted lines in Fig. 38). The particle spectrum shows a pronounced non-thermal component in all the cases, regardless of whether the secondary plasmoid instability is triggered or not in the current sheets (the results presented in Fig. 39 correspond to the cases displayed in Fig. 37). This suggests that in our setup any acceleration mechanism that relies on plasmoid mergers is not very important, but rather that the dominant source of energy is direct acceleration by the reconnection electric field (see the previous subsection).

At the time when the electric energy peaks, most of the particles are still in the thermal component (at $\gamma \sim 1$ in the left panel and $\gamma \sim 3kT/mc^2$ in the right panel of Fig. 39), i.e., bulk heating is still negligible. Yet, a dramatic event of particle acceleration is taking place, with a few lucky particles accelerated much beyond the mean energy per particle $\sim \gamma_{\rm th}\sigma_{\rm in}/2$ (for comparison, we point out that $\gamma_{\rm th} \sim 1$ and $\sigma_{\rm in} = 42$ for the cases in the left panel). Since most of the particles are at the thermal peak, this is not violating energy conservation. As described by Sironi & Spitkovsky (2014) and Werner et al. (2016), for a power law spectrum $dN/d\gamma \propto \gamma^{-p}$ of index $1 < p < 2$ extending from $\gamma \sim \gamma_{\rm th}$ up to $\gamma_{\rm max}$, the fact that the mean energy per particle is $\gamma_{\rm th}\sigma_{\rm in}/2$ yields a constraint on the upper cutoff of the form

$$\gamma_{\rm max} \lesssim \gamma_{\rm th}\left[\frac{\sigma_{\rm in}}{2}\frac{2-p}{p-1}\right]^{1/(2-s)} \tag{32}$$

This constraint does not apply during the explosive phase, since most of the particles lie at the thermal peak (so, the distribution does not resemble a single power law), but it does apply at late times (e.g., see the final spectrum in Fig. 31, similar to a power law). However, as the bulk of the particles shift up to higher energies (see the evolution of the thermal peak in Fig. 30), the spectrum at late times tends to be softer than in the early explosive phase (compare light blue and red curves in Fig. 30), which helps relaxing the constraint in Eq. (32).

The spectra in Fig. 39 (main panels for $\gamma dN/d\gamma$, to emphasize the particle content; insets for $\gamma^2 dN/d\gamma$, to highlight the energy census) confirm the trend of $\gamma_{\rm max}$ anticipated above. At fixed $\sigma_{\rm in} = 42$ (left panel), we see that $\gamma_{\rm max} \propto L$ (L changes by a factor of two in between each pair of curves);[17] on the other hand, at fixed $L/r_{\rm L,hot} = 63$ (right panel), we find that $\gamma_{\rm max} \propto \sigma_{\rm in}$ ($\sigma_{\rm in}$ changes by a factor of four in between each pair of curves).

The spectral hardness is primarily controlled by the average in-plane magnetization $\sigma_{\rm in}$. The right panel in Fig. 39 shows that at fixed $L/r_{\rm L,hot}$ the spectrum becomes systematically harder with increasing $\sigma_{\rm in}$, approaching the asymptotic shape $\gamma dN/d\gamma \propto$ const found for plane-parallel steady-state reconnection in the limit of high magnetizations (Sironi & Spitkovsky 2014; Guo et al. 2015; Werner et al. 2016). At large $L/r_{\rm L,hot}$, the hard spectrum of the high-$\sigma_{\rm in}$ cases will necessarily run into constraints of energy conservation (see Eq. (32)), unless the pressure feedback of the accelerated particles onto the flow structure ultimately leads to a spectral softening (in analogy to the case of cosmic ray modified shocks, see Amato & Blasi 2006). This argument seems to be supported by the left panel in Fig. 39. At fixed $\sigma_{\rm in}$ (left panel), the spectral slope is nearly insensitive to $L/r_{\rm L,hot}$. The only (marginal) evidence for a direct dependence on $L/r_{\rm L,hot}$ emerges at large $L/r_{\rm L,hot}$, with larger systems leading to steeper slopes (compare the yellow and red lines in the left panel), which possibly reconciles the increase in $\gamma_{\rm max}$ with the argument of energy conservation illustrated in Eq. (32).

In application to the GeV flares of the Crab Nebula, which we attribute to the explosive phase of ABC instability, we envision an optimal value of $\sigma_{\rm in}$ between ~ 10 and ~ 100. Based on our results, smaller $\sigma_{\rm in} \lesssim 10$ would correspond to smaller reconnection speeds (in units of the speed of light), and so weaker accelerating electric fields. On the other hand, $\sigma_{\rm in} \gtrsim 100$ would give hard spectra with slopes $p < 2$, which would prohibit particle acceleration up to $\gamma_{\rm max} \gg \gamma_{\rm th}$

[17] The fact that the dependence is a little shallower than linear is due to the fact that the reconnection rate, which enters in the full expression $\gamma_{\rm max} \propto v_{\rm rec}^2 \sigma_{\rm in}(L/r_{\rm L,hot})$, is slightly decreasing with increasing $L/r_{\rm L,hot}$, as detailed above.

without violating energy conservation (for the sake of simplicity, here we ignore the potential spectral softening at high $\sigma_{\rm in}$ and large $L/r_{\rm L,hot}$ discussed above).

As we have mentioned above, we invoke the early phases of ABC collapse as an explanation for the Crab GeV flares. As shown in Fig. 31, after this initial stage the maximum particle energy is only increasing by a factor of three (on long timescales, of order $\sim 10L/c$). When properly accounting for the rapid synchrotron losses of the highest energy particles (which our simulations do not take into account), it is even questionable whether the spectrum will ever evolve to higher energies, after the initial collapse. This is the reason why we have focused most of our attention on how the spectrum at the most violent time of ABC instability depends on $L/r_{\rm L,hot}$ or $\sigma_{\rm in}$. For the sake of completeness, we now describe how the spectrum at late times (corresponding to the bottom right panel in Fig. 29) depends on the flow conditions. In analogy to what we have described above, the effect of different kT/mc^2 is only to change the overall energy scale, and the results are nearly insensitive to the flow temperature, as long as $c/\omega_{\rm p}$ and $\sigma_{\rm in}$ properly account for temperature effects. The role of $\sigma_{\rm in}$ and $L/r_{\rm L,hot}$ can be understood from the following simple argument (see also Sironi & Spitkovsky 2011a). In the $\sigma_{\rm in} \lesssim 10-100$ cases in which the spectral slope is always $p > 2$ and the high-energy spectral cutoff is not constrained by energy conservation, we have argued that $\gamma_{\rm max}/\gamma_{\rm th} \propto \sigma_{\rm in}(L/r_{\rm L,hot})$ (here, we have neglected the dependence on the reconnection speed, for the sake of simplicity). As a result of bulk heating, the thermal peak of the particle distribution shifts at late times — during the island mergers that follow the initial explosive phase — from $\gamma_{\rm th}$ up to $\sim \gamma_{\rm th}\sigma_{\rm in}/2$. By comparing the final location of the thermal peak with $\gamma_{\rm max}$, one concludes that there must be a critical value of $L/r_{\rm L,hot}$ such that for small $L/r_{\rm L,hot}$ the final spectrum is close to a Maxwellian, whereas for large values of $L/r_{\rm L,hot}$ the non-thermal component established during the explosive phase is still visible at late times. We have validated this argument with our results, finding that this critical threshold for the shape of the final spectrum is around $L/r_{\rm L,hot} \sim 100$.

7. Driven evolution of a system of magnetic islands

As we have seen in §6, a periodic 2D ABC equilibrium configuration of magnetic islands is unstable to merger. Such equilibrium configuration is naturally an idealized simplification. As we demonstrate below, in the case of a modified initial configuration which is compressed along one direction the rapid island merger sets up straight away. What could create such a stressed configuration and promote rapid reconnection which may give rise to Crab's gamma-ray flares? One possibility which comes to mind is a strong shock. Shocks in strongly magnetized relativistic plasma are often described as weakly compressive and indeed in the shock frame the plasma density and the magnetic field strength are almost the same. However, when measured in the fluid frame, these quantities may experience huge jumps, of the order of the shock Mach number (Komissarov 2012). This is accompanied by similarly large variation of the flow Lorentz factor, which may also accelerate the rate of physical processes via the relativistic time dilation effect. PIC simulations of shocked striped wind by Sironi & Spitkovsky (2011a) spectacularly illustrate this possibility. In these simulations, the shock is triggered via collision of the wind with a stationary wall. At some distance downstream of the shock the flow decelerates from high Lorentz factor to full stop, which shortens the time scale of all processes via the relativistic time-dilation effect. Reconnection in the current sheets accelerates and the magnetic field of stripes dissipates, with its energy used to heat the wind plasma. The conversion of magnetic energy to heat is accompanied by a decrease of the specific volume and hence by additional plasma compression. As the result, relative to the shocked plasma the shock propagates at speed well below the speed of light but close to that of a shock in ultra-relativistic unmagnetized plasma, $v_s \simeq c/3$. The role of magnetic dissipation of the shock speed has been studied theoretically by Lyubarsky (2003)

In the following, we discuss the results of driven evolution of ABC structure using both fluid and PIC simulations. We find that using both fluid and PIC codes, that imposing finite amplitude perturbations from the beginning triggers the instability much faster.

7.1. Evolution of compressed 2D ABC equilibrium:force-free simulations

In force-free simulations we added an initial perturbation $\delta A_z = \delta a * (\sin(kx) + \sin(ky)) * \cos(k(y-x)/2)$, where δa is an amplitude of a perturbations. We find that this leads to the earlier onset of the non-linear stage of instability depending on the amplitude of perturbations, Fig. 40.

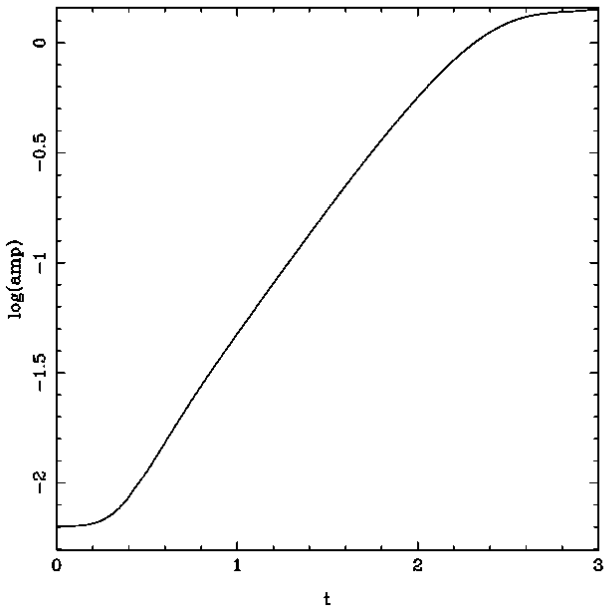

Fig. 40.— *Left Panel* Electromagnetic energy and perturbation amplitude of force-free simulations as functions of time for a case of initial state with finite amplitude perturbations, chosen to have a large contribution from unstable modes. In comparison with the unstressed system of magnetic islands (*Left Panel* Fig. 28), the instability starts to grow immediately.

To find configurations that immediately display a large reconnecting electric field, we turn to the stressed single island case. This is just a cut-out of the muliple-island ABC fields, adopting an aspect ratio $R \neq 1$. We choose $R = 0.9$ as initial perturbation. We choose three different values for the parallel conductivity $\kappa_{||} \in [500, 1000, 2000]$ and set the perpendicular component to zero $\kappa_{\perp} = 0$.

The over-all evolution is displayed in Figs. 41, 42 and 43.

7.2. Collision-triggered merger of magnetic islands: MHD simulations

Next, we study the role of collisions in triggering magnetic reconnection and dissipation using the framework of resistive force-free electrodynamics (magnetodynamics). In the fluid frame, the structure of colliding flows is that of the unstressed 2D ABC configuration. In order obtain its structure in the lab-frame one can simply apply the Lorentz transformation for the electromagnetic field. Hence for the flow moving along the x axis to the left with speed v, we have

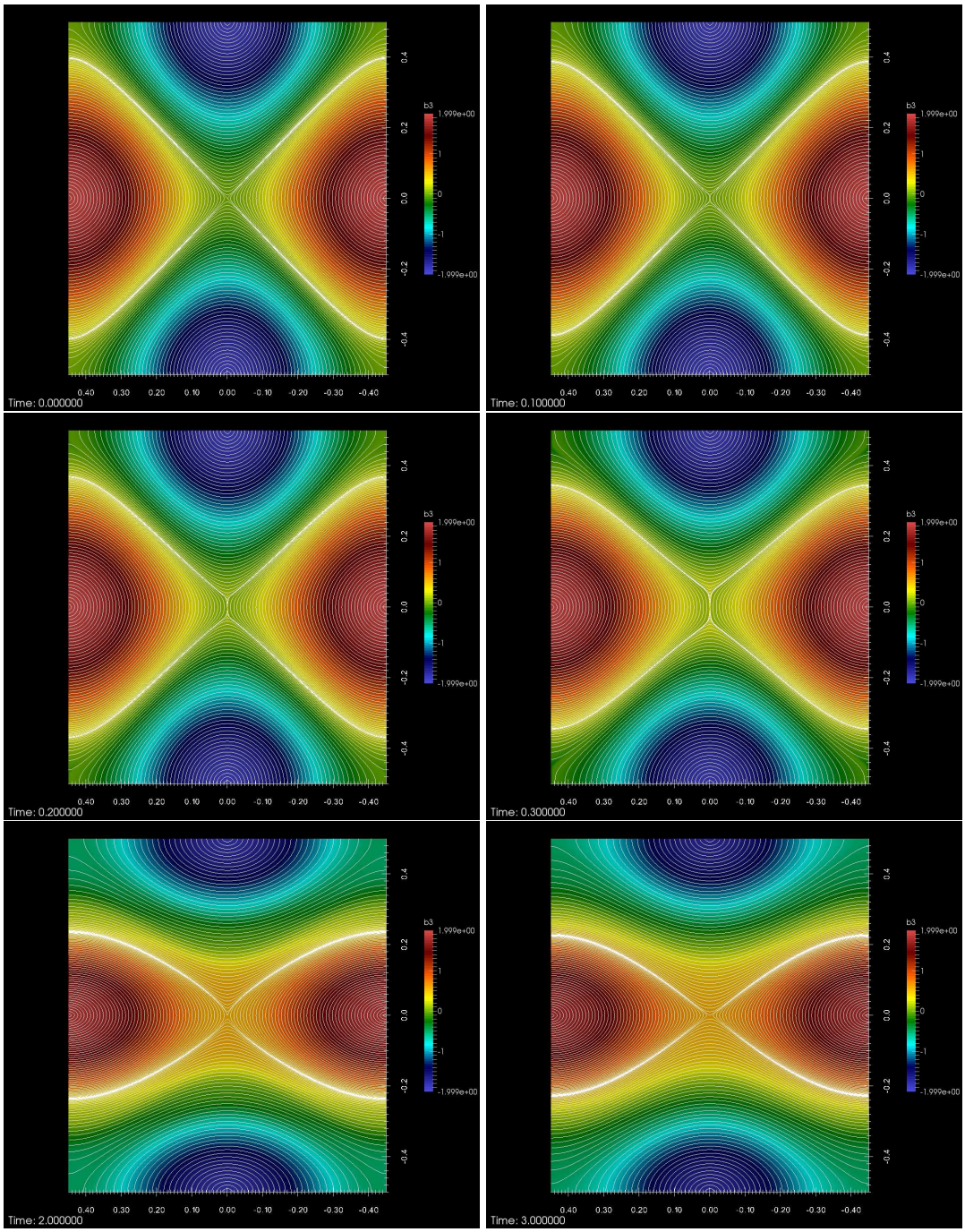

Fig. 41.— Time evolution of the out-of-plane field, case $\kappa_{||} = 2000$, triggered collapse of magnetic islands. The initial X-point collapses and forms a rapidly expanding current-sheet. After $t = 1$, the fast evolution is over and the islands oscillate. Times are $t \in [0, 0.1, 0.2, 0.3, 2, 3]$.

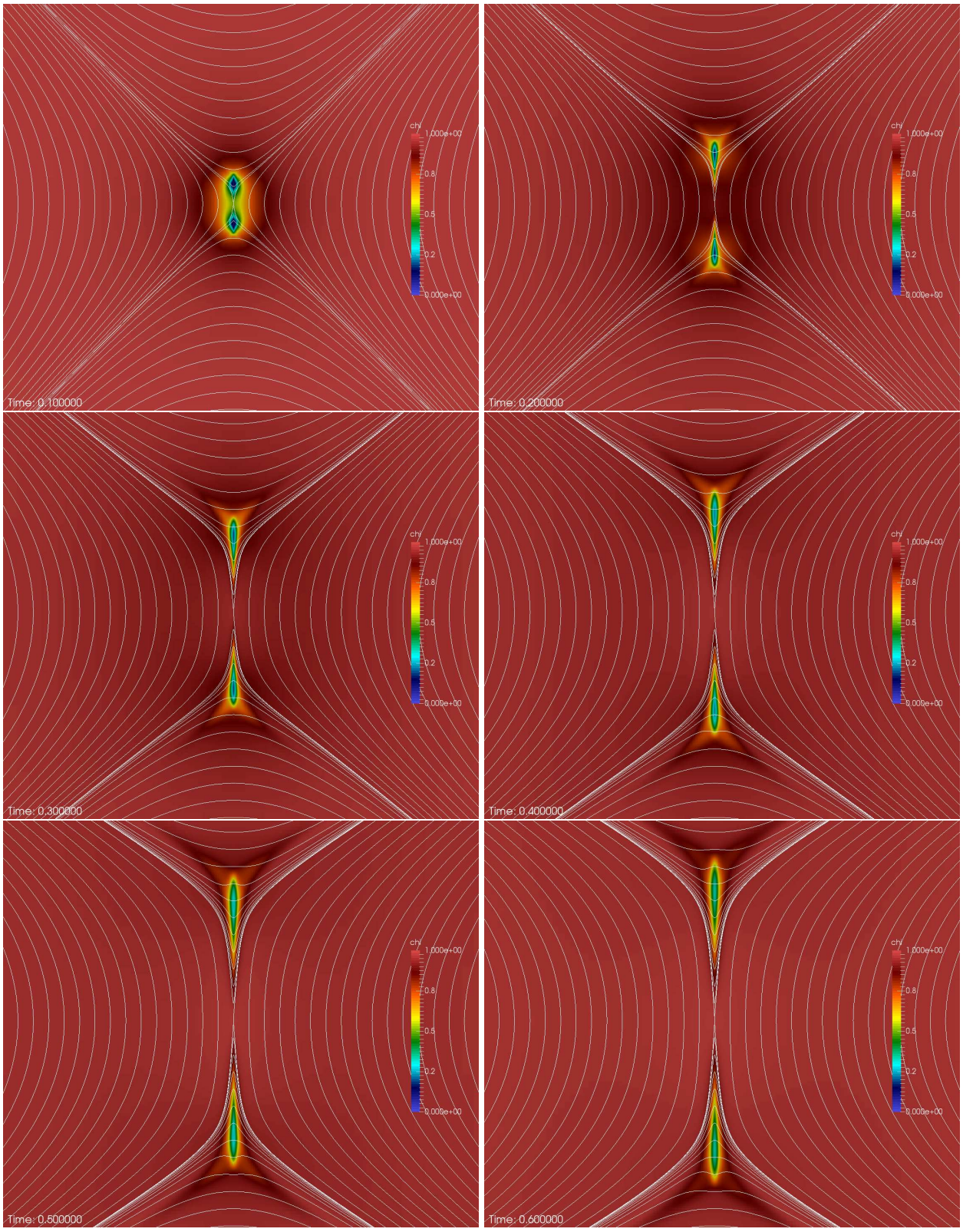

Fig. 42.— Zoom into the central region showing the quantity $1 - E^2/B^2$, triggered collapse of magnetic islands. At $t = 0.1$, two disconnected regions of $E \sim B$ exist which rapidly expand. E/B in these regions gets smaller as time progresses. Actually, before $t = 0.1$, E/B reaches values as high as 3 for this case with $\kappa_{||} = 2000$ (see Fig. 43).

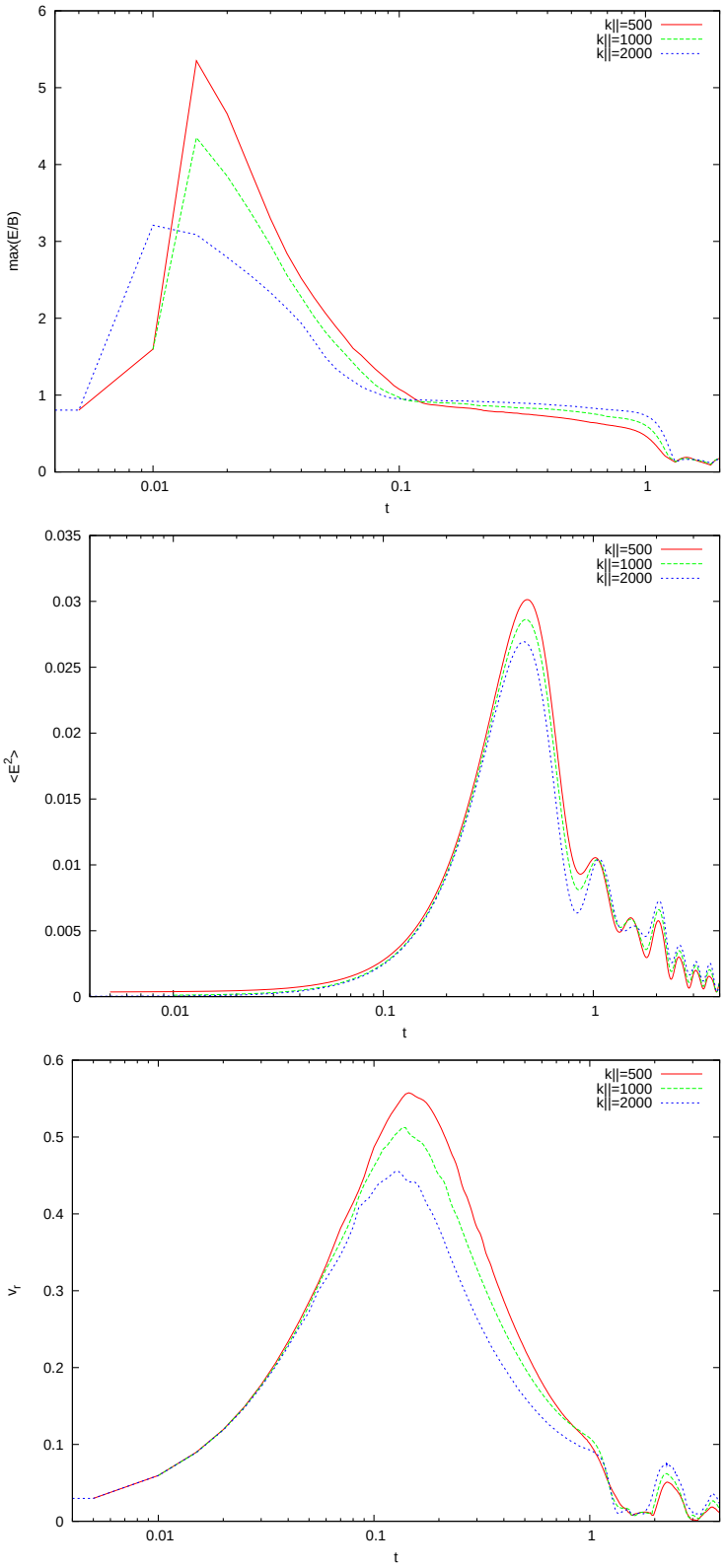

Fig. 43.— Evolution of critical quantities in the stressed island case for various conductivities. Immediately a region of $E > B$ is established. All cases agree in the initial growth rates of v_r and $\langle E^2 \rangle$ and in the over-all time of the evolution. This result is consistent with the initial *ideal* evolution of the instability.

$$
\begin{aligned}
B_x &= -\sin(2\pi y/L)B_0\,,\\
B_y &= \Gamma\sin(2\pi\Gamma x/L)B_0\,,\\
B_z &= \Gamma\left[(\cos(2\pi\Gamma x/L)+\cos(2\pi y/L))\right]B_0\,,\\
E_x &= 0\,,\\
E_y &= -v\Gamma\left[(\cos(2\pi\Gamma x/L)+\cos(2\pi y/L))\right]B_0\,,\\
E_z &= v\Gamma\sin(2\pi\Gamma x/L)B_0\,,
\end{aligned}
\tag{33}
$$

where Γ is the Lorentz factor. Via replacing v with $-v$, we obtain the solution for the flow moving to right with the same speed. To initiate the collision, one can introduce at $t=0$ a discontinuity at $x=0$ so that the flow is moving to the left for $x>0$ and to the right for $x<0$. The corresponding jumps at $x=0$ are

$$
[B_x]=[B_z]=[E_x]=[E_z=0],\qquad [B_y]=2B_y^{(r)},\qquad [E_y]=2E_y^{(r)}\,,
\tag{34}
$$

where index (r) refers to the value to the right of the discontinuity. Instead of studying the domain which includes both flows, one can treat $x=0$ as a boundary with the boundary conditions described by Eqs. (34) and deal only with the left (or the right) half of the domain. This is exactly what we did in our simulations.

In the simulations, we set $B_0=1$, $\Gamma=3$ and used the computational domain $(0,3L)\times(-L,L)$, with a uniform grid of 600×400 computational cells. The boundary at $x=3L$ is treated as an inlet of the flow described by Eq. (33). Hence the solution at this boundary is given by these equation with x replaced by $x+vt$. The magnetic Reynolds number is $Re_m=10^3$.

Figure 44 illustrates the solution at $t=4$. To the right of $x=2$ the flow structure is the same as in the initial solution. In the plot of B_z (top panel), one can clearly see the lattice of magnetic islands. It appears compressed along the x axis, which is a signature of the relativistic length contraction effect. To the left of $x=2$, the islands rapidly merge and form horizontal stripes of oppositely directed B_z. The in-plane magnetic field is concentrated in the current sheets separating these stripes.

Figure 45 shows the time evolution of the flow using the Lorentz-invariant parameter $p_m=(B^2-E^2)/2$, which plays the role of magnetic pressure. One can see that the evolution can be described as a wave propagation in the direction away from the plane of collision. Behind this wave the magnetic pressure increases and the wave speed is significantly lower than the speed of light.

The wave properties are very different from those of the basic hyperbolic waves of magnetodynamics. To illustrate this fact, Figure 46 shows the solution of the Riemann problem

$$
\text{Left state:}\quad B=(2,1,2),\quad E=(0,0,-v)\,;\qquad \text{Right state:}\quad B=(2,-1,2),\quad E=(0,0,v)\,,
$$

which describes the collision of two uniform flows. The collision speed v is the same as before ($\Gamma=3$). The collision creates both the fast wave (FW) and the Alfvén wave (AW). One can see that, the fast wave propagates with the speed of light and the magnetic pressure is invariant across AW (Komissarov, 2002).

Comparing the results of the test Rienmann problem with the main simulations, we conclude that the main wave is not AW because the magnetic pressure is not invariant and not FW as its speed is significantly less than the speed of light. In fact, the top-left panel ($t=1$) of Figure 45 shows a weak linear feature located at $x=1$ which can be identified with the FW produced by the collision. A similar, but weaker feature can also be seen in the top-right panel ($t=2$). Presumable, this wave gets scattered by the inhomogeneities of the incoming flow and gradually looses coherence. Other

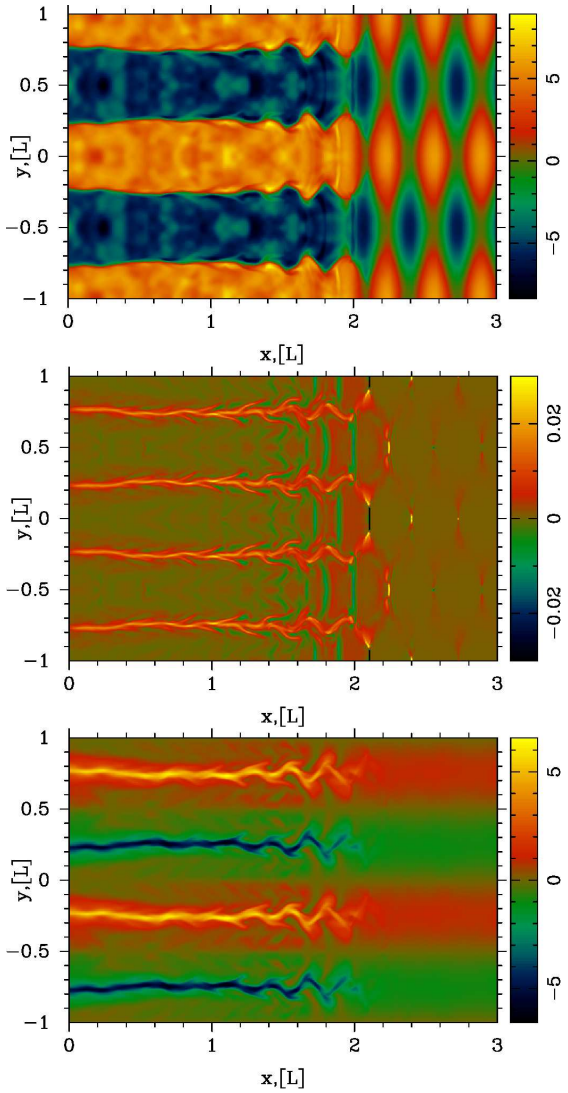

Fig. 44.— Collision-induced merger of magnetic islands. The plots show the distribution of B_z (top), $B \cdot E$ (middle) and B_x at time $t = 4$.

fine arc-like features seen in front of the main wave (e.g. in the region $1.2 < x < 1.7$) are likely to be fast waves emitted by the turbulence downstream of the main wave.

The main wave, which we will refer to as the dissipation front, seems to start as an Alfvén wave. Immediately downstream of the Alfvén wave, the B_z component of the magnetic field increases (see the middle panel of Fig.46), and hence the ABC configuration remains highly squashed along the x-axis. However, the flow comes to halt in the x direction and the X-points are now highly stressed in the fluid frame[18]. This leads to their immediate collapse and rapid merger of the ABC islands, as described in §7.1. The increase of p_m seems to be a product of magnetic dissipation that

[18]In magnetodynamics, there no unique way to define the fluid frame. If the electric field vanishes in one frame then it also vanishes in any other frame moving relative to this one along the magnetic field.

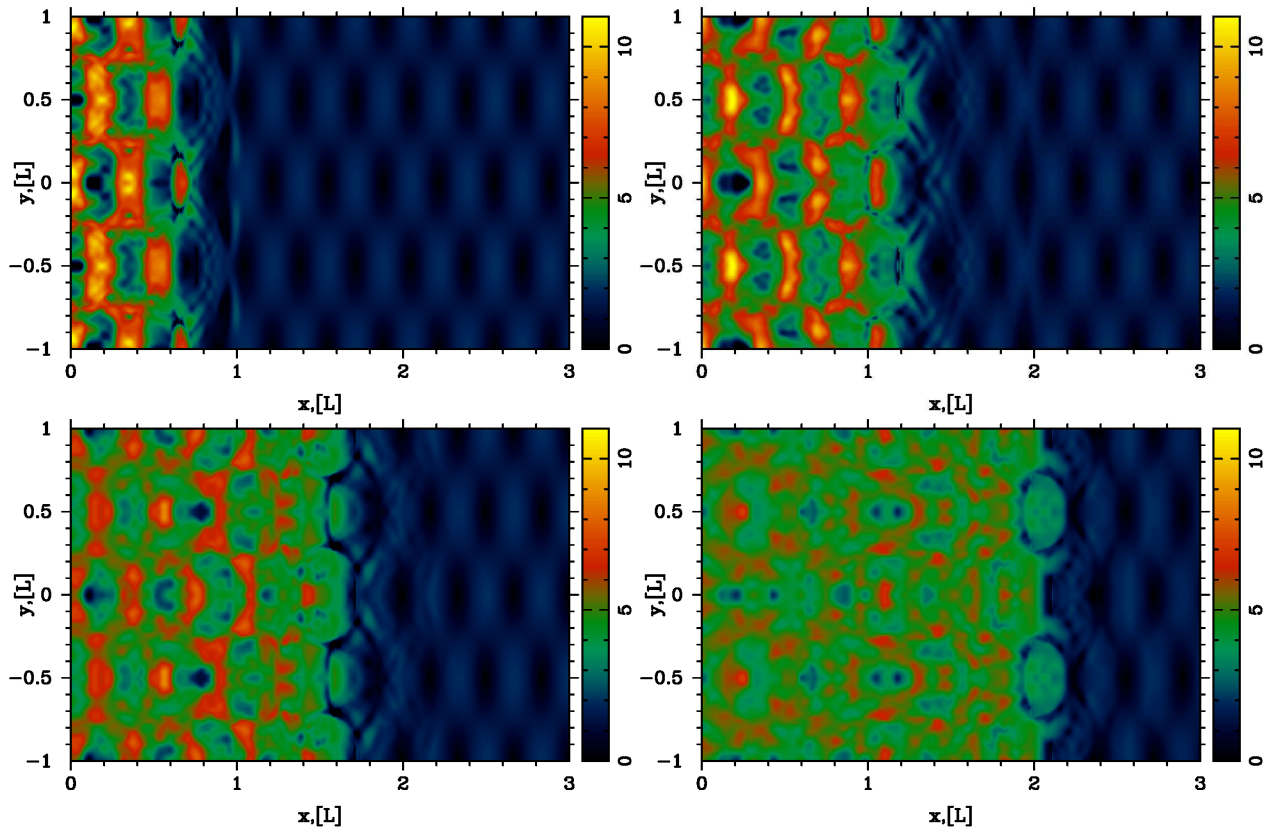

Fig. 45.— Shock-induced merger of magnetic islands. The plots show the distribution of the magnetic pressure $p_m = (B^2 - E^2)/2$ at time $t = 1, 2, 3$ and 4 (increasing from left to right and from top to bottom).

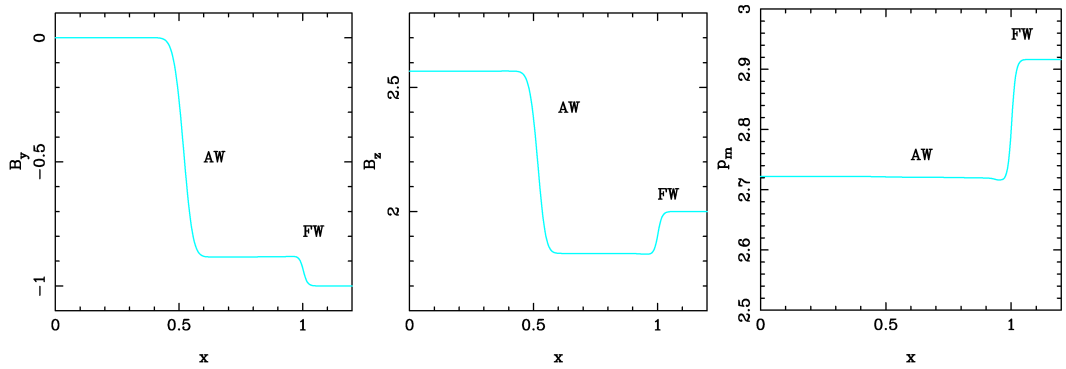

Fig. 46.— Collision of uniform flows. *Left panel:* The B_y component of the magnetic field at $t = 1$. Both the fast wave and Alvfén waves are easily identified on the plot. *Middle panel:* The B_z component of the magnetic field. *Right panel:* The magnetic pressure $p_m = (B^2 - E^2)/2$ at the same time. Only the fast wave can be seen on this plot.

follows the merger.

Since the dissipation front is not a well defined surface of fixed shape, it is rather difficult to measure its speed.

However even naked eye inspection of the plots suggest that it monotonically decreases with time with saturation towards the end of the run. Crude measurements based on the position of first features showing strong deviation from the properties of incoming flow give $v_{df} \simeq 0.73\,, 0.47\,, 0.45\,, 0.40\,, 0.38$ and 0.37.

To see how the magnetic dissipation can influence the front speed, we analyze the energy and momentum conservation in our problem. (This approach is similar to that used by (Lyubarsky 2003).) To simplify the analysis we ignore the complicated electromagnetic structure of flow and assume that the magnetic field is parallel to the front. Denote the front position as x_{df} and use indexes 1 and 2 to indicate the flow parameters upstream of the front and downstream of its dissipation zone the front respectively. Since our equations do not include particles pressure and energy, and the dissipated electromagnetic energy simply vanishes this analysis is only relevant for the case of rapid radiative cooling.

Since the flow grounds to halt downstream of the dissipation front, the momentum conservation in the computational box $[0, x_r]$

$$\frac{d}{dt}\left(-v_1 B_1^2 (x_b - x_{df})\right) = \frac{B_2^2}{2} - \frac{1}{2}(B_1^2 + v_1^2 B_1^2)\,, \tag{35}$$

where $v_1 = E_1/B_1$. Hence

$$B_1^2 v_{df} v_1 = \frac{B_2^2}{2} - \frac{1}{2} B_1^2 (1 + v_1^2)\,. \tag{36}$$

Similarly, we obtain the energy conservation law

$$\frac{B_2^2}{2} v_{df} - \frac{1}{2} v_{df} B_1^2 (1 + v_1^2) = v_1 B_1^2 - Q_d\,, \tag{37}$$

where Q_d is the dissipation rate of the front. Solving the last two equation for B_2 and v_{df}, we obtain the simple result

$$v_s^2 = 1 - \alpha\,, \tag{38}$$

where $\alpha = Q_d / v_1 B_1^2$ is the fraction of the incoming energy flux which is dissipated and lost in the dissipation front, the dissipation efficiency. From this we find that in the absence of dissipation the shock speed equals to the speed of light and thus recover the result for ideal magnetodynamics. In the opposite case of total dissipation, the front speed vanishes, as expected. The final value of $v_s = 0.37$ found in our simulations corresponds to the dissipation efficiency $\alpha = 86\%$.

7.3. Driven ABC evolution: PIC simulation

7.3.1. 2D ABC structures with initial shear

Next we investigate a driven evolution of the ABC structures using PIC simulations. Inspired by the development of the oblique mode described in Fig. 23, we set up our system with an initial velocity in the oblique direction, so that two neighboring chains of ABC islands will shear with respect to each other. More precisely, we set up an initial velocity profile of the form

$$\begin{aligned} v_x &= -v_{\rm push}\cos[\pi(x+y)/L]/\sqrt{2} \\ v_y &= -v_x \\ v_z &= 0 \end{aligned} \tag{39}$$

and we explore the effect of different values of $v_{\rm push}$.[19]

Fig. 47 shows that the evolution of the electric energy (top panel, in units of the total initial energy) is remarkably independent of $v_{\rm push}$, apart from an overall shift in the onset time. In all the cases, the electric energy grows exponentially as $\propto \exp(4ct/L)$ (compare with the black dashed line) until it peaks at $\sim 10\%$ of the total initial energy (the time when the electric energy peaks is indicated with the vertical colored dotted lines). In parallel, the maximum particle energy $\gamma_{\rm max}$ grows explosively (bottom panel in Fig. 47), with a temporal profile that is nearly indentical in all the cases (once

[19] In addition to initializing a particle distribution with a net bulk velocity, we also set up the resulting $-\mathbf{v}\times\mathbf{B}/c$ electric field.

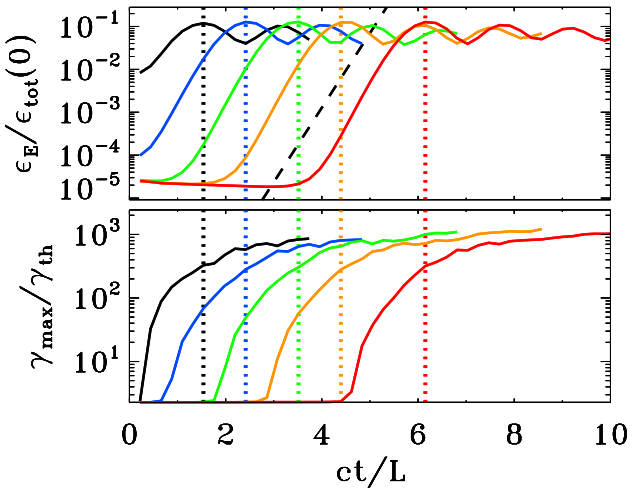

Fig. 47.— Temporal evolution of the electric energy (top panel, in units of the total initial energy) and of the maximum particle Lorentz factor (bottom panel; $\gamma_{\rm max}$ is defined in Eq. (16), and it is normalized to the thermal Lorentz factor $\gamma_{\rm th}\simeq 1+(\hat{\gamma}-1)^{-1}kT/mc^2$), for a suite of five PIC simulations of ABC collapse with fixed $kT/mc^2=10^2$, $\sigma_{\rm in}=42$ and $L/r_{\rm L,hot}=126$, but different magnitudes of the initial velocity shear (see Eq. (39)): $v_{\rm push}/c=10^{-1}$ (black), $v_{\rm push}/c=10^{-2}$ (blue), $v_{\rm push}/c=10^{-3}$ (green), $v_{\rm push}/c=10^{-4}$ (yellow) and $v_{\rm push}/c=0$ (red). The dashed black line in the top panel shows that the electric energy grows exponentially as $\propto\exp(4ct/L)$. The vertical dotted lines mark the time when the electric energy peaks (colors correspond to the five values of $v_{\rm push}/c$, as described above).

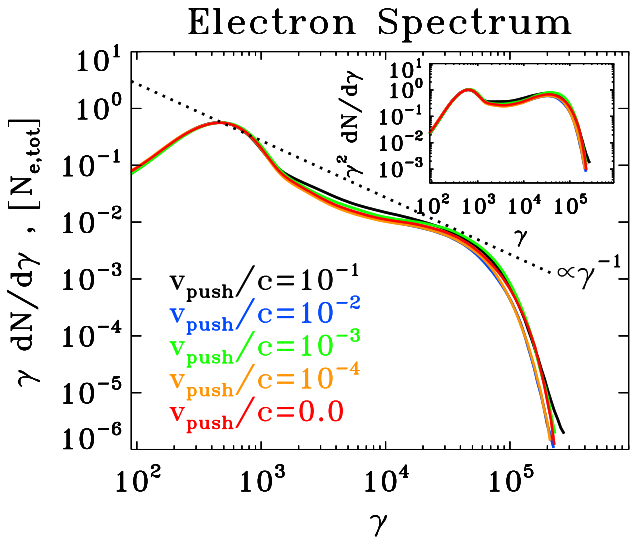

Fig. 48.— Particle spectrum at the time when the electric energy peaks, for a suite of five PIC simulations of ABC collapse with fixed $kT/mc^2 = 10^2$, $\sigma_{\rm in} = 42$ and $L/r_{\rm L,hot} = 126$, but different magnitudes of the initial velocity shear (same runs as in Fig. 47): $v_{\rm push}/c = 10^{-1}$ (black), $v_{\rm push}/c = 10^{-2}$ (blue), $v_{\rm push}/c = 10^{-3}$ (green), $v_{\rm push}/c = 10^{-4}$ (yellow) and $v_{\rm push}/c = 0$ (red). The main plot shows $\gamma dN/d\gamma$ to emphasize the particle content, whereas the inset presents $\gamma^2 dN/d\gamma$ to highlight the energy census. The dotted black line is a power law $\gamma dN/d\gamma \propto \gamma^{-1}$, corresponding to equal energy content per decade (which would result in a flat distribution in the inset).

again, apart from an overall time shift). The initial value of the electric energy scales as $v_{\rm push}^2$ for large $v_{\rm push}$ (black for $v_{\rm push}/c = 10^{-1}$ and blue for $v_{\rm push}/c = 10^{-2}$), just as a consequence of the electric field $-\mathbf{v}_{\rm push} \times \mathbf{B}/c$ that we initialize. At smaller values of $v_{\rm push}$, the initial value of the electric energy is independent of $v_{\rm push}$ (green to red curves in the top panel). Here, we are sensitive to the electric field required to build up the particle currents implied by the steady ABC setup. Overall, the similarity of the different curves in Fig. 47 (all the way to the undriven case of $v_{\rm push} = 0$, in red) confirms that the oblique "shearing" mode is a natural instability avenue for 2D ABC structures.

As a consequence, it is not surprising that the particle spectrum measured at the time when the electric energy peaks (as indicated by the vertical colored lines in Fig. 47) bears no memory of the driving speed $v_{\rm push}$. In fact, the five curves in Fig. 48 nearly overlap.

7.3.2. 2D ABC structures with initial stress

We now investigate the evolution of ABC structures in the presence of an initial stress, quantified by the stress parameter λ (see Sect. 4.2 for the definition of λ in the context of solitary X-point collapse). The unstressed cases discussed so far would correspond to $\lambda = 1$. The simulation box will be a rectangle with size $2L$ along the x direction and $2\lambda L$ along the y direction, with periodic boundary conditions.

Fig. 49 shows the temporal evolution of the 2D pattern of the out-of-plane field B_z (in units of $B_{0,\rm in}$) from a PIC simulation with $kT/mc^2 = 10^{-4}$, $\sigma_{\rm in} = 42$ and $L = 126\, r_{\rm L,hot}$. The system is initially squeezed along the y direction, with a stress parameter of $\lambda = 0.94$ (top left panel). The initial stress leads to X-point collapse and formation of current sheets (see the current sheet at $x = 0$ and $y = 0.5L$ in the top right panel). This early phase results in a minimal amount of magnetic energy dissipation (see the top panel in Fig. 50, with the solid blue line indicating the magnetic energy and the red line indicating the particle kinetic energy), but significant particle acceleration. As indicated in the bottom panel of Fig. 50, the high-energy cutoff $\gamma_{\rm max}$ of the particle distribution grows quickly (within one dynamical time) up to $\gamma_{\rm max}/\gamma_{\rm th} \sim 1.5 \times 10^2$. At this point, the increase in the maximum particle energy stalls. In Fig. 49, we find that this corresponds to a phase in which the system tends to counteract the initial stress. In particular, the reconnection outflows emanating from the current sheets in the top right panel of Fig. 49 push away neighboring magnetic structures (the current sheet at $x = 0$ and $y = 0.5L$ pushes away the two blue islands at $y = 0.5L$ and $x = \pm 0.5L$). The system gets squeezed along the x direction (middle left panel), i.e., the stress is now opposite to the initial stress. Shortly thereafter, the ABC structure goes unstable on a dynamical timescale (middle right panel), with a pattern similar to the case of spontaneous (i.e., unstressed) ABC instability. In particular, the middle right panel in Fig. 49 shows that in this case the instability proceeds via the "parallel" mode depicted in Fig. 24 (but other simulations are dominated by the "oblique" mode sketched in Fig. 23). The subsequent evolution closely resembles the case of spontaneous ABC instability shown in Fig. 29, with the current sheets stretching up to a length $\sim L$ and the merger of islands having the same B_z polarity (bottom left panel in Fig. 49), until only two regions remain in the box, with B_z fields of opposite polarity (bottom right panel in Fig. 49).

The second stage of evolution — resembling the spontaneous instability of unstressed ABC structures — leads to a dramatic episode of particle acceleration (see the growth in $\gamma_{\rm max}$ in the bottom panel of Fig. 50 at $ct/L \sim 4$), with the energy spectral cutoff extending beyond $\gamma_{\rm max}/\gamma_{\rm th} \sim 10^3$ within one dynamical time. This fast increase in $\gamma_{\rm max}$ is indeed reminiscent of what we had observed in the case of unstressed ABC instability (compare with the bottom panel in Fig. 30 at $ct/L \sim 5$). In analogy to the case of unstressed ABC structures, the instability leads to dramatic particle acceleration, but only minor energy dissipation (the mean kinetic energy reaches a fraction ~ 0.1 of the overall energy budget). Additional dissipation of magnetic energy into particle heat (but without much non-thermal particle acceleration) occurs at later times ($ct/L \gtrsim 6$) during subsequent island mergers, once again imitating the evolution of

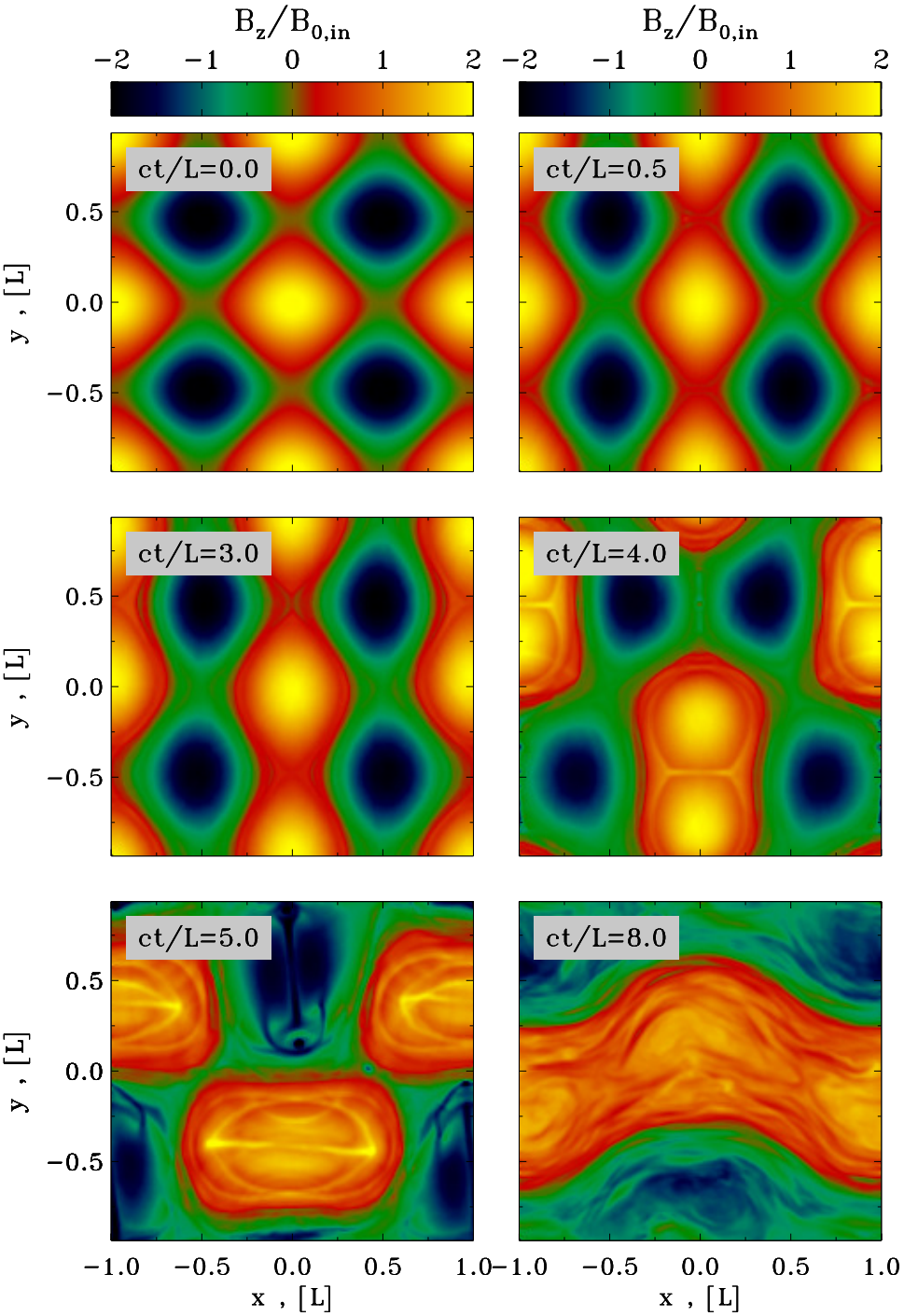

Fig. 49.— Temporal evolution of the instability of a typical 2D ABC structure (time is indicated in the grey box of each panel) with an initial stress of $\lambda = 0.94$ (see Sect. 4.2 for the definition of λ in the context of solitary X-point collapse). The plot presents the 2D pattern of the out-of-plane field B_z (in units of $B_{0,\rm in}$) from a PIC simulation with $kT/mc^2 = 10^{-4}$, $\sigma_{\rm in} = 42$ and $L = 126\, r_{\rm L,hot}$, performed within a domain of size $2L \times 2\lambda L$. The system is initially squeezed along the y direction. This leads to X-point collapse and formation of current sheets (see the current sheet at $x = 0$ and $y = 0.5L$ in the top right panel). The resulting reconnection outflows push away neighboring magnetic structures (the current sheet at $x = 0$ and $y = 0.5L$ pushes away the two blue islands at $y = 0.5L$ and $x = \pm 0.5L$). The system is now squeezed along the x direction (middle left panel), and it goes unstable on a dynamical time (middle right panel), similarly to the case of spontaneous (i.e., unstressed) ABC instability. The subsequent evolution closely resembles the case of spontaneous ABC instability shown in Fig. 29.

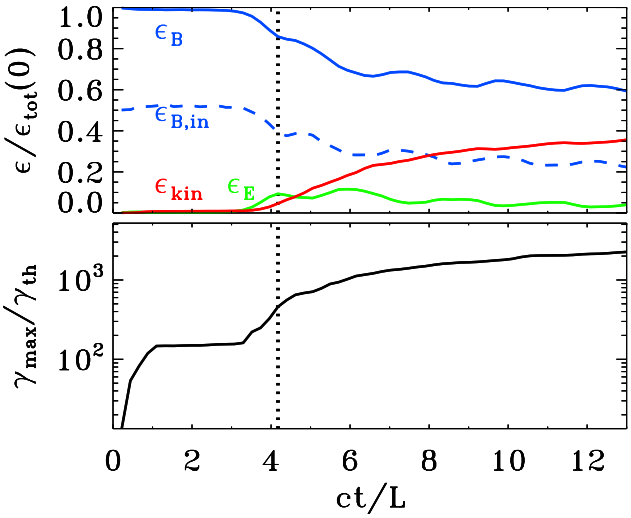

Fig. 50.— Temporal evolution of various quantities, from a 2D PIC simulation of ABC instability with $kT/mc^2 = 10^{-4}$, $\sigma_{\rm in} = 42$ and $L = 126\, r_{\rm L,hot}$ and stress parameter $\lambda = 0.94$, performed within a domain of size $2L \times 2\lambda L$ (the same run as in Fig. 49). Top panel: fraction of energy in magnetic fields (solid blue), in-plane magnetic fields (dashed blue, with $\epsilon_{B,\rm in} = \epsilon_B/2$ in the initial configuration), electric fields (green) and particles (red; excluding the rest mass energy), in units of the total initial energy. Bottom panel: evolution of the maximum Lorentz factor $\gamma_{\rm max}$, as defined in Eq. (16), relative to the thermal Lorentz factor $\gamma_{\rm th} \simeq 1 + (\hat{\gamma} - 1)^{-1} kT/mc^2$, which for our case is $\gamma_{\rm th} \simeq 1$. The early growth of $\gamma_{\rm max}$ up to $\gamma_{\rm max}/\gamma_{\rm th} \sim 1.5 \times 10^2$ is due to particle acceleration at the current sheets induced by the initial stress. The subsequent development of the ABC instability at $ct/L \simeq 4$ is accompanied by little field dissipation ($\epsilon_{\rm kin}/\epsilon_{\rm tot}(0) \sim 0.1$) but dramatic particle acceleration, up to $\gamma_{\rm max}/\gamma_{\rm th} \sim 10^3$. In both panels, the vertical dotted black line indicates the time when the electric energy peaks.

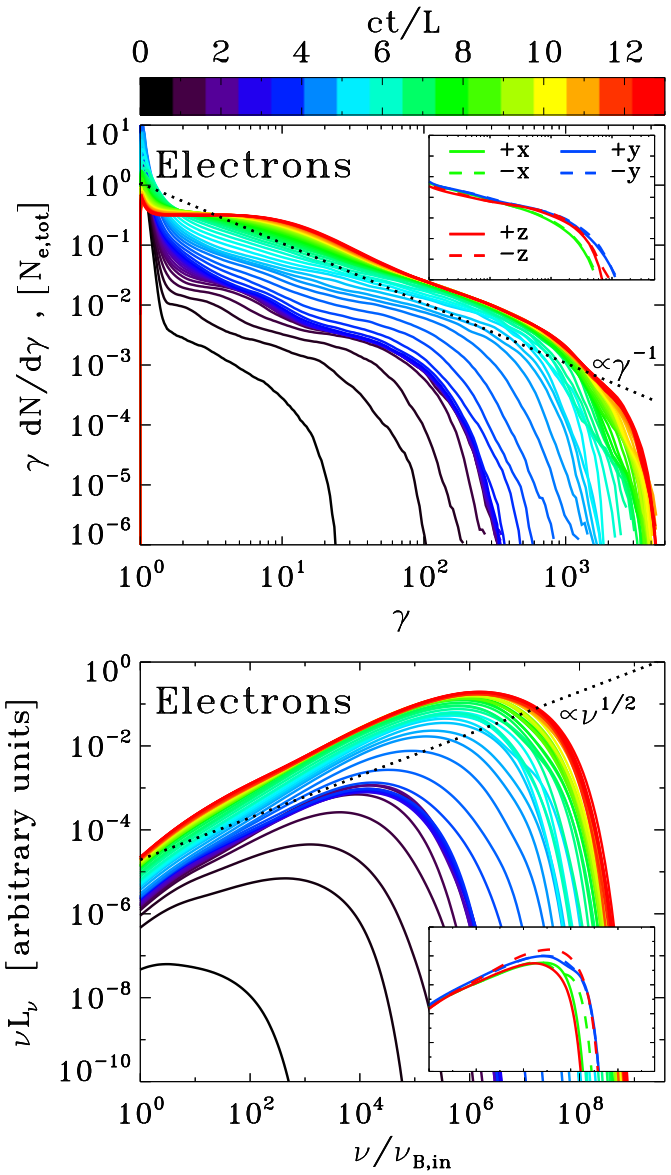

Fig. 51.— Particle spectrum and synchrotron spectrum from a 2D PIC simulation of ABC instability with $kT/mc^2 = 10^{-4}$, $\sigma_{\rm in} = 42$ and $L = 126\,r_{\rm L,hot}$ and stress parameter $\lambda = 0.94$, performed within a domain of size $2L \times 2\lambda L$ (the same run as in Fig. 49 and Fig. 50). Time is measured in units of L/c, see the colorbar at the top. Top panel: evolution of the electron energy spectrum normalized to the total number of electrons. At late times, the spectrum approaches a distribution of the form $\gamma dN/d\gamma \propto \gamma^{-1}$, corresponding to equal energy content in each decade of γ (compare with the dotted black line). The inset in the top panel shows the electron momentum spectrum along different directions (as indicated in the legend), at the time when the electric energy peaks (as indicated by the dotted black line in Fig. 50). Bottom panel: evolution of the angle-averaged synchrotron spectrum emitted by electrons. The frequency on the horizontal axis is normalized to $\nu_{B,\rm in} = \sqrt{\sigma_{\rm in}}\omega_{\rm p}/2\pi$. At late times, the synchrotron spectrum approaches $\nu L_\nu \propto \nu^{1/2}$ (compare with the dotted black line), which just follows from the electron spectrum $\gamma dN/d\gamma \propto \gamma^{-1}$. The inset in the bottom panel shows the synchrotron spectrum at the time indicated in Fig. 50 (dotted black line) along different directions (within a solid angle of $\Delta\Omega/4\pi \sim 3\times10^{-3}$), as indicated in the legend in the inset of the top panel.

unstressed ABC instability.

The two distinct evolutionary phases — the early stage driven by the initial stress, and the subsequent dynamical ABC collapse resembling the unstressed case — are clearly apparent in the evolution of the particle energy spectrum (top panel in Fig. 51) and of the angle-averaged synchrotron emission (bottom panel in Fig. 51). The initial stress drives fast particle acceleration at the resulting currrent sheets (from black to dark blue in the top panel). Once the stress reverses, as part of the self-consistent evolution of the system (top right panel in Fig. 49), the particle energy spectrum freezes (see the clustering of the dark blue lines). Correspondingly, the angle-averaged synchrotron spectrum stops evolving (see the clustering of the dark blue lines in the bottom panel). A second dramatic increase in the particle and emission spectral cutoff (even more dramatic than the initial growth) occurs between $ct/L \sim 3$ and $ct/L \sim 6$ (dark blue to cyan curves in Fig. 51), and it directly corresponds to the phase of ABC instability resembling the unstressed case. The particle spectrum quickly extends up to $\gamma_{\rm max} \sim 10^3$ (cyan lines in the top panel), and correspondigly the peak of the νL_ν emission spectrum shifts up to $\sim \gamma_{\rm max}^2 \nu_{B,\rm in} \sim 10^6 \nu_{B,\rm in}$ (cyan lines in the bottom panel). At times later than $c/L \sim 6$, the evolution proceeds slower, similarly to the case of unstressed ABC instability: the high-energy cutoff in the particle spectrum shifts up by only a factor of three before saturating (green to red curves in the top panel), and the peak frequency of the synchtron spectrum increases by less than a factor of ten (green to red curves in the bottom panel). Rather than non-thermal particle acceleration, the late evolution is accompanied by substantial heating of the bulk of the particles, with the peak of the particle spectrum shifting from $\gamma \sim 1$ up to $\gamma \sim 10$ after $ct/L \sim 6$ (see also the red line in the top panel of Fig. 50 at $ct/L \gtrsim 6$, indicating efficient particle heating). Once again, this closely parallels the late time evolution of unstressed ABC instability.

Finally, we point out that the particle distribution at the time when the electric energy peaks (indicated by the vertical dotted line in Fig. 50) is nearly isotropic, as indicated by the inset in the top panel of Fig. 51. In turn, this results in quasi-isotropic synchrotron emission (inset in the bottom panel). We refer to the unstressed case in Fig. 31 for an explanation of this result, which is peculiar to the ABC geometry employed here.

We conclude this subsection by investigating the effect of the initial stress, as quantified by the squeezing parameter λ. In Figs. 52 and 53, we present the results of a suite of five PIC simulations of ABC collapse with fixed $kT/mc^2 = 10^{-4}$, $\sigma_{\rm in} = 42$ and $L/r_{\rm L,hot} = 126$, but different magnitudes of the initial stress: $\lambda = 0.78$ (black), 0.87 (blue), 0.94 (green), 0.97 (yellow) and 1 (red; i.e., unstressed). In all the cases, the early phase (until $ct/L \sim 3$) bears memory of the prescribed stress parameter λ. In particular, the value of the electric energy at early times increases for decreasing λ (top panel in Fig. 52 at $ct/L \lesssim 3$), as the initial stress becomes stronger. In parallel, the process of particle acceleration initiated at the stressed X-points leads to a maximum particle energy $\gamma_{\rm max}$ that reaches higher values for stronger stresses (i.e., smaller λ, see the bottom panel of Fig. 52 at $ct/L \lesssim 3$). While the early stage is sensitive to the value of the initial stress, the dramatic evolution happening at $ct/L \sim 4$ is remarkably similar for all the values of $\lambda \neq 1$ explored in Fig. 52 (black to yellow curves). In all the cases, the electric energy grows exponentially as $\propto \exp(4ct/L)$. Both the growth rate and the peak level of the electric energy (~ 0.1 of the total energy) are remarkably insensitive to λ, and they resemble the unstressed case $\lambda = 1$ (red curve in Fig. 52), aside from a temporal offset of $\sim 2L/c$. The fast evolution occurring at $ct/L \sim 4$ leads to dramatic particle acceleration (bottom panel in Fig. 52), with the high-energy spectral cutoff reaching $\gamma_{\rm max} \sim 10^3$ within a dynamical time, once again imitating the results of the unstressed case, aside from a temporal shift of $\sim 2L/c$.

As we have just described, the electric energy peaks during the second phase, when the stressed systems evolve in close similarity with the unstressed setup. In Fig. 53, we present a comparison of the particle spectra for different λ (as indicated in the legend), measured at the peak time of the electric energy (as indicated by the vertical dotted lines in Fig. 52). The spectral shape for all the stressed cases is nearly identical, especially if the initial stress is not too strong (i.e., with the only exception of the black line, corresponding to $\lambda = 0.78$). In addition, the spectral cutoff is in remarkable agreement with the result of the unstressed setup (red curve in Fig. 53), confirming that the evolution of

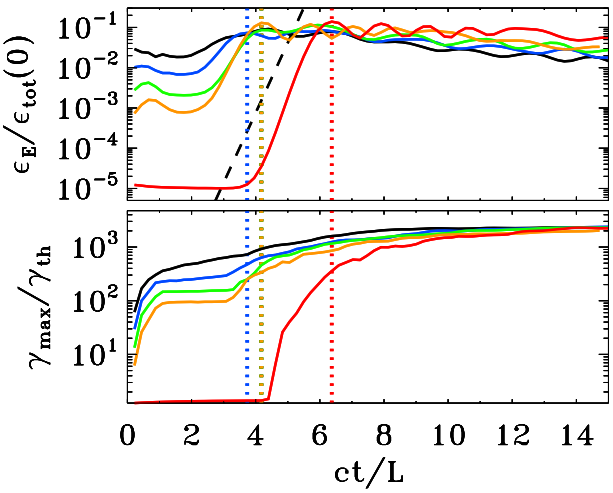

Fig. 52.— Temporal evolution of the electric energy (top panel, in units of the total initial energy) and of the maximum particle Lorentz factor (bottom panel; $\gamma_{\rm max}$ is defined in Eq. (16), and it is normalized to the thermal Lorentz factor $\gamma_{\rm th} \simeq 1 + (\hat{\gamma} - 1)^{-1} kT/mc^2$), for a suite of five PIC simulations of ABC collapse with fixed $kT/mc^2 = 10^{-4}$, $\sigma_{\rm in} = 42$ and $L/r_{\rm L,hot} = 126$, but different magnitudes of the initial stress: $\lambda = 0.78$ (black), 0.87 (blue), 0.94 (green), 0.97 (yellow) and 1 (red; i.e., unstressed). The early phases (until $ct/L \sim 3$) bear memory of the prescribed stress parameter λ, whereas the evolution subsequent to the ABC collapse at $ct/L \sim 4$ is remarkably similar for different values of λ. The dashed black line in the top panel shows that the electric energy grows exponentially as $\propto \exp(4ct/L)$, during the dynamical phase of the ABC instability. The vertical dotted lines mark the time when the electric energy peaks (colors correspond to the five values of λ, as described above; the black, green and yellow vertical lines overlap).

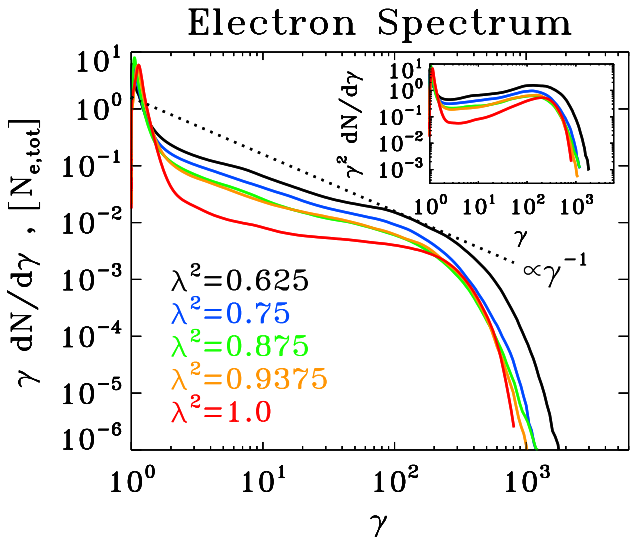

Fig. 53.— Particle spectrum at the time when the electric energy peaks, for a suite of five simulations of ABC collapse with fixed $kT/mc^2 = 10^{-4}$, $\sigma_{\rm in} = 42$ and $L/r_{\rm L,hot} = 126$, but different magnitudes of the initial stress (same runs as in Fig. 52): $\lambda = 0.78$ (black), 0.87 (blue), 0.94 (green), 0.97 (yellow) and 1 (red; i.e., unstressed). The main plot shows $\gamma dN/d\gamma$ to emphasize the particle content, whereas the inset presents $\gamma^2 dN/d\gamma$ to highlight the energy census. The dotted black line is a power law $\gamma dN/d\gamma \propto \gamma^{-1}$, corresponding to equal energy content per decade (which would result in a flat distribution in the inset). The particle spectrum at the time when the electric energy peaks has little dependence on the initial stress parameter λ, and it resembles the result of the spontaneous ABC instability (red curve).

the stressed cases closely parallels the spontaneous ABC instability.

We conclude that this setup — with an initially imposed stress — is not a preferred mode of instability for the ABC structure (unlike the shearing setup described in the previous subsection, which directly leads to ABC collapse). Still, the perturbation imposed onto the system eventually leads to ABC instability, which proceeds in close analogy to the unstressed case. Particle acceleration to the highest energies is not achieved in the initial phase, which still bears memory of the imposed stress, but rather in the quasi-spontaneous ABC collapse at later times. In order to further test this claim, we have performed the following experiment. After the initial evolution (driven by the imposed stress), we artificially reduce the energies of the highest energy particles (but still keeping them ultra-relativistic, to approximately preserve the electric currents). The subsequent evolution of the high-energy particle spectrum is similar to what we observe when we do not artificially "cool" the particles, which is another confirmation of the fact that the long-term physics is independent from the initial stress.

8. Merging flux tubes carrying zero total current

In Sections 3-6-7 we considered evolution of the unstable configurations – those of the stressed X-point and 2D ABC configurations (both stressed and unstressed). We found that during the development of instability of the 2D ABC configurations the particles are efficiently accelerated during the initial dynamical phase of the merger of current-carrying flux tubes (when the evolution is mostly due to the X-point collapse). There are two key feature of the preceding model that are specific to the initial set-up: (i) each flux tube carries non-zero poloidal current; (ii) the initial 2D ABC configuration is an unstable equilibrium. It is not clear how generic these conditions and how the details of particle acceleration are affected by these specific properties.

In this section we relax these conditions. We investigate a merger of two flux tubes with zero total current. We will study, using relativistic MHD and PIC simulations, the evolution of colliding flux tubes with various internal structure. Importantly, all the cases under investigation have a common property: they carry zero net poloidal current (either completely distributed electric currents as in the case of configurations (40) and (8.2), or balanced by the surface current, (44)). Thus, two flux tubes are not attracted to each other - at least initially. All the configurations considered have a common property: the current in the core of the flux tube is balanced by the reverse current in the outer parts.

8.1. Force-free simulations

8.1.1. Merger of Lundquist's magnetic ropes

First we consider Lundquist's force-free cylinders, surrounded by uniform magnetic field,

$$\mathbf{B}_L(r \leq r_\mathrm{j}) = J_1(r\alpha)\mathbf{e}_\phi + J_0(r\alpha)\mathbf{e}_z\,, \tag{40}$$

Here, J_0, J_1 are Bessel functions of zeroth and first order and the constant $\alpha \simeq 3.8317$ is the first root of J_0. We chose to terminate this solution at the first zero of J_1, which we denote as r_j and hence continue with $B_z = B_z(r_j)$ and $B_\phi = 0$ for $r > r_j$. Thus the total current of the flux tube is zero. As the result, the azimuthal field vanishes at the boundary of the rope, whereas the poloidal one changes sign inside the rope.

We start with the position of two ropes just touching each other and set the centre positions to be $\mathbf{x_c} = (-r_\mathrm{j}, 0)$ and $\mathbf{x_c} = (r_\mathrm{j}, 0)$. The evolution is very slow, given the fact that at the contact the reconnecting field vanishes. To speed things up, we "push" the ropes towards each other by imposing a drift velocity. That is, we initialize the electric field

$$\mathbf{E} = -(1/c)\mathbf{v}_\mathrm{kick}\times\mathbf{B}\,, \tag{41}$$

where $\mathbf{v}_\mathrm{kick} = (\pm v_\mathrm{kick}, 0, 0)$ inside the ropes and here we set $v_\mathrm{kick} = 0.1c$.

The numerical setup is as follows: We have adopted the force-free algorithm of Komissarov et al. (2007) to create a physics module in the publicly available code MPI-AMRVAC[20] Porth et al. (2014b); Keppens et al. (2012). We simulate a 2D Cartesian domain with $x \in [-6, 6]$ and $y \in [-3, 3]$ at a base-resolution of 128×64 cells. In the following, the scales are given in units of r_j. During the evolution, we ensure that the FWHM of the current density in the current sheet is resolved by at least 16 cells via local adaptive mesh refinement of up to eight levels, each increasing the resolution by a factor of two. Boundary conditions are set to "periodic".

The results are illustrated in Figure 2, which shows the distribution of B_z and $\chi \equiv 1 - E^2/B^2$ at $t = 0, 2, 5, 6, 9$. Interestingly, around the time $t \approx 5$, the cores (with B_z of the same sign) of the flux tubes begin to merge. This leads to zero guide field in the current sheet and increased reconnection rate. The sudden increase in reconnection rate leads to a strong wave being emitted from the current sheet which is also seen in the decrease to $\chi \approx 0.7$ in the outer part of the flux tubes, i.e. in the fourth panel of figure 54.

The influence of the guide field is investigated in Figure 55. In the left panel, we show cuts of B^z along the $y = 0$ plane. As the in-plane magnetic flux reconnects in the current sheet, the out-of-plane component remains and accumulates, leading to a steep profile with magnetic pressure that opposes the inward motion of reconnecting field lines. At $t = 5.2$, the guide field changes sign and the reconnection rate spikes rapidly at a value of $v_r \approx 0.6$. This is clearly seen in the right panel of figure 55. Thereafter, a guide field of the opposite sign builds up and the reconnection rate slows down again. The position of the flux-tube core as quantified by the peak of B^z evolves for $t < r_\mathrm{j}/c$ according to the prescribed velocity kick Eq. (41) but then settles for a slower evolution governed by the resistive timescale.

[20] https://gitlab.com/mpi-amrvac/amrvac

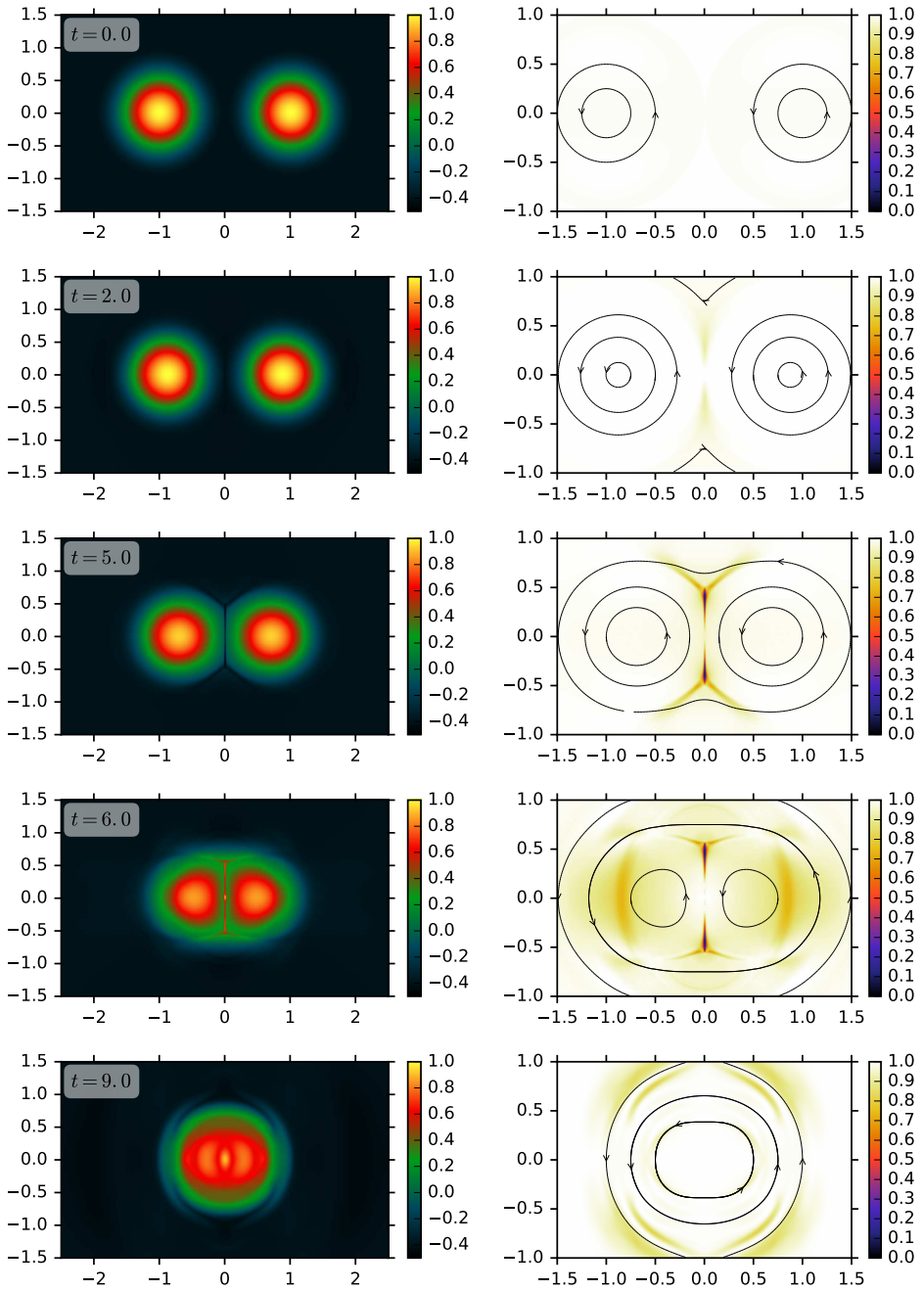

Fig. 54.— Merging Lundquist flux tubes with initial kick velocity $v_{\rm kick} = 0.1$c and $\eta_{||} = 1/1000$. From to to bottom, we show snapshots at $t = [0, 2, 5, 6, 9]$ where the coordinates are given in units of initial flux tube radius $r_{\rm j}$ and time is measured in units of $c/r_{\rm j}$. *Left:* Magnitude of out-of-plane component B_z. *Right:* Plots of $\chi = 1 - E^2/B^2$ indicating that regions with $E \sim B$ emerge in the outflow region of the current-sheet. Starting from the small kick velocity, the merger rate starts with initial small kick velocity and speeds up until $t \sim 5$. Exemplary field lines are traced and shown as black lines in the right panels.

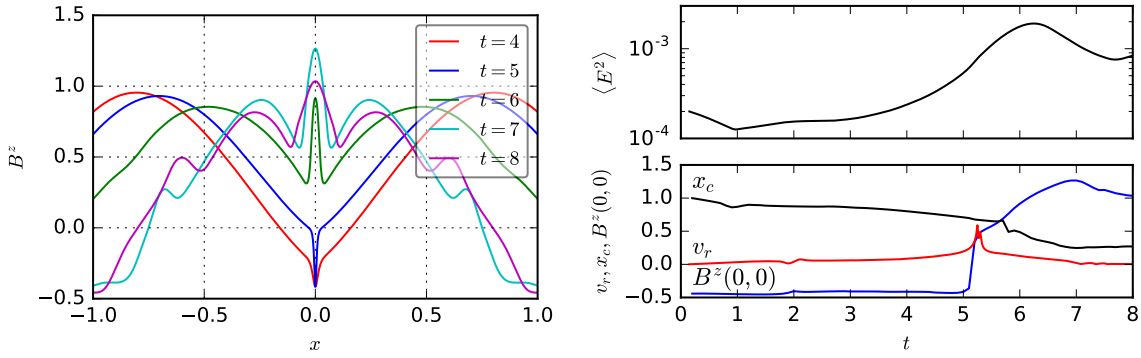

Fig. 55.— Merging Lundquist flux tubes. *Left:* cuts along the $y = 0$ plane, showing the profile of the guide-field for various times. Coordinates are given in terms of r_j and times in units of r_j/c. At $t \simeq 5.2$, the guide field in the current sheet at $x = 0$ changes sign which results in a sharp rise in the reconnection rate and accelerated merger of the cores. *Right:* Domain averaged electric field $\langle E^2 \rangle$ (top) and other quantities of interest (bottom): reconnection rate, measured as drift velocity through $x = \pm 0.1$ (red), x-coordinate of the core quantified as peak in B^z (black) and guide field at the origin $B^z(0, 0)$ (blue). When the guide-field changes sign, the reconnection rate spikes at $v_r \simeq 0.6c$. This equivalent PIC result is discussed in Figure 71

8.2. Modified Lundquist's magnetic ropes

8.2.1. Description of setup

For the future analysis, we consider a modified version of Lundquist's force-free cylinders discussed in the previous section 8.1.1. The toroidal field is the same as given by equation 40, but the vertical field reads

$$B_z(r \leq r_\mathrm{j}) = \sqrt{J_0(\alpha r)^2 + C} \tag{42}$$

within a flux tube and is set to $B_z(r_\mathrm{j})$ in the external medium. As a result, the sign-change of the guide-field is avoided and only positive values of B_z are present. The additional constant C sets the minimum (positive) vertical magnetic field component. In the following, we always set $C = 0.01$.

In this section, we will investigate dependence of reconnection rate and electric field magnitude on the kick velocity and magnetic Reynolds number.

8.2.2. Overall evolution

As the current vanishes on the surface of the flux tubes, the initial Lorentz force also vanishes and the flux tubes approach each other on the time scale given by the kick velocity. Then a current sheet is formed at the intersection which reconnects in-plane magnetic flux resulting in an engulfing field. This evolution is illustrated in figure 56 for an exemplary run with $(v_\mathrm{kick}, \eta_{||}) = (0.03c, 10^{-3})$, showing out-of plane magnetic field strength B_z and the previously introduced parameter $\chi = 1 - E^2/B^2$. It can be seen that in the outflow region of the current sheet, χ assumes values as small as $\chi_\mathrm{min} = 0.09$ but the distributed region of $\chi \approx 0.7$ that is observed for the unmodified Lundquist tubes is absent. After the peak reconnection rate which for the shown parameters is reached at $t \simeq 9$, the system undergoes oscillations between prolate and oblate shape during which the current sheet shrinks. The oscillation frequency corresponds to a

light-crossing time across the structure.

8.2.3. Dependence on kick velocity

We now vary the magnitude of the initial perturbation in the interval $v_{\rm kick} \in [0.03c, 0.3c]$. Figure 57 gives an overview of the morphology when the peak reconnection rate is reached. The reconnection rate is measured as inflowing drift velocity at $x = \pm 0.05$ and is averaged over a vertical extent of $\Delta y = 0.1$. For the lower three kick velocities, we obtain a very similar morphology when the peak reconnection rate is reached. With $v_{\rm kick} = 0.3c$, the flux tubes rebound, resulting in emission of waves in the ambient medium. As the flux tubes dynamically react to the large perturbation, it is not possible to force a higher reconnection rate by smashing them together with high velocity, they simply bounce off due to the magnetic tension in each flux tube. However, high velocity perturbations of $v_{\rm kick} = 0.1c$ and $v_{\rm kick} = 0.3c$ lead to the formation of plasmoids which are absent in the cases with small perturbation and this in turn can impact on the reconnection rate.

A more quantitative view is shown in Figure 58 illustrating the evolution of the mean electric energy in the domain $\langle E^2 \rangle(t)$ and reconnection rate as previously defined. One can see that all simulations reach a comparable electric field strength in the domain, independent of the initial perturbation. The electric field grows exponentially with comparable growth rate and also the saturation values are only weakly dependent on the initial perturbation. Indeed, comparing highest and lowest kick velocities, we find that $\langle E^2 \rangle_{\rm max}$ is within a factor of two for a range of 30 in the velocity perturbation.

In the evolution of $\langle E^2 \rangle(t)$, one can also read off the oscillation period of $P \approx 1 r_{\rm j}/c$, most pronounced in the strongly perturbed case. The span of peak reconnection rates is similar to the mean electric field strength with a range from $v_{\rm r} = 0.2$ down to $v_r = 0.11$. The reconnection rate saturates at $\sim 0.1c$ for vanishing initial perturbation. When plasmoids are triggered, as for the case $v_r = 0.1$ and $v_r = 0.3$, the run of $v_{\rm r}$ shows additional substructure leading to secondary peaks as seen e.g. in the green curve on the lower panel.

8.2.4. Scaling with magnetic Reynolds number

We next investigate the scaling of reconnection rate with magnetic Reynolds number while keeping a fixed kick velocity of $0.1c$. As astrophysical Reynolds numbers are typically much larger than what can be achieved numerically, this is an important check for the applicability of the results. For the force-free case, we simply define the Lundquist number

$$S = \frac{r_{\rm j} c}{\eta_{||}} \simeq \eta_{||}^{-1} \tag{43}$$

and check the scaling via the resistivity parameter $\eta_{||}$.

Figure 59 (left panel), shows the run of the domain averaged electric field and the reconnection rate as in Figure 58. In general, the initial evolution progresses faster when larger resistivities are considered, suggesting a scaling with the resistive time. However, once a significant amount of magnetic flux has reconnected, the electric energy in the domain peaks at values within a factor of 1.5 for a significant range of Reynolds numbers $\eta_{||} \in [1/100, 1/4000]$. Very good agreement is found for the peak reconnection rate of $v_{\rm r} \simeq 0.15c$. The $\eta_{||} = 4000$ run developed plasmoids at $t \simeq 8$ which were not observed in the other runs.

We have also conducted a range of experiments in resistive relativistic magnetohydrodynamics (RMHD). The setup is as the force-free configuration described above, however we now choose constant values for density and pressure such

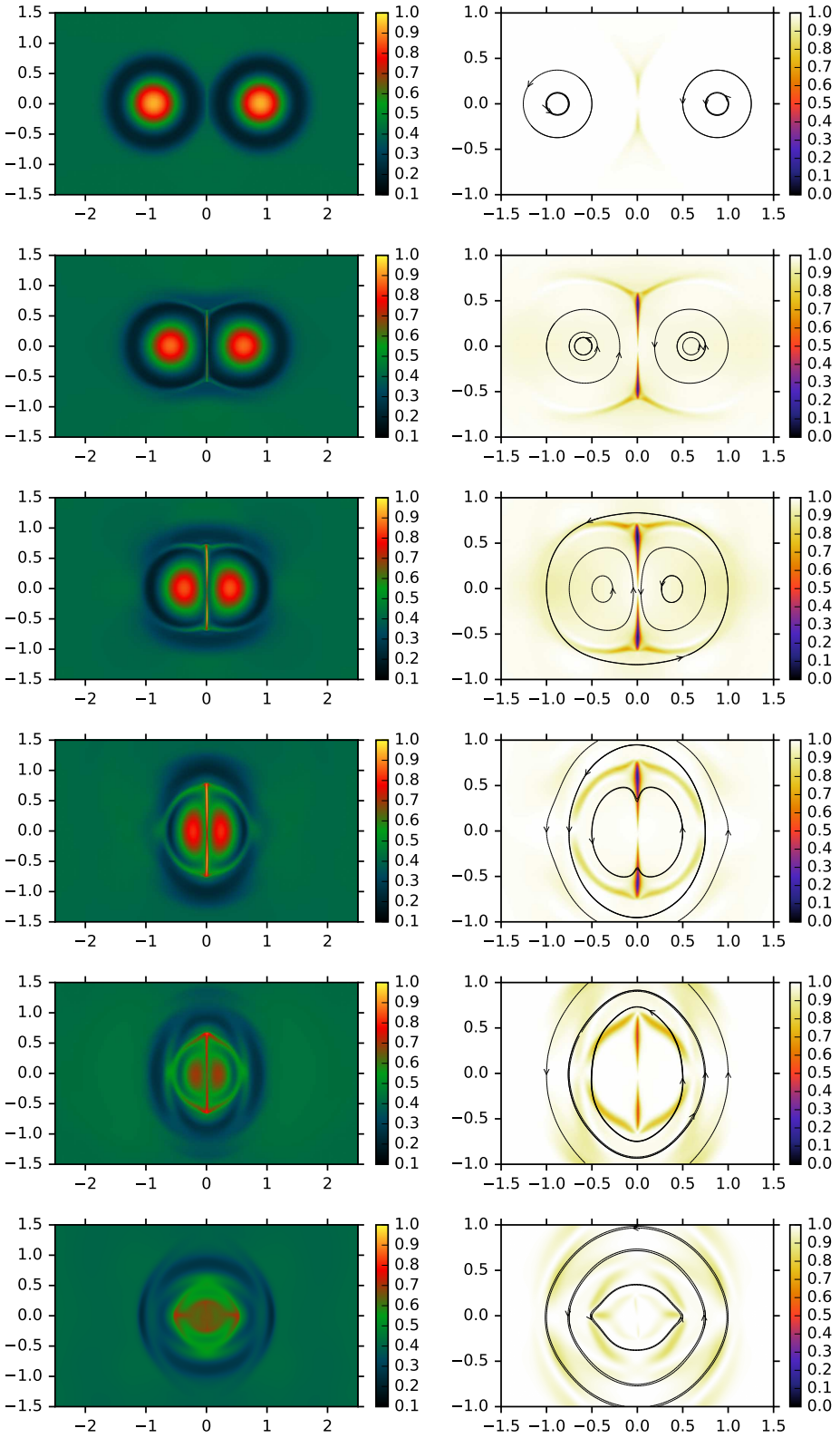

Fig. 56.— Merger of 2D modified Lundquist flux tubes with initial kick velocity $v_{\rm kick} = 0.03$c and $\eta_{||} = 1000$. From to to bottom, we show snapshots at $t = [6, 9, 10, 11, 1214]$ where the coordinates are given in units of initial flux tube radius $r_{\rm j}$ and time is measured in units of $c/r_{\rm j}$. *Left:* Magnitude of out-of-plane component B_z. *Right:* Plots of $\chi = 1 - E^2/B^2$ indicating that regions with $E \sim B$ emerge in the outflow region of the current-sheet. Starting from the small kick velocity, the merger rate starts with initial small kick velocity and speeds up until $t \sim 9$. Exemplary field lines are traced and shown as black lines in the right panels.

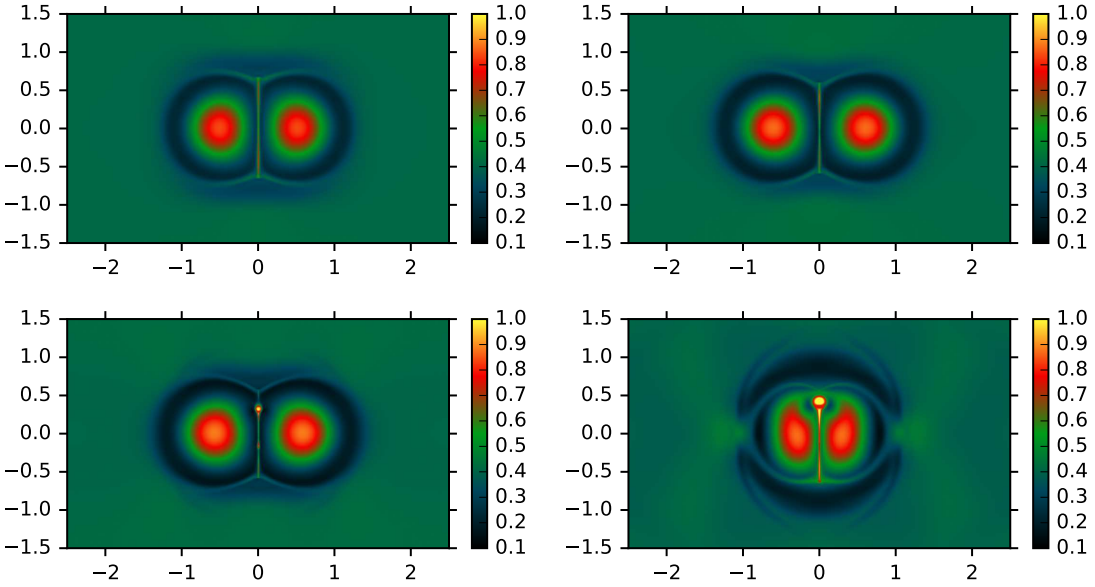

Fig. 57.— Merger of 2D modified Lundquist flux tubes showing B_z with varying kick velocity: $v_{\rm kick} = 0.01c$ at $t = 12$ (top left), $v_{\rm kick} = 0.03c$ at $t = 9$ (top right), $v_{\rm kick} = 0.1c$ at $t = 6$ (bottom left) and $v_{\rm kick} = 0.3c$ at $t = 5$ (bottom right). The snapshot times are chosen to reflect the maximum reconnection rate v_r, measured as inflow velocity at $x = \pm 0.05$. See text for details.

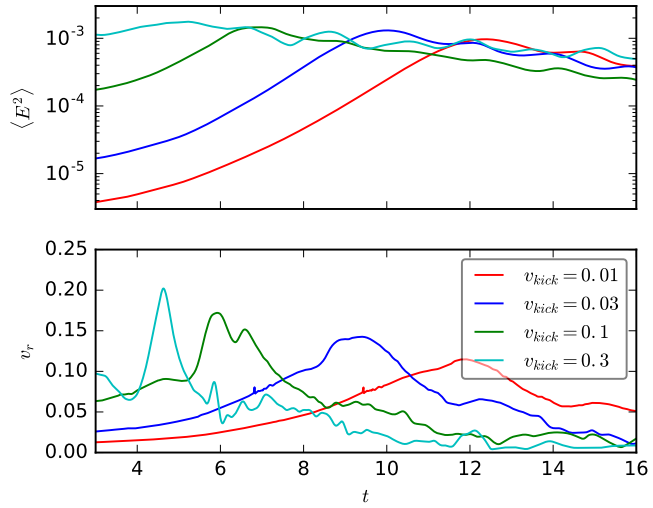

Fig. 58.— Merger of 2D modified Lundquist flux tubes showing the evolution of domain averaged electric field $\langle E^2 \rangle$ (top) and reconnection rate v_r (bottom). We vary the initial driving velocity from $v = 0.01c$ to $v = 0.3c$. See text for discussion.

that the magnetisation in the flux rope has the range $\sigma \in [1.7, 10]$ and the Alfvén velocity ranges in $v_A \in [0.8, 0.95]$. The adiabatic index was chosen as $\gamma = 4/3$. Figure 59 (right panel) shows the resulting evolution of electric field and reconnection rate for a variety of resistivity parameter $\eta \in [1/250, 1/4000]$. Note that the green curves in the left and right panel correspond to the same resistivity parameter of $\eta_{||}, \eta = 1/1000$ and cyan (left) and red (right) curves both correspond to $\eta_{||}, \eta = 1/4000$. The initial evolution up to the wave-reflection feature at $t = 2$ is very similar in both realisations. Afterwards the evolution differs: while the reconnection rate in the force-free run with $\eta_{||} = 1/4000$ increases to reach a peak of $v_{\rm r} \simeq 0.15c$ at $t \simeq 9$, $v_{\rm r}$ remains approximately constant in the corresponding RMHD run. In contrast to the force-free scenario, the RMHD runs did not feature any plasmoids at the Reynolds numbers considered here. Better agreement is found for $\eta_{||}, \eta = 1/1000$ (green curves in both panels). Here, the force-free reconnection rate reaches its peak value of $v_{\rm r} \simeq 0.14$ at $t \simeq 6$ and the RMHD peaks at $t \simeq 7$ with $v_{\rm r} \simeq 0.07c$. Increasing the magnetisation improves the match between both cases: In the green dashed (dotted) curve, we have doubled (quadrupled) the magnetization by lowering plasma density and pressure in the SRMHD runs at $\eta = 1/1000$. One can see that the evolution speeds up and higher reconnection rates are achieved: For the highest magnetisation run, we reach the peak reconnection rate of $\simeq 0.1c$ and the peak is reached already at $t \simeq 6.2$ very similar to the corresponding force-free run which peaked at $t \simeq 6$ with $v_{\rm r} \simeq 0.13c$. This indicates that the RMHD model indeed approaches the force-free limit for increasing magnetization.

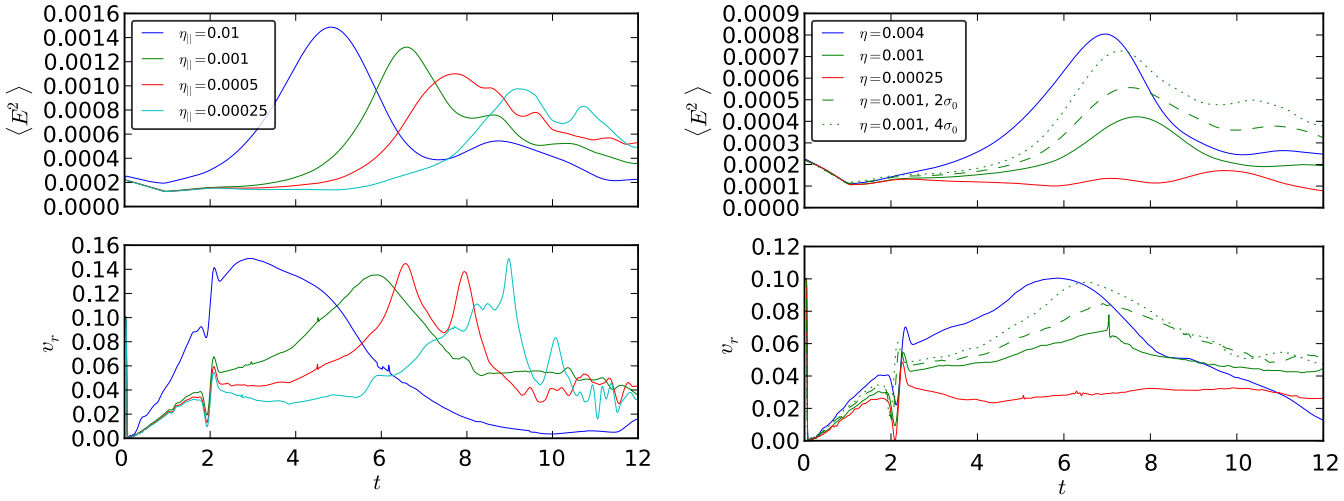

Fig. 59.— Merger of 2D modified Lundquist flux tubes for different resistivities $\eta_{||}$ with initial kick velocity of $0.1c$. Mean squared electric field in the domain *(top)* and reconnection speed in units of c *(bottom)*. *Left:* Force-free dynamics. The initial evolution depends on the resistivity but comparable values for the reconnection rate of $v_{\rm r} \approx 0.15c$ are obtained for all considered Reynolds numbers. Note that in the case $\eta_{||} = 1/4000$ plasmoids appear at $t \simeq 8$ which are not observed in the other runs. *Right:* Corresponding resistive MHD evolution with $\sigma \in [1.7, 10]$ and doubled (dashed) and quadrupled (dotted) magnetization. One can see that the force-free result is approached both in the evolution of $\langle E^2 \rangle$ and $v_{\rm r}$.

8.3. Core-envelope magnetic ropes

8.3.1. Description of setup

We now adopt a setup where the current does no return volumetrically within the flux tube, but returns as a current sheet on the surface. The solution is based on the "core-envelope" solution of Komissarov (1999), with the gas pressure replaced by the pressure of the poloidal field. Specifically, the profiles read

$$B^{\phi}(r) = \begin{cases} B_m(r/r_m) & ; \quad r < r_m \\ B_m(r_m/r) & ; \quad r_m < r < r_j \\ 0 & ; \quad r > r_j \end{cases} , \tag{44}$$

$$B_z^2(r)/2 = \begin{cases} p_0 \left[\alpha + \frac{2}{\beta_m}(1-(r/r_m)^2)\right] & ; \quad r < r_m \\ \alpha p_0 & ; \quad r_m < r < r_j \\ p_0 & ; \quad r > r_j \end{cases} , \tag{45}$$

where

$$\beta_m = \frac{2p_0}{B_m^2}, \qquad \alpha = 1 - (1/\beta_m)(r_m/r_j)^2 , \tag{46}$$

r_j is the outer radius of the rope and r_m is the radius of its core. In the simulations, $r_m = 0.5$, $B_m = 1$, $\alpha = 0.2$ and the coordinates are scaled to $r_{\rm j} = 1$. As in the previous cases, two identical current tubes are centred at $(x, y) = (-1, 0)$ and $(x, y) = (1, 0)$. They are at rest and barely touch each other at $(x, y) = (0, 0)$. In this scenario, since the current closes discontinuously at the surface of the flux tubes, the Lorentz-force acting on the outer field lines is non-vanishing. Thus we can dispense with the initial perturbation and always set $v_{\rm kick} = 0$.

8.3.2. Overall evolution

The overall evolution is characterised as follows: Immediately, a current-sheet forms at the point (0,0) and two Y-points get expelled in vertical direction with initial speed of c. The expansion of the Y-points is thereafter slowed down by the accumulating pressure of B^z in the ambient medium. Snapshots of B^z for the case $\eta_{||} = 1/500$ are shown in figure 60. The stage of most rapid evolution of the cores is at $t \simeq 4$. At this time, the morphology is comparable to the modified Lundquist ropes, i.e. Figure 57.

We quantify the evolution of Y-point $(0, y_{yp})$ via the peak in E^x along the $x = 0$ line and the core location $(x_c, 0)$ as peak of B^z along the $y = 0$ line. The data is shown in the top panel of figure 61. One can see the Y-point slowing down from its initial very fast motion. Gradually, the cores accelerate their approach, reaching a maximal velocity at $t \simeq 4$. The evolution stalls as the guide-field at $(0, 0)$ reaches its maximum and magnetic pressure in the current sheet balances the tension of the encompassing field.

8.3.3. Scaling with magnetic Reynolds number

As for the modified Lundquist ropes, section 8.2.4, we investigate the dependence of the dynamics with magnetic Reynolds number by varying the resistivity parameter. An overview of relevant quantities is given in Figure 62 for the range $\eta_{||} \in [1/500, 1/8000]$. After the onset-time of $\approx r_{\rm j}/c$, all runs enter into a phase where the electric energy grows according to $\propto \exp(tc/r_{\rm j})$. As expected, the electric energy decreases when the conductivity is increased. Between $t \simeq 4$ and $t \simeq 5$, the growth of the electric energy saturates and the evolution slows down. In general, we observe two

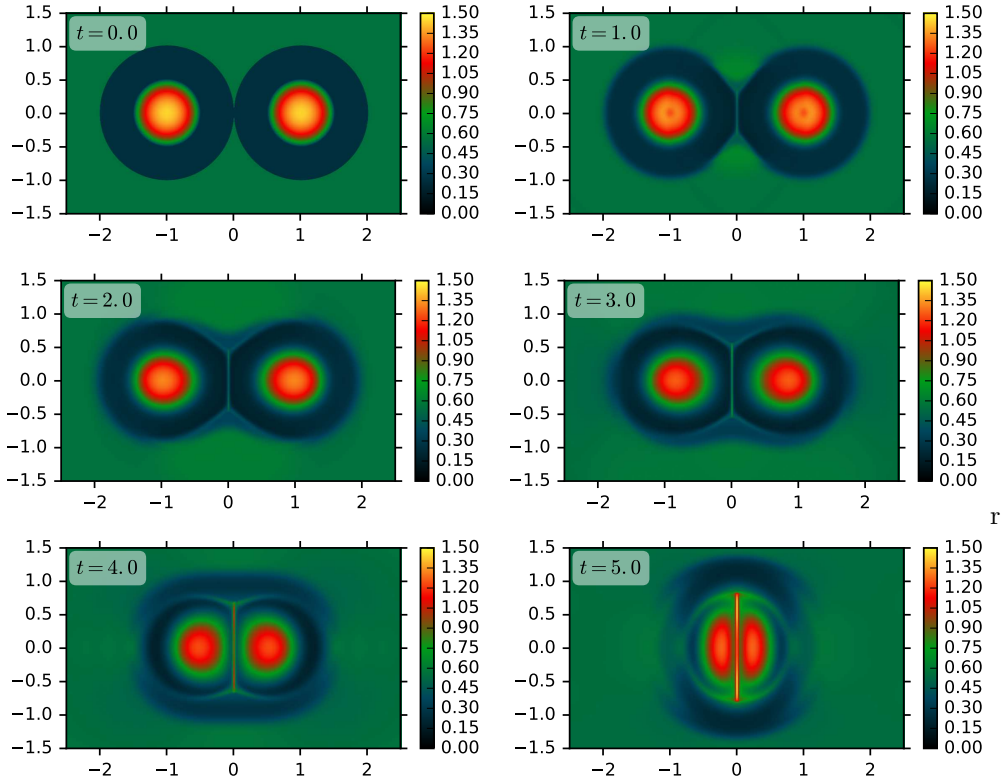

Fig. 60.— Merger of 2D core-envelope flux tubes with $\eta_{||} = 500$. We show snapshots showing B^z at $t = [1, 2, 3, 4, 5]$ as indicated in each panel, where the coordinates are given in units of initial flux tube radius r_j and time is measured in units of c/r_j. This figure is to be compared to the PIC results as shown in Figure 73.

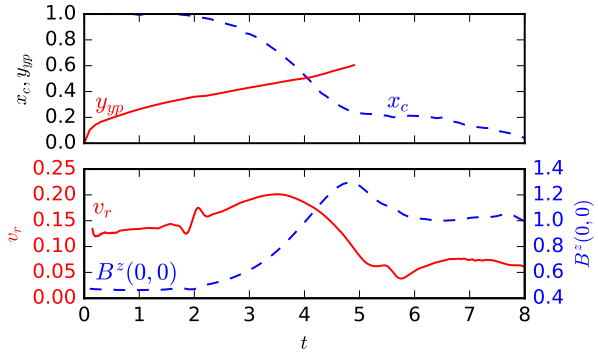

Fig. 61.— Merger of 2D core-envelope flux tubes with $\eta_{||} = 500$. *Top:* Position of the upper Y-Point (solid red) quantified as peak of E^x on the $x = 0$ line and right core position (blue dashed) obtained from the peak of B^z on the $x = 0$ line. *Bottom:* Reconnection rate, measured as drift velocity through $x = \pm 0.1$ (solid red) and guide field at the origin $B^z(0, 0)$ (blue dashed). This figure can be compared to the PIC results shown in Figure 74.

regimes: Up to $\eta_{||} = 1/4000$, the reconnection rate decreases with increasing conductivity, as would be expected in a Sweet-Parker scaling. In this regime, also the motion of the cores slows down when $\eta_{||}$ is decreased. Whereas the most rapid motion for $\eta_{||} = 1/500$ was found at $t \simeq 4$, for $\eta_{||} = 1/4000$ it is delayed to $t \simeq 5$ (c.f. 62, lower panel).

The case with the highest conductivity, $\eta_{||} = 1/8000$ breaks the trend of the low conductivity cases. Here, the reconnection rate increases continuously up to $t \simeq 4.5$ at which point it rapidly flares to a large value of $v_{\rm r} \simeq 0.25c$ where it remains for somewhat less than $r_{\rm j}/c$. Also the slowing of the core-motion is halted at $\eta_{||} = 1/8000$: Up to $t \simeq 5$, the core position lines up well with the case $\eta_{||} = 1/4000$. Just after the flare, the flux tube merger is accelerated as evidenced by the rapid decline of x_c.

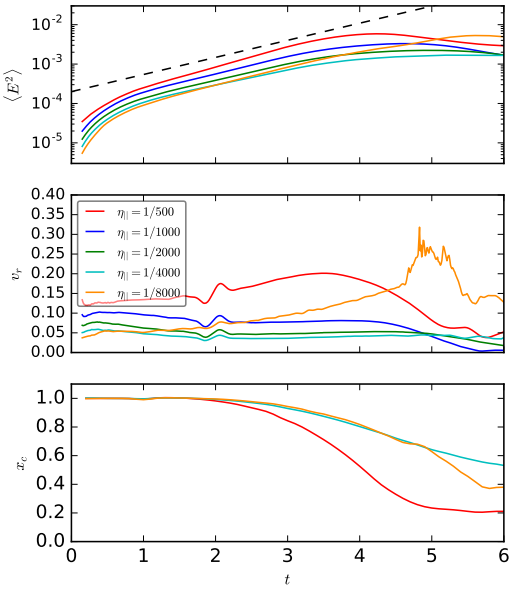

Fig. 62.— Merger of 2D core-envelope flux tubes for different resistivities $\eta_{||} \in [1/500, 1/8000]$. *Top:* Domain averaged electric field strength $\langle E^2 \rangle$. After one light-crossing time we observe a growth according to $\propto \exp(tc/r_{\rm j})$ indicated as black dashed line. *Middle:* Reconnection rate, measured as drift velocity through $x = \pm 0.1$. The dynamical evolution for $\eta_{||} = 1/8000$ is very different from the cases $\eta_{||} = 1/1000, 1/2000, 1/4000$. In those cases, one large plasmoid would form and remain stationary in the current sheet until very late times ($t > 6$). In the lowest resistivity case however, many small plasmoids are created which expel flux continuously to both sides. Thus the magnetic tension surrounding the structure grows more rapidly, leading to the explosive increase of reconnection at $t \simeq 4.5$. *Bottom:* Core position for the three selected cases $\eta_{||} = 1/500, 1/4000, 1/8000$. In the regime $\eta_{||} \in [1/500, 1/4000]$, the merging of the cores slows down as electric conductivity increases. For $\eta_{||} = 1/8000$ however, this trend is halted and reversed as the motion of the cores actually speeds up after the peak in reconnection rate at $t \simeq 5$. This figure can be compared to the PIC results shown in Figure 78.

It is interesting to ask why the dynamics changed so dramatically for the case $\eta_{||} = 1/8000$. In figure 63, we show snapshots of $\chi = 1 - E^2/B^2$ at the time $t = 5$ for the two highest conductivity cases. At this point, in the lower conductivity case, a single large central plasmoid has formed that remains in the current sheet for the entire evolution. This qualitative picture also holds for the cases $\eta_{||} = 1/1000, 1/2000$. Flux that accumulates in the central plasmoid does not get expelled from the current sheet and so does not add to the magnetic tension which pushes the ropes together. Furthermore, the single island opposes the merger via its magnetic pressure of the accumulated B^z.

For the case $\eta_{||} = 1/8000$, the large-scale plasmoid does not form, instead smaller plasmoids are expelled symmetrically in both directions. The expelled flux continues to contribute to the large scale stresses and the merger of the islands is accelerated further which is reflected also in the continued exponential rise of the electric energy shown in figure 62. As in the case of the Lundquist and modified Lundquist flux tubes and as required for rapid particle acceleration, macroscopic regions of $E > B$ are found also in this configuration in the outflow regions of the current sheet, illustrated in figure 63.

In conclusion, our force-free experiments of coalescing flux tubes show that scale stresses can lead to high reconnection rates in the range of $0.1c - 0.3c$, independent of the magnetic Reynolds number. The dynamics is highly nonlinear and depends on the details of the reconnection in the current sheet: When a single large plasmoid is formed in the current sheet, rapid instability can be avoided. This was the case in the three intermediate resistivity cases for the core-envelope configuration considered here. Also the original Lundquist tubes showed a rapid reconnection flare of $v_{\rm r} \simeq 0.6c$. The reason is the sign change of the B^z component, leading to vanishing guide field and a missing restoring force in the current sheet. As guide field with opposite polarity builds up in the current sheet thereafter, the fast reconnection is quickly stalled.

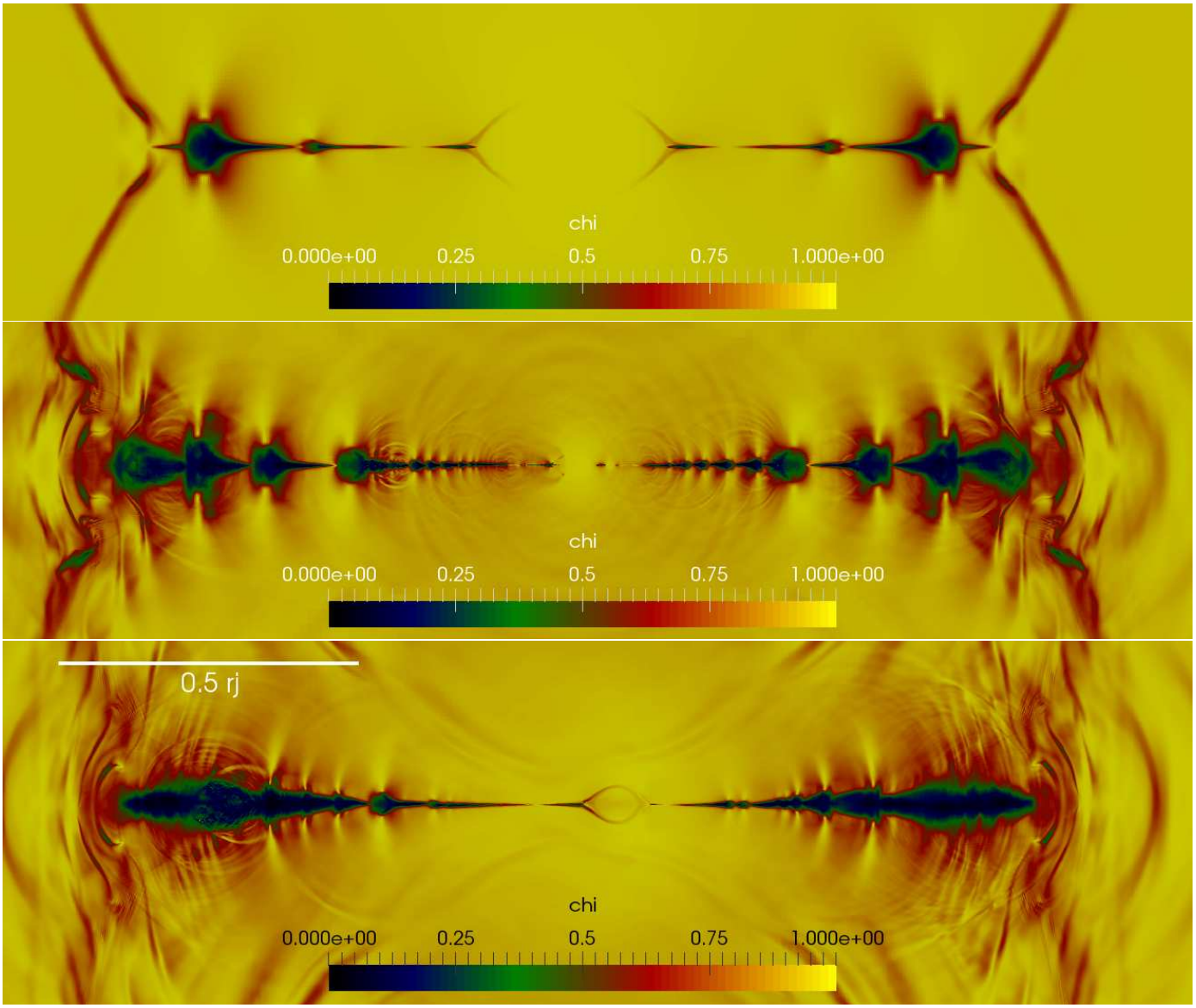

Fig. 63.— Merger of 2D core-envelope flux tubes. Comparison of χ in the central region for the two highest conductivity cases at the time of the reconnection flare at $t = 5$: $\eta_{||} = 1/4000$ (top) and $\eta_{||} = 1/8000$ (middle). One can clearly see the different qualitative behaviour: In the former case, a single large plasmoid grows in the centre of the current sheet, in the latter case, instead small scale plasmoids are expelled in both directions. At this time, there are also clear differences in the position of the Y-point: in the high conductivity case, the Y-point is notably further out as the evolution has progressed faster. As the evolution progresses, a large connected charge starved area develops as seen in the bottom panel for $\eta_{||} = 1/8000$ at $t = 5.5 r_j/c$.

8.4. PIC simulations of 2D flux tube mergers: simulation setup

We study the evolution of 2D flux tubes with PIC simulations, employing the electromagnetic PIC code TRISTAN-MP (Buneman 1993; Spitkovsky 2005). We analyze two possible field configurations: (*i*) Lundquist magnetic ropes (see Eq. 40), containing zero total current (so, the azimuthal magnetic field vanishes at the boundaries of the rope); (*ii*) core-envelope ropes (see Eqs. 44 and 45) this configuration has nonzero total volumetric current, which is cancelled by the surface current.

Our computational domain is a rectangle in the $x-y$ plane, with periodic boundary conditions in both directions. The simulation box is initialized with a uniform density of electron-positron plasma at rest and with the magnetic field appropriate for the Lundquist or core-envelope configuration. Since the azimuthal magnetic field vanishes at the boundaries of the Lundquist ropes, the evolution is very slow. Actually, we do not see any sign of evolution up to the final time $\sim 20\,c/\,r_{\rm j}$ of our simulation of undriven Lundquist ropes. For this reason, we push by hand the two ropes toward each other, with a prescribed $v_{\rm push}$ whose effects will be investigated below. It follows that inside the ropes we start with the magnetic field in Eq. 40 and with the electric field $\mathbf{E}=-\mathbf{v}_{\rm push}\times\mathbf{B}/c$, whereas the electric field is initially zero outside the ropes.

The azimuthal magnetic field does not vanish at the boundaries of the core-envelope ropes, and the system evolves self-consistently (so, we do not need to drive the system by hand). Here, both the azimuthal field and the poloidal field are discontinuous at the boundary of the ropes. A particle current would be needed to sustain the curl of the field. In our setup, the computational particles are initialized at rest, but such electric current gets self-consistently built up within a few timesteps. To facilitate comparison with the force-free results, our core-envelope configuration has $r_{\rm m}/\,r_{\rm j}=0.5$ and $\alpha=0.2$, the same values as in the force-free simulation of Fig. 60.

For our fiducial runs, the spatial resolution is such that the plasma skin depth $c/\omega_{\rm p}$ is resolved with 2.5 cells, but we have verified that our results are the same up to a resolution of $c/\omega_{\rm p}=10$ cells. We only investigate the case of a cold background plasma, with initial thermal dispersion $kT/mc^2=10^{-4}$.[21] Each cell is initialized with two positrons and two electrons, but we have checked that our results are the same when using up to 64 particles per cell. In order to reduce noise in the simulation, we filter the electric current deposited onto the grid by the particles, mimicking the effect of a larger number of particles per cell (Spitkovsky 2005; Belyaev 2015).

Our unit of length is the radius $r_{\rm j}$ of the flux ropes, and time is measured in units of $r_{\rm j}/c$. Our domain is typically a large rectangle of size $10\,r_{\rm j}$ along x (i.e., along the direction connecting the centers of the two ropes) and of size $6\,r_{\rm j}$ along y (but we have tested that a smaller domain with $5\,r_{\rm j}\times 3\,r_{\rm j}$ gives the same results). A large domain is needed to minimize the effect of the boundary conditions on the evolution of the system.

We explore the dependence of our results on the flow magnetization. We identify our runs via the mean value $\sigma_{\rm in}$ of the magnetization measured within the flux ropes using the initial in-plane fields (so, excluding the B_z field). As we argue below, it is the dissipation of the in-plane fields that primarily drives efficient heating and particle acceleration. In addition, this choice allows for a direct comparison of our results between the two configurations (Lundquist and core-envelope) and with the ABC structures of Sect. 6.4. The mean in-plane field corresponding to $\sigma_{\rm in}$ shall be called $B_{0,\rm in}$, and it will be our unit of measure of the electromagnetic fields. We will explore a wide range of magnetizations, from $\sigma_{\rm in}=3$ up to $\sigma_{\rm in}=170$.

It will be convenient to compare the radius $r_{\rm j}$ of the ropes to the characteristic Larmor radius $r_{\rm L,hot}=\sqrt{\sigma_{\rm in}}\,c/\omega_{\rm p}$ of the high-energy particles heated/accelerated by reconnection (rather than to the skin depth $c/\omega_{\rm p}$). We will explore a

[21] For a hot background plasma, the results are expected to be the same (apart from an overall shift in the energy scale), once the skin depth and the magnetization are properly defined. We point to Sect. 6.4 for a demonstration of this claim in the context of ABC structures.

wide range of $r_j/r_{L,hot}$, from $r_j/r_{L,hot} = 31$ up to 245. We will demonstrate that the two most fundamental parameters that characterize the system are the magnetization σ_{in} and the ratio $r_j/r_{L,hot}$.

8.5. PIC simulations of 2D flux tube mergers: Lundquist ropes

The temporal evolution of the merger of two Lundquist ropes is shown in Fig. 64. The plot presents the 2D pattern of the out-of-plane field B_z (left column; in units of $B_{0,in}$) and of the in-plane magnetic energy fraction $\epsilon_{B,in} = (B_x^2+B_y^2)/8\pi nmc^2$ (right column; with superimposed magnetic field lines), from a PIC simulation with $kT/mc^2 = 10^{-4}$, $\sigma_{in} = 42$ and $r_j = 61\, r_{L,hot}$. The magnetic ropes are initially driven toward each other with a speed $v_{push}/c = 0.1$ (below, we study the dependence on the driving speed). Time is measured in units of r_j/c and indicated in the grey boxes within each panel. The figure should be compared with the force-free result in Fig. 54 (even though $vpush/c = 0.3$ in that case).

As the two magnetic ropes slowly approach, driven by the initial velocity push (compare the first and second row in Fig. 64), reconnection is triggered in the plane $x = 0$, as indicated by the formation and subsequent ejection of small-scale plasmoids (third and fourth row in Fig. 64). So far (i.e., until $ct/\,r_j \sim 4.5$), the cores of the two islands have not significantly moved (black line in the middle panel of Fig. 65, indicating the x_c location of the center of the rightmost island), the reconnection speed is quite small (red line in the middle panel of Fig. 65) and no significant energy exchange has occurred from the fields to the particles (compare the in-plane magnetic energy, shown by the dashed blue line in the top panel of Fig. 65, with the particle kinetic energy, indicated with the red line).[22] The only significant evolution before $ct/\,r_j \sim 4.5$ is the reconnection-driven increase in the maximum particle Lorentz factor up to $\gamma_{max}/\gamma_{th} \sim 40$ occurring at $ct/\,r_j \sim 2.5$ (see the black line in the bottom panel of Fig. 65).

As a result of reconnection, an increasing number of field lines, that initially closed around one of the ropes, are now engulfing both magnetic islands. Their tension force causes the two ropes to approach and merge on a quick (dynamical) timescale, starting at $ct/\,r_j \sim 4.5$ and ending at $ct/\,r_j \sim 7.5$ (see that the distance of the rightmost island from the center rapidly decreases, as indicated by the black line in the middle panel of Fig. 65). The tension force drives the particles in the flux ropes toward the center, with a fast reconnection speed peaking at $v_{rec}/c \sim 0.3$ (red line in the middle panel of Fig. 65).[23] The reconnection layer at $x = 0$ stretches up to a length of $\sim 2\, r_j$, it becomes unstable to the secondary tearing mode (Uzdensky et al. 2010), and secondary plasmoids are formed (e.g., see the plasmoid at $(x, y) \sim (0, 0)$ at $ct/\,r_j = 6$). Below, we demonstrate that the formation of secondary plasmoids is primarily controlled by the ratio $r_j/r_{L,hot}$. In the central current sheet, it is primarily the in-plane field that gets dissipated (compare the dashed and solid blue lines in the top panel of Fig. 65), driving an increase in the electric energy (green) and in the particle kinetic energy (red).[24] In this phase of evolution, the fraction of initial energy released to the particles is small ($\epsilon_{kin}/\epsilon_{tot}(0) \sim 0.1$), but the particles advected into the central X-point experience a dramatic episode of acceleration.

[22] We remark that the energy balance described in the top panel of Fig. 65 is dependent on the overall size of the box, everything else being the same. More specifically, while the in-plane fields (which are the primary source of dissipation) are nonzero only within the flux ropes, the out-of-plane field pervades the whole domain. It follows that for a larger box the relative ratios between ϵ_{kin} (red line; or ϵ_E, green line) and $\epsilon_{B,in}$ (dashed blue line) will not change, whereas they will all decrease as compared to the total magnetic energy ϵ_B (blue solid line).

[23] This value of the reconnection rate is roughly comparable to the results of solitary X-point collapse presented in Sect. 4.2. However, a direct comparison cannot be established, since in that case we either assumed a uniform nonzero guide field or a vanishing guide field, whereas here the guide field strength is not uniform in space.

[24] The out-of-plane field for the Lundquist configuration in Eq. 40 switches sign inside the flux ropes. In force free simulations, this leads to the formation of large areas with $E > B$ in the outermost regions of the ropes. We do not observe the formation of such features in PIC simulations.

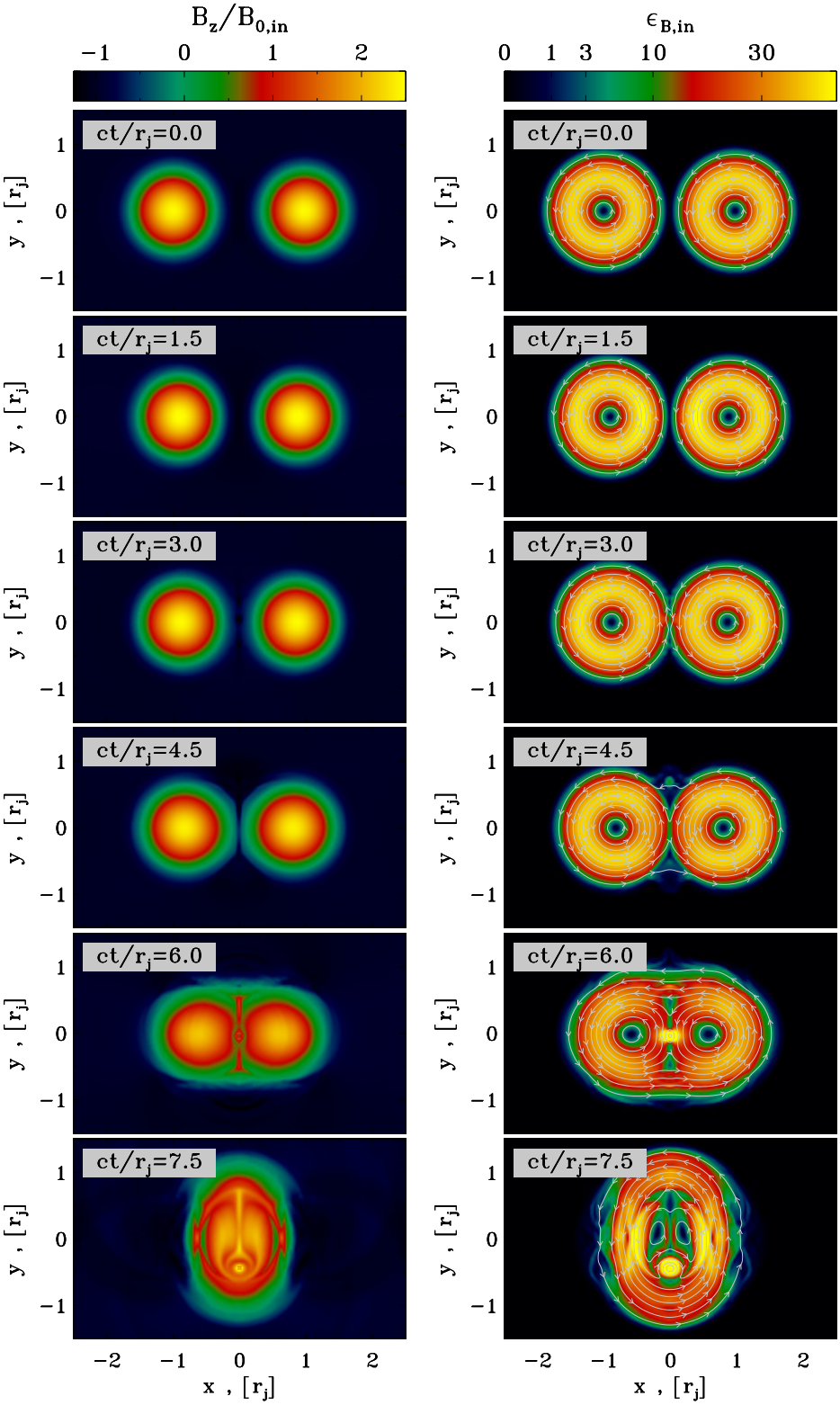

Fig. 64.— Temporal evolution of 2D Lundquist ropes (time is measured in $c/\,r_{\rm j}$ and indicated in the grey box of each panel, increasing from top to bottom). The plot presents the 2D pattern of the out-of-plane field B_z (left column; in units of $B_{0,\rm in}$) and of the in-plane magnetic energy fraction $\epsilon_{B,\rm in} = (B_x^2+B_y^2)/8\pi nmc^2$ (right column; with superimposed magnetic field lines), from a PIC simulation with $kT/mc^2 = 10^{-4}$, $\sigma_{\rm in} = 42$ and $r_{\rm j} = 61\,r_{\rm L,hot}$, performed within a rectangular domain of size $10\,r_{\rm j} \times 6\,r_{\rm j}$ (but we only show a small region around the center). The evolution is driven with a velocity $v_{\rm push}/c = 0.1$. Reconnection at the interface between the two flux ropes (i.e., around $x = y = 0$) creates an envelope of field lines engulfing the two islands, whose tension force causes them to merge on a dynamical time. This figure should be compared with the force-free result in Fig. 54 (even though $v_{\rm push}/c = 0.3$ in that case).

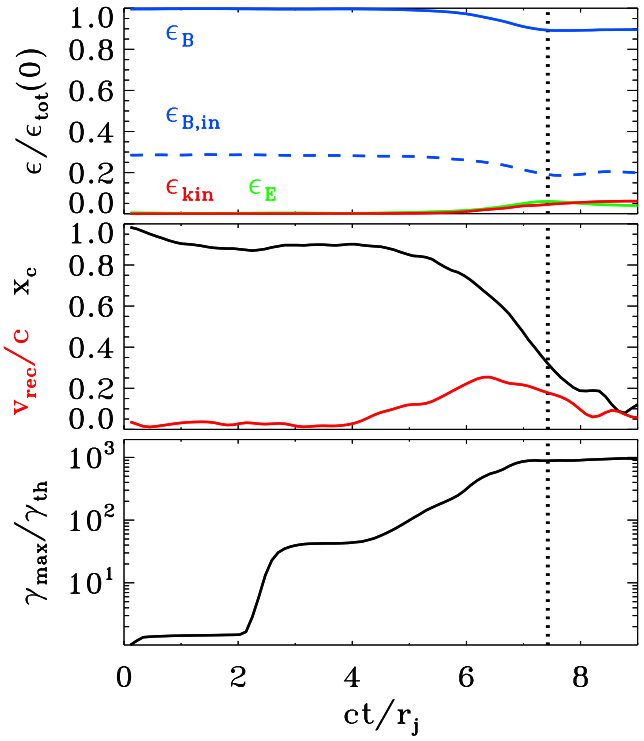

Fig. 65.— Temporal evolution of various quantities, from a 2D PIC simulation of Lundquist ropes with $kT/mc^2 = 10^{-4}$, $\sigma_{in} = 42$ and $r_j = 61\,r_{L,hot}$ (the same as in Fig. 64), performed within a rectangular domain of size $5\,r_j \times 3\,r_j$. The evolution is driven with a velocity $v_{push}/c = 0.1$. Top panel: fraction of energy in magnetic fields (solid blue), in-plane magnetic fields (dashed blue), electric fields (green) and particles (red; excluding the rest mass energy), in units of the total initial energy. Middle panel: reconnection rate v_{rec}/c (red), defined as the inflow speed along the x direction averaged over a square of side equal to r_j centered at $x = y = 0$; and location x_c of the core of the rightmost flux rope (black), in units of r_j. Bottom panel: evolution of the maximum Lorentz factor γ_{max}, as defined in Eq. (16), relative to the thermal Lorentz factor $\gamma_{th} \simeq 1 + (\hat{\gamma} - 1)^{-1} kT/mc^2$, which for our case is $\gamma_{th} \simeq 1$. In response to the initial push, γ_{max} increases at $ct/\,r_j \sim 2$ up to $\gamma_{max}/\gamma_{th} \sim 40$, before stalling. At this stage, the cores of the two islands have not significantly moved (black line in the middle panel). At $ct/\,r_j \sim 5$, the tension force of the common envelope of field lines starts pushing the two islands toward each other (and the x_c location of the rightmost rope decreases, see the middle panel), resulting in a merger event occurring on a dynamical timescale. During the merger (at $ct/\,r_j \sim 6$), the reconnection rate peaks (red line in the middle panel), a fraction of the in-plane magnetic energy is transferred to the plasma (compare dashed blue and solid red lines in the top panel), and particles are quickly accelerated up to $\gamma_{max}/\gamma_{th} \sim 10^3$ (bottom panel). In all the panels, the vertical dotted black line indicates the time when the electric energy peaks, shortly after the most violent phase of the merger event.

As shown in the bottom panel of Fig. 65, the cutoff Lorentz factor γ_{max} of the particle spectrum presents a dramatic evolution, increasing up to $\gamma_{max}/\gamma_{th} \sim 10^3$ within a couple of dynamical times. It is this phase of extremely fast particle acceleration that we associate with the generation of the Crab flares.

The two distinct evolutionary phases — the early stage driven by the initial velocity push, and the subsequent dynamical merger driven by large-scale electromagnetic stresses — are clearly apparent in the evolution of the particle

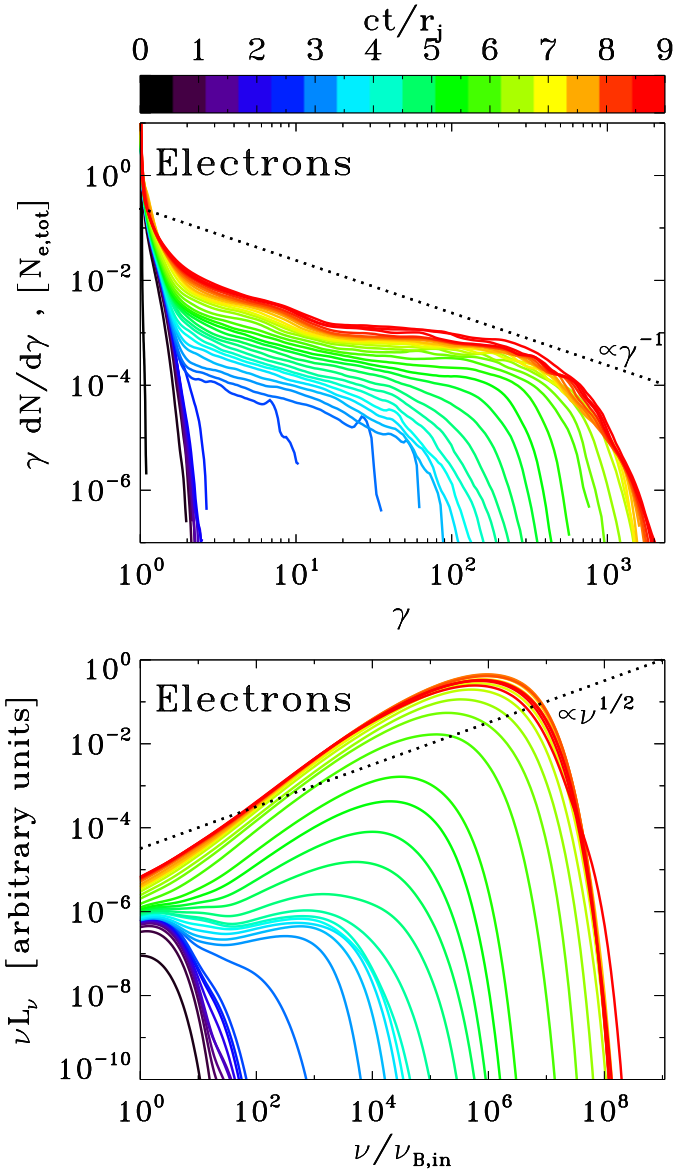

Fig. 66.— Particle energy spectrum and synchrotron spectrum from a 2D PIC simulation of Lundquist ropes with $kT/mc^2 = 10^{-4}$, $\sigma_{\rm in} = 42$ and $r_{\rm j} = 61\, r_{\rm L,hot}$ (the same as in Fig. 64 and Fig. 65), performed within a domain of size $10\, r_{\rm j} \times 6\, r_{\rm j}$. The evolution is driven with a velocity $v_{\rm push}/c = 0.1$. Time is measured in units of $r_{\rm j}/c$, see the colorbar at the top. Top panel: evolution of the electron energy spectrum normalized to the total number of electrons. At late times, the high-energy spectrum approaches a hard distribution $\gamma dN/d\gamma \propto$ const (for comparison, the dotted black line shows the case $\gamma dN/d\gamma \propto \gamma^{-1}$ corresponding to equal energy content in each decade of γ). Bottom panel: evolution of the angle-averaged synchrotron spectrum emitted by electrons. The frequency on the horizontal axis is in units of $\nu_{B,\rm in} = \sqrt{\sigma_{\rm in}}\omega_{\rm p}/2\pi$. At late times, the synchrotron spectrum approaches a power law with $\nu L_\nu \propto \nu$, which just follows from the fact that the electron spectrum at high energies is close to $\gamma dN/d\gamma \propto$ const. This is harder than the dotted line, which indicates the slope $\nu L_\nu \propto \nu^{1/2}$ resulting from an electron spectrum $\gamma dN/d\gamma \propto \gamma^{-1}$.

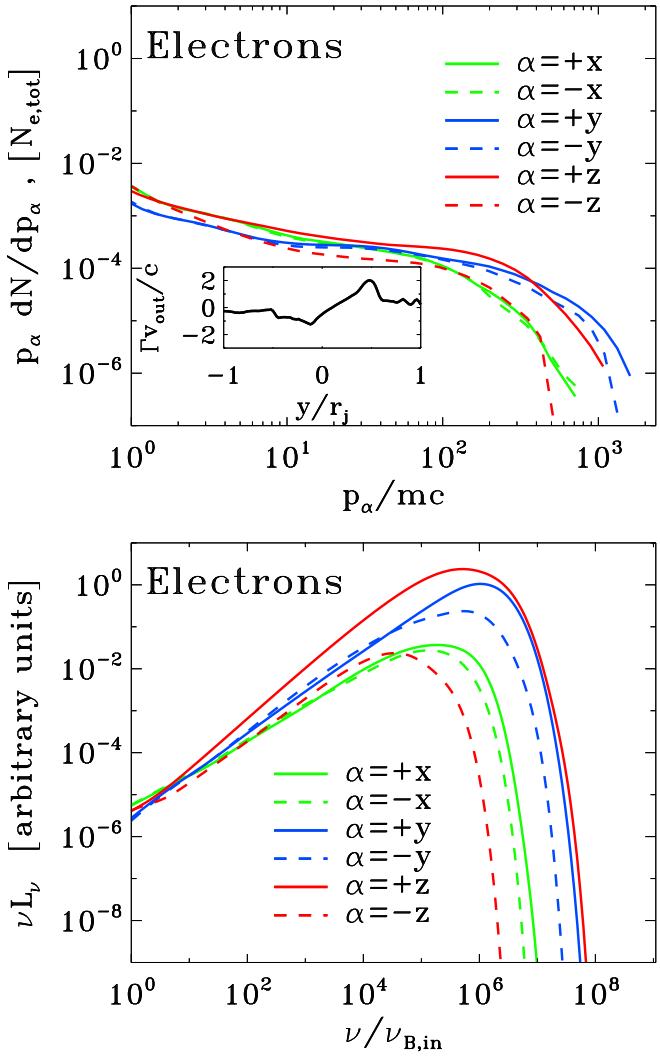

Fig. 67.— Particle momentum spectrum and anisotropy of the synchrotron emission from a 2D PIC simulation of Lundquist ropes with $kT/mc^2 = 10^{-4}$, $\sigma_{\rm in} = 42$ and $r_{\rm j} = 61\, r_{\rm L,hot}$ (the same as in Fig. 64, Fig. 65 and Fig. 66), performed within a domain of size $10\, r_{\rm j} \times 6\, r_{\rm j}$. The evolution is driven with a velocity $v_{\rm push}/c = 0.1$. Top panel: electron momentum spectrum along different directions (as indicated in the legend), at the time when the electric energy peaks (as indicated by the vertical dotted black line in Fig. 65). The highest energy electrons are beamed along the direction y of the reconnection outflow (blue lines) and along the direction $+z$ of the accelerating electric field (red solid line; positrons will be beamed along $-z$, due to the opposite charge). The inset shows the 1D profile along y of the bulk four-velocity in the outflow direction (i.e., along y), measured at $x = 0$. Bottom panel: synchrotron spectrum at the time indicated in Fig. 65 (vertical dotted black line) along different directions (within a solid angle of $\Delta\Omega/4\pi \sim 3 \times 10^{-3}$), as indicated in the legend. The resulting anisotropy of the synchrotron emission is consistent with the particle anisotropy illustrated in the top panel.

energy spectrum (top panel in Fig. 66) and of the angle-averaged synchrotron emission (bottom panel in Fig. 66). The initial velocity push drives reconnection in the central current sheet, which leads to fast particle acceleration (from dark blue to cyan in the top panel). This is only a transient event, and the particle energy spectrum then freezes (see the clustering of the cyan lines, and compare with the phase at $2.5 \lesssim ct/\,r_{\rm j} \lesssim 4$ in the bottom panel of Fig. 65). Correspondingly, the angle-averaged synchrotron spectrum stops evolving (see the clustering of the cyan lines in the bottom panel). A second dramatic increase in the particle and emission spectral cutoff (even more dramatic than the initial growth) occurs between $ct/\,r_{\rm j} \sim 4.5$ and $ct/\,r_{\rm j} \sim 7$ (cyan to yellow curves in Fig. 66), and it directly corresponds to the dynamical merger of the two magnetic ropes, driven by large-scale stresses. The particle spectrum quickly extends up to $\gamma_{\rm max} \sim 10^3$ (yellow lines in the top panel), and correspondigly the peak of the νL_ν emission spectrum shifts up to $\sim \gamma_{\rm max}^2 \nu_{B,\rm in} \sim 10^6 \nu_{B,\rm in}$ (yellow lines in the bottom panel). The system does not show any sign of evolution at times later than $c/\,r_{\rm j} \sim 7.5$ (see the clustering of the yellow to red lines). At late times, the high-energy spectrum approaches a hard distribution $\gamma dN/d\gamma \propto$ const (for comparison, the dotted black line shows the case $\gamma dN/d\gamma \propto \gamma^{-1}$ corresponding to equal energy content in each decade of γ). The synchrotron spectrum approaches a power law with $\nu L_\nu \propto \nu$, which just follows from the fact that the electron spectrum at high energies is close to $\gamma dN/d\gamma \propto$ const. This is harder than the dotted line, which indicates the slope $\nu L_\nu \propto \nu^{1/2}$ resulting from an electron spectrum $\gamma dN/d\gamma \propto \gamma^{-1}$.

The particle distribution is significantly anisotropic. In the top panel of Fig. 67, we plot the electron momentum spectrum at the time when the electric energy peaks (see the vertical black dotted line in Fig. 65) along different directions, as indicated in the legend. The highest energy electrons are beamed along the direction y of the reconnection outflow (blue lines) and along the direction $+z$ anti-parallel to the accelerating electric field (red solid line; positrons will be beamed along $-z$, due to the opposite charge). This is consistent with our results for solitary X-point collapse in Sect. 4.2. Most of the anisotropy is to be attributed to the "kinetic beaming" discussed by Cerutti et al. (2012c), rather than beaming associated with the bulk motion (which is only marginally relativistic, see the inset in the top panel of Fig. 67). The anisotropy of the synchrotron emission (bottom panel in Fig. 67) is consistent with the particle anisotropy illustrated in the inset of the top panel.

8.5.1. Dependence on the flow conditions

We now investigate the dependence of our results on the magnetization $\sigma_{\rm in}$ and the ratio $r_{\rm j}/r_{\rm L,hot}$, where $r_{\rm L,hot} = \sqrt{\sigma_{\rm in}}\, c/\omega_{\rm p}$. In Fig. 68, we present the 2D pattern of the out-of-plane field B_z (in units of $B_{0,\rm in}$) during the most violent phase of rope merger (i.e., when the electric energy peaks, as indicated by the vertical dotted lines in Fig. 69) from a suite of PIC simulations in a rectangular domain of size $5\,r_{\rm j} \times 3\,r_{\rm j}$. In the left column, we fix $kT/mc^2 = 10^{-4}$ and $\sigma_{\rm in} = 11$ and we vary the ratio $r_{\rm j}/r_{\rm L,hot}$, from 31 to 245 (from top to bottom). In the right column, we fix $kT/mc^2 = 10^{-4}$ and $r_{\rm j}/r_{\rm L,hot} = 61$ and we vary the magnetization $\sigma_{\rm in}$, from 3 to 170 (from top to bottom). The evolution is driven with a velocity $v_{\rm push}/c = 0.1$ in all the cases.

The 2D pattern of B_z presented in Fig. 68 shows that the merger proceeds in a similar way in all the runs. The only difference is that larger $r_{\rm j}/r_{\rm L,hot}$ lead to thinner current sheets, when fixing $\sigma_{\rm in}$ (left column in Fig. 68). Roughly, the thickness of the current sheet is set by the Larmor radius $r_{\rm L,hot}$ of the high-energy particles heated/accelerated by reconnection. In the right column, with $r_{\rm j}/r_{\rm L,hot}$ fixed, the thickness of the current sheet is then a fixed fraction of the box size. In contrast, in the left column, the ratio of current sheet thickness to box size will scale as $r_{\rm L,hot}/\,r_{\rm j}$, as indeed it is observed. A long thin current sheet is expected to fragment into a chain of plasmoids/magnetic islands (e.g., Uzdensky et al. 2010; Werner et al. 2016), when the length-to-thickness ratio is much larger than unity. It follows that all the cases in the right column will display a similar tendency for fragmentation (and in particular, they do not appreciably fragment), whereas the likelihood of fragmentation is expected to increase from top to bottom in the left column. In fact, for the case with $r_{\rm j}/r_{\rm L,hot} = 245$ (left bottom panel), a number of small-scale plasmoids appear in

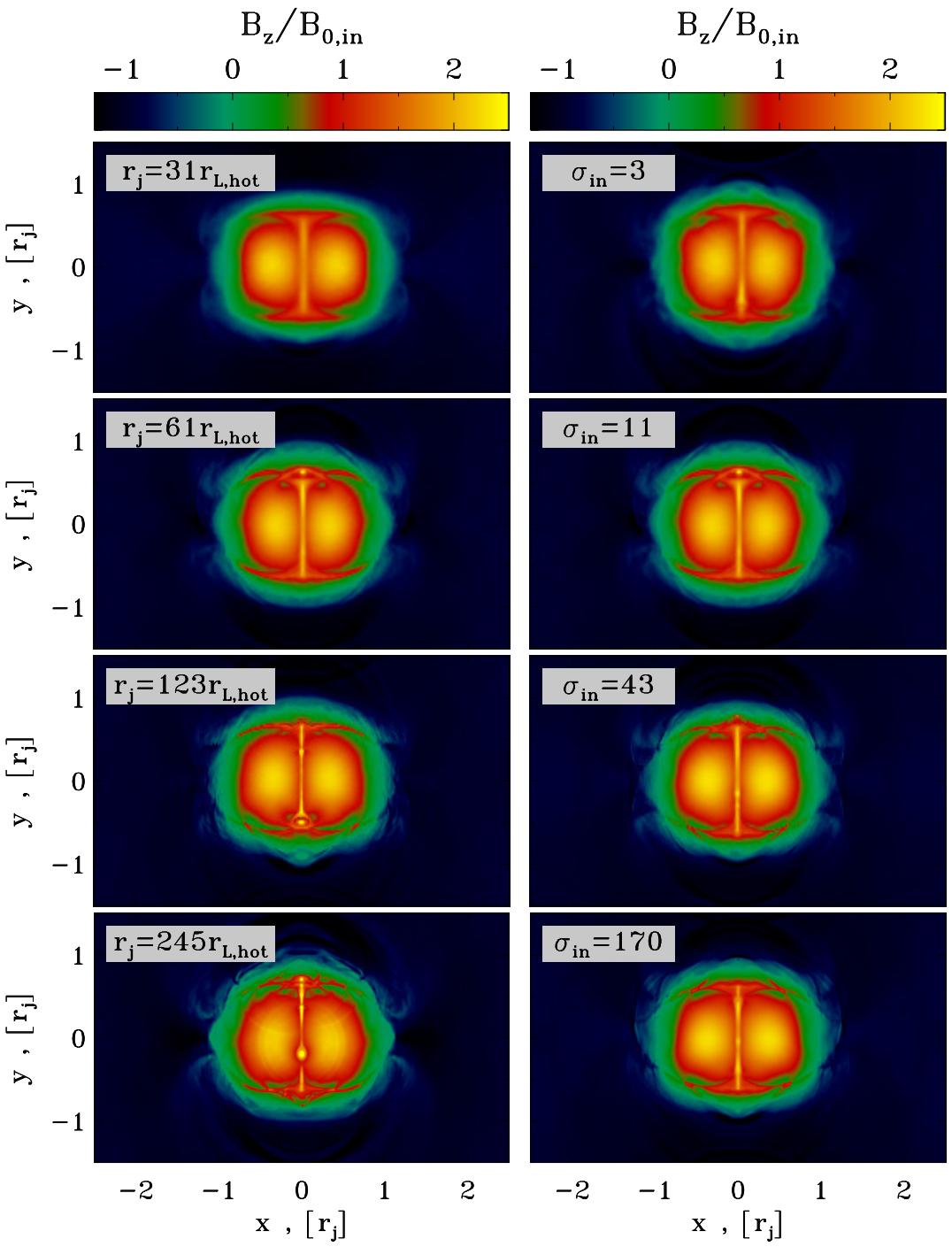

Fig. 68.— 2D pattern of the out-of-plane field B_z (in units of $B_{0,\rm in}$) at the most violent time of the merger of Lundquist ropes (i.e., when the electric energy peaks, as indicated by the vertical dotted lines in Fig. 69) from a suite of PIC simulations. The evolution is driven with a velocity $v_{\rm push}/c = 0.1$. In the left column, we fix $kT/mc^2 = 10^{-4}$ and $\sigma_{\rm in} = 11$ and we vary the ratio $r_{\rm j}/r_{\rm L,hot}$, from 31 to 245 (from top to bottom). In the right column, we fix $kT/mc^2 = 10^{-4}$ and $r_{\rm j}/r_{\rm L,hot} = 61$ and we vary the magnetization $\sigma_{\rm in}$, from 3 to 170 (from top to bottom). In all cases, the simulation box is a rectangle of size $5\,r_{\rm j} \times 3\,r_{\rm j}$. The 2D structure of B_z in all cases is quite similar, apart from the fact that larger $r_{\rm j}/r_{\rm L,hot}$ tend to lead to a more pronounced fragmentation of the current sheet.

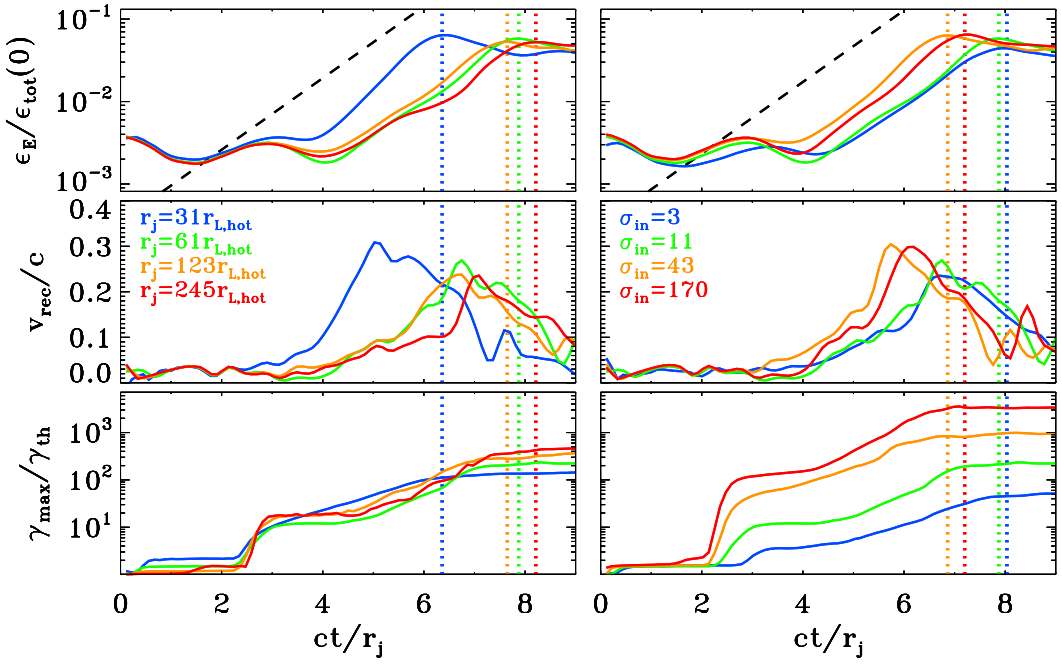

Fig. 69.— Temporal evolution of the electric energy (top panel; in units of the total initial energy), of the reconnection rate (middle panel; defined as the mean inflow velocity in a square of side r_j centered at $x = y = 0$) and of the maximum particle Lorentz factor (bottom panel; γ_{max} is defined in Eq. (16), and it is normalized to the thermal Lorentz factor $\gamma_{th} \simeq 1 + (\hat{\gamma} - 1)^{-1} kT/mc^2$), for a suite of PIC simulations of Lundquist ropes (same runs as in Fig. 68). In all the cases, the evolution is driven with a velocity $v_{push}/c = 0.1$. In the left column, we fix $kT/mc^2 = 10^{-4}$ and $\sigma_{in} = 11$ and we vary the ratio $r_j/r_{L,hot}$ from 31 to 245 (from blue to red, as indicated in the legend). In the right column, we fix $kT/mc^2 = 10^{-4}$ and $r_j/r_{L,hot} = 61$ and we vary the magnetization σ_{in} from 3 to 170 (from blue to red, as indicated in the legend). The maximum particle energy $\gamma_{max}mc^2$ resulting from the merger increases for increasing $r_j/r_{L,hot}$ at fixed σ_{in} (left column) and for increasing σ_{in} at fixed $r_j/r_{L,hot}$. The dashed black line in the top panel shows that the electric energy grows exponentially as $\propto \exp(ct/r_j)$. The vertical dotted lines mark the time when the electric energy peaks (colors as described above).

the current sheets (e.g., see the plasmoid at $x \sim 0$ and $y \sim -0.1\, r_j$ in the left bottom panel). We find that as long as $\sigma_{in} \gg 1$, the secondary tearing mode discussed by Uzdensky et al. (2010) — that leads to current sheet fragmentation — appears at $r_j/r_{L,hot} \gtrsim 100$, in the case of Lundquist ropes.[25]

In Fig. 69 we present the temporal evolution of the runs whose 2D structure is shown in Fig. 68. In the left column, we fix $kT/mc^2 = 10^{-4}$ and $\sigma_{in} = 11$ and we vary the ratio $r_j/r_{L,hot}$, from 31 to 245 (from blue to red, as indicated in the legend of the middle panel). In the right column, we fix $kT/mc^2 = 10^{-4}$ and $r_j/r_{L,hot} = 61$ and we vary the magnetization σ_{in}, from 3 to 170 (from blue to red, as indicated in the legend of the middle panel). The top panels show that the evolution of the electric energy (in units of the total initial energy) is similar for all the values of $r_j/r_{L,hot}$ and σ_{in} we explore. In particular, the electric energy grows approximately as $\propto \exp(ct/r_j)$ in all the cases (compare with the dashed black lines), and it peaks at $\sim 5\%$ of the total initial energy. The only marginal exception is the

[25] A similar result had been found for the case of ABC collapse, see Sect.6.4.

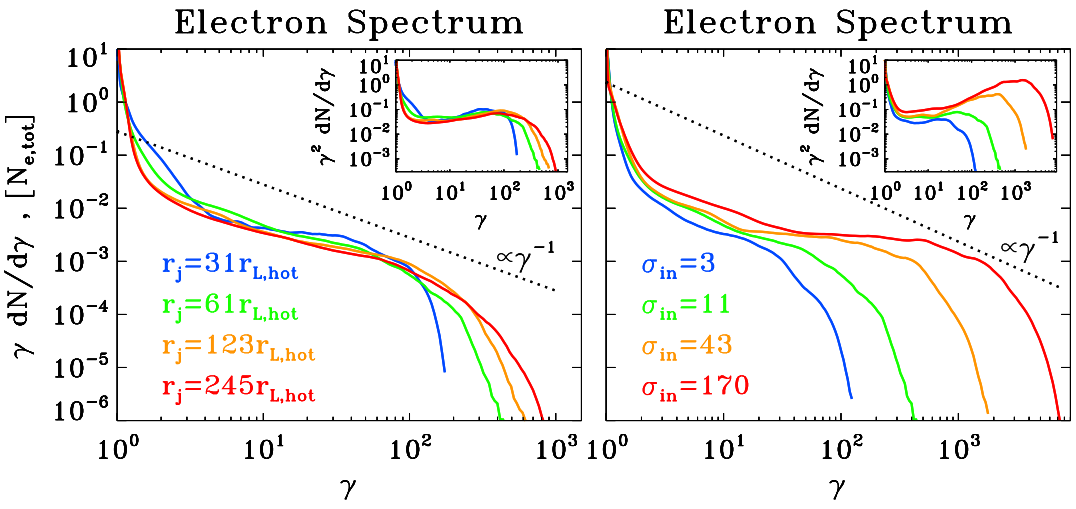

Fig. 70.— Particle spectrum at the time when the electric energy peaks, for a suite of PIC simulations of Lundquist ropes (same runs as in Fig. 68 and Fig. 69). In all the cases, the evolution is driven with a velocity $v_{\rm push}/c = 0.1$. In the left column, we fix $kT/mc^2 = 10^{-4}$ and $\sigma_{\rm in} = 11$ and we vary the ratio $r_{\rm j}/r_{\rm L,hot}$ from 31 to 245 (from blue to red, as indicated by the legend). In the right column, we fix $kT/mc^2 = 10^{-4}$ and $r_{\rm j}/r_{\rm L,hot} = 61$ and we vary the magnetization $\sigma_{\rm in}$ from 3 to 170 (from blue to red, as indicated by the legend). The main plot shows $\gamma dN/d\gamma$ to emphasize the particle content, whereas the inset presents $\gamma^2 dN/d\gamma$ to highlight the energy census. The dotted black line is a power law $\gamma dN/d\gamma \propto \gamma^{-1}$, corresponding to equal energy content per decade (which would result in a flat distribution in the insets). The spectral hardness is not a sensitive function of the ratio $r_{\rm j}/r_{\rm L,hot}$, but it is strongly dependent on $\sigma_{\rm in}$, with higher magnetizations giving harder spectra, up to the saturation slope of -1.

trans-relativistic case $\sigma_{\rm in} = 3$ and $r_{\rm j}/r_{\rm L,hot} = 61$ (blue line in the top right panel), whose peak value is slightly smaller, due to the lower Alfvén speed. The onset time of the instability is also nearly independent of $\sigma_{\rm in}$ (top right panel), although the low-magnetization cases $\sigma_{\rm in} = 3$ and 11 (blue and green lines) seem to be growing slightly later. As regard to the dependence of the onset time on $r_{\rm j}/r_{\rm L,hot}$ at fixed $\sigma_{\rm in}$, the top left panel in Fig. 69 shows that larger values of $r_{\rm j}/r_{\rm L,hot}$ tend to grow later, but the variation is only moderate (with the exception of the case with the smallest $r_{\rm j}/r_{\rm L,hot} = 31$, blue line in the top left panel, that grows quite early).

The peak reconnection rate in all the cases we have explored is around $v_{\rm rec}/c \sim 0.2 - 0.3$ (middle row in Fig. 69). It marginally decreases with increasing $r_{\rm j}/r_{\rm L,hot}$ (but we have verified that it saturates at $v_{\rm rec}/c \sim 0.25$ in the limit $r_{\rm j}/r_{\rm L,hot} \gg 1$, see the middle left panel in Fig. 69), and it moderately increases with $\sigma_{\rm in}$ (especially as we transition from the non-relativistic regime to the relativistic regime, but it saturates at $v_{\rm rec}/c \sim 0.3$ in the limit $\sigma_{\rm in} \gg 1$, see the middle right panel in Fig. 69). We had found similar values and trends for the peak reconnection rate in the case of ABC collapse, see Sect.6.4.

In the evolution of the maximum particle Lorentz factor $\gamma_{\rm max}$ (bottom row in Fig. 69), one can distinguish two phases. At early times ($ct/\,r_{\rm j} \sim 2.5$), the increase in $\gamma_{\rm max}$ is moderate, when reconnection is triggered in the central region by the initial velocity push. At later times ($ct/\,r_{\rm j} \sim 6$), as the two magnetic ropes merge on a dynamical timescale, the maximum particle Lorentz factor grows explosively. Following the same argument detailed in Sect.6.4, we estimate that the high-energy cutoff of the particle spectrum at the end of the merger event (which lasts for a few $r_{\rm j}/c$) should scale as $\gamma_{\rm max}/\gamma_{\rm th} \propto v_{\rm rec}^2 \sqrt{\sigma_{\rm in}}\, r_{\rm j} \propto v_{\rm rec}^2 \sigma_{\rm in} (\,r_{\rm j}/r_{\rm L,hot})$. If the reconnection rate does not significantly depend on $\sigma_{\rm in}$, this implies that $\gamma_{\rm max} \propto r_{\rm j}$ at fixed $\sigma_{\rm in}$. The trend for a steady increase of $\gamma_{\rm max}$ with $r_{\rm j}$ at fixed $\sigma_{\rm in}$ is confirmed in the

bottom left panel of Fig. 69, both at the final time and at the peak time of the electric energy (which is slightly different among the four different cases, see the vertical dotted colored lines).[26] Similarly, if the reconnection rate does not significantly depend on $r_j/r_{L,hot}$, this implies that $\gamma_{max} \propto \sigma_{in}$ at fixed $r_j/r_{L,hot}$. This linear dependence of γ_{max} on σ_{in} is confirmed in the bottom right panel of Fig. 69.

The dependence of the particle spectrum on $r_j/r_{L,hot}$ and σ_{in} is illustrated in Fig. 70 (left and right panel, respectively), where we present the particle energy distribution at the time when the electric energy peaks (as indicated by the colored vertical dotted lines in Fig. 69). In the main panels we plot $\gamma dN/d\gamma$, to emphasize the particle content, whereas the insets show $\gamma^2 dN/d\gamma$, to highlight the energy census. The particle spectrum shows a pronounced non-thermal component in all the cases, regardless of whether the secondary plasmoid instability is triggered or not in the current sheets (the results presented in Fig. 70 correspond to the cases displayed in Fig. 68). This suggests that in our setup any acceleration mechanism that relies on plasmoid mergers is not very important, but rather that the dominant source of energy is direct acceleration by the reconnection electric field, in analogy to what we had demonstrated for the solitary X-point collapse and the ACB instability.

At the time when the electric energy peaks, most of the particles are still in the thermal component (at $\gamma \sim 1$), i.e., bulk heating is negligible. Yet, a dramatic event of particle acceleration is taking place, with a few lucky particles accelerated much beyond the mean energy per particle $\sim \gamma_{th}\sigma_{in}/2$ (for comparison, we point out that $\gamma_{th} \sim 1$ and $\sigma_{in} = 11$ for the cases in the left panel). At fixed $\sigma_{in} = 11$ (left panel), we see that the high-energy spectral cutoff scales as $\gamma_{max} \propto r_j$ (r_j changes by a factor of two in between each pair of curves).[27] On the other hand, at fixed $r_j/r_{L,hot} = 61$ (right panel), we find that $\gamma_{max} \propto \sigma_{in}$ (σ_{in} changes by a factor of four in between each pair of curves).

The spectral hardness is primarily controlled by the average in-plane magnetization σ_{in}. The right panel in Fig. 70 shows that at fixed $r_j/r_{L,hot}$ the spectrum becomes systematically harder with increasing σ_{in}, approaching the asymptotic shape $\gamma dN/d\gamma \propto$ const found for plane-parallel steady-state reconnection in the limit of high magnetizations (Sironi & Spitkovsky 2014; Guo et al. 2015; Werner et al. 2016). At large $r_j/r_{L,hot}$, the hard spectrum of the high-σ_{in} cases will necessarily run into constraints of energy conservation (see Eq. (32)), unless the pressure feedback of the accelerated particles onto the flow structure ultimately leads to a spectral softening (in analogy to the case of cosmic ray modified shocks, see Amato & Blasi 2006). This argument seems to be supported by the left panel in Fig. 70. At fixed σ_{in}, the left panel shows that the spectral slope is nearly insensitive to $r_j/r_{L,hot}$, but larger systems seem to lead to steeper slopes, which possibly reconciles the increase in γ_{max} with the argument of energy conservation illustrated in Eq. (32).

8.5.2. Dependence on the collision speed

So far, we have investigated the merger of Lundquist flux ropes with a prescribed collision speed $v_{push}/c = 0.1$. In Figs. 71 and 72, we explore the effect of different values of the driving speed on the temporal evolution of the merger and the resulting particle spectrum, for a suite of four PIC simulations with fixed $kT/mc^2 = 10^{-4}$, $\sigma_{in} = 42$ and $r_j/r_{L,hot} = 61$, but different magnitudes of v_{push}: $v_{push}/c = 3 \times 10^{-1}$ (blue), $v_{push}/c = 10^{-1}$ (green), $v_{push}/c = 3 \times 10^{-2}$ (yellow) and $v_{push}/c = 10^{-2}$ (red).

Fig. 71 shows the evolution of the electric energy (top panel, in units of the total initial energy). The initial value of the electric energy scales as v_{push}^2, just as a consequence of the electric field $-\mathbf{v}_{push} \times \mathbf{B}/c$ that we initialize in the

[26] The fact that the dependence appears slightly sub-linear is due to the fact that the reconnection rate is slightly larger for smaller $r_j/r_{L,hot}$.

[27] The fact that the dependence is a little shallower than linear is due to the fact that the reconnection rate, which enters in the full expression $\gamma_{max} \propto v_{rec}^2 \sigma_{in}(r_j/r_{L,hot})$, slightly decreases with increasing $r_j/r_{L,hot}$, as detailed above.

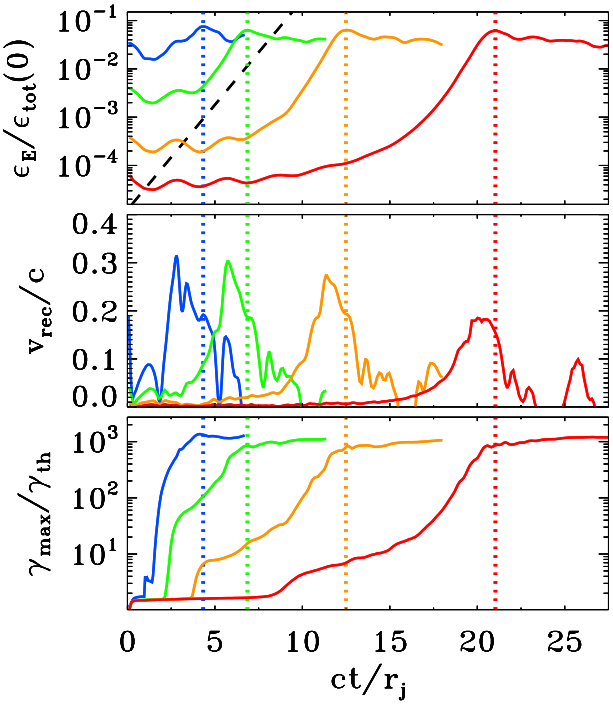

Fig. 71.— Temporal evolution of the electric energy (top panel; in units of the total initial energy), of the reconnection rate (middle panel; defined as the mean inflow velocity in a square of side r_j centered at $x = y = 0$) and of the maximum particle Lorentz factor (bottom panel; γ_{max} is defined in Eq. (16), and it is normalized to the thermal Lorentz factor $\gamma_{th} \simeq 1 + (\hat{\gamma} - 1)^{-1} kT/mc^2$), for a suite of four PIC simulations of Lundquist ropes with fixed $kT/mc^2 = 10^{-4}$, $\sigma_{in} = 42$ and $r_j/r_{L,hot} = 61$, but different magnitudes of the initial velocity: $v_{push}/c = 3 \times 10^{-1}$ (blue), $v_{push}/c = 10^{-1}$ (green), $v_{push}/c = 3 \times 10^{-2}$ (yellow) and $v_{push}/c = 10^{-2}$ (red). The dashed black line in the top panel shows that the electric energy grows exponentially as $\propto \exp(ct/r_j)$. The vertical dotted lines mark the time when the electric energy peaks (colors correspond to the four values of v_{push}/c, as described above).

magnetic ropes. However, the subsequent evolution is remarkably independent of v_{push}, apart from an overall shift in the onset time. In all the cases, the electric energy grows exponentially as $\propto \exp(ct/r_j)$ (compare with the black dashed line) until it peaks at $\sim 5 - 10\%$ of the total initial energy (the time when the electric energy peaks is indicated with the vertical colored dotted lines). The peak of electric energy corresponds to the most violent phase of merger, and it shortly follows the peak time of the reconnection rate. As shown in the middle panel, the reconnection speed peaks at $v_{rec}/c \sim 0.2 - 0.3$, with only a weak dependence on the driving speed v_{push}. Driven by fast reconnection during the dynamical merger event, the maximum particle energy γ_{max} grows explosively (bottom panel in Fig. 71), ultimately reaching $\gamma_{max}/\gamma_{th} \sim 10^3$ regardless of the initial driving speed v_{push}. The initial phase of growth of γ_{max} is sensitive to the value of v_{push}, reaching higher values for larger v_{push} (compare the plateau at $\gamma_{max}//\gamma_{th} \sim 10^2$ in the green line at $ct/r_j \sim 3$ with the corresponding plateau at $\gamma_{max}//\gamma_{th} \sim 5$ in the red line at $ct/r_j \sim 12$). In contrast, the temporal profile of γ_{max} during the merger (i.e., shortly before the time indicated by the vertical dotted lines) is nearly indentical in all the cases (apart from an overall time shift). Overall, the similarity of the different curves in Fig. 71 confirms that the evolution during the dynamical merger event is driven by self-consistent large-scale electromagnetic stresses, independently of the initial driving speed.

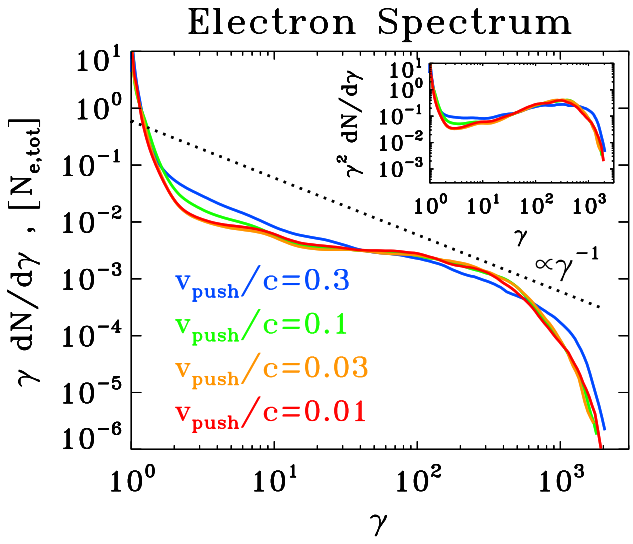

Fig. 72.— Particle spectrum at the time when the electric energy peaks, for a suite of four PIC simulations of Lundquist ropes with fixed $kT/mc^2 = 10^{-4}$, $\sigma_{\rm in} = 42$ and $r_{\rm j}/r_{\rm L,hot} = 61$, but different magnitudes of the initial velocity (same runs as in Fig. 71): $v_{\rm push}/c = 3 \times 10^{-1}$ (blue), $v_{\rm push}/c = 10^{-1}$ (green), $v_{\rm push}/c = 3 \times 10^{-2}$ (yellow) and $v_{\rm push}/c = 10^{-2}$ (red). The main plot shows $\gamma dN/d\gamma$ to emphasize the particle content, whereas the inset presents $\gamma^2 dN/d\gamma$ to highlight the energy census. The dotted black line is a power law $\gamma dN/d\gamma \propto \gamma^{-1}$, corresponding to equal energy content per decade (which would result in a flat distribution in the inset). The particle spectrum is remarkably independent from the initial $v_{\rm push}$.

As a consequence, it is not surprising that the particle spectrum measured at the time when the electric energy peaks (as indicated by the vertical colored lines in Fig. 71) bears no memory of the driving speed $v_{\rm push}$. In fact, the four curves in Fig. 72 nearly overlap (with the only marginal exception of the case with the largest $v_{\rm push}/c = 0.3$, in blue).

8.6. PIC simulations of 2D flux tube mergers: core-envelope ropes

The temporal evolution of the merger of two core-envelope ropes is shown in Fig. 73, which should be compared with the force-free result in Fig. 60. The plot presents the 2D pattern of the out-of-plane field B_z (left column; in units of $B_{0,\rm in}$) and of the in-plane magnetic energy fraction $\epsilon_{B,\rm in} = (B_x^2 + B_y^2)/8\pi nmc^2$ (right column; with superimposed magnetic field lines), from a PIC simulation with $kT/mc^2 = 10^{-4}$, $\sigma_{\rm in} = 42$ and $r_{\rm j} = 61\, r_{\rm L,hot}$. Time is measured in units of $r_{\rm j}/c$ and indicated in the grey boxes within each panel.

For the core-envelope geometry, the initial in-plane magnetic field is discontinuous at the interface $x = 0$ between the two magnetic ropes. There, magnetic reconnection spontaneously starts since early times (in contrast to the case of Lundquist ropes, where the system needs to be driven by hand with a prescribed velocity push). The ongoing steady-state reconnection is manifested in Fig. 73 by the formation and subsequent ejection of small-scale plasmoids, as the current sheet at $x = 0$ stretches up to a length $\sim 2\, r_{\rm j}$. So far (i.e., until $ct/\, r_{\rm j} \sim 2$), the cores of the two islands have not significantly moved (black line in the middle panel of Fig. 74, indicating the $x_{\rm c}$ location of the center of the rightmost island), the reconnection speed is small (around $v_{\rm rec}/c \sim 0.1$, red line in the middle panel of Fig. 74) and no significant energy exchange has occurred from the fields to the particles (compare the in-plane magnetic energy, shown by the

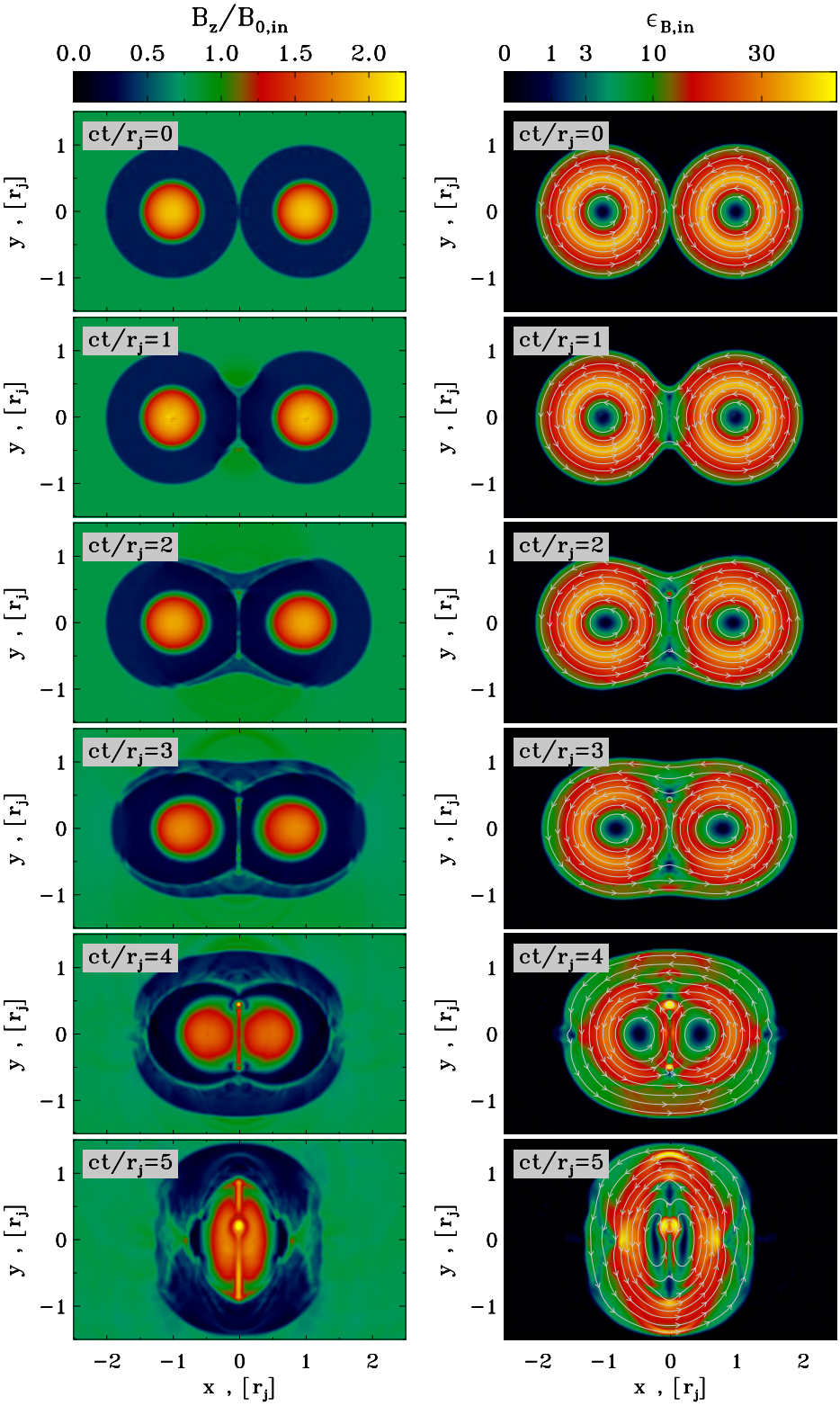

Fig. 73.— Temporal evolution of 2D core-envelope ropes (time is measured in $c/\,r_{\rm j}$ and indicated in the grey box of each panel, increasing from top to bottom). The plot presents the 2D pattern of the out-of-plane field B_z (left column; in units of $B_{0,\rm in}$) and of the in-plane magnetic energy fraction $\epsilon_{B,\rm in} = (B_x^2+B_y^2)/8\pi nmc^2$ (right column; with superimposed magnetic field lines), from a PIC simulation with $kT/mc^2 = 10^{-4}$, $\sigma_{\rm in} = 42$ and $r_{\rm j} = 61\,r_{\rm L,hot}$, performed within a rectangular domain of size $10\,r_{\rm j} \times 6\,r_{\rm j}$ (but we only show a small region around the center). Spontaneous reconnection at the interface between the two flux ropes (i.e., around $x = y = 0$) creates an envelope of field lines engulfing the two islands, whose tension force causes them to merge on a dynamical time. This figure should be compared with the force-free result in Fig. 60.

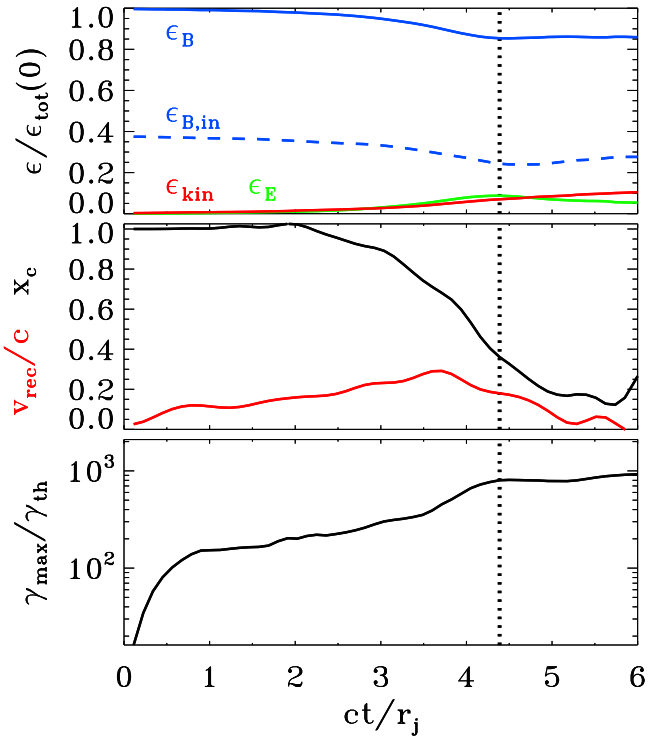

Fig. 74.— Temporal evolution of various quantities, from a 2D PIC simulation of core-envelope ropes with $kT/mc^2 = 10^{-4}$, $\sigma_{\rm in} = 42$ and $r_{\rm j} = 61\, r_{\rm L,hot}$ (the same as in Fig. 73), performed within a rectangular domain of size $5\, r_{\rm j} \times 3\, r_{\rm j}$. Top panel: fraction of energy in magnetic fields (solid blue), in-plane magnetic fields (dashed blue), electric fields (green) and particles (red; excluding the rest mass energy), in units of the total initial energy. Middle panel: reconnection rate $v_{\rm rec}/c$ (red), defined as the inflow speed along the x direction averaged over a square of side equal to $r_{\rm j}$ centered at $x = y = 0$; and location $x_{\rm c}$ of the core of the rightmost flux rope (black), in units of $r_{\rm j}$. Bottom panel: evolution of the maximum Lorentz factor $\gamma_{\rm max}$, as defined in Eq. (16), relative to the thermal Lorentz factor $\gamma_{\rm th} \simeq 1 + (\hat{\gamma} - 1)^{-1} kT/mc^2$, which for our case is $\gamma_{\rm th} \simeq 1$. Spontaneous reconnection at the interface between the two islands drives the early increase in $\gamma_{\rm max}$ up to $\gamma_{\rm max}/\gamma_{\rm th} \sim 20$, before stalling. At this stage, the cores of the two islands have not significantly moved (black line in the middle panel). At $ct/\, r_{\rm j} \sim 3$, the tension force of the common envelope of field lines starts pushing the two islands toward each other (and the $x_{\rm c}$ location of the rightmost rope decreases, see the middle panel), resulting in a merger event occurring on a dynamical timescale. During the merger (at $ct/\, r_{\rm j} \sim 4$), the reconnection rate peaks (red line in the middle panel), a fraction of the in-plane magnetic energy is transferred to the plasma (compare dashed blue and solid red lines in the top panel), and particles are quickly accelerated up to $\gamma_{\rm max}/\gamma_{\rm th} \sim 10^3$ (bottom panel). In all the panels, the vertical dotted black line indicates the time when the electric energy peaks, shortly after the most violent phase of the merger event.

dashed blue line in the top panel of Fig. 74, with the particle kinetic energy, indicated with the red line).[28] The only

[28] As we have also pointed out for the case of Lundquist ropes, we remark that the energy balance described in the top panel of Fig. 74 is dependent on the overall size of the box, everything else being the same. More specifically, for a larger box the relative ratios between $\epsilon_{\rm kin}$ (red line; or $\epsilon_{\rm E}$, green line) and $\epsilon_{B,\rm in}$ (dashed blue line) will not change, whereas they will all decrease as compared to the total magnetic energy ϵ_B (blue solid line).

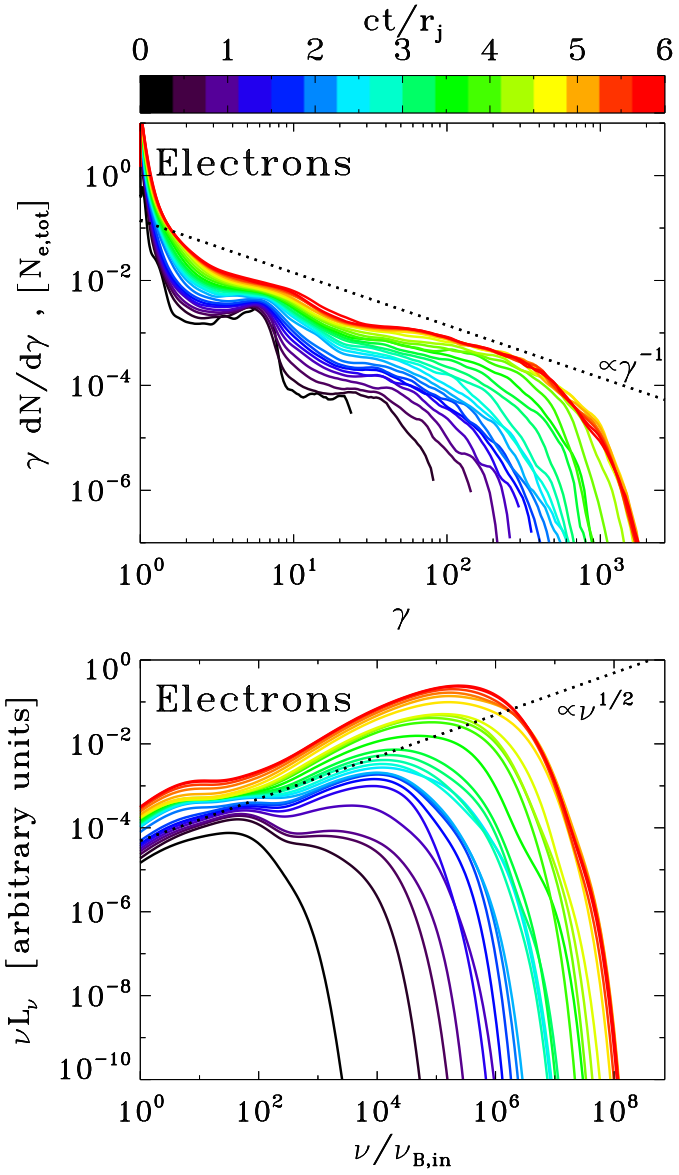

Fig. 75.— Particle energy spectrum and synchrotron spectrum from a 2D PIC simulation of core-envelope ropes with $kT/mc^2 = 10^{-4}$, $\sigma_{\rm in} = 42$ and $r_{\rm j} = 61\,r_{\rm L,hot}$ (the same as in Fig. 73 and Fig. 74), performed within a domain of size $10\,r_{\rm j} \times 6\,r_{\rm j}$. Time is measured in units of $r_{\rm j}/c$, see the colorbar at the top. Top panel: evolution of the electron energy spectrum normalized to the total number of electrons. At late times, the high-energy spectrum approaches a distribution with $\gamma dN/d\gamma \propto \gamma^{-1}$, corresponding to equal energy content in each decade of γ (compare with the dotted black line). Bottom panel: evolution of the angle-averaged synchrotron spectrum emitted by electrons. The frequency on the horizontal axis is in units of $\nu_{B,\rm in} = \sqrt{\sigma_{\rm in}}\omega_{\rm p}/2\pi$. At late times, the synchrotron spectrum approaches a power law with $\nu L_\nu \propto \nu^{1/2}$ (compare with the dotted black line), as expected from an electron spectrum $\gamma dN/d\gamma \propto \gamma^{-1}$.

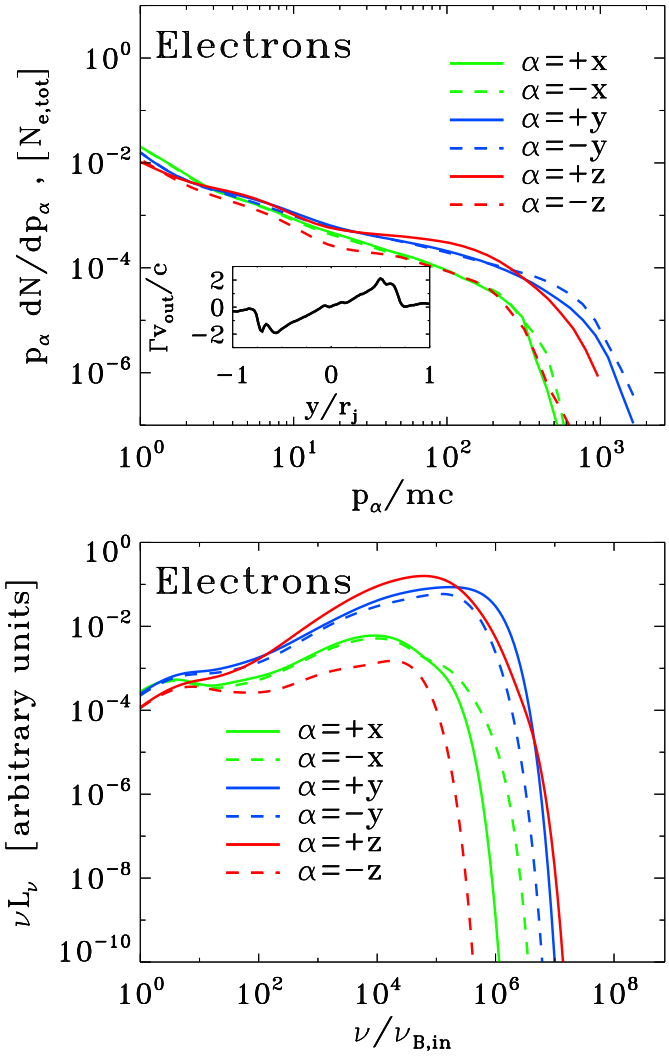

Fig. 76.— Particle momentum spectrum and anisotropy of the synchrotron emission from a 2D PIC simulation of core-envelope ropes with $kT/mc^2 = 10^{-4}$, $\sigma_{\rm in} = 42$ and $r_{\rm j} = 61\, r_{\rm L,hot}$ (the same as in Fig. 73, Fig. 74 and Fig. 75), performed within a domain of size $10\, r_{\rm j} \times 6\, r_{\rm j}$. Top panel: electron momentum spectrum along different directions (as indicated in the legend), at the time when the electric energy peaks (as indicated by the vertical dotted black line in Fig. 74). The highest energy electrons are beamed along the direction y of the reconnection outflow (blue lines) and along the direction $+z$ of the accelerating electric field (red solid line; positrons will be beamed along $-z$, due to the opposite charge). The inset shows the 1D profile along y of the bulk four-velocity in the outflow direction (i.e., along y), measured at $x = 0$. Bottom panel: synchrotron spectrum at the time indicated in Fig. 74 (vertical dotted black line) along different directions (within a solid angle of $\Delta\Omega/4\pi \sim 3 \times 10^{-3}$), as indicated in the legend. The resulting anisotropy of the synchrotron emission is consistent with the particle anisotropy illustrated in the top panel.

significant evolution before $ct/r_j \sim 2$ is the reconnection-driven increase in the maximum particle Lorentz factor up to $\gamma_{max}/\gamma_{th} \sim 150$ occurring at $ct/r_j \sim 0.5$ (see the black line in the bottom panel of Fig. 74).

As a result of reconnection, an increasing number of field lines, that initially closed around one of the ropes, are now forming a common envelope around both magnetic islands. In analogy to the case of Lundquist ropes, the magnetic tension force causes the two islands to approach and merge on a quick (dynamical) timescale, starting at $ct/r_j \sim 3$ and ending at $ct/r_j \sim 5$ (see that the distance of the rightmost island from the center rapidly decreases, as indicated by the black line in the middle panel of Fig. 74). The tension force drives the particles in the flux ropes toward the center, with a fast reconnection speed peaking at $v_{rec}/c \sim 0.3$ (red line in the middle panel of Fig. 74).[29] In the reconnection layer at $x = 0$, it is primarily the in-plane field that gets dissipated (compare the dashed and solid blue lines in the top panel of Fig. 74), driving an increase in the electric energy (green) and in the particle kinetic energy (red). In this phase of evolution, the fraction of initial energy released to the particles is small ($\epsilon_{kin}/\epsilon_{tot}(0) \sim 0.1$), but the particles advected into the central X-point experience a dramatic episode of acceleration. As shown in the bottom panel of Fig. 74, the cutoff Lorentz factor γ_{max} of the particle spectrum presents a dramatic evolution, increasing up to $\gamma_{max}/\gamma_{th} \sim 10^3$ within a couple of dynamical times. It is this phase of extremely fast particle acceleration that we associate with the generation of the Crab flares.

The two distinct evolutionary phases — the early stage governed by steady-state reconnection at the central current sheet, and the subsequent dynamical merger driven by large-scale electromagnetic stresses — are clearly apparent in the evolution of the particle energy spectrum (top panel in Fig. 75) and of the angle-averaged synchrotron emission (bottom panel in Fig. 75). Steady-state reconnection in the central current sheet leads to fast particle acceleration at early times (from black to light blue in the top panel).[30] The particle energy spectrum then freezes (see the clustering of the light blue and cyan lines, and compare with the phase at $1 \lesssim ct/r_j \lesssim 2.5$ in the bottom panel of Fig. 74). Correspondingly, the angle-averaged synchrotron spectrum stops evolving (see the clustering of the light blue and cyan lines in the bottom panel). A second dramatic increase in the particle and emission spectral cutoff (even more dramatic than the initial growth) occurs between $ct/r_j \sim 3.5$ and $ct/r_j \sim 4.5$ (green to yellow curves in Fig. 75), and it directly corresponds to the dynamical merger of the two magnetic ropes, driven by large-scale stresses. The particle spectrum quickly extends up to $\gamma_{max} \sim 10^3$ (yellow lines in the top panel), and correspondigly the peak of the νL_ν emission spectrum shifts up to $\sim \gamma_{max}^2 \nu_{B,in} \sim 10^6 \nu_{B,in}$ (yellow lines in the bottom panel). The system does not show any sign of evolution at times later than $c/r_j \sim 5$ (see the clustering of the yellow to red lines). At late times, the high-energy spectrum approaches a distribution of the form $\gamma dN/d\gamma \propto \gamma^{-1}$ corresponding to equal energy content in each decade of γ (compare with the dotted black line in the top panel). Consequently, the synchrotron spectrum approaches a power law with $\nu L_\nu \propto \nu^{1/2}$ (compare with the dotted black line in the bottom panel).

The particle distribution is significantly anisotropic. In the top panel of Fig. 76, we plot the electron momentum spectrum at the time when the electric energy peaks (see the vertical black dotted line in Fig. 74) along different directions, as indicated in the legend. The highest energy electrons are beamed along the direction y of the reconnection outflow (blue lines) and along the direction $+z$ anti-parallel to the accelerating electric field (red solid line; positrons will be beamed along $-z$, due to the opposite charge). This is consistent with our results for solitary X-point collapse in Sect. 4.2 and for merger of Lundquist ropes presented above. Most of the anisotropy is to be attributed to the "kinetic beaming" discussed by Cerutti et al. (2012c), rather than beaming associated with the bulk motion (which is only

[29] This value of the reconnection rate is roughly comparable to the results of Lundquist ropes.

[30] We point out that the spectral bump at $\gamma \sim 5 \sim 0.5\sigma_{in}$, which is apparent since early times and later evolves up to $\gamma \sim 10$, is an artifact of the core-envelope solution. In this geometry, both the azimuthal field and the poloidal field are discontinuous at the boundary of the ropes. The discontinuity has to be sustained by the particles (everywhere around each rope), via their pressure and electric current. The system self-consistently builds up the pressure and current by energizing a few particles, thereby producing the bump at $\gamma \sim 5$.

marginally relativistic, see the inset in the top panel of Fig. 76). The anisotropy of the synchrotron emission (bottom panel in Fig. 76) is consistent with the particle anisotropy illustrated in the top panel.

8.6.1. Dependence on the flow conditions

We now investigate the dependence of our results on the magnetization $\sigma_{\rm in}$ and the ratio $r_{\rm j}/r_{\rm L,hot}$, where $r_{\rm L,hot} = \sqrt{\sigma_{\rm in}}\, c/\omega_{\rm p}$. In Fig. 68, we present the 2D pattern of the out-of-plane field B_z (in units of $B_{0,\rm in}$) during the most violent phase of rope merger (i.e., when the electric energy peaks, as indicated by the vertical dotted lines in Fig. 78) from a suite of PIC simulations in a rectangular domain of size $5\,r_{\rm j} \times 3\,r_{\rm j}$. In the left column, we fix $kT/mc^2 = 10^{-4}$ and $\sigma_{\rm in} = 11$ and we vary the ratio $r_{\rm j}/r_{\rm L,hot}$, from 31 to 245 (from top to bottom). In the right column, we fix $kT/mc^2 = 10^{-4}$ and $r_{\rm j}/r_{\rm L,hot} = 61$ and we vary the magnetization $\sigma_{\rm in}$, from 3 to 170 (from top to bottom).

The 2D pattern of B_z presented in Fig. 77 shows that the merger proceeds in a similar way in all the runs. The only difference is that larger $r_{\rm j}/r_{\rm L,hot}$ lead to thinner current sheets, when fixing $\sigma_{\rm in}$ (left column in Fig. 77). In the right column, with $r_{\rm j}/r_{\rm L,hot}$ fixed, the thickness of the current sheet ($\sim r_{\rm L,hot}$) is a fixed fraction of the box size. In contrast, in the left column, the ratio of current sheet thickness to box size will scale as $r_{\rm L,hot}/\,r_{\rm j}$, as indeed it is observed. The tendency for fragmentation into secondary plasmoids is known to be an increasing function of the length-to-thickness ratio (e.g., Uzdensky et al. 2010; Werner et al. 2016). It follows that all the cases in the right column will display a similar tendency for fragmentation (and in particular, they do not appreciably fragment), whereas the likelihood of fragmentation is expected to increase from top to bottom in the left column. In fact, for the case with $r_{\rm j}/r_{\rm L,hot} = 245$ (left bottom panel), a number of small-scale plasmoids appear in the current sheets. We find that as long as $\sigma_{\rm in} \gg 1$, the secondary tearing mode discussed by Uzdensky et al. (2010) — that leads to current sheet fragmentation — appears at $r_{\rm j}/r_{\rm L,hot} \gtrsim 100$, in the case of core-envelope ropes.[31]

In Fig. 78 we present the temporal evolution of the runs whose 2D structure is shown in Fig. 77. In the left column, we fix $kT/mc^2 = 10^{-4}$ and $\sigma_{\rm in} = 11$ and we vary the ratio $r_{\rm j}/r_{\rm L,hot}$, from 31 to 245 (from blue to red, as indicated in the legend of the middle panel). In the right column, we fix $kT/mc^2 = 10^{-4}$ and $r_{\rm j}/r_{\rm L,hot} = 61$ and we vary the magnetization $\sigma_{\rm in}$, from 3 to 170 (from blue to red, as indicated in the legend of the middle panel). The top panels show that the evolution of the electric energy (in units of the total initial energy) is similar for all the values of $r_{\rm j}/r_{\rm L,hot}$ and $\sigma_{\rm in}$ we explore. In particular, the electric energy grows approximately as $\propto \exp\left(ct/\,r_{\rm j}\right)$ in all the cases (compare with the dashed black lines), and it peaks at $\sim 5-10\%$ of the total initial energy. The onset time of the instability is also nearly independent of $\sigma_{\rm in}$ (top right panel). As regard to the dependence of the onset time on $r_{\rm j}/r_{\rm L,hot}$ at fixed $\sigma_{\rm in}$, the top left panel in Fig. 78 shows that larger values of $r_{\rm j}/r_{\rm L,hot}$ tend to grow later, but the variation is only moderate.

The peak reconnection rate in all the cases we have explored is around $v_{\rm rec}/c \sim 0.2-0.3$ (middle row in Fig. 78). It is nearly insensitive to $\sigma_{\rm in}$ (middle right panel in Fig. 78) and it marginally decreases with increasing $r_{\rm j}/r_{\rm L,hot}$ (but we have verified that it saturates at $v_{\rm rec}/c \sim 0.25$ in the limit $r_{\rm j}/r_{\rm L,hot} \gg 1$, see the middle left panel). We had found similar values and trends for the peak reconnection rate in the case of ABC collapse, see Sect.6.4, and in the merger of Lundquist ropes. This places our results on solid footing, since our main conclusions do not depend on the specific properties of a given field geometry.

In the evolution of the maximum particle Lorentz factor $\gamma_{\rm max}$ (bottom row in Fig. 78), one can distinguish two phases. At early times ($ct/\,r_{\rm j} \sim 3$), the increase in $\gamma_{\rm max}$ is moderate, when reconnection proceeds in a steady state fashion in the central region. At later times ($ct/\,r_{\rm j} \sim 4.5$), as the two magnetic ropes merge on a dynamical timescale,

[31] A similar result had been found for the case of ABC collapse, see Sect.6.4, and for the merger of Lundquist ropes.

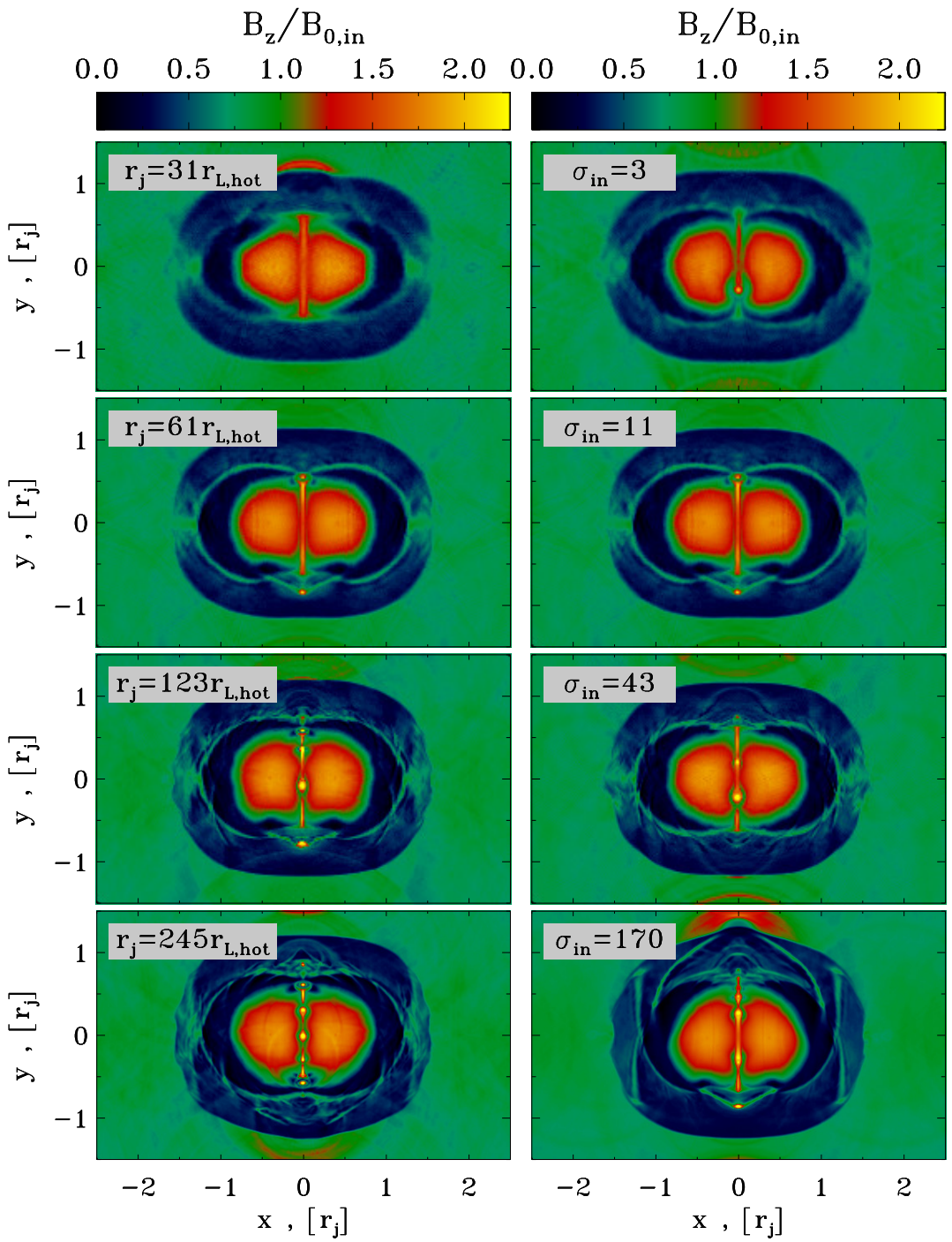

Fig. 77.— 2D pattern of the out-of-plane field B_z (in units of $B_{0,\rm in}$) at the most violent time of the merger of core-envelope ropes (i.e., when the electric energy peaks, as indicated by the vertical dotted lines in Fig. 78) from a suite of PIC simulations. In the left column, we fix $kT/mc^2 = 10^{-4}$ and $\sigma_{\rm in} = 11$ and we vary the ratio $r_{\rm j}/r_{\rm L,hot}$, from 31 to 245 (from top to bottom). In the right column, we fix $kT/mc^2 = 10^{-4}$ and $r_{\rm j}/r_{\rm L,hot} = 61$ and we vary the magnetization $\sigma_{\rm in}$, from 3 to 170 (from top to bottom). In all cases, the simulation box is a rectangle of size $5\,r_{\rm j} \times 3\,r_{\rm j}$. The 2D structure of B_z in all cases is quite similar, apart from the fact that larger $r_{\rm j}/r_{\rm L,hot}$ tend to lead to a more pronounced fragmentation of the current sheet.

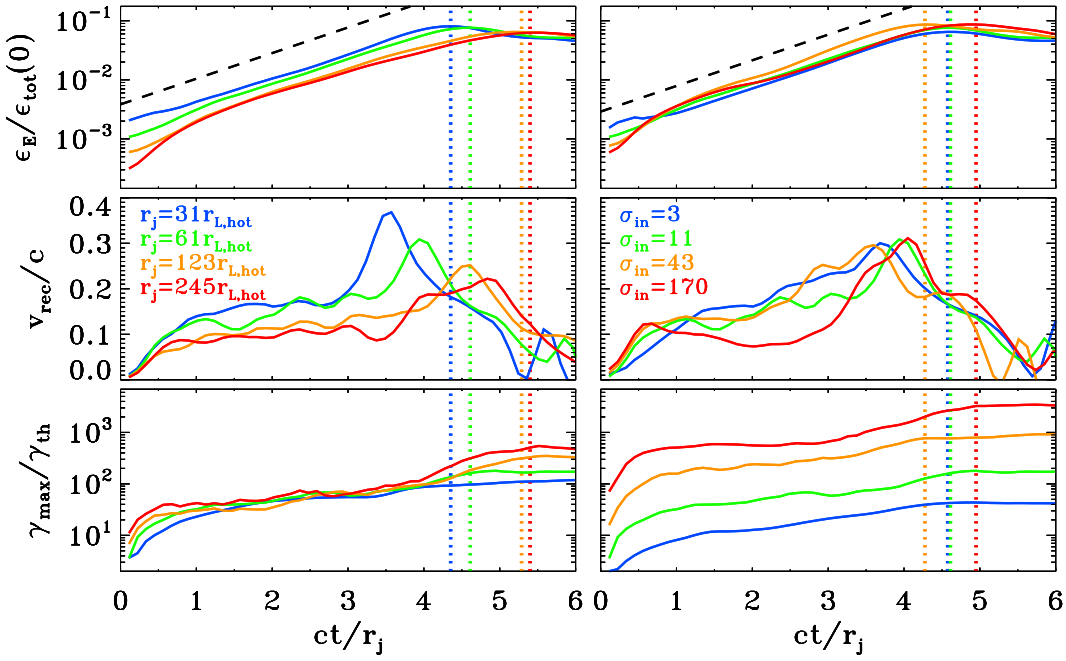

Fig. 78.— Temporal evolution of the electric energy (top panel; in units of the total initial energy), of the reconnection rate (middle panel; defined as the mean inflow velocity in a square of side r_j centered at $x = y = 0$) and of the maximum particle Lorentz factor (bottom panel; γ_{max} is defined in Eq. (16), and it is normalized to the thermal Lorentz factor $\gamma_{th} \simeq 1 + (\hat{\gamma} - 1)^{-1} kT/mc^2$), for a suite of PIC simulations of core-envelope ropes (same runs as in Fig. 77). In the left column, we fix $kT/mc^2 = 10^{-4}$ and $\sigma_{in} = 11$ and we vary the ratio $r_j/r_{L,hot}$ from 31 to 245 (from blue to red, as indicated in the legend). In the right column, we fix $kT/mc^2 = 10^{-4}$ and $r_j/r_{L,hot} = 61$ and we vary the magnetization σ_{in} from 3 to 170 (from blue to red, as indicated in the legend). The maximum particle energy $\gamma_{max}mc^2$ resulting from the merger increases for increasing $r_j/r_{L,hot}$ at fixed σ_{in} (left column) and for increasing σ_{in} at fixed $r_j/r_{L,hot}$. The dashed black line in the top panel shows that the electric energy grows exponentially as $\propto \exp(ct/r_j)$. The vertical dotted lines mark the time when the electric energy peaks (colors as described above).

the maximum particle Lorentz factor grows explosively. Following the same argument detailed in Sect.6.4 for the ABC instability, we estimate that the high-energy cutoff of the particle spectrum at the end of the merger event (which lasts for a few r_j/c) should scale as $\gamma_{max}/\gamma_{th} \propto v_{rec}^2 \sqrt{\sigma_{in}}\, r_j \propto v_{rec}^2 \sigma_{in} (r_j/r_{L,hot})$. If the reconnection rate does not significantly depend on σ_{in}, this implies that $\gamma_{max} \propto r_j$ at fixed σ_{in}. The trend for a steady increase of γ_{max} with r_j at fixed σ_{in} is confirmed in the bottom left panel of Fig. 78, both at the final time and at the peak time of the electric energy (which is slightly different among the four different cases, see the vertical dotted colored lines).[32] Similarly, if the reconnection rate does not significantly depend on $r_j/r_{L,hot}$, this implies that $\gamma_{max} \propto \sigma_{in}$ at fixed $r_j/r_{L,hot}$. This linear dependence of γ_{max} on σ_{in} is confirmed in the bottom right panel of Fig. 78. Once again, these conclusions parallel closely our findings for the instability of ABC structures and the merger of Lundquist ropes.

The dependence of the particle spectrum on $r_j/r_{L,hot}$ and σ_{in} is illustrated in Fig. 79 (left and right panel, respectively), where we present the particle energy distribution at the time when the electric energy peaks (as indicated by

[32]The fact that the dependence appears slightly sub-linear is due to the fact that the reconnection rate is slightly larger for smaller $r_j/r_{L,hot}$.

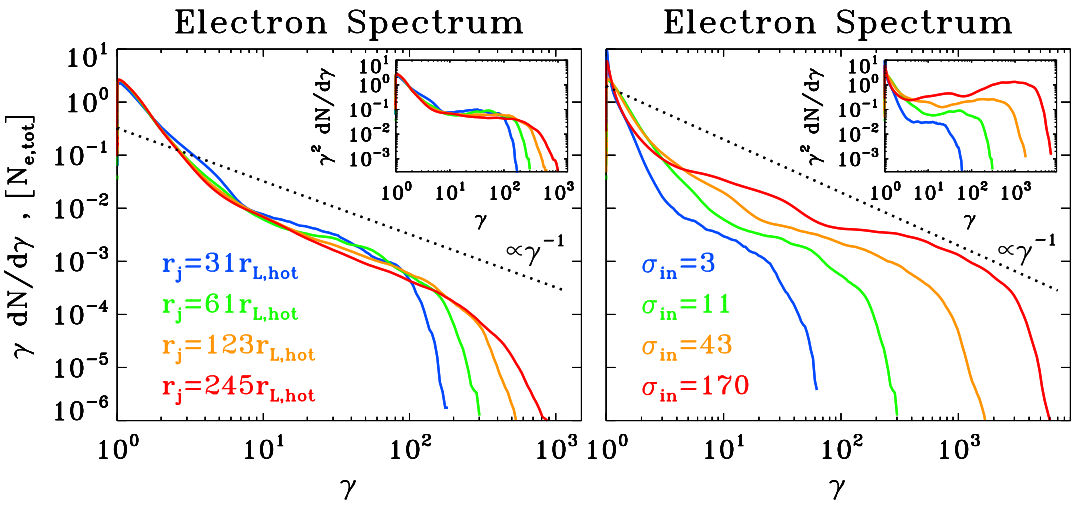

Fig. 79.— Particle spectrum at the time when the electric energy peaks, for a suite of PIC simulations of core-envelope ropes (same runs as in Fig. 77 and Fig. 78). In the left column, we fix $kT/mc^2 = 10^{-4}$ and $\sigma_{\rm in} = 11$ and we vary the ratio $r_{\rm j}/r_{\rm L,hot}$ from 31 to 245 (from blue to red, as indicated by the legend). In the right column, we fix $kT/mc^2 = 10^{-4}$ and $r_{\rm j}/r_{\rm L,hot} = 61$ and we vary the magnetization $\sigma_{\rm in}$ from 3 to 170 (from blue to red, as indicated by the legend). The main plot shows $\gamma dN/d\gamma$ to emphasize the particle content, whereas the inset presents $\gamma^2 dN/d\gamma$ to highlight the energy census. The dotted black line is a power law $\gamma dN/d\gamma \propto \gamma^{-1}$, corresponding to equal energy content per decade (which would result in a flat distribution in the insets). The spectral hardness is not a sensitive function of the ratio $r_{\rm j}/r_{\rm L,hot}$, but it is strongly dependent on $\sigma_{\rm in}$, with higher magnetizations giving harder spectra, up to the saturation slope of -1.

the colored vertical dotted lines in Fig. 78). In the main panels we plot $\gamma dN/d\gamma$, to emphasize the particle content, whereas the insets show $\gamma^2 dN/d\gamma$, to highlight the energy census.

At the time when the electric energy peaks, most of the particles are still in the thermal component (at $\gamma \sim 1$), i.e., bulk heating is negligible.[33] Yet, a dramatic event of particle acceleration is taking place, and the particle spectrum shows a pronounced non-thermal component, with a few lucky particles accelerated much beyond the mean energy per particle $\sim \gamma_{\rm th}\sigma_{\rm in}/2$ (for comparison, we point out that $\gamma_{\rm th} \sim 1$ and $\sigma_{\rm in} = 11$ for the cases in the left panel). The spectral hardness is primarily controlled by the average in-plane magnetization $\sigma_{\rm in}$. The right panel in Fig. 79 shows that at fixed $r_{\rm j}/r_{\rm L,hot}$ the spectrum becomes systematically harder with increasing $\sigma_{\rm in}$, approaching the asymptotic shape $\gamma dN/d\gamma \propto$ const found for plane-parallel steady-state reconnection in the limit of high magnetizations (Sironi & Spitkovsky 2014; Guo et al. 2015; Werner et al. 2016). At large $r_{\rm j}/r_{\rm L,hot}$, the hard spectrum of the high-$\sigma_{\rm in}$ cases will necessarily run into constraints of energy conservation (see Eq. (32)), unless the pressure feedback of the accelerated particles onto the flow structure ultimately leads to a spectral softening (in analogy to the case of cosmic ray modified shocks, see Amato & Blasi 2006). This argument seems to be supported by the left panel in Fig. 79. At fixed $\sigma_{\rm in}$, the left panel shows that larger systems (i.e., larger $r_{\rm j}/r_{\rm L,hot}$) lead to systematically steeper slopes, which possibly reconciles the increase in $\gamma_{\rm max}$ with the argument of energy conservation illustrated in Eq. (32).

In application to the GeV flares of the Crab Nebula, which we attribute to the dynamical phase of rope merger

[33] As we have explained above, the low-energy bump at $\gamma \sim \sigma_{\rm in}/2$ visible in the yellow and red curves on the right panel of Fig. 79 is due to hot particles at the boundaries of the ropes, where the initial fields are sharply discontinuous.

(either Lundquist ropes or core-envelope ropes), we envision an optimal value of $\sigma_{\rm in}$ between ~ 10 and ~ 100. Based on our results, smaller $\sigma_{\rm in} \lesssim 10$ would correspond to smaller reconnection speeds (in units of the speed of light), and so weaker accelerating electric fields. On the other hand, $\sigma_{\rm in} \gtrsim 100$ would give hard spectra with slopes $s < 2$, which would prohibit particle acceleration up to $\gamma_{\rm max} \gg \gamma_{\rm th}$ without violating energy conservation (for the sake of simplicity, here we ignore the potential spectral softening at high $\sigma_{\rm in}$ and large $r_{\rm j}/r_{\rm L,hot}$ discussed above).

8.7. Merger of two flux tubes: conclusion

In this section we have conducted a number of numerical simulations of merging flux tubes with zero poloidal current. The key difference between this case and the 2D ABC structures, §6, is that two zero-current flux tubes immersed either in external magnetic field or external plasma represent a stable configuration, in contrast with the unstable 2D ABC structures. Two barely touching flux tubes, basically, do not evolve - there is no large scale stresses that force the islands to merge. When the two flux tubes are pushed together, the initial evolution depends on the transient character of the initial conditions.

In all the different configurations that we investigated the evolution proceeded according to the similar scenario: initially, perturbation lead to the reconnection of outer field lines and the formation of common envelope. This initial stage of the merger proceeds very slowly, driven by resistive effects. With time the envelope grew in size and a common magnetic envelope develops around the cores. The dynamics changes when the two cores of the flux tube (which carry parallel currents) come into contact. Starting this moment the evolution of the two merging cores resembles the evolution of the current-carrying flux tubes in the case of 2D ABC structures: the cores start to merge explosively and, similarly, later balanced by the forming current sheet. *Similar to the 2D ABC case, the fastest rate of particle acceleration occurs at this moment of fast dynamic merger.*

Thus, in the second stage of the flux tubes merger the dynamics is determined mostly by the properties of the cores, and not the details of the initial conditions (*e.g.,* how flux tubes are pushed together). Also, particle acceleration proceeds here in a qualitatively similar way as in the case of 2D ABC structure - this is expected since the cores of merging flux tubes do carry parallel currents that attract, similar to the 2D ABC case.

9. The model of Crab Nebula flares

Based on the above discussion we develop a model of Crab flares that satisfies the following criteria: (i) particle acceleration should proceed very fast, with the accelerating electric field of the order of the magnetic field; (ii) reconnection region is macroscopically large, not related to the plasma microscopic parameters like the skin depth; (iii) only a relatively small number of particles are accelerated to the full potential available within the acceleration region (otherwise $\gamma \leq \sigma_w$). These are three very demanding criteria.

9.1. Available potential in the wind

Let us first give order-of-magnitude estimates of the overall size and the location of the flare emission region. Taking the variability time scale of $\tau_f \sim 1$ day (Tavani et al. 2011; Abdo et al. 2011) as representative of the size of the emission region, we can estimate the distance of the emission region from the pulsar based on the measured parameters of the Crab pulsar and this variability time scale.

The magnetic field in the wind (Michel 1973) scales as (below we use basic order-of-magnitude estimates, for more detailed discussion see, *e.g.,* Bogovalov 1999; Tchekhovskoy et al. 2016)

$$B = \frac{B_{NS} R_{NS}^3 \Omega^2}{c^2 r} \sin\theta \tag{47}$$

where subscript NS refers to values on the pulsar and θ is the polar angle. The total wind power (spindown power) is

$$\dot{E} = \frac{2}{3} B^2 r^2 c = \frac{2}{3} \frac{B_{NS}^2 R_{NS}^6 \Omega^4}{c^3} \tag{48}$$

At polar angle θ the potential in the wind with respect to the axis is

$$\Phi(\theta) = \sqrt{6\dot{E}/c} \sin^2\theta/2 \tag{49}$$

If the emission region is located between two flux surfaces θ_1 and θ_2, the value of potential difference $\Delta\Phi = \Phi(\theta_2) - \Phi(\theta_1)$ can be used to estimate the maximal accelerating potential within the region. For radial flow the potential difference between two magnetic flux surfaces is independent of the distance from pulsar – we can use the scaling of the potential (49) to estimate the angular extent of the emission region as seen from the pulsar. For Crab pulsar with $\dot{E} = 4 \times 10^{38}$ erg s $^{-1}$ a particle passing through a potential from the axis up to polar angle θ would be accelerated to

$$\gamma_{\max}(\theta) = \gamma_{\max} \sin^2\theta/2, \; \gamma_{\max} = \frac{\sqrt{6\dot{E}}e}{m_e c^{5/2}} = 1.6 \times 10^{11} \tag{50}$$

An important parameter is the wind magnetization Kennel & Coroniti (1984),

$$\sigma_w = \dot{E}/(\gamma_w \dot{N} m_e c^2) = 1.5 \times 10^3 \gamma_{w,4}^{-1} \lambda_4^{-1}. \tag{51}$$

where $\dot{N}$ is the total rate of particle production by the pulsar, parametrized by the multiplicity λ:

$$\dot{N} = \lambda \frac{B_{NS} R_{NS}^3 \Omega^2}{2c} = 6 \times 10^{37} \, \lambda_4 \, \mathrm{s}^{-1} \tag{52}$$

where γ_w is the wind Lorentz factor.

The potential (49) is not easily accessible for the particles advected with the wind - in order to get accelerated a particle needs to cross between different magnetic flux surfaces. To do this, the wind first needs to be decelerated to non-relativistic velocities (otherwise a causally connected region has only a small fraction of the total potential, of the order $1/\gamma_w$), and, second non-ideal process should allow a particle to cross the flux surfaces. The flow deceleration occurs at the oblique termination shock and subsequent evolution flow evolution (Komissarov & Lyubarsky 2003; Porth et al. 2014a). As we discuss next, the post-shock flow evolution leads to natural formation of highly magnetized regions in the bulk of the nebula (see §2 for the discussion of corresponding large scale simulations)

9.2. Post-shock flow - formation of highly magnetized regions

To understand the formation of highly magnetized regions starting with only mildly magnetized conditions at the reverse shock, Fig. 1, let us consider the post oblique shock evolution of the wind. Let the wind magnetization be $\sigma_w \gtrsim 1$, Eq. (51), and wind Lorentz factor $\gamma_w \gg 1$. Let us consider evolution of plasma magnetization in the post-shock flow. Magnetization first changes at the shock. As a guide we can use solutions for the normal shocks (Kennel & Coroniti 1984) - in oblique relativistic shocks the compression ratio differs considerably from that of the normal shock only for very small angles of attack (see, *e.g.,* Fig. A2 of Lyutikov et al. 2016). In the $\sigma_w \gg 1$ case the post-shock magnetization parameter, defined in terms of the ratio of the magnetic energy to plasma enthalpy, is $\sigma = 2\sigma_w$, while typical thermal Lorentz factor is $\gamma_T \approx \gamma_w/(8\sqrt{\sigma_w})$ (Kennel & Coroniti 1984; Pétri & Lyubarsky 2007b). Note, that magnetization increases at the shock - σ is the measure of the ratio of the magnetic energy density to plasma energy density in the flow frame; in a highly magnetized strong shock the rest-frame magnetic field increases due to flow deceleration (observer-frame magnetic field remains nearly the same). This increase if rest-frame magnetic field over-compensates the dissipated part of the magnetic energy. At the same time the post-shock Lorentz factor is $\gamma_2 \sim \sqrt{\sigma_w}/\sin\delta_1$, where $\delta_1 \sim 0.1 - 0.5$ is the angle of attack. This value can reach $\sim$ tens for $\sigma_w \geq 100$; as a conservative lower limit let us use $\gamma_2 \geq 10$.

As a highly relativistic, $\gamma_2 \gg 1$ flow propagates into the nebula, it is decelerated by the nebular material. As long as it remains relativistic, the flow remains nearly radial (also, for $\sigma \gg 1$ the deflection angle at the shock is small Lyutikov et al. 2012, 2016). As a result of deceleration the magnetic field is further amplified within the nebula (the Cranfill effect Cranfill 1974), leading to formation of high-σ regions even for mild pre-shock magnetization.

The increased magnetization regions within the nebula are clearly seen in numerical simulations. For example, in Fig. 1 we show plasma magnetization in simulations of Porth et al. (2014a). A high σ region originates from smaller σ parts of the wind (in the simulations that part of the wind has $\sigma_w = 3$), then σ gets amplified at the shock, and later on it gets even more amplified in the bulk. At the same time the bulk Lorentz factor decreases, while the flow trajectory becomes substantially non-radial. Thus, *creation of highly magnetized regions, even starting from mildly magnetized flows, is a natural consequence of flow evolution within the nebula.*

Guided by the results of the numerical simulations (which used mild magnetization and wind Lorentz factors Porth et al. 2013), we can estimate the general behavior of the post-shock flow. Simulations show that, approximately, in doubling the radius, the flow decelerates from highly relativistic post-shock value, $\gamma_2 \gg 1$, to a non-relativistic one $v/c \sim 0.1$, while the enthalpy drops by a factor of a few. This must results in a huge increase of the rest-frame magnetic field and plasma magnetization, as we discuss next. From the induction equation $B\Gamma r v \approx$ constant for quasi-stationary radial flow, the magnetic field B_f in the flare region can be estimated as

$$B_f \approx \left(\frac{r_s}{r_f}\right)\left(\frac{c}{v_f}\right)\Gamma_2 B_2 \tag{53}$$

where r_s is a shock radius along a given flow line, B_2 is a value of the magnetic field at the shock, Γ_2 is the immediate

post-shock Lorentz factor; B_f, r_f, v_f are evaluated in the flare region. Since $r_f/r_s \sim 2$, while $\Gamma_2 \approx \sqrt{\sigma_w}/\delta_1 \gg 1$ and $c/v_f \sim$ few, we find that the rest-frame magnetic field in the flare region may *exceeds* the values at the shock. At the same time, density (from $\rho\Gamma r^2 v \approx$ constant) is

$$\rho_f \approx \left(\frac{r_s}{r_f}\right)^2 \left(\frac{c}{v_f}\right) \Gamma_2 \rho_s. \tag{54}$$

For relativistic fluid with adiabatic index of 4/3 the magnetization in the flare region is then related to the magnetization at the shock σ_2 and in the wind σ_w as

$$\sigma_f = \left(\frac{r_f}{r_s}\right)^{2/3} \left(\frac{c}{v_f}\right)^{2/3} \Gamma_2^{2/3} \sigma_2 \tag{55}$$

(here σ is defined as the ratio of two times the magnetic energy to enthalpy, assuming highly relativistic EoS). All factors in Eq. (55) in front of the shock magnetization parameter σ_2 are larger than unity, thus $\sigma_f \gg \sigma_2$. Thus, even for $\sigma_w \sim$ few, there is strong amplification of σ right at the shock (by as much as a factor of 2, $\sigma_2 \sim 2\sigma_w$), and then another amplification in the bulk, $\sigma_f \gg \sigma_2$.

Based on the above discussion, we expect that in the post-shock flow the magnetization may increase by a large value. Though the above considerations are approximate, and neglect a number of important details (most importantly, the development of non-radial and non-axisymmetric velocity field), the expected effect - a large growth of the magnetization, is huge. Thus, we conclude that highly magnetized structures are naturally formed in the post-shock flow.

9.3. Relativistic boosting of the emission

The emission resulting in the Crab flares needs to be relativistically boosted by a factor of a few. The main argument in favor of the relativistic bulk motion of the emitters is the fact that the peak energy of flares, 400 MeVs, exceeds by a factor of a few the absolute synchrotron limit, Eq. (1). (In this context, Clausen-Brown & Lyutikov (2012) discussed a flare model based on the idea of randomly oriented mini-jets - flares' emission is beamed by relativistically moving emission sites. A strong increase in the observed flux is seen only when the beaming is directed towards the observer.) Cerutti et al. (2012b,c) discussed a related effect: directed acceleration of the particles along the neutral current sheet – kinetic beaming. As we discuss next, bulk motion of the emitting plasma is important not only for the high spectral peak of the flare emission, but also to account for the energy budget of flares, see §9.4 and Eq. (62).

Our simulations also show the effect of kinetic beaming - the highest energy particles are highly anisotropic, *e.g.*, in X-point collapse (§4.2.4 and Fig. 20) and flux tube mergers, §8.4. In case of 2D ABC structures, §6.4.2, particle isotropy is due to averaging over the simulation volume that contains many reconnection sheets (and, in some sense, an artificial consequence of the idealized ABC geometry).

As a qualitative estimate of the anisotropy of the highest energy particles we can use the scaling of the outflow Lorentz factor in a relativistic Petschek-type reconnection (Lyubarsky 2005), see also Lyutikov & Uzdensky (2003), $\Gamma \sim \sqrt{\sigma} \approx 10 - 20$ for the preferred values of the magnetization in the emission region of $\sigma = 100 - 500$. We stress that Clausen-Brown & Lyutikov (2012) used this estimate as an educated guess, while in the present study this scaling comes from the PIC simulations.

9.4. Radiation physics

Let us consider synchrotron radiation by particles moving with bulk Lorentz factor Γ with respect to the observer. (See §9.3 for the discussion of the origin of bulk motion in the nebula). To be on the conservative side, we scale the

relations to the bulk Lorentz factor of $\Gamma = 5$. Let us assume that the observed flare duration $\tau_f \sim 1$ day is limited by synchrotron losses. In the frame moving with the flow the synchrotron losses occur on time scale τ'_f (values measured int he rest frame are denoted with prime).

$$\tau'_f = \frac{9}{4}\frac{m_e^3 c^5}{e^4 B'^2 \gamma'} \tag{56}$$

where γ' is the typical Lorentz factor of the emitting particles in the flow rest frame. In the observer frame the loss time is Γ times larger, but the observed duration will be $\approx 1/(2\Gamma^2)$ shorter (assuming motion along the line of sight), so that

$$\tau_f = \frac{9}{8}\frac{m_e^3 c^5}{e^4 B'^2 \gamma' \Gamma} \tag{57}$$

Emission will peak at

$$\epsilon_2 \approx \hbar \gamma'^2 \Gamma \omega_B \tag{58}$$

Using (57-58), we find the Lorentz factor and magnetic field in the emission region

$$\gamma' \approx \left(\frac{e^2 \epsilon_2^2 \tau_f}{c^3 \hbar^2 m_e \Gamma}\right)^{1/3} = 4.8 \times 10^9 (\Gamma/5)^{-1/3}$$
$$B' \approx \left(\frac{c^9 \hbar m_e^5}{e^7 \epsilon_2 \tau_f \Gamma}\right)^{1/3} = 3.8 \times 10^{-4} (\Gamma/5)^{-1/3} \tag{59}$$

The magnetic field in the observer frame is $B = \Gamma B' = 2 \times 10^{-3} (\Gamma/5)^{2/3}$ G.

9.5. Emission region: size, location and microphysical parameters

Combining estimate of the magnetic field in the emission region (59) with the scaling in the wind, Eq. (47), we find the distance of the flare site from the pulsar:

$$r = \frac{e^{7/3}}{c^5 \hbar^{1/3} m_e^{5/3} \Gamma^{5/3}} B_{NS} \epsilon_2^{1/3} \tau_f^{2/3} \Omega^2 = 2 \times 10^{16} (\Gamma/5)^{-5/3} \mathrm{cm} \tag{60}$$

(compare with Fig. 1 - the highly magnetized region is indeed located within the nebula at distances few $\times 10^{16}$ cm). The angular size of the emission region, as seen from the pulsar, is

$$\Delta\theta \geq \frac{\gamma'}{\gamma_{max}} \sim \text{few} \times 10^{-2} (\Gamma/5)^{-1/3} \sin^{-2}\theta/2 \tag{61}$$

This implies that the emission region cannot be too close to the axis, $\theta \geq 0.3(\Gamma/5)^{-1/6}$ (otherwise, since the field is small near the axis, there is not enough potential to accelerate the particles to the needed energy).

We conclude that the emission region is located at intermediate polar angles, not too close to the axis; it occupies a size comparable to the distance to the axis. (If emission region is located new the equator, its size is about $0.05(\Gamma/5)^{-1/6}$ of the distance to the pulsar.) These estimates nicely agree with the location of highly magnetized region deduced in large scale numerical simulations, Fig. 1.

Using the estimates above, the total energy within the emitting volume is

$$E_B = (4\pi/3)\frac{B^2}{8\pi}(c\tau_f)^3 (2\Gamma^2) \sim 8 \times 10^{41} (\Gamma/5)^{10/3} erg \tag{62}$$

The factor $(2\Gamma^2)$ appears because the size of the emitting region along the line of sight (and along its motion) is larger that $c\tau_f$. This is comparable to the total observed flare energetics of $\sim 10^{41}$ erg (Tavani et al. 2011; Abdo et al. 2011). The estimate (62) is an important one: without relativistic boosting there is not enough energy within the emitting volume to power the flares - relativistic boost is needed. Even for a fairly mild boost of $\Gamma \sim 5$ the available energy budget increases by a factor $\Gamma^{10/3} \sim 200$.

We can also estimate the total number of particles producing a flare. Assuming that emission occurs in the radiation-reaction limited regime, the luminosity in the frame of the blob is

$$L' = N_{em} \frac{\gamma m_e c^2}{\tau'_f} \tag{63}$$

where N_{em} is the goal number of particles participating in the emission and $\tau'_f = 2\Gamma\tau_f$ is the flare duration in the blob's frame. The observed luminosity $L \approx (2\Gamma)^3 L'$. For the peak isotropic γ-ray luminosity of $L_\gamma \sim 10^{36}$ erg s^{-1} (Tavani et al. 2011; Abdo et al. 2011) the number of emitting particles is then

$$N_{em} = 3 \times 10^{35} L_{36} (\Gamma/5)^{-5/3} \tag{64}$$

The number of particles required to produce a flare, Eq. (64) the pulsar produces within less than a second, see Eq. (52)

We can also verify that the total number of particles within volume $(c\tau_f)^3$ is much larger that the estimate (64):

$$N_{tot} = (c\tau_f)^3 \frac{\dot{N}}{4\pi c r^2} = 4 \times 10^{40} (\Gamma/5)^{10/3} \lambda_4 \tag{65}$$

Thus, only a small fraction of particles within the emission volume needs to be accelerated to the terminal Lorentz factor.

This is an important result: only a small relative number of partciles is needed to produce a flare. If all particles within a region are accelerated, the terminal Lorentz factor is limited by the magnetization of the wind, (51), $\gamma_{max} \leq \sigma_w$. Since the required Lorentz factors of the emitting particles is $\gamma \sim 10^9$, it would then require $\sigma_w \geq 10^9$ - an unreasonable constraint.

9.6. Microphysical parameters in the emission zone: acceleration region is macroscopic

Next, let us estimate the microphysical parameters in the emission region. The key point that we would like to make is that the acceleration should occur on macroscopic scales, not related to the plasma skin depth. Since the concluding inequality is strong (Eq. 69) we neglect factors of a few.

Consider a high-σ shock (for simplicity, we neglect the effects of the angle of attack) located at radius r from the pulsar. For the wind Lorentz factor γ_w and magnetization σ_w the post-shock rest-frame density and magnetic field follow from conservation of mass flux and induction equation,

$$\begin{aligned} n'_w \gamma_w &= n_2 \sqrt{\sigma_w} \\ B'_w \gamma_w &= B_2 \sqrt{\sigma_w} \end{aligned} \tag{66}$$

where n'_w and B'_w are upstream density and magnetic field in the wind frame and we took into account that the

post-shock Lorentz factor is $\gamma_2 \approx \sqrt{\sigma_w}$. Thus,

$$n_2 \approx \frac{m_e c^2}{e^2 r^2}\frac{\gamma_{max}\lambda}{\sqrt{\sigma_w}}$$
$$B_2 \approx \frac{m_e c^2}{er}\frac{\gamma_{max}}{\sqrt{\sigma_w}} \tag{67}$$

Since the thermal post-shock Lorentz factor is $\gamma_T \approx \gamma_w/(8\sqrt{\sigma_w})$, the post-shock skin depth is

$$\delta_s = c\sqrt{\gamma_T}/\omega_{p,s} \approx \frac{r}{\lambda\sqrt{\sigma_w}} \ll r \tag{68}$$

The maximal Lorentz factor that a particle can achieve on a skin depth scale is then

$$\gamma_{s,skin} \approx e\delta_s B/(m_e c^2) \approx \frac{\gamma_{max}}{\lambda\sigma_w} \tag{69}$$

The current models of pair production in the pulsar magnetosphere predict $\lambda \sim 10^4$ (Arons & Scharlemann 1979; Daugherty & Harding 1982; Cheng et al. 2000) (the model of Crab Nebula emission require $\lambda \sim 10^6$ (Shklovsky 1970)). The typical magnetization of the pulsar wind $\sigma_w \sim 10^3 - 10^6$. Thus, *the maximal Lorentz factor that can be reached on microscopic scales, of the order of the skin depth, is much smaller than required by observations, Eq. (59), by many orders of magnitude.* (It may also be demonstrated that this conclusion does not change if we take into account the post-shock evolution of the flow.)

We conclude that *acceleration of particles producing Crab flares occurs on spacial scales many orders of magnitude larger than the plasma skin depth.* This is an important result. In our view it is inconsistent with the reconnection processes occurring during the development of the tearing mode (Cerutti et al. 2012a,c) in collisionless plasmas, since the typical scale of a current sheet that collisionless tearing mode creates is of the order of the skin depths. The size of plasmoids, at late times can reach 100s of skin depths, but the reconnection rate at those times becomes small, especially in the realistic 3D geometry (Sironi & Spitkovsky 2014).

9.7. Maximal Lorentz factor

Our PIC simulations indicate that the spectrum of the accelerated particles depend on the overall magnetization. This introduces an important constraint on the plasma parameters in the acceleration region that we discuss next.

If the spectrum of accelerated particles is soft, $p > 2$, most of the energy of the non-thermal particles is concentrated at lower energies; in this case there is no limit on the possible highest energy of a particle. Our PIC simulations indicate that $p > 2$ requires that the plasma magnetization in the emission region be not too high $\sigma \leq 100$. For higher σ the particle spectrum is hard, $p < 2$. Since magnetization increases both at the shock front and during the post-shock flow evolution, the corresponding requirement on the wind magnetization is $\sigma_w \leq 10$; this value is well below what models of particle acceleration in pulsar magnetospheres predict (Arons & Scharlemann 1979; Daugherty & Harding 1982; Cheng et al. 2000). Regions of higher magnetization will produce flatter spectra, $1 < p < 2$, so that the density is dominated by the low energy particles, while the energy is dominated by the high energy particles. Flatter spectra run into energy limitation: the maximal energy of a particle is limited from above. Assuming that the initial magnetic energy per particle (magnetization) is $\sigma/2$ and the initial typical Lorentz factor is γ_T, the maximal energy is (see Eq. (32), Sironi & Spitkovsky (2011b))

$$\gamma_{max} = \gamma_T \left(\frac{(2-p)}{2(p-1)}\right)^{1/(2-p)} \gamma_{min}^{-(p-1)/(2-p)} \sigma^{-(2-p)} \approx \gamma_T \sigma^{-1/(2-p)} \tag{70}$$

So that even for substantially hard spectrum of $p = 1.5$, $\gamma_{max} \approx \gamma_T \sigma^2$.

Let us next do the estimate of the parameters of the wind required to accelerate particles to $\gamma_{max} \sim 5 \times 10^9$. Let the wind Lorentz factor and magnetization be $\gamma_w, \sigma_w \gg 1$. Immediately after the oblique shock magnetization increases $\sigma_2 = 2\sigma_w$ while particles are heated to $\gamma_T = \gamma_w/\sqrt{\sigma_w}$. The post oblique shock bulk Lorentz factor is $\gamma_2 = \sqrt{\sigma_w}/\sin\delta_1$ ($\delta_1 \approx 0.3$ is the angle of attack). Further in the emission region σ_f is related to σ_2 by Eq. (55). Estimating $\sigma_f = \eta_f \sigma_2$, $\eta_f \gg 1$, neglecting mild adiabatic compression in the decelerating post-shock flow, and assuming power-law index $p = 3/2$ (so that $\gamma_{max} \approx \gamma_T \sigma_f^2$), we find

$$\gamma_{max} = (1/2)\gamma_w \eta_f^2 \sigma_w^{3/2} \tag{71}$$

For example for $\sigma_w = 50, \eta_f = 5, \gamma_w = 10^6$, we find $\gamma_{max} = 4.5 \times 10^9$, sufficient to explain γ-ray flares. The corresponding magnetization in the emission region is $\sigma_f = 500$. The value of σ_f is only somewhat larger our best case scenario for magnetization $\sigma \sim 100$.

Importantly, these estimates show that γ-ray flares come from parts of the wind that is not extremely highly magnetized $\sigma_w \sim 10 - 100$ (otherwise the increase of σ at the shock and further increase in the pos-shock flow would create regions with magnetization well exceeding our best case scenario, so that the resulting spectra will be hard and the maximal Lorentz factor will be low.) This value of magnetization is lower than predicted by the pair formation models (Arons & Scharlemann 1979; Daugherty & Harding 1982; Cheng et al. 2000). It is not clear whether the models underestimate the pair formation multiplicity, or if the highly magnetized sections of the wind mix downstream of the termination shock with the lower magnetized parts.

9.8. Potential-Luminosity relationship and the Alfvén current

There is important, yet somewhat subtle, relationship between the parameters of the flares that serve as a confirmation of the basic principles of our approach. Qualitatively, the electromagnetic power of relativistic outflows can be estimated as (Blandford & Znajek 1977; Blandford 2002)

$$L_{EM} \approx V^2/\mathcal{R} \tag{72}$$

where V is a typical values of the electric potential produced by the central engine and $\mathcal{R} \approx 1/c$ is the impedance of free space. In case of Crab flares, the available potential,

$$V \sim \sqrt{L/c} \approx 1.7 \times 10^{15}\,\mathrm{V}, \tag{73}$$

corresponds to $\gamma \approx 3.4 \times 10^9$ - very close to the estimate (59).

Similarly, the electric current associated with flares

$$I \approx \sqrt{Lc} \approx 5 \times 10^{22}\,\mathrm{cgs\,units} = 1.7 \times 10^{13}\,\mathrm{Ampers} \tag{74}$$

is similar to the (relativistic) Alfvén current (Alfvén 1939; Lawson 1973) for the required Lorentz factor (59):

$$I_A = \gamma \frac{m_e c^3}{e} = 1.7 \times 10^{23}, \mathrm{cgs\,units} = 6 \times 10^{13}\,\mathrm{Ampers} \tag{75}$$

This is important: the Lorentz factor that we derived from radiation modeling (from the peak energy and duration of flares) nearly coincides with the expected Lorentz factor of particles derived from the assumption that the radiated power is similar to the intrinsic electromagnetic power of flares. In a related "coincidence", the current required to

produce a given luminosity nearly coincides with the corresponding Alfvén current, calculated using the Lorentz factor of the emitting particles.

These coincidences, in our view, are not accidental: they imply that flares are produced by charge-separated flow. This is indeed expected in the acceleration models based on DC-type acceleration. This is also consistent with our PIC simulation that show effects of kinetic beaming - highly anisotropic distribution of the highest energy particles.

10. Discussion

In this paper we developed models of particle acceleration during explosive reconnection events in highly magnetized plasma and applied the results to explain the origin of Crab Nebula flares.

There is a number of important basic plasma physics results.

X-point collapse in highly magnetized plasma. We extended to the new regime, that of a highly magnetized plasma, the concept of explosive current sheet formations during catastrophic X-point collapse (Sweet 1969; Imshennik & Syrovatskiı̈ 1967; Syrovatskii 1981). Analytical results were cross-checked with force-free, MHD and PIC simulations. We find that the reconnection rates in our set-ups are typically much higher than in the plane-parallel cases due to large-scale magnetic forces. A key feature of the relativistic case is that macroscopically large regions with $E \sim B$ appear. It is in these specials regions that particles are efficiently accelerated by charge-starved electric fields(see below).

Instability of 2D magnetic ABC structures. We have studied the instability of the 2D magnetic ABC structures and identified two main instability modes (see also East et al. 2015). The instability is of the kind "parallel currents attract". (Parker 1983; Longcope & Strauss 1994, considered a similar model problem for the magnetic field structure of the Solar corona and generation of Solar flares.) We identified two stages of the instability - (i) the explosive stage, when the accelerating electric fields reach values close to the magnetic fields, but little magnetic energy is dissipated; the most important process during this stage is the X-point collapse; (ii) slower, forced reconnection stage, whereas a large fraction of the initial magnetic field energy is dissipated; at this stage the newly formed central current sheet repels the attracting currents. Though the model is highly idealized, it illustrates two important concepts: (i) that ubiquitous magnetic null lines (*e.g.,* Albright 1999) serve as sites of current sheet formation, dissipation of magnetic energy and particle acceleration; (ii) that the evolution is driven by large-scale magnetic stresses. The case of 2D ABC structures is different from the 3D ABC, which is stable (Moffatt 1986).

Triggered collapse of 2D ABC structures. We have studied a number of set-ups that greatly accelerate the development of the instability of 2D ABC structures - either by a inhomogeneous large-scale compression or by a strong fast-mode wave. Large-scale perturbations can greatly speed-up the development of instability.

Collision of magnetic flux tubes. We have discussed the merger of magnetic flux tubes carrying no net electric current. In this case the tubes first develop a common envelope via resistive evolution and then merge explosively. In comparison to two stages of the merger of current-carrying flux tubes the zero-current flux tubes have in addition a slow initial stage of development of the common envelope.

Particle acceleration: different stages. We have discussed intensively the properties of particle acceleration during the X-point collapse, during the development of the 2D ABC instability and during the merger of flux tube with zero total current. These three different set-ups allow us to concentrate on somewhat different aspects of particle acceleration. In all the cases that we investigated the efficient particle acceleration always occurs in the region with $E \geq B$ - by the charge-starved electric fields. This stage is best probed with the X-point collapse simulations. In the case of ABC structures and flux tube mergers the most efficiently particles are accelerated during the initial explosive stage; during that stage not much of magnetic energy is dissipated. In case of 2D ABC system, this initial stage of rapid acceleration is followed by a forced reconnection stage; at this stage particles are further accelerated to higher energies, but the rate of acceleration is low. In case of the colliding/merging zero-current flux tubes, the fast dynamic stage is *preceded* by the slow resistive stage, when the outer field lines form an overlaying shroud that pushes the parallel current-carrying cores together. When these parallel current-carrying cores come in contact

the evolution proceeds similarly to the unstable ABC case. We stress that *the fastest particle acceleration occurs in the beginning of the dynamical stage of the merger* (right away in the X-point collapse simulations, in the initial stage of the instability of the ABC configuration, after the slow resistive evolution in case of colliding/merging flux tubes).

Reconnection rates. The key advantage of the suggested model, if compared with the plane parallel case (that mostly invokes tearing mode Uzdensky et al. 2011; Cerutti et al. 2012a,c, 2013), is that *macroscopic large scale magnetic stresses lead to much higher reconnection rate and much faster particle acceleration.* Specifically, the dynamics stage, associated with the X-point collapse, produces exceptionally high reconnection/acceleration rates, as large as ~ 0.8; most importantly, this occurs over macroscopic spacial scales. This high acceleration rate is nearly an order of magnitude larger than is achieved in plane-parallel tearing mode-based models.

Particle acceleration: particle spectra and bulk magnetization. In all the cases we investigated the power-law slope of particle distribution depends on magnetization: higher σ produce harder spectra. The critical case of $p = 2$ corresponds approximately to $\sigma \leq 100$. For $p \geq 2$ the maximal energy that particles can achieve grows linearly with the size of the acceleration region. In the regime $100 \leq \sigma \leq 1000$ particle spectra indices are $p < 2$, yet the maximal energy can still exceed σ by orders of magnitude. For very large $\sigma \geq 10^3$ the spectrum becomes hard, $p \to 1$, so that the maximal energy is limited by $\gamma_{p,max} \leq \sigma$. For small $\sigma \leq$ few the acceleration rate becomes slow, non-relativistic (see also Werner et al. 2016).

Anisotropy of accelerated particles. In all the cases we investigated the distribution of accelerated particles, especially those with highest energy, turned out to be highly anisotropic. Since the highest energy particles have large Larmor radii, this anisotropy is kinetic; qualitatively it resembles beaming along the magnetic null line (and the direction of accelerating electric field). Importantly, this kinetic anisotropy shows on macroscopic scales.

We apply the above listed results to explain the origin of Crab Nebula γ-ray flares. Our model of Crab flares has a number of key features, that are both required by observations and/or have not been previously explored.

Acceleration mechanism. We argued that the particles producing Crab flares are accelerated in explosive magnetic reconnection events. This is, arguably, the first solidly established case in high energy astrophysics of direct acceleration in reconnection events (as opposed to shock acceleration). In addition, since in our mode the maximal energy that particles can achieve grows with the size of the acceleration region, it is possible that smaller *reconnection events are responsible for the acceleration of the majority of high-energy emitting particles in the Crab Nebula*; shock acceleration does work - producing the Crab inner knot (Lyutikov et al. 2016) - but it may be subdominant for the acceleration of high energy particles.

Location of flares. The flare-producing region is located at polar intermediate latitudes, between 10 and ~ 45 degrees, where the wind magnetization is expected to be high (the lower limit on the flare latitude comes from available required potential, Eq. (61), while upper limit comes from modeling of the Crab inner knot Lyutikov et al. (2016)). The sectors of the wind that eventually become the acceleration sites for flare particle have mild magnetization, $\sigma_w \sim 10 - 100$. Magnetization first increases at the oblique termination shock and later in the bulk, during the deceleration of the mildly relativistic post-shock flow, Fig. 1. As the flow decelerates to sub-relativistic velocities, large scale kink instabilities lead to formation of current-carrying flux tubes, Fig. 3. We hypothesize that the ensuing evolution of flux tubes is captured by our model problems considered in §6 - 8 - current-carrying flux tubes are attracted and merge explosively.

Size of the accelerating region. In our model the acceleration occurs on *macroscopic scales, not related to the plasma microscopic scales, like the skin depth.* (Previous models of reconnection in Crab flares, *e.g.,* Cerutti et al. 2012a,c,

were based on the development of the tearing mode and achieved acceleration on scale related to the skin depth - there is not enough potential on scales of few skin depths to account for Crab flares.)

Relativistic beaming motion of the flare producing region. The peak frequency of flares, the energy and the energetics of flares all require mildly relativistic "bulk" motion of the flare producing particles, with $\Gamma \sim$ few. This is achieved via "kinetic beaming", and not through a genuine, fluid-like bulk motion of the lower energy component.)

11. Implication for other high energy sources: acceleration by shocks and/or magnetic reconnection

The Crab Nebula is the paragon of the high energy astrophysical source. Understanding physical processes operating in the Crab has enormous implications for high energy astrophysics in general. Many models of Active Galactic Nuclei and Gamma Ray Bursts use the unipolar inductor paradigm - they are driven by highly magnetized rotating compact sources (*e.g.,* Blandford & Znajek 1977; Usov 1992; Lyutikov 2006b; Komissarov & Barkov 2007; Thompson et al. 2004). In case of AGN jets acceleration of particles in reconnection events, and at shocks, might play an important role in jet emission (Blandford 2002; Lyutikov 2003b; Uzdensky 2011; Sironi et al. 2015). Similarly, in case of Gamma-Ray Bursts particles might be accelerated via reconnection events (Lyutikov et al. 2003; Lyutikov 2006b). Possibly, high energy flares in AGNs as well as spikes in GRBs' profiles may resemble the flares from the Crab Nebula, as discussed by Lyutikov (2006a); Giannios et al. (2010); Clausen-Brown & Lyutikov (2012). Thus, the reconnection models developed here for the particular case of Crab Nebula might be applicable to magnetized jets of Active Galactic Nuclei and Gamma Ray Bursts.

These results further strengthen the argument that particles producing Crab flares, and possibly most of the Crab Nebula high energy emission, are accelerated via reconnection events, and not at shock via Fermi mechanisms, a major change of paradigm. Though the shock acceleration paradigm has been recently confirmed by the observations (Rudy et al. 2015b) and theoretical interpretation of the inner knot (Lyutikov et al. 2016; Yuan & Blandford 2015), the relative contribution of reconnection and shock acceleration to the overall nebular emissivity at various frequency bands remains unclear. To produce flares a very small amount of particles needs to be accelerated to the radiation reaction limit. It is possible that more ubiquitous smaller reconnection events accelerated the majority of particles producing X-ray Crab nebula emission.

We would like to thank Roger Blandford, Krzystof Nalewajko Dmitri Uzdensky and Jonathan Zrake for discussions.

The simulations were performed on XSEDE resources under contract No. TG-AST120010, and on NASA High-End Computing (HEC) resources through the NASA Advanced Supercomputing (NAS) Division at Ames Research Center. ML would like to thank for hospitality Osservatorio Astrofisico di Arcetri and Institut de Ciencies de l'Espai, where large parts of this work were conducted. This work had been supported by NASA grant NNX12AF92G and NSF grant AST-1306672. OP is supported by the ERC Synergy Grant "BlackHoleCam – Imaging the Event Horizon of Black Holes" (Grant 610058).

REFERENCES

Abdo et al. 2011, Science, 331, 739

Albright, B. J. 1999, Physics of Plasmas, 6, 4222

Alfvén, H. 1939, Physical Review, 55, 425

Amato, E. & Blasi, P. 2006, MNRAS, 371, 1251

Arnold, V. I. 1974, Proc. Summer School in Differential Equations, Erevan. Armenian SSR A d Sci.

Arons, J. & Scharlemann, E. T. 1979, ApJ, 231, 854

Bai, X.-N., Caprioli, D., Sironi, L., & Spitkovsky, A. 2015, ApJ, 809, 55

Begelman, M. C. 1998, ApJ, 493, 291

Belyaev, M. A. 2015, New A, 36, 37

Bessho, N. & Bhattacharjee, A. 2012, ApJ, 750, 129

Birdsall, C. K. & Langdon, A. B. 1991, Plasma Physics via Computer Simulation

Blandford, R. D. 2002, in Lighthouses of the Universe: The Most Luminous Celestial Objects and Their Use for Cosmology, ed. M. Gilfanov, R. Sunyeav, & E. Churazov, 381

Blandford, R. D. & Znajek, R. L. 1977, MNRAS, 179, 433

Bogovalov, S. V. 1999, A&A, 349, 1017

Buehler, R., Scargle, J. D., Blandford, R. D., Baldini, L., Baring, M. G., Belfiore, A., Charles, E., Chiang, J., D'Ammando, F., Dermer, C. D., Funk, S., Grove, J. E., Harding, A. K., Hays, E., Kerr, M., Massaro, F., Mazziotta, M. N., Romani, R. W., Saz Parkinson, P. M., Tennant, A. F., & Weisskopf, M. C. 2012, ApJ, 749, 26

Buneman, O. 1993, in "Computer Space Plasma Physics", Terra Scientific, Tokyo, 67

Cerutti, B., Uzdensky, D. A., & Begelman, M. C. 2012a, ApJ, 746, 148

—. 2012b, ApJ, 746, 148

Cerutti, B., Werner, G. R., Uzdensky, D. A., & Begelman, M. C. 2012c, ApJ, 754, L33

—. 2013, ApJ, 770, 147

—. 2014a, Physics of Plasmas, 21, 056501

—. 2014b, ApJ, 782, 104

Cheng, K. S., Ruderman, M., & Zhang, L. 2000, ApJ, 537, 964

Clausen-Brown, E. & Lyutikov, M. 2012, MNRAS, 426, 1374

Cowley, S. C. & Artun, M. 1997, Phys. Rep., 283, 185

Cranfill, C. W. 1974, Ph.D. Thesis

Daugherty, J. K. & Harding, A. K. 1982, ApJ, 252, 337

Daughton, W., Roytershteyn, V., Karimabadi, H., Yin, L., Albright, B. J., Bergen, B., & Bowers, K. J. 2011, Nature Physics, 7, 539

Del Zanna, L., Amato, E., & Bucciantini, N. 2004, A&A, 421, 1063

Deng, W., Li, H., Zhang, B., & Li, S. 2015, ApJ, 805, 163

Dungey, J. W. 1953, MNRAS, 113, 180

East, W. E., Zrake, J., Yuan, Y., & Blandford, R. D. 2015, Physical Review Letters, 115, 095002

Fisch, N. J. 1987, Reviews of Modern Physics, 59, 175

Giannios, D., Uzdensky, D. A., & Begelman, M. C. 2010, MNRAS, 402, 1649

Graf von der Pahlen, J. & Tsiklauri, D. 2014, Physics of Plasmas, 21, 012901

Green, R. M. 1965, in IAU Symposium, Vol. 22, Stellar and Solar Magnetic Fields, ed. R. Lust, 398

Gruzinov, A. 1999, ArXiv Astrophysics e-prints

Guo, F., Liu, Y.-H., Daughton, W., & Li, H. 2015, ApJ, 806, 167

Hockney, R. W. & Eastwood, J. W. 1981, Computer Simulation Using Particles

Imshennik, V. S. & Syrovatskiĭ, S. I. 1967, Soviet Journal of Experimental and Theoretical Physics, 25, 656

Kagan, D., Nakar, E., & Piran, T. 2016, ArXiv e-prints

Karimabadi, H., Roytershteyn, V., Wan, M., Matthaeus, W. H., Daughton, W., Wu, P., Shay, M., Loring, B., Borovsky, J., Leonardis, E., Chapman, S. C., & Nakamura, T. K. M. 2013, Physics of Plasmas, 20, 012303

Kennel, C. F. & Coroniti, F. V. 1984, ApJ, 283, 694

Keppens, R., Meliani, Z., van Marle, A., Delmont, P., Vlasis, A., & van der Holst, B. 2012, Journal of Computational Physics, 231, 718

Komissarov, S. S. 1999, MNRAS, 308, 1069

—. 2012, MNRAS, 422, 326

—. 2013, MNRAS, 428, 2459

Komissarov, S. S., Barkov, M., & Lyutikov, M. 2007, MNRAS, 374, 415

Komissarov, S. S. & Barkov, M. V. 2007, MNRAS, 382, 1029

Komissarov, S. S. & Lyubarsky, Y. E. 2003, MNRAS, 344, L93

—. 2004, MNRAS, 349, 779

Komissarov, S. S. & Lyutikov, M. 2011, MNRAS, 414, 2017

Lawson, J. D. 1973, Physics of Fluids, 16, 1298

Li, J., Spitkovsky, A., & Tchekhovskoy, A. 2012, ApJ, 746, 60

Liu, Y.-H., Guo, F., Daughton, W., Li, H., & Hesse, M. 2015, Physical Review Letters, 114, 095002

Longcope, D. W. & Strauss, H. R. 1994, ApJ, 437, 851

Lyubarsky, Y. E. 2003, MNRAS, 345, 153

—. 2005, MNRAS, 358, 113

—. 2012, MNRAS, 427, 1497

Lyutikov, M. 2003a, MNRAS, 346, 540

—. 2003b, New A Rev., 47, 513

—. 2006a, MNRAS, 369, L5

—. 2006b, New Journal of Physics, 8, 119

—. 2010, MNRAS, 405, 1809

Lyutikov, M., Balsara, D., & Matthews, C. 2012, MNRAS, 422, 3118

Lyutikov, M., Komissarov, S. S., & Porth, O. 2016, MNRAS, 456, 286

Lyutikov, M. & Lazarian, A. Topics in Microphysics of Relativistic Plasmas, ed. A. M. Davis, 383

Lyutikov, M., Pariev, V. I., & Blandford, R. D. 2003, ApJ, 597, 998

Lyutikov, M. & Uzdensky, D. 2003, ApJ, 589, 893

Michel, F. C. 1973, ApJ, 180, 207

Mignone, A., Striani, E., Tavani, M., & Ferrari, A. 2013, MNRAS, 436, 1102

Mizuno, Y., Lyubarsky, Y., Nishikawa, K.-I., & Hardee, P. E. 2011, ApJ, 728, 90

Moffatt, H. K. 1986, Journal of Fluid Mechanics, 166, 359

Molodensky, M. M. 1974, Sol. Phys., 39, 393

Nalewajko, K., Uzdensky, D. A., Cerutti, B., Werner, G. R., & Begelman, M. C. 2015, ApJ, 815, 101

Parker, E. N. 1983, ApJ, 264, 635

Pétri, J. & Lyubarsky, Y. 2007a, A&A, 473, 683

—. 2007b, A&A, 473, 683

Porth, O., Komissarov, S. S., & Keppens, R. 2013, MNRAS, 431, L48

—. 2014a, MNRAS, 438, 278

Porth, O., Xia, C., Hendrix, T., Moschou, S. P., & Keppens, R. 2014b, ApJS, 214, 4

Priest, E. & Forbes, T. 2000, Magnetic Reconnection

Rees, M. J. & Gunn, J. E. 1974, MNRAS, 167, 1

Roberts, G. O. 1972, Royal Society of London Philosophical Transactions Series A, 271, 411

Rudy, A., Horns, D., DeLuca, A., Kolodziejczak, J., Tennant, A., Yuan, Y., Buehler, R., Arons, J., Blandford, R., Caraveo, P., Costa, E., Funk, S., Hays, E., Lobanov, A., Max, C., Mayer, M., Mignani, R., O'Dell, S. L., Romani, R., Tavani, M., & Weisskopf, M. C. 2015a, ArXiv e-prints

—. 2015b, ApJ, 811, 24

Shklovsky, I. S. 1970, ApJ, 159, L77

Sironi, L., Petropoulou, M., & Giannios, D. 2015, MNRAS, 450, 183

Sironi, L. & Spitkovsky, A. 2011a, ApJ, 741, 39

—. 2011b, ApJ, 726, 75

—. 2012, Computational Science and Discovery, 5, 014014

—. 2014, ApJ, 783, L21

Sironi, L., Spitkovsky, A., & Arons, J. 2013, ApJ, 771, 54

Spitkovsky, A. 2005, in AIP Conf. Ser., Vol. 801, Astrophysical Sources of High Energy Particles and Radiation, ed. T. Bulik, B. Rudak, & G. Madejski, 345

Sweet, P. A. 1969, ARA&A, 7, 149

Syrovatskii, S. I. 1975, Akademiia Nauk SSSR Izvestiia Seriia Fizicheskaia, 39, 359

—. 1981, ARA&A, 19, 163

Tavani et al. 2011, Science, 331, 736

Taylor, J. B. 1974, Phys. Rev. Lett., 33, 1139

Tchekhovskoy, A., Philippov, A., & Spitkovsky, A. 2016, MNRAS, 457, 3384

Thompson, T. A., Chang, P., & Quataert, E. 2004, ApJ, 611, 380

Tsiklauri, D. & Haruki, T. 2007, Physics of Plasmas, 14, 112905

—. 2008, Physics of Plasmas, 15, 102902

Uchida, T. 1997, Phys. Rev. E, 56, 2181

Usov, V. V. 1992, Nature, 357, 472

Uzdensky, D. A. 2011, Space Sci. Rev., 160, 45

Uzdensky, D. A., Cerutti, B., & Begelman, M. C. 2011, ApJ, 737, L40

Uzdensky, D. A., Loureiro, N. F., & Schekochihin, A. A. 2010, Physical Review Letters, 105, 235002

Vay, J.-L. 2008, Physics of Plasmas, 15, 056701

von der Pahlen, J. G. & Tsiklauri, D. 2014, Physics of Plasmas, 21, 060705

Weisskopf, M. C., Tennant, A. F., Arons, J., Blandford, R., Buehler, R., Caraveo, P., Cheung, C. C., Costa, E., de Luca, A., Ferrigno, C., Fu, H., Funk, S., Habermehl, M., Horns, D., Linford, J. D., Lobanov, A., Max, C., Mignani, R., O'Dell, S. L., Romani, R. W., Striani, E., Tavani, M., Taylor, G. B., Uchiyama, Y., & Yuan, Y. 2013, ApJ, 765, 56

Werner, G. R., Uzdensky, D. A., Cerutti, B., Nalewajko, K., & Begelman, M. C. 2016, ApJ, 816, L8

Woltier, L. 1958, Proc. Nat. Acad. Sci., 44, 489

Yuan, Y. & Blandford, R. D. 2015, MNRAS, 454, 2754

Zenitani, S. & Hoshino, M. 2007, ApJ, 670, 702

—. 2008, ApJ, 677, 530

Zrake, J. 2014, ApJ, 794, L26

A. Stability of unstressed X-point

The above analytical solution shows that the steady-state X-point solution is kind of unstable. This rises the question of how such configuration can be created in a first place. Indeed, unstable states of a dynamical system cannot be reached via its natural evolution. However, the X-point configuration considered in this analyses occupies the whole space and so is the perturbation that leads to its collapse. In reality, X-points and their perturbations occupy only finite volume and in order to address the stability issue comprehensively one has to study finite size configurations.

In this section we describe the response of X-point to small-scale perturbations studied via force-free simulations. In one of our experiments, we perturbed the steady-state X-point configuration by varying only the x-component of the magnetic field:

$$\delta B_x = B_\perp \sin(\pi y/L) \exp(-(y/L)^2)\,.$$

Obviously, the length scale this perturbation is L and to ensure that it is small we select a computational domain whose size is much larger than L. In this particular case we put $B_\perp = L = 1$ and use the computational domain $(-6,6)\times(-6,6)$ with 300 cells in each direction. Fig. 80 shows the initial configuration and the solution at $t = 7$. One can see that the perturbation does not push the X-point away from its steady-state. On the contrary, the waves created by the perturbation leave the central area on the light crossing time and the steady-state configuration is restored. Although, here we present the results only for this particular type of perturbation, we have tried several other types and obtained the same outcome. Thus, we conclude that the magnetic X-point is stable to perturbations on a length scale which is much smaller compared to its size, even when the perturbation amplitude is substantial.

We have also verified the stability of unstressed X-points with PIC simulations. Here, no initial perturbation is imposed on the system. In the standard setup of anti-parallel reconnection, the system would grow unstable from particle noise. Here, we have demonstrated that an unstressed X-point is stable to noise-level fluctuations.

This preprint was prepared with the AAS LaTeX macros v5.2.

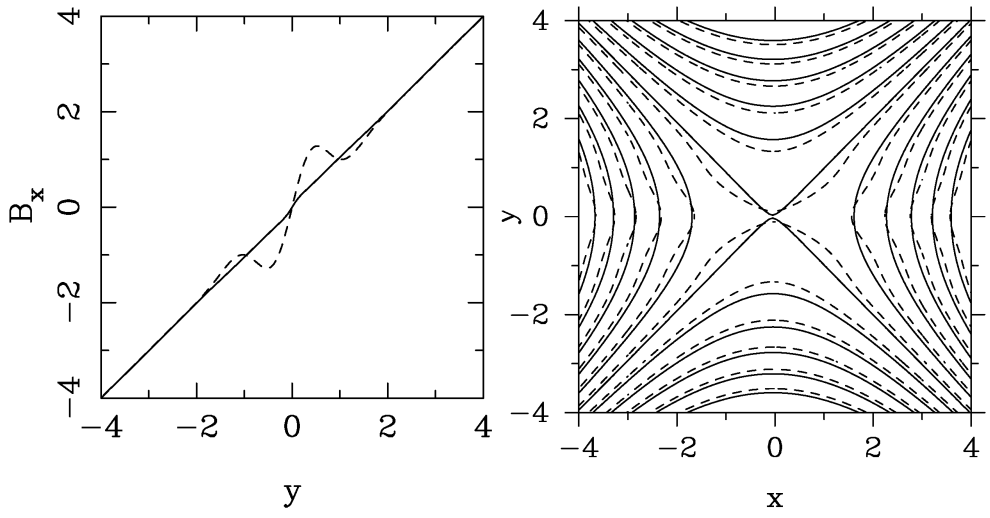

Fig. 80.— Stability of the X-point to small-scale perturbations in force-free simulations. The left panel shows the x component of the magnetic field along the line $y = 0$. The dashed line corresponds to the initial perturbed solution. The solid line corresponds to the numerical soultion at $t = 7$. The right panel shows the magnetic field lines of the initial solution (dashed lines) and the solution at $t = 7$.

B. Ideal instability of 2D magnetic ABC structures

As another look at the instability, consider fluctuations of the island sizes in $x - y$ direction. The following flux function

$$\Phi = B_0\alpha(t)\left(\cos(\alpha x(t)) - \cos\left(\frac{y}{\alpha(t)}\right)\right) \tag{B1}$$

with

$$\begin{aligned}
&\mathbf{B} = \nabla\Phi \times \mathbf{e}_z + \alpha(t)\Phi\mathbf{e}_z \\
&\mathbf{E} = \left\{B_0\alpha\alpha'\left(y\cos\left(\frac{y}{\alpha}\right) - 3\alpha\sin\left(\frac{y}{\alpha}\right)\right), -B_0\alpha'(\sin(\alpha x) + \alpha x\cos(x\alpha)),\right. \\
&\left.\frac{B_0\alpha'\left(\alpha x^2\sin(\alpha x) + \alpha\left(\cos\left(\frac{y}{\alpha}\right) - \cos(\alpha x)\right) + y\sin\left(\frac{y}{\alpha}\right)\right)}{\alpha}\right\}
\end{aligned} \tag{B2}$$

satisfies

$$\nabla \times \mathbf{E} + \partial_t\mathbf{B} = 0 \tag{B3}$$

The current is

$$\mathbf{J} = \frac{\mathbf{E}\times\mathbf{B}\,\mathrm{div}\,\mathbf{E} + \mathbf{B}\left(\mathbf{B}\cdot\mathrm{curl}\times\mathbf{B} - \mathbf{E}\mathrm{curl}\times\mathbf{E}\right)}{B^2} + \eta\frac{(\mathbf{E}\cdot\mathbf{B})}{B^2}\mathbf{B} \tag{B4}$$

Consider small fluctuations, so that $\alpha = 1 + \epsilon\alpha_1$, $\epsilon \ll 1$. Maxwell equation

$$\nabla \times \mathbf{B} = \mathbf{J} + \partial_t\mathbf{E} \tag{B5}$$

in the limit $x, y \to 0$ gives

$$2\eta\alpha_1' + 2\alpha_1'' - 2\alpha_1 = 0 \tag{B6}$$

with solutions

$$\alpha_1 = e^{\frac{1}{2}\left(-\sqrt{\eta^2+4}\pm\eta\right)t} = e^{\pm t}e^{-\eta t/2} \tag{B7}$$

Thus, there is exponential growth of perturbations even for zero resistivity.

C. The inverse cascade

The Woltjer-Taylor relaxation principle (Woltier 1958; Taylor 1974) states that magnetic plasma configuration try to reach so-called constant-α configuration, conserving helicity in the process of relaxation. Such relaxation process is necessarily dissipative, though the hope typically is that it is weakly dissipative. In case of 2D magnetic ABC structures the energy per helicity $\propto \alpha$; thus, according to the Woltjer-Taylor relaxation principle the system will try to reach a state with smallest α consistent with the boundary condition. This, formally, constitutes an inverse-type cascade of magnetic energy to largest scales. On the other hand, such cascade is highly dissipative: conservation of helicity requires that $B \propto \alpha^{3/2}$, thus magnetic energy per flux tube $B^2/\alpha^2 \propto \alpha$ decreases with the size of the tube (α is proportional to the inverse radius). This implies that a large fraction of the magnetic energy is dissipated at each scale of the inverse cascade - cascade is highly non-inertial. In contrast, the Woltjer-Taylor relaxation principle assumes a weakly resistive process. Highly efficient dissipation of magnetic energy is confirmed by our numerical results that indicate that during merger approximately half of the magnetic energy is dissipated, §6. As a results such cascade cannot lead to an efficient energy accumulation on the largest scales.

To find the scaling of the cascade, consider a helicity-conserving merger of two islands parametrized by B_1 and α_1. Conservation of helicity requires that in the final stage (subscript 2) $H_2 \equiv B_2^2/\alpha_2^3 = 2H_1 = 2B_1^2/\alpha_1^3$. From the conservation of area $\alpha_2 = \alpha_1/\sqrt{2}$; then $B_2 = B_1/\sqrt{2}$. The magnetic energy of the new state $E_2 = \sqrt{2}B_1^2/\alpha_1^2 < 2B_1^2/\alpha_1^2$. Thus a fraction $1 - 1/\sqrt{2} = 0.29$ of the magnetic energy is dissipated in each step.

Next, in each step the size of the island growth by $\sqrt{2}$. After n steps the scale is $\propto \sqrt{2}^n$, while the energy $\propto (1-1/\sqrt{2})^n$. The two power-laws are connected by the index $p = -\ln 2/(2\ln(1-1/\sqrt{2})) = 3.54$. This is very close to the result of Zrake (2014) who concluded that the power-law index is close to 7/2 (the initial conditions used by Zrake 2014, are different from ours).

The efficient dissipation of the magnetic energy is confirmed by our numerical results that indicate that during merger a large fraction of the magnetic energy is dissipated. As a results such cascade cannot lead to an efficient energy accumulation on largest scales.

In addition, we have verified that the final states are close to force-free. Due to square box size and periodic boundary conditions, the following family of force-free solutions is then appropriate:

$$\begin{aligned} A_z &= \cos ax \sin \sqrt{\alpha^2 - a^2}y, \\ \mathbf{B} &= \nabla \times A_z + \alpha A_z \mathbf{e}_z \end{aligned} \tag{C1}$$

In particular, $A_z = \cos(x/\sqrt{5})\sin(2y\sqrt{5})$ produces two islands, Fig. 81.

Thus, we conclude that the inverse cascade of 2D magnetic ABC structures proceeds through (nearly) force-free self-similar configurations of ever increasing size. But the cascade is non-inertial (highly dissipative) with the approximate index of 3.54.

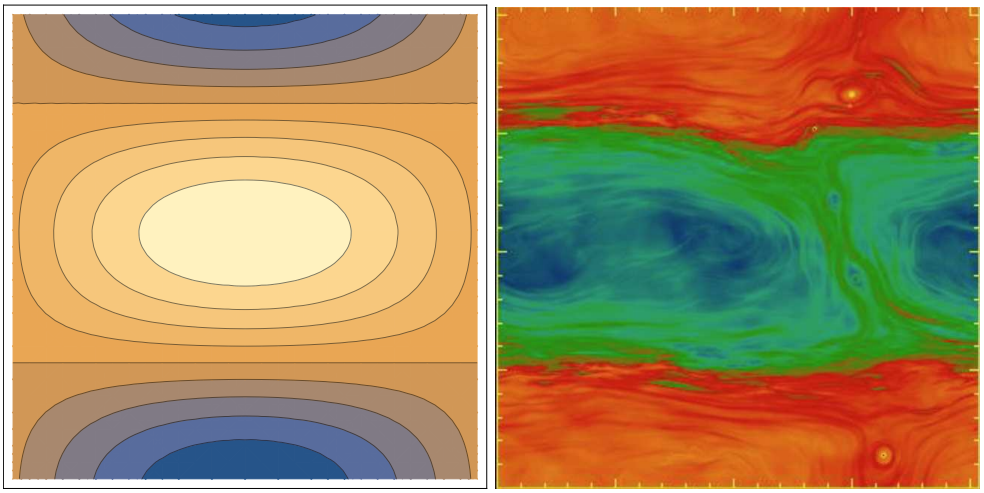

Fig. 81.— Comparison of a 2:1 force-free state with the final structure of PIC simulations (at time 19.01).